

# **The Development of an Electro-optical Goniometric Sensor for Tracking Articulated Hand Motion**



**LEFAN WANG**

School of Engineering  
Cardiff University

This thesis is submitted in fulfilment of the requirement for the degree of  
*Doctor of Philosophy*

# Declaration

## **DECLARATION**

This work has not been submitted in substance for any other degree or award at this or any other university or place of learning, nor is being submitted concurrently in candidature for any degree or other award.

Signed .....(candidate)      Date.....

## **STATEMENT 1**

This thesis is being submitted in partial fulfilment of the requirements for the degree of Doctor of Philosophy (PhD).

Signed .....(candidate)      Date.....

## **STATEMENT 2**

This thesis is the result of my own independent work/investigation, except where otherwise stated, and the thesis has not been edited by a third party beyond what is permitted by Cardiff University's Policy on the Use of Third Party Editors by Research Degree Students. Other sources are acknowledged by explicit references. The views expressed are my own.

Signed .....(candidate)      Date.....

## **STATEMENT 3**

I hereby give consent for my thesis, if accepted, to be available online in the University's Open Access repository and for inter-library loan, and for the title and summary to be made available to outside organisations.

Signed .....(candidate)      Date.....

## Abstract

The study of hand kinematics has developed into an important research area. Several techniques have been proposed for recording hand movements, however the majority suffer from poor accuracy and limited functionality. To overcome these limitations, this research aims to develop a novel goniometric sensor for tracking articulated hand motion.

This research is the first attempt to use Malus' law as a sensing principle for monitoring human hand kinematics. Three distinct electro-optical sensors (sensor#1, sensor#2, and sensor#3) with compact configurations are developed. They are coupled with the rotation of the finger joints and detect angular motion by analysing the attenuation of light transmitted through linear polarising films.

The three goniometric sensors are designed with different measurement capabilities to suit different types of finger articulation. Sensor#1 has a single rotation axis and a measuring range of  $0^\circ$  to  $90^\circ$ , which can be used for the distal interphalangeal joints. Sensor#2 can measure the movements spanning  $180^\circ$  with an improved sensitivity in a single plane; this is ideal for the proximal interphalangeal joints. Sensor#3 consists of two measurement axes, each having a measurement range up to  $180^\circ$ . These properties make sensor#3 suitable for monitoring the finger joints with two degrees of freedom (DOFs), e.g. the metacarpophalangeal joints; this is unique in designing a single sensor for monitoring the two-DOF finger joints.

In comparison with a commonly used commercial bend sensor, the electro-optical sensors demonstrate higher measurement accuracy (mean absolute error:  $\leq 0.28^\circ$ ) and faster response time under laboratory conditions. Furthermore, the developed sensors all successfully tracked the dynamic finger motion when attached to human finger joints. This work verifies that the developed electro-optical sensors offer a viable sensing technique for tracking articulated human motion directly with high measurement accuracy.

## **Acknowledgements**

First, I would like to express my sincere appreciation to my supervisors, Dr Turgut Meydan and Dr Paul Ieuan Williams for giving me the opportunity to pursue the bio-engineering sensing technology at Cardiff University, for their continuous support, guidance, motivation, inspiration, and beneficial suggestions during my PhD research.

I would also like to thank the staff at Wolfson Centre for Magnetism, in particularly Dr Tomasz Kutrowski, Dr Shaikh Hashimdeen, and Dr Jerome Cuenca for their kind assistance, criticism, and great patience in helping solve the research problems.

My sincere thanks also go to my colleagues and friends: Sahar, Noor, Maha, Gregory, Warrick, Robert, David, and Saddam, for the regular discussions, suggestions, concerns, and also the enjoyable time they provided. They made my research life full of interests.

I also appreciate the support from the staff in School of Engineering, Cardiff University for everything that facilitated my research work.

Last but not least, I would like to thank my parents and my grandparents for their endless emotional support and unconditional love. A special thanks to my boyfriend Mr Pingfan Song who gave me spiritual support, encouragement, and great care and love, helped me to be confident, and shared the latest technology news. I would have never had made this work without them.

# Publications

## Journal articles

- **L. Wang**, T. Meydan, and P. I. Williams. A two-axis goniometric sensor for tracking finger motion. *Sensors*, vol. 17, no. 4, p. 770, 2017.
- **L. Wang**, T. Meydan, and P. I. Williams. Design and evaluation of a 3-D printed optical sensor for monitoring finger flexion. *IEEE Sens. J.*, vol. 17, no. 6, pp. 1937–1944, 2017.

## Conference papers

- **L. Wang**, T. Meydan, and P. I. Williams, and T. Kutrowski. A proposed optical-based sensor for assessment of hand movement. In *Proc. IEEE Sensors 2015*, Busan, South Korea, pp. 1-4.
- **L. Wang**, T. Meydan, and P. I. Williams. An optical sensor for tracking hand articulations. In *Proc. IEEE Sensors 2016*, Orlando, FL, USA, pp. 1–3.

# Contents

<b>Declaration</b>	<b>ii</b>
<b>Abstract</b>	<b>iii</b>
<b>Acknowledgements</b>	<b>iv</b>
<b>Publications</b>	<b>v</b>
<b>Contents</b>	<b>vi</b>
<b>List of figures</b>	<b>ix</b>
<b>List of tables</b>	<b>xvi</b>
<b>Nomenclature</b>	<b>xvii</b>
<b>1 Introduction</b>	<b>1</b>
1.1 Motivation . . . . .	1
1.2 Thesis Outline . . . . .	3
<b>2 Human Hand Kinematics and Polarisation of Light</b>	<b>5</b>
2.1 Human Hand Skeleton and Kinematics . . . . .	5
2.1.1 Hand Skeleton and Structure of Articulated Finger Joints . . . . .	5
2.1.2 Human Finger Kinematics . . . . .	7
2.2 Polarisation of Light . . . . .	10
2.2.1 Introduction to Polarisation . . . . .	11
2.2.2 Malus' Law . . . . .	12
2.3 Summary . . . . .	14
<b>3 Review on Sensing Technologies and Instrumented Systems for Tracking Hand Motion</b>	<b>15</b>
3.1 Sensing Technologies for Tracking Finger Motion . . . . .	15
3.1.1 Flexible Resistive Sensors – Strain Gauges and Bend Sensors . . . . .	16
3.1.2 Optical Angle Sensors . . . . .	26
3.1.3 MEMS Gyroscopes and Accelerometers . . . . .	34
3.1.4 Magnetic Induction-based Sensors . . . . .	39
3.1.5 Other Sensing Techniques . . . . .	41
3.2 Hand Motion Tracking Devices . . . . .	43
3.2.1 Camera-based Motion Capture Systems . . . . .	43
3.2.2 Surface Electromyography (EMG)-based Systems . . . . .	45
3.2.3 Instrumented Glove Devices for Hand Motion Acquisition . . . . .	45

---

3.3	Summary . . . . .	53
<b>4</b>	<b>Electro-optical Goniometric Sensor Design and Experimental Methods</b>	<b>54</b>
4.1	Electro-optical Goniometric Sensor Design . . . . .	54
4.1.1	Operating Principle of the Electro-optical Goniometric Sensors	54
4.1.2	Sensor Models for 3D Printing and Integrated Goniometric Sensors . . . . .	58
4.2	Motorised Measurement System and Software Design to Investigate Sensor Characteristics . . . . .	63
4.2.1	Measurement System Overview . . . . .	63
4.2.2	Sensor Signal Conditioning Circuitry Design . . . . .	66
4.2.3	Weighted-average Fusion Method for Multichannel Signal Data	68
4.2.4	Software for Measurement System Control and Sensor Data Acquisition . . . . .	72
4.3	Summary . . . . .	79
<b>5</b>	<b>Sensor Static and Dynamic Characteristics</b>	<b>81</b>
5.1	Sensor Static Characteristics . . . . .	81
5.1.1	Performance of the Single-axis Electro-optical Sensor . . . . .	81
5.1.2	Performance of the Single-axis Electro-optical Sensor Using Data Fusion Approach . . . . .	89
5.1.3	Performance of the Two-axis Electro-optical Sensor Using Data Fusion Method . . . . .	95
5.1.4	Performance of the Commonly Used Commercial Resistive Bend Sensor . . . . .	104
5.1.5	Comparison of Sensor Static Characteristics . . . . .	110
5.2	Evaluation of the Dynamic Responses of the Electro-optical Goniometric Sensor and the Commercial Bend Sensor . . . . .	117
5.3	Summary . . . . .	119
<b>6</b>	<b>Electro-optical Goniometric Sensors for Tracking Finger Motion</b>	<b>121</b>
6.1	The DIP Joint Motion Detection Using the Single-axis Electro-optical Sensor . . . . .	121
6.1.1	Sensor Attachment to Finger DIP Joint . . . . .	121
6.1.2	Monitoring Flexion and Extension of the DIP Joint . . . . .	122
6.2	Measurement of the PIP joint Motion Using the Single-axis Sensor with Data Fusion Method . . . . .	124
6.2.1	Sensor Attachment to Finger PIP Joint . . . . .	124
6.2.2	Measuring Flexion and Extension of the PIP Joint . . . . .	125
6.3	Motion Detection of the MCP Joints . . . . .	128
6.3.1	Flexion and Extension of the Index MCP Joint . . . . .	128
6.3.2	Abduction and Adduction of the Index MCP Joint . . . . .	130
6.3.3	Simultaneous Flexion/Extension and Abduction/Adduction of the Index MCP Joint . . . . .	131
6.3.4	Circumduction of the Index MCP Joint . . . . .	132
6.4	Summary . . . . .	132
<b>7</b>	<b>Conclusion and Future Work</b>	<b>134</b>
7.1	Conclusions . . . . .	134

---

7.2 Future Directions . . . . .	137
<b>Bibliography</b>	<b>139</b>
<b>Appendix A Technical Drawings of the Electro-optical Goniometric Sensors</b>	<b>159</b>
<b>Appendix B Software Design</b>	<b>171</b>

# List of figures

1.1	Manual goniometer typically used to measure the range of motion of the finger joints in clinics. . . . .	2
2.1	Left hand bones and joints. . . . .	6
2.2	Structure of the synovial joints involved in human fingers. <b>(a)</b> Hinge joint, performing motion in one plane; <b>(b)</b> ellipsoid joint, allowing movements in two planes; <b>(c)</b> saddle joint, allowing limited motion in two planes. . . . .	7
2.3	Finger motion: flexion, extension, abduction, adduction, circumduction, and thumb opposition. . . . .	8
2.4	The electric fields of three different polarisations. <b>(a)</b> Linear polarisation; <b>(b)</b> circular polarisation; <b>(c)</b> elliptical polarisation. . . . .	11
2.5	P and S polarisations. . . . .	12
2.6	Illustration of Malus' Law. . . . .	13
3.1	Textile-based strain sensors and the instrumented sensing gloves. <b>(a)</b> Prototype of an instrumented glove using screen printing technique. <b>(b)</b> Instrumented glove coated with conductive mixture. <b>(c)</b> Sensing glove equipped with double-layered knitted piezoresistive fabrics. . . . .	17
3.2	Nanomaterial composited strain sensors. <b>(a)</b> Highly elastic strain sensor based on CNT fibres. <b>(b)</b> Multi-walled CNTs based strain sensor. <b>(c)</b> Wrinkled CNTs thin film strain sensor. <b>(d)</b> Transparent graphene strain sensor in a form of rosette. <b>(e)</b> Flexible nanopaper based on crumpled graphene and nanocellulose. <b>(f)</b> Graphene foam based strain sensor. <b>(g)</b> Conductive hybrids of graphene and AgNPs based sensor. <b>(h)</b> Sandwich-structured and simple-structured AgNW-PDMS nanocomposite strain sensors. . . . .	19
3.3	Microfluidic strain sensors. <b>(a)</b> Soft strain sensor embedded with eGaIn-filled microchannel. <b>(b)</b> Two types of eGaIn-filled microfluidic strain sensors. <b>(c)</b> Microfluidic strain sensor filled with hybrid liquid conductors. <b>(d)</b> Artificial skin prototype embedded with hybrid-liquid-based strain sensors. . . . .	21

3.4	Images of commercial bend sensors. <b>(a)</b> Bi-directional bend sensors manufactured by Images SI. <b>(b)</b> Bend sensors produced by Spectra Symbol. <b>(c)</b> Bend sensors with different lengths manufactured by Flexpoint SS. <b>(d)</b> Custom design, bend sensor array produced by Flexpoint SS. . . . .	23
3.5	Instrumented glove systems equipped with resistive bend sensors manufactured by Flexpoint SS. <b>(a)</b> Shadow Monitor. <b>(b)</b> NeuroAssess Glove. <b>(c)</b> WU-Glove. <b>(d)</b> Sensing glove designed by Borghetti et al. <b>(e)</b> Tyndall/UU glove (ver. 1). <b>(f)</b> HITEG-Glove. . . . .	25
3.6	Self-developed bend sensors. <b>(a)</b> PEDOT:PSS patterned bend sensor. <b>(b)</b> Different bend sensor patterns. <b>(c)</b> Glove cover embedded with 3D printed bend sensors. . . . .	26
3.7	Images of the FBG-based sensing polymer matrix. . . . .	27
3.8	Basic structure of hetero-core optical fibre. . . . .	29
3.9	Configuration of the embedded hetero-core fibre-optic sensor on human hand. . . . .	30
3.10	Optical fibre bending transducer based on the microbending attenuation.	30
3.11	SmartGlove integrated with ten commercial optical linear encoders. . . . .	32
3.12	<b>(a)</b> Wearable input device, SCURRY. <b>(b)</b> The UU/Tyndall smart glove equipped with 16 IMUs. <b>(c)</b> Motion-capture glove. <b>(d)</b> PowerGlove equipped with multiple IMUs. <b>(e)</b> Modified PowerGlove only equipped with gyroscopes and accelerometers. <b>(f)</b> Hand motion tracking systems with IMU-based sensing strips. . . . .	37
3.13	<b>(a)</b> Positions of the sensing and generator coils. <b>(b)</b> Structure of the magnetic hand tracking system. <b>(c)</b> <i>uTrack</i> , a 3D input device. <b>(d)</b> <i>Finexus</i> , a multiple fingertip capturing system. . . . .	40
3.14	Sensor configurations in glove-based systems. <b>(a)</b> CyberGlove II, in which the abduction sensors are in an arched configuration. <b>(b)</b> Soft strain sensor based system, in which the abduction sensor was attached to the proximal phalanxes of adjacent fingers in a straight line. . . . .	51
3.15	Problems of using one-DOF flexible sensors to track the movements of two-DOF joints. <b>(a)</b> Normal sensor position. <b>(b)</b> Finger flexion/extension without ABD/ADD. <b>(c)</b> Crossed finger gesture. . . . .	52
4.1	The schematic diagram of sensor#1, a basic single-axis sensor. . . . .	55
4.2	The schematic diagram of sensor#2, an improved single-axis sensor. PL <sub>20</sub> represents a linear polariser. AL <sub>2j</sub> and PD <sub>2j</sub> represent the linear analyser and the photodiode in the channel CH <sub>2j</sub> ( $j = 1, 2$ ), respectively. . . . .	56

4.3	The schematic diagram of sensor#3, a two-axis electro-optical goniometric sensor. $PL_{3j}$ , $AL_{3j}$ , and $PD_{3j}$ represent a linear polariser, a linear analyser and a photodiode in the channel $CH_{3j}$ ( $j = 1, 2, 3$ , and $4$ ), respectively. . . . .	58
4.4	Sensor#1, a single-axis electro-optical sensor with a measuring range of $90^\circ$ . All units are in millimetres. <b>(a)</b> The 3D model design; <b>(b)</b> the images of the complete sensor and the PCBs for the LED and photodiode.	60
4.5	Sensor#2, a single-axis electro-optical sensor with improved measuring capability. All units are in millimeters. <b>(a)</b> The 3D model design; <b>(b)</b> a photograph of the integrated sensor. . . . .	61
4.6	Sensor#3, a two-axis goniometric sensor. All units are in millimetres. <b>(a)</b> The 3D model design; <b>(b)</b> a photograph of the integrated sensor and the two rectangular hollow parts glued on the adhesive plasters; <b>(c)</b> an example of the sensor's placement on the MCP joint of the left index finger. . . . .	62
4.7	The block diagram of the automated measurement apparatus. Under the drive of the controller BS201, the motorised stage NR360S is used to adjust the rotation speed and angle. The sensor is connected to the rotation stage by the clamps. The sensor outputs are conditioned, acquired, and stored in the PC. . . . .	63
4.8	The photograph of the automated measurement apparatus. . . . .	64
4.9	<b>(a)</b> Photograph of the mechanical set-up for holding sensors; <b>(b)</b> the method to hold the electro-optical goniometric sensor; <b>(c)</b> the approach to fix the commercial bend sensor. . . . .	65
4.10	The conditioning circuits. <b>(a)</b> The current-to-voltage converter for a single channel of the optical sensors, $R_2=3\text{ M}\Omega$ , $R_3=820\ \Omega$ , $C_1=3.3\text{ pF}$ , $C_2=0.1\ \mu\text{F}$ , $R_1=3.3\text{ M}\Omega$ (sensor#2 and sensor#3) or $6.6\text{ M}\Omega$ (sensor#1); <b>(b)</b> the resistance-to-voltage converter for the bend sensor, $V_{ref}=0.5\text{ V}$ , $R_5=39\text{ k}\Omega$ , and $R_b$ represents the sensor resistance. . . . .	66
4.11	The simulated signals ( $y_1$ and $y_2$ ) with the same amplitude but a phase difference of $45^\circ$ . They are proportional to the square of the cosine of the angle variable $\beta_1$ . The signals can be divided into three regions: I, II, and III according to the output amplitudes, and they can be further divided into six subregions (A-F) based on the angular position with the maximum or minimum output. . . . .	69
4.12	The angle variables calculated using the simulated output signals and the mathematical model. . . . .	70
4.13	Incremental sensitivity for $0.5^\circ$ steps. . . . .	71

4.14	The simplified LabVIEW block diagram for evaluating the sensor's static characteristics. The iterative actions included motor rotation, data acquisition, data display and storage. . . . .	73
4.15	The simplified LabVIEW block diagram for evaluating the sensor dynamic responses. The motorised stage keeps rotating continuously until it reaches to the specified angular position. Synchronous to the motor's rotation, the data acquisition and processing of the motor's trajectory and the sensor outputs are performed in two producer/consumer loops. . . . .	74
4.16	The LabVIEW graphical user interface for testing sensor characteristics.	75
4.17	The simplified LabVIEW block diagram for evaluating the data fusion method. A sequence of uniformly distributed pseudorandom angle values is generated to control the system rotation. After the motor moves to the specific angle, the sensor data acquisition and processing is performed. . . . .	76
4.18	The user interface for evaluating the efficiency of the data fusion method for sensor#2 and sensor#3. . . . .	77
4.19	The simplified LabVIEW block diagram for monitoring finger motion. After the confirmation of the finger joint to be measured, the sensor output acquisition and the data processing are triggered in the producer and consumer loops, respectively; meanwhile, the single-camera system also starts to record the finger movements. . . . .	78
4.20	The user interface for monitoring finger motion. . . . .	79
5.1	The voltage-to-angle relationship of sensor#1 in the range of $-20^{\circ}$ to $100^{\circ}$ .	82
5.2	The clockwise and anticlockwise outputs of sensor#1 for the rotations ranging from $-20^{\circ}$ to $100^{\circ}$ . . . . .	84
5.3	The output voltages of sensor#1 during the five repeated rotation tests in the range of $-20^{\circ}$ to $100^{\circ}$ . The readings at $10^{\circ}$ and $45^{\circ}$ are enlarged as examples. . . . .	85
5.4	The rotation angles derived from the output voltages of sensor#1 during the five repeated tests in the range of $0^{\circ}$ to $90^{\circ}$ . The results at $10^{\circ}$ and $45^{\circ}$ are enlarged as examples. . . . .	86
5.5	The outputs of sensor#1 at different rotating angles over 180 minutes. <b>(a)</b> is the sensor output at the rotation angle of $30^{\circ}$ ; <b>(b)</b> for $45^{\circ}$ ; <b>(c)</b> for $60^{\circ}$ ; and <b>(d)</b> for $90^{\circ}$ . $V_{\text{aver}}(\delta)$ represents the averaged output reading of sensor#1 at the angular position $\delta$ ( $\delta=30^{\circ}, 45^{\circ}, 60^{\circ},$ and $90^{\circ}$ ). . . .	88
5.6	The voltage-to-angle relationship of the two sensing channels of sensor#2 ( $CH_{21}$ and $CH_{22}$ ) in the range of $-90^{\circ}$ to $110^{\circ}$ . . . . .	89

5.7	The clockwise and anticlockwise output voltages of the two sensing channels of sensor#2. CH <sub>21</sub> _Clockwise and CH <sub>21</sub> _Anticlockwise represent the outputs of CH <sub>21</sub> when sensor#2 rotates from -90° to 110°, and then back to -90°. Similarly, CH <sub>22</sub> _Clockwise and CH <sub>22</sub> _Anticlockwise represent the corresponding readings of CH <sub>22</sub> . . . . .	91
5.8	The output readings of CH <sub>21</sub> of sensor#2 during the five repeated measurements in the range of -90° to 110°. The readings at -10° and 55° are enlarged as examples. . . . .	92
5.9	The output readings of CH <sub>22</sub> of sensor#2 during the five repeated measurements in the range of -90° to 110°. The readings at -10° and 55° are enlarged as examples. . . . .	92
5.10	The rotation angles derived from the outputs of sensor#2 for the five repeated tests in the range of -70° to 110°. . . . .	93
5.11	The differences between the measured readings of sensor#2 and the predefined pseudorandom testing angle for the range of -70° to 110°. . . . .	94
5.12	The voltage-to-angle relationship of CH <sub>31</sub> and CH <sub>33</sub> of sensor#3 for the rotations about the x-axis in the range of -100° to 100°. . . . .	96
5.13	The voltage-to-angle relationship of CH <sub>32</sub> and CH <sub>34</sub> of sensor#3 for the rotations about the y-axis in the range of -100° to 100°. . . . .	97
5.14	The outputs of sensor#3 for the clockwise and the anticlockwise rotations about the x-axis. CH <sub>31</sub> _Clockwise and CH <sub>31</sub> _Anticlockwise represent the outputs of CH <sub>31</sub> when sensor#3 rotates from -100° to 100°, and then back to -100°. Similarly, CH <sub>33</sub> _Clockwise and CH <sub>33</sub> _Anticlockwise represent the corresponding readings of CH <sub>33</sub> . . . . .	99
5.15	The outputs of sensor#3 for the clockwise and the anticlockwise rotations about the y-axis. CH <sub>32</sub> _Clockwise and CH <sub>32</sub> _Anticlockwise represent the outputs of CH <sub>32</sub> when sensor#3 rotates from -100° to 100°, and then back to -100°. Similarly, CH <sub>34</sub> _Clockwise and CH <sub>34</sub> _Anticlockwise represent the corresponding readings of CH <sub>34</sub> . . . . .	100
5.16	The measured results of sensor#3 during the five repeated tests. <b>(a)</b> Outputs of CH <sub>31</sub> ; <b>(b)</b> outputs of CH <sub>33</sub> ; <b>(c)</b> outputs of CH <sub>32</sub> ; <b>(d)</b> outputs of CH <sub>34</sub> . For each channel, the reading at 35° are enlarged as an example.	101
5.17	The rotation angles derived from the outputs of CH <sub>31</sub> and CH <sub>33</sub> of sensor#3 for the five repeated tests about the x-axis in the range of -80° to 100°. The readings at -20° and 35° are enlarged as examples. . . . .	102
5.18	The rotation angles derived from the outputs of CH <sub>32</sub> and CH <sub>34</sub> of sensor#3 for the five repeated tests about the y-axis in the range of -90° to 90°. The readings at -20° and 35° are enlarged as examples. . . . .	102

5.19	The differences between the measured angular outputs of sensor#3 and the predefined pseudorandom testing angles spanning 180°. <b>(a)</b> The results for the rotations about the x-axis; <b>(b)</b> the results for the rotations about the y-axis. . . . .	104
5.20	The voltage-to-angle relationship of the commercial bend sensor in the flexion range of -20° to 100°. . . . .	105
5.21	The outputs of the commercial bend sensor during clockwise and anticlockwise flexion ranging from -20° to 100°. . . . .	106
5.22	The output readings of the commercial bend sensor for the five repeated measurements in the range of -20° to 100°. . . . .	107
5.23	The flexion angles derived from the outputs of the commercial bend sensor for the five repeated tests in the range of 0° to 100°. The orange dashed line represents the ideal sensor outputs, i.e. the derived sensor angles equal to the predefined flexion. . . . .	108
5.24	The outputs of the commercial bend sensor at different bending angles over 180 minutes. <b>(a)</b> is the sensor outputs with the flexion angle of 30°; <b>(b)</b> for 45°; <b>(c)</b> for 60°; and <b>(d)</b> for 90°. . . . .	109
5.25	Drift ratios of the commercial bend sensor and the developed optical sensor (sensor#1) at different bending angles over 180 minutes: <b>(a)</b> is the result with the flexion angle of 30°; <b>(b)</b> for 45°; <b>(c)</b> for 60°; <b>(d)</b> for 90°. IV_O represents the initial voltage reading of sensor#1 at the corresponding angular position, and IV_B is for the commercial bend sensor. . . . .	111
5.26	Dynamic performance of sensor#1 and the commercial bend sensor at different rotation speeds. Sensor performance at the maximum velocity: <b>(a)</b> for 15°/s; <b>(b)</b> for 25°/s; <b>(c)</b> for 35°/s; <b>(d)</b> for 45°/s. . . . .	118
6.1	The attachment of sensor#1 to a left handed nylon glove (the DIP joint of the index finger) and the motion estimation method using video sequences. (a) The front view of sensor attachment; (b) the lateral view of sensor attachment; (c) the video-based method used to estimate finger movements. The four blue markers (A-D) are put for the video recordings.	122
6.2	The continuous flexion and extension of the DIP joint of the index finger. The actions in the dotted box were repeated continuously. . . . .	123

6.3	Examples of the sensors' attachment to the left handed nylon glove, <b>(a)</b> red mark indicating the location of the commercial bend sensor, which was embedded under sensor#2; <b>(b)</b> attachment detail of the commercial bend sensor, on the dorsal surface of the PIP joint; <b>(c)</b> attachment detail of sensor#2, above the dorsal surface of the PIP joint of the left index finger. . . . .	125
6.4	The flexion and extension of the PIP joint of the left index finger recorded by sensor#2 and the commercial bend sensor. The actions in the dotted box were repeated continuously. . . . .	126
6.5	The dynamic motion of the PIP joint of the left index finger recorded by sensor#2, the commercial bend sensor, and the video camera. The actions in the dotted box were repeated continuously over six cycles. . . . .	127
6.6	The method to estimate the flexion angle of the MCP joint. . . . .	129
6.7	The flexion and extension of the MCP joint of the left index finger. Fingers repeated the actions in the dotted box continuously, and finally returned to the initial state. . . . .	129
6.8	The abduction and adduction of the MCP joint of the participant's index finger. The fingers repeated the actions in the dotted box continuously, and finally returned to the initial state. . . . .	130
6.9	The simultaneous movements of the flexion/extension and ABD/ADD of the MCP joint of the index finger. The actions in the dotted box were repeated continuously. . . . .	131
6.10	The circumduction of the MCP joint of the index finger. . . . .	132

# List of tables

2.1	The general range of motion of each finger joint. . . . .	9
3.1	Summary of glove-based devices. . . . .	47
4.1	Calculation of the angular positions of the two simulated signals. . . . .	70
5.1	The amplification factor $k$ and the distance $r$ between the LED and the photodiode for the three electro-optical goniometric sensors. . . . .	98
5.2	Comparison of the sensor static characteristics. . . . .	112

# Nomenclature

## Roman Symbols

$a$	Offset output
$b$	Amplitude shift
$C$	Capacitance
$DH$	Hysteresis
$DR$	Drift ratio
$E$	Electric field
$I$	Light intensity
$i$	Electric current
$k$	Amplification factor
$m$	Amplification factor
$n$	Amplification factor
$R$	Resistance
$r$	Distance
$s$	Complex number (frequency parameter)
$V$	Voltage
$w$	Weight
$y_1$	Number sequence
$y_2$	Number sequence

## Greek Symbols

$\beta$	angle sequence
$\Delta$	change
$\delta$	relative rotation/flexion angle
$\phi$	angular position
$\varphi$	phase shift
$\theta_{DIP}$	flexion of the distal interphalangeal joint
$\theta$	angle of rotation
$\theta_{PIP}$	flexion of the proximal interphalangeal joint

## Subscripts

<i>b</i>	commercial bend sensor
<i>i</i>	the label of the electro-optical goniometric sensor
<i>ini</i>	initial value
<i>j</i>	sensing channel
max	the maximum value
min	the minimum value
<i>o</i>	electro-optical goniometric sensor
<i>out</i>	output value
<i>ref</i>	reference value
<i>t</i>	time
<i>x</i>	along the x-axis
<i>x'</i>	along the x'-axis
<i>y</i>	along the y-axis
<i>y'</i>	along the y'-axis

#### **Acronyms / Abbreviations**

3D	Three-dimension
ABD	Abduction
ADD	Adduction
AgNP	Silver Nanoparticle
AgNW	Silver Nanowire
AL	Analyser
CCD	Charge-coupled Device
CH	Channel
CMC	Carpometacarpal
CNT	Carbon Nanotube
Corp.	Corporation
Cu	Copper
DAQ	Data Acquisition
DIP	Distal Interphalangeal
DOF	Degree of Freedom
e.g.	Exempli gratia (Latin phrase, meaning 'for example')
eGaIn	Eutectic Gallium Indium
EMG	Electromyography
et al.	Et alia or et alii or et aliae (Latin phrase, meaning 'and others')
etc.	Et cetera (Latin phrase, meaning 'and so forth')
FBG	Fibre Bragg Grating
Flexpoint SS	Flexpoint Sensor Systems, Inc.
GF	Gauge Factor
HCI	Human-computer Interaction

---

i.e.	Id est (Latin phrase, meaning ‘that is’)
Images SI	Images Science Instruments, Inc.
IMU	Inertial Measurement Unit
Inc.	Incorporation
IP	Interphalangeal
KPF	Knitted Piezoresistive Fabric
Lab	Laboratory
LED	Light-emitting Diode
LLC.	Limited Liability Company
LPFG	Long Period Fibre Grating
Ltd.	Limited Company
MAE	Mean Absolute Error
MCP	Metacarpophalangeal
MEMS	Microelectromechanical Systems
MIT	Massachusetts Institute of Technology
Ni/SiO <sub>2</sub> /Si	Nickel/Silicon Dioxide/Silicon
NI	National Instruments
PCB	Printed Circuit Board
PC	Personal Computer
PDMS	Polydimethylsiloxane
PD	Photodiode
PEDOT:PSS	Poly(3,4-ethylenedioxythiophene) Polystyrene Sulfonates
PIP	Proximal Interphalangeal
plc	Public Limited Company
PL	Polariser
POF	Plastic Optical Fibre
ROM	Range of Motion
RSD	Relative Standard Deviation
SD	Standard Deviation
sensor#1	A single-axis goniometric sensor with a measurement range of 90°
sensor#2	A single-axis goniometric sensor with a wide measurement range of 180°
sensor#3	A two-axis goniometric sensor each axis capable of measuring 180°
SR	Statistical Range
ver.	Version
VR	Virtual Reality
ZnO	Zinc Oxide

# Chapter 1

## Introduction

### 1.1 Motivation

The human hand is complex, exhibiting multiple degrees of freedom (DOFs). It plays a vital role in performing daily activities combining motor and sensory functions. The hand's motor function can be impaired by disease, for instance, it is reported that 40 percent of people will at some point be affected by arthritis in at least one hand [1]. Other diseases such as Dupuytren's contracture and carpal tunnel syndrome also affect fine motor control and restrict movement. Inherited disorders such as epidermolysis bullosa cause a gradual loss of motor function due to generalised skin contracture. Hand function is also inhibited due to damage caused by sports and workplace injuries. For example, hand or wrist injuries account for 25% of all sports-related injuries [2] and approximately 13% of work-related injuries involve the hand [3]. Assessment of hand motor function is therefore essential to enable therapists to develop suitable hand treatments.

In clinics, range of motion (ROM) is considered an important aspect to evaluate hand motor function [4]. Hand therapists typically use a simple manual goniometer to assess the ROM of the fingers [5, 6]. The Rolyan® finger goniometer (Pattern Medical Ltd. [7], Nottingham, UK) shown in Figure 1.1 is most frequently used [4]. Such a method is only effective for static measurements, and is tedious and time-consuming when whole hand assessments are required [8]. The measurement accuracy ( $4^{\circ}$  -  $5^{\circ}$ ) is largely determined by the skill of the clinician or therapist [9]. Continuous and accurate monitoring of hand motion is highly desirable. This is not only essential for therapists to select an appropriate treatment but also important for evaluating the progress of recovery. An accurate sensing system that is able to provide continuous monitoring

of hand movements is long overdue, and there is a real need to develop a sensing technology to supplant existing clinical methods.



**Figure 1.1** Manual goniometer typically used to measure the range of motion of the finger joints in clinics [10].

Since the 1970s, considerable attention has been focused on researching methods for capturing hand dynamic movements. Various sensing techniques including vision-based sensors, flexible resistive sensors, optical fibre-based sensors, and magnetic sensors have been proposed and investigated. Using one or more of these sensing techniques, several motion tracking systems have been designed and evaluated [11, 12]. They can roughly monitor single or multiple finger joints and are mainly used for applications not requiring high accuracy, such as in entertainment and virtual control systems. However, the majority of these devices suffer from one or more major disadvantages including lack of measurement accuracy, limited functionality, time-consuming calibration procedures, complex signal processing and large computation times for multiple finger articulations. These disadvantages hinder the current instrumented systems from being used as reliable tools for high-accuracy applications, e.g. in clinical practice. Additionally, the available motion tracking systems detect finger movements in most cases using one-DOF sensors to track flexion and/or extension. This presents an obvious limitation for two-DOF finger joints (e.g. metacarpophalangeal) where finger abduction (ABD) and adduction (ADD) also occur. When single-DOF sensors are adopted to monitor the motion of two-DOF finger joints, the measurement accuracy is usually adversely affected by the crosstalk problem. Clearly, more efforts are still required to overcome these challenges.

The intensity of polarised light through two polarisers is described by Malus' law as a function of the angle between the two polarisation axes. It has previously been used as a sensing principle for measuring the relative rotation of mechanical objects [13–15]. The potential of this principle for high accuracy and direct measurement of rotation angles, were the main reasons for adopting this methodology in this work.

The main purpose of this research is to develop an effective sensing technique for tracking finger motion, providing a solution to solve the major problems faced in clinical practice and the current hand motion tracking systems. Since each finger joint generally possesses one or two DOFs in a limited space, the developed sensor must be capable of detecting various motion patterns and also be compact enough to suit the joint size. The specific objectives of this research include:

- Design and characterise a stable, repeatable, sensitive, and compact angle sensor which can be used to track the entire motion of the finger joint with one DOF, i.e. to capture finger flexion and extension.
- Develop and evaluate an accurate angle sensor for monitoring the movements of the two-DOF finger joints, e.g. the metacarpophalangeal joints. Accurate and simultaneous monitoring of two-DOF motion in human hand joints is an area underexplored in current glove-based systems.
- Investigate the performance of a typical commercial sensor. This can be used as a reference point for the developed sensors.
- Attach the developed sensors and the commercial sensor to finger segments and investigate their capabilities of measuring finger movements in real time. Use video and photography of hand gestures as a reference tool.

## 1.2 Thesis Outline

The contents discussed in each of the remaining chapters are summarised as follows.

**Chapter 2:** A brief introduction to the hand skeleton and kinematics is given, laying the foundation for a better understanding of the challenges in this research topic and the creation of possible solutions. The fundamental concepts of physical optics, including polarisation and Malus' law, are also introduced in this chapter, providing a theoretical framework for the sensing techniques adopted in this research work.

**Chapter 3:** This chapter reviews academic work and commercial sensing techniques used for tracking hand kinematics. The available hand motion tracking systems using one or more of these sensing techniques are also discussed and compared. Finally, the unsolved problems and challenges in hand motion detection are highlighted.

**Chapter 4:** In this chapter, the operating principle and the design method of the proposed electro-optical sensors are presented. The details of the automated

measurement system and the software design to characterise the sensor performance are also included. A data fusion approach is introduced to process the sensor outputs. Furthermore, a user-friendly graphical interface is also developed using LabVIEW programming to control the measurements of real finger motion.

**Chapter 5:** The characteristics of the three goniometric sensors including linearity, hysteresis, repeatability, temporal stability, measurement accuracy, as well as the dynamic response are investigated and discussed in this chapter. They are compared with a commonly used commercial bend sensor and also several other sensors reported for detecting finger motion.

**Chapter 6:** This chapter evaluates the capabilities of the goniometric sensors for tracking finger movements. The individual sensor is attached to the corresponding finger joint. When monitoring the proximal interphalangeal joint, the commercial bend sensor is also attached. The sensor outputs are analysed and compared with the video or photographic recordings which were obtained during the measurements.

**Chapter 7:** This chapter provides a conclusion of this thesis followed by a discussion on potential avenues for future research.

# Chapter 2

## Human Hand Kinematics and Polarisation of Light

The hand is an amazing feat of human evolution enabling incredible physical dexterity and the ability to manipulate and develop tools. Measuring hand motion is a major requisite in areas such as virtual reality (VR), robotics, hand therapy and rehabilitation, but it is difficult due to the highly complicated nature of the hand. Understanding anatomy is critical to develop methodologies for monitoring hand motion. In this chapter, the hand skeleton and kinematics are introduced along with the sensing principles adopted in this thesis.

### 2.1 Human Hand Skeleton and Kinematics

#### 2.1.1 Hand Skeleton and Structure of Articulated Finger Joints

The human hand is a remarkably complicated system which includes the palm and five digits, i.e. the thumb, index, middle, ring, and little finger. As illustrated in Figure 2.1, the skeleton of the human hand consists of 27 bones: eight small carpal bones, five metacarpal bones, and fourteen phalanges [16]. The carpal bones are commonly classified as two transverse rows: a proximal row ('A'-'D' in Figure 2.1) and a distal row ('E'-'H'). Among them, the four carpal bones of the distal row articulate with the bases of the metacarpals, forming five carpometacarpal (CMC) joints. The CMC joint of the thumb, which is also known as the trapeziometacarpal joint, differs significantly from the other four CMC joints and is therefore highlighted separately. The heads of the five metacarpal bones each articulate with the bases of the proximal phalanges of

the five digits, forming metacarpophalangeal (MCP) joints known as the knuckles. The phalanx bones including the proximal, middle, and distal phalanges make up the five fingers. The thumb only consists of two phalanges (proximal and distal), while the other four fingers each have three phalanx bones. The articulations between these phalanges are interphalangeal (IP) joint (only for thumb) or proximal interphalangeal (PIP) and distal interphalangeal (DIP) joints.

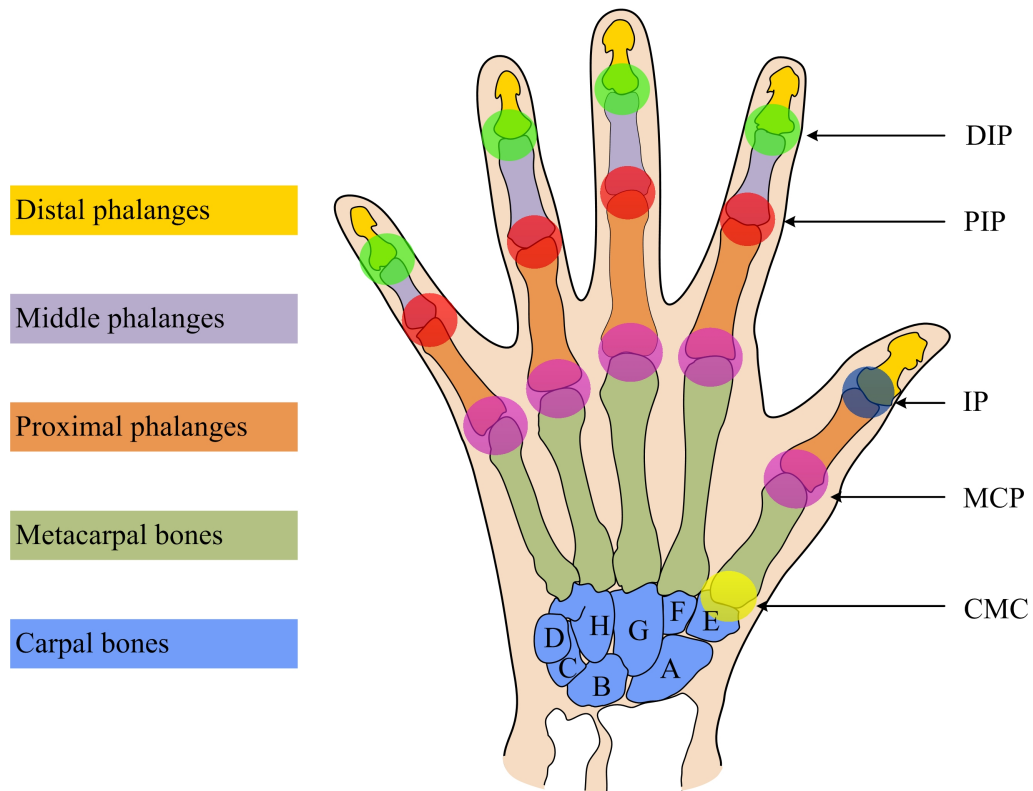


**Figure 2.1** Left hand bones and joints [17].

The phalanges together with the metacarpal bones form five articulated chains, which may move independently. However, the type and extent of the possible movements are largely determined by the structure of the joints. In the human body, synovial joints are predominant in the limbs. According to the shape of the articular surfaces, they typically can be divided into six types [18]: plane joints, hinge joints, pivot joints, ellipsoidal joints, saddle joints, and ball and socket joints. Human fingers only have hinge, ellipsoid, and saddle joints, which are illustrated in Figure 2.2.

Palastanga and Soames [16] have provided detailed anatomical descriptions of the finger joints. Hinge joints are essentially uniaxial joints, only allowing the back-and-forth movements in one plane (see Figure 2.2(a)). The PIP, DIP, and IP joints of human fingers are examples of the hinge type. Ellipsoidal joints, also known as condyloid joints, consist of two oval articular surfaces (see Figure 2.2(b)); one is concave, and the other one is convex. They are biaxial joints which permit movements in two planes.

MCP joints are examples of the ellipsoidal type. Saddle joints shown in Figure 2.2(c) are also biaxial joints; both bones form two reciprocally concave-convex surfaces. Compared with the ellipsoidal joints, they have relatively limited movement due to the saddle-shaped interlocking mechanism. The CMC joint of the thumb is regarded as a typical saddle joint.

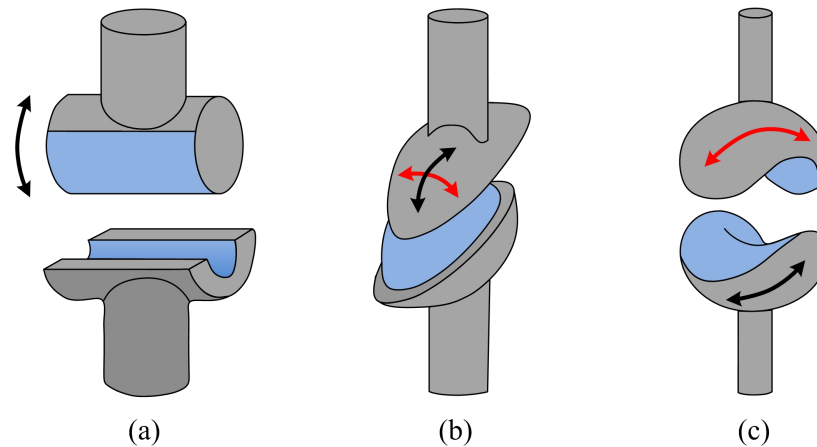


**Figure 2.2** Structure of the synovial joints involved in human fingers [19]. (a) Hinge joint, performing motion in one plane; (b) ellipsoid joint, allowing movements in two planes; (c) saddle joint, allowing limited motion in two planes.

### 2.1.2 Human Finger Kinematics

The human hand's interactions with the environment involve a series of basic finger motions, i.e. flexion, extension, ABD, ADD, circumduction, and opposition [16, 20]. The fingers except the thumb perform similar movements. As demonstrated in Figure 2.3, finger flexion refers to the joint motion towards the palm relative to the standard anatomical position with extension occurring in the opposite direction. The finger position in line with the back of the hand is defined as zero degrees flexion, and also called full extension. Some finger joints can extend past zero degrees - this is called hyperextension. An injury can occur when joints are hyperextended too much [21]; in this thesis only hyperextension within normal limits is of interest. Finger ABD and ADD are the movements away from or towards the hand's midline (dotted line in Figure 2.3) respectively; the middle finger is usually regarded as a reference point. Circumduction is a circular motion combining flexion, extension, ABD, and ADD. These movements of the thumb are defined in a different way since the thumb is rotated about  $90^\circ$  with respect to the plane of the hand. The flexion and extension of the thumb take place in a plane parallel to the palm, so do the ABD and ADD of the other four digits; and the ABD and ADD are the motion in a plane perpendicular to the palm, so

are the flexion and extension of the other fingers. Finger opposition is unique to the thumb, and refers to the motion of the thumb when touching the finger tips.

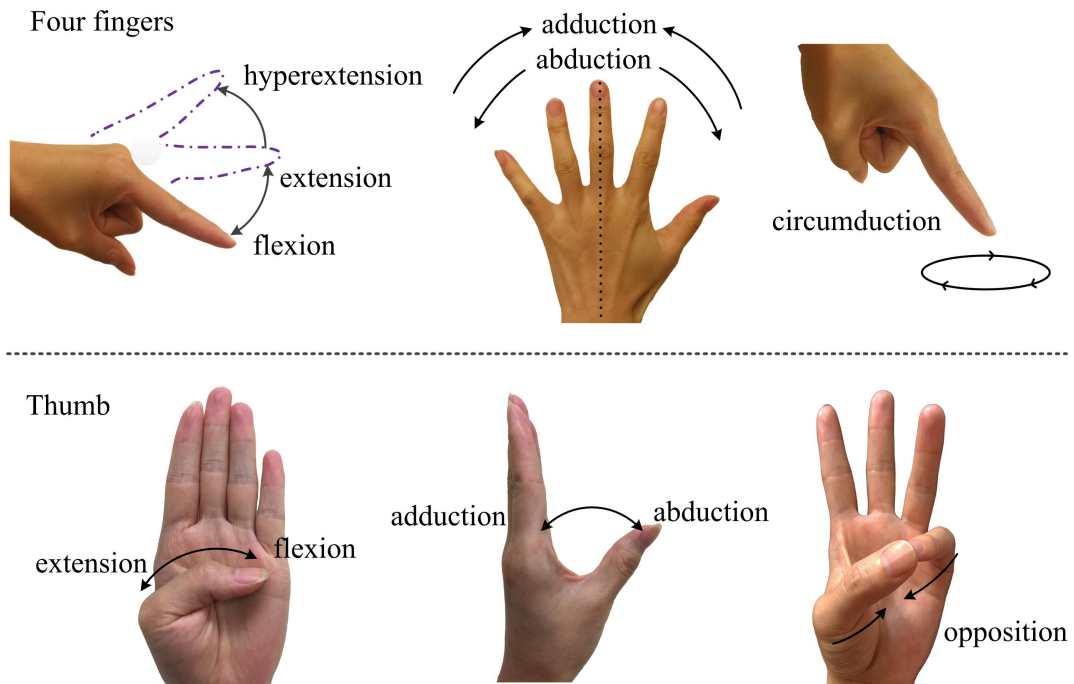


**Figure 2.3** Finger motion: flexion, extension, abduction, adduction, circumduction, and thumb opposition.

The stable hinge joints, e.g. IP, PIP, and DIP, with one DOF only allow flexion/extension. The two-DOF MCP finger joints are capable of flexion/extension, ABD/ADD, and coupled circumduction. The CMC joint of the thumb also has two DOFs but with a more complicated mechanism [22], performing motion including flexion/extension, ABD/ADD, and opposition in three anatomic planes [23].

Each hand has roughly 27 DOFs, 21 of which are contributed by the five finger joints for local movements and the other 6 for global hand movements [24, 25]. Each digit, except the thumb, possesses 4 DOFs, one each for the PIP and DIP joints, and the other two for the MCP joint. The thumb has a more complicated structure possessing 5 DOFs, one for the IP joint, two for the MCP joint, and two more for the CMC joint [24]. In the reported hand kinematic models, the DOFs distributed for the five fingers generally accord with these anatomical characteristics, even though the models are presented with different amount of the DOFs, such as 19 DOFs [26], 23 DOFs [27–29], 24 DOFs [30], and 27 DOFs [24, 25]. In these literature only the CMC joint of the thumb and the joints for global hand motion are modelled in a different way.

The human hand is highly articulated, but constrained at the same time and cannot make arbitrary gestures. Hand constraints can be roughly divided into static constraints, intra-finger constraints, and inter-finger constraints. The static constraints refer to the

**Table 2.1** The general range of motion of each finger joint.

Finger	Joint	Flexion/Extension	Hyperextension	ABD/ADD
Thumb	CMC	40°-50°	\	80°
	MCP	45°	0°	15°
	IP	90°	10°	\
Index, middle, ring, and little fingers	MCP	90°	50°	30°
	PIP	90°-135°	1°-2°	\
	DIP	90°	5°	\

*Note:* the symbol ‘\’ means that the finger joints generally cannot perform the corresponding motion.

normal ROM of finger joints. The intra-finger constraints are the constraints between joints of the same finger and inter-finger constraints are those imposed on adjacent fingers [31]. The inter- and intra-finger constraints are often called dynamic constraints which are more complex and somewhat ambiguous due to their dependency on various biomechanical factors [32].

The ROM of each finger joint varies between individuals [33], but they generally fall into a specific range. According to Palastanga’s study [16], the average ROM of each finger joint is listed in Table 2.1, which is consistent with the findings by Lin et al. [31].

For the thumb, the CMC joint is capable of flexing no more than 50° in the plane parallel to the palm and abducting about 80°. The two-DOF MCP joint has a smaller range, 45° for flexion/extension and 15° for ABD/ADD. The IP joint can perform flexion/extension about 90° as well as hyperextension normally no more than 10°.

At the MCP joints of the other four fingers, from Table 2.1 it can be seen that the range of flexion is about 90°; in fact, it is slightly less than 90° for the index finger, but progressively increases towards the little finger. The active hyperextension can reach approximately 50°. The ABD/ADD generally have a greater range when the fingers are fully extended, being as much as 30° in each direction. However, the middle finger displays very limited ABD/ADD motion [24], which can be approximated to 0° according to Lin et al. [31]. The total flexion/extension ranges of the PIP and DIP joints of the four digits are no more than 135° and 90° respectively, and they both gradually decrease from the little finger towards the index finger. In general, both the PIP and DIP

joints cannot hyperextend, but in a few cases a slight hyperextension can occur equal to  $1^\circ$  or  $2^\circ$  for the PIP joints and less than  $5^\circ$  for the DIP joints.

For the intra-finger constraints, the most accepted one is related to the angular motion of the DIP and PIP joints, which is usually represented by equation (2.1) [24]. This correlation can be used to reduce the number of the sensing elements in glove-based systems [31, 34, 35].

$$\theta_{DIP} = \frac{2}{3}\theta_{PIP} \quad (2.1)$$

However, Park et al. [36] stated that this linear approximation may not be precise due to the complicated activation mechanism for joint motion. They measured the simultaneous motion of the PIP and DIP joints of five subjects' index finger, and found a second-order function to approximate the interdependence well.

The inter-finger constraints relate to the associations between the adjacent finger joints. Lee and Kunii [24] performed the measurements on several participants and presented a set of inequalities for approximating the interdependence of the limits of the adjacent MCP joints' flexion angles. Here the details will not be discussed.

Researchers have been attempting to express the finger constraints in a quantitative way [24, 28, 30, 31]. However, there still exist many motion constraints of the human hand, which cannot be explicitly represented as mathematical equations due to the large variation in finger motion. For instance, the fingers' ability of abducting or adducting is reduced as they bend towards the palm [28], and ABD/ADD is no longer possible when the fingers bend to form a fist. Furthermore, the most natural way for people to make a fist from an open hand is to curl all fingers simultaneously, instead of bending them successively [31].

## 2.2 Polarisation of Light

The sensing technique used in this thesis exploits Malus' law of polarised light as described in the following section.

### 2.2.1 Introduction to Polarisation

Light is a transverse electromagnetic wave. It consists of coupled oscillating electric and magnetic fields which are always perpendicular to the direction of the wave propagation [37]. Polarisation is an expression of the geometrical orientation of the transverse wave's oscillation. Since the electric field and the magnetic field of an electromagnetic wave are always perpendicular, by convention the “polarisation” refers to the direction of the electric field. As shown in Figure 2.4, polarisation can be classified into three different types [38]: linear polarisation, circular polarisation, and elliptical polarisation.

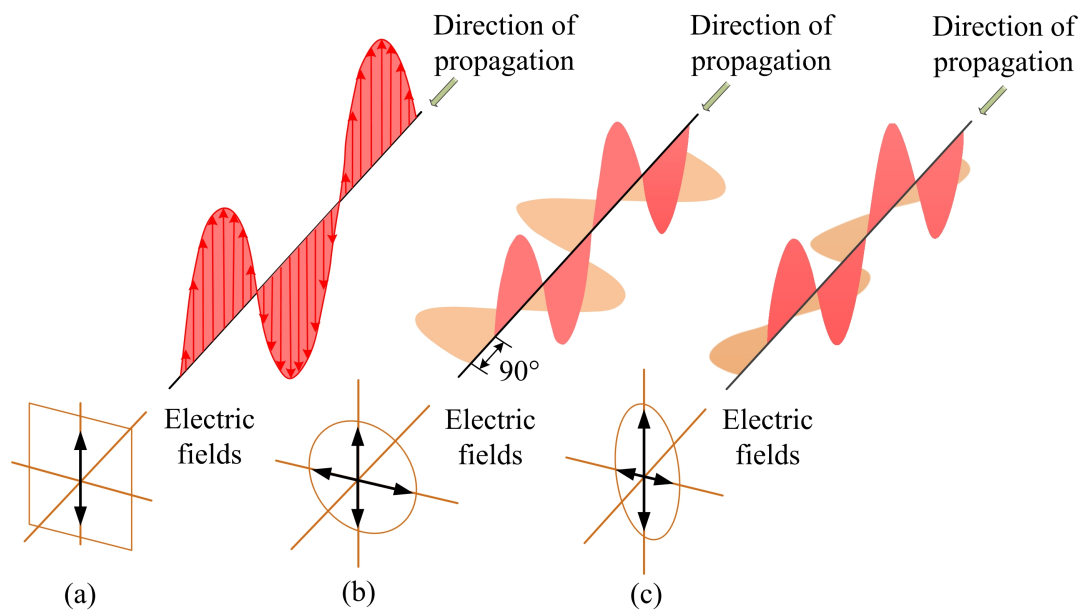


**Figure 2.4** The electric fields of three different polarisations. (a) Linear polarisation; (b) circular polarisation; (c) elliptical polarisation.

In linearly polarised light (see Figure 2.4(a)), the electric field vector is confined to a single plane in space, oscillating perpendicular to the direction of wave propagation. In contrast, the circularly polarised light is composed of two plane waves with equal amplitude but a phase difference of  $90^\circ$ . As illustrated in Figure 2.4(b), the resulting electric field rotates in a plane perpendicular to the direction of the wave propagation. Similarly, elliptically polarised light is also a combination of two linear components (see Figure 2.4(c)), however the two plane waves differ in amplitude and their phase difference is not a multiple of  $90^\circ$ , resulting in the electric field vector describing an elliptical motion. Elliptical polarisation is the most common form of polarised light, with linear and circularly polarised light considered as special cases.

Most common light sources such as the sun, incandescent lamps, and LED spotlights, are unpolarised and emit incoherent light waves with the electric field vibrating randomly in all directions [39]. Polarised light is produced by passing unpolarised light through a

polarising filter which only transmits the waves of a specific polarisation while blocking the rest of the light.

By far, linear polarisers are the most common polarising filters. Many different categories are currently available, including wire-grid polarisers, dichroic polarisers, birefringent polarisers, and thin film polarisers. Amongst them, the thin-film linear polarisers are featured with high transmission, low scattering and distortion, low cost, and the availability of multiple dimensions, therefore they are usually the best choice for high power applications. Thin film polarisers are glass substrates coated with a special optical layer, e.g. nanoparticles in Sodium Glass [40]. Based on either interference effects or Brewster's angle reflections, they work as beam-splitting polarisers which split the incident light into two orthogonally polarised beams, i.e. p-polarised light and s-polarised light. As shown in Figure 2.5, p-polarised light is the linearly polarised beam with a polarisation direction parallel to the plane of incidence, while s-polarised light has an electric field perpendicular to the plane of incidence. The "plane of incidence" is the plane containing the incident ray and the transmitted and reflected rays. S-polarised light is always more highly reflected than p-polarised light [41]. In fact, the p-polarised component can be completely transmitted when the coated plate is oriented at the Brewster's angle with respect to the incident beam, and thus the thin-film coating performs the function of a linear polariser [42].

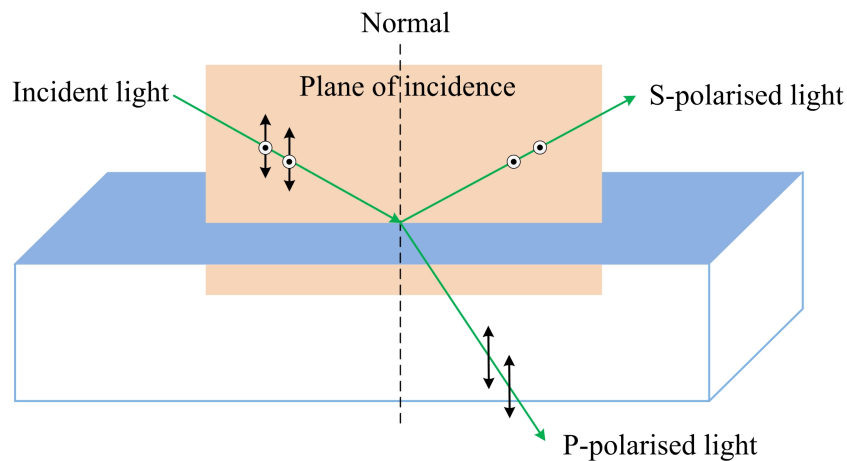


**Figure 2.5** P and S polarisations.

### 2.2.2 Malus' Law

As illustrated in Figure 2.6, when linearly polarised light with an electric field vector  $E_0$  passes through a linear polariser, the  $E_0$  vector of the incident light can be resolved into two mutually perpendicular components,  $E_{0x'}$  and  $E_{0y'}$ . Suppose the electric field  $E_0$  is

oriented at an angle  $\theta_0$  with respect to the direction of the linear polariser's transmission axis  $y'$ , the two components can be expressed by the following equations.

$$|E_{0x'}(\theta_0)| = |E_0| \sin \theta_0 \quad \text{and} \quad |E_{0y'}(\theta_0)| = |E_0| \cos \theta_0 \quad (2.2)$$

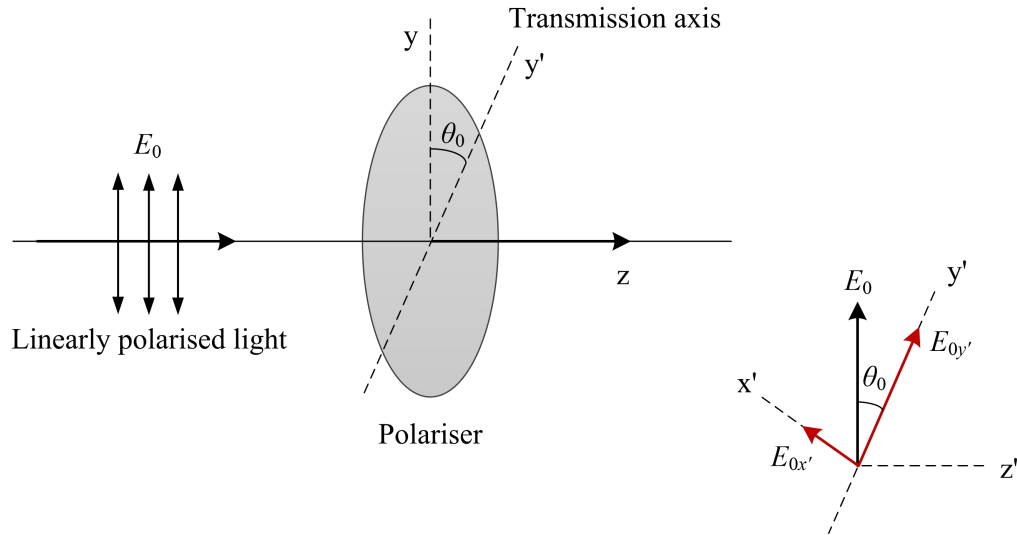


**Figure 2.6** Illustration of Malus' Law.

Across the linear polariser, only the second component  $E_{0y'}$  which is parallel to the polariser's transmission axis can be transmitted, while the component  $E_{0x'}$  is blocked. Light intensity is proportional to the square of the amplitude of the electric field, and thus the transmitted intensity can be expressed using equation (2.3).

$$I(\theta_0) = \frac{cn\epsilon_0}{2} |E_{0y'}(\theta_0)|^2 = \frac{cn\epsilon_0}{2} |E_0|^2 \cos^2 \theta_0 \quad (2.3)$$

where  $n$  is the refractive index,  $c$  is the light speed in vacuum (approximately  $3.00 \times 10^8 \text{ m} \cdot \text{s}^{-1}$ ) and  $\epsilon_0$  is the permittivity of free space with a defined value of  $8.85 \times 10^{-12} \text{ F} \cdot \text{m}^{-1}$ .

Since the initial light intensity is

$$I_0 = \frac{cn\epsilon_0}{2} |E_0|^2 \quad (2.4)$$

The final light intensity  $I(\theta_0)$  would be

$$I(\theta_0) = I_0 \cos^2 \theta_0 \quad (2.5)$$

Equation (2.5) is known as Malus' law [38], named after Étienne-Louis Malus. Clearly, the transmitted light intensity varies as the square of the cosine of the intersection angle between the initial polarisation and the polariser's transmission axis. When the parameter  $\theta_0$  equals  $0^\circ$ , i.e. the electric field is parallel to the polariser's transmission axis, the transmitted light intensity is maximum. When the electric field is perpendicular to the transmission axis ( $\theta_0=90^\circ$ ), in theory the incident light will be completely blocked.

## 2.3 Summary

The human hand is a sophisticated and dexterous system which is highly articulated but constrained at the same time. Such features make the hand motion detection difficult and challenging.

According to Malus' law, the rotation angle of a linear polariser with respect to the polarising direction of the incident light can be detected by measuring the light intensity passing through the polariser. It is possible to use this principle as a sensing method to track finger flexure by coupling the movement of the polariser with the rotation of the finger joint.

## **Chapter 3**

# **Review on Sensing Technologies and Instrumented Systems for Tracking Hand Motion**

Various sensing technologies have been proposed and investigated to track hand motion. Among them, flexible resistive sensors including stretchable strain gauges, bend sensors, optical sensors, inertial sensors, and magnetic sensors are the most widely researched sensing methods [43, 44]. Other sensing techniques including potentiometers [36], capacitive sensors [45], inductive sensors [46] and surface electrodes [47] are also reported for monitoring finger motion. Using one or more of these sensing techniques, several instrumented systems have been developed to capture hand movements. They can be mainly categorised into camera-based systems, surface electromyography (EMG)-based devices, and glove-based systems. In this chapter, these sensing techniques and the available systems for tracking hand motion are reviewed and studied.

### **3.1 Sensing Technologies for Tracking Finger Motion**

This section provides an overview of the sensing technologies which are used to monitor hand motion.

### 3.1.1 Flexible Resistive Sensors – Strain Gauges and Bend Sensors

Flexible resistive sensors respond to mechanical deformation with a change in resistance; increasing the deformation is generally associated with an increased electrical resistance. They are particularly favoured in wearable electronics due to their flexibility, light weight, easy operation, and low cost. According to their stretchability, wearable resistive sensors can be mainly classified into strain gauges and bend sensors, the former being stretchable and the latter inextensible.

#### 3.1.1.1 Stretchable Strain Gauges

Strain gauges are stretchable sensors which produce a changing electrical signal in response to an applied strain. They are typically composed of conductive materials coupled with highly stretchable substrates including polydimethylsiloxane (PDMS) [48–62], Ecoflex elastomer [63–71], and elastic fabrics [26, 72–76]. A variety of conductive materials are currently being explored and adopted to fabricate wearable strain sensors, such as metallic films [49, 50, 77, 78], carbon blacks [52, 79, 80], carbon nanotubes (CNTs) [51, 61, 64, 66, 67, 71], graphene [54–57, 81], silver nanowires (AgNWs) [45, 59, 82], silver nanoparticles (AgNPs) [58, 60, 83], conductive ionic liquids [63, 68–70, 84, 85], zinc oxide (ZnO) nanowires [53], ink filaments [65], graphite [48, 86], platinum nanobelts [62], carbon-coated fibre [87, 88] or rubber [73] and conductive polypyrrole [74, 89]. Generally, the majority of the metal/carbon-based resistive strain sensors employ either piezoresistive effect or dimensional changes to measure the applied strain [26, 53, 72, 75, 77, 86–89]. Microfluidic sensors are mainly based on the changes in geometrical dimensions of ionic liquids [63, 69, 70, 85]. Nanomaterial-based sensors exploit the mechanisms including the micro-crack propagation in thin films and the disconnection between sensing elements [45, 51, 55, 56, 58–60, 66, 81]. A few strain sensors involve multiple mechanisms when responding to bending deformations [71, 90]. For instance, the wrinkled CNTs thin film depended on both the separation of the wrinkled structure and the changes in the wrinkle's geometry to respond the strain below 400% [71]. The properties of the wearable strain sensors are discussed as follows.

##### (a) Metallic strain sensors

Conventional metal-foil strain sensors consist of a fine wire or metallic film arranged on flexible substrate in a grid pattern [77, 91]. Despite their simple structure, they typically have small strains (maximum strain of 5%) and low sensitivity (gauge factor (GF)  $\sim 2$ ,

i.e. the ratio of the relative change in resistance to the mechanical strain), which make them unsuitable for measuring human motion (strain as high as 55%) [57, 59, 90, 91]. Recently, Hadrien et al. proposed a class of stretchable strain sensors by thermally evaporating gold film patterns on silicone substrate and micro-plotting liquid metal as conductive wires [49, 78] or terminals [50]. These resistive sensors are capable of detecting large strains up to 50%, but still suffer from a small GF less than 5.

### (b) Fabric-based strain sensors

To offer comfortable and unobtrusive measurements, several resistive fibre-meshed strain sensors have been proposed for monitoring hand motion. They can be produced by incorporating conductive materials into the non-conductive base textile using different techniques, such as sewing, knitting, weaving, coating, and printing [76]. In 2003, Scilingo et al. [74] fabricated a prototype instrumented glove to record human gesture using a screen printing technique (see Figure 3.1(a)). Masking is used to determine the position and geometry of conductive polypyrrole deposited on the fabrics as sensing units. In 2005, they developed another instrumented glove by spreading carbon-filled silicone rubber mixture over the textile fabrics [73]. As shown in Figure 3.1(b), this prototype avoided the usage of metallic conducting wires and improved the electrical response. These methods, however, require predetermined sensor positions before fabrication, making the subsequent adjustment of sensor location impossible for individuals.

To enhance the flexibility of sensor attachment and characterise the sensor before tracking hand motion, researchers [26, 75, 79, 83, 86, 87, 92] began to design and study separate strain sensors. It was reported that the performance of the fabric-based strain

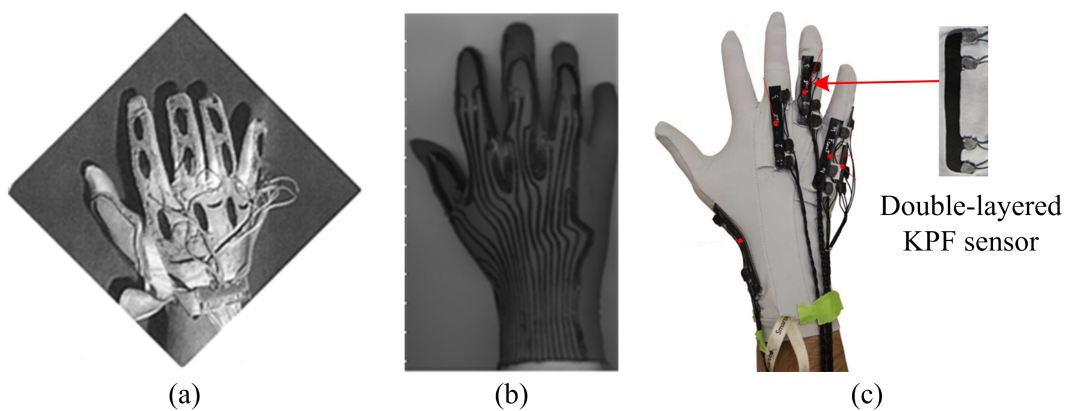


**Figure 3.1** Textile-based strain sensors and the instrumented sensing gloves. (a) Prototype of an instrumented glove using screen printing technique [74]. (b) Instrumented glove coated with conductive mixture [73]. (c) Sensing glove equipped with double-layered knitted piezoresistive fabrics [26].

sensors is highly dependent on the coating/knitting topology [72, 87]. In 2008, Huang et al. [87] stated that the sensor with double wrapping yarns (a core yarn wrapped with two carbon-coated fibres, one in the clockwise direction and the other one in the anticlockwise direction) produced a higher linearity but yielded a lower sensitivity in comparison with the sensor with single wrapping yarns (a core yarn wrapped with a single fibre). In 2014, Tognetti et al. [72] declared that the knitted piezoresistive fabrics (KPFs) configured in a double-layer structure demonstrated a better performance than the single-layer KPF sensor in terms of angle reconstruction. Using the double-layered KPFs, they later implemented a textile glove (see Figure 3.1(c)) for hand grasp recognition [26].

The fabric-based strain sensors offer high wearability, but slippage of the conductive materials on the textile fabrics [72, 87] usually deteriorates the measurement accuracy and productivity. Additionally, it is difficult to establish a reliable relationship between the applied strains and the kinematic parameters such as bending angles, since the textile sensors have a large contact area and human skin tends to be uneven [93].

### (c) Nanomaterial-based strain sensors

Alternatively, nanomaterial-based strain gauges have recently attracted tremendous attention due to their outstanding performance. Several reported sensing prototypes are illustrated in Figure 3.2.

Among the available nanomaterial-based sensors, CNT-based sensors have demonstrated excellent stretchability with maximum strains of 280% (single-walled CNTs) [51], 400% (super-aligned CNT films) [61], 450% (vertically aligned CNT forest) [67], 510% (multi-walled CNTs) [64], 750% (wrinkled CNTs) [71], and 960% (CNT fibres) [66]. They nevertheless suffer from large mechanical hysteresis (up to 33% [71]) and low GFs ( $< 1$ ) [51, 61, 64, 67, 71, 94]. For instance, in 2015 Ryu et al. [66] reported a CNT-fibre-based strain sensor (see Figure 3.2(a)) with a high GF of 64 when subjected to strains larger than 400%. However, they experimentally found the strain caused by finger flexion/extension on the developed sensor was no more than 297% where the GF was only 0.54. The CNTs-Ecoflex nanocomposite strain sensor shown in Figure 3.2(b) demonstrated a high stretchability of 510%, but low GFs of 0.61 and large hysteresis errors (about 4.6% under 60% strain) [64]. In 2016, Park et al. [71] fabricated a wearable strain sensor by depositing nano- to micro-sized wrinkled CNTs on Ecoflex substrate (see Figure 3.2(c)). The wrinkled structure increased the sensor's strain to 750%; however, the GF was as small as 0.65 for strains below 400%.

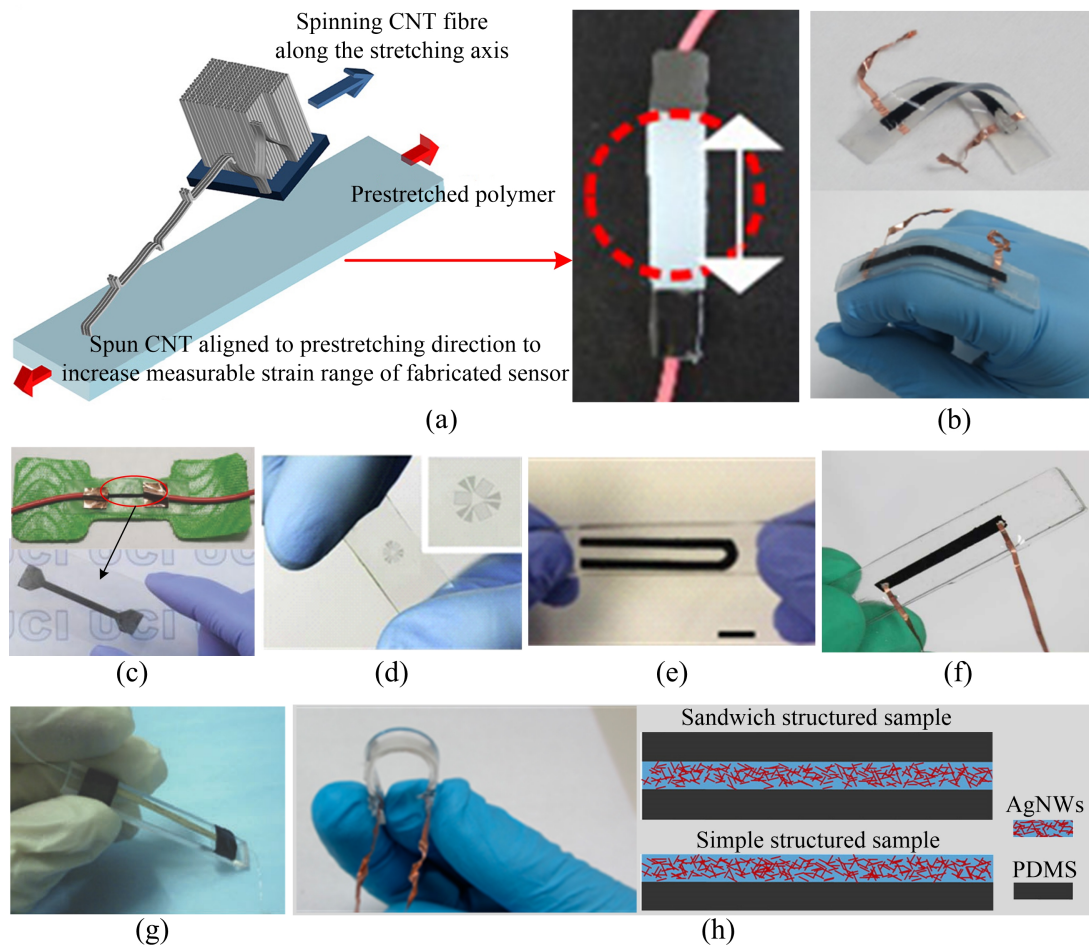


**Figure 3.2** Nanomaterial composites strain sensors. **(a)** Highly elastic strain sensor based on CNT fibres [66]. **(b)** Multi-walled CNTs based strain sensor [64]. **(c)** Wrinkled CNTs thin film strain sensor [71]. **(d)** Transparent graphene strain sensor in a form of rosette [54]. **(e)** Flexible nanopaper based on crumpled graphene and nanocellulose [57]. **(f)** Graphene foam based strain sensor [56]. **(g)** Conductive hybrids of graphene and AgNPs based sensor [60]. **(h)** Sandwich-structured and simple-structured AgNW-PDMS nanocomposite strain sensors [59].

Graphene-based strain sensors generally demonstrate higher sensitivities than CNT sensors. Using the conductive composite Ni/SiO<sub>2</sub>/Si, Bae et al. [54] fabricated a transparent strain sensor in rosette form to monitor finger motion (see Figure 3.2(d)). This graphene sensor showed variable GFs ranging from 2.4 to 14. Yan et al. [57] embedded crumpled graphene and nanocellulose in the elastomer matrix to obtain a stretchable strain sensor with a GF from 1.6 to 7.1. The image of the sensor prototype is shown in Figure 3.2(e). In 2016, Li et al. [56] reported a 3D-graphene-foam/PDMS strain sensor (see Figure 3.2(f)) with the GF of 47.74 to 98.66. Despite their high sensitivity, graphene-based strain sensors generally possess limited strains due to the intrinsic brittleness of the conductive materials. The maximum strain for the reported wearable graphene sensors was limited to 5% [55], 7.1% [54], 30% [56, 81], and 100% [57], much smaller than that of the CNTs strain sensors. To balance the stretchability and sensitivity, Chen et al. [60] incorporated synergistic conductive hybrids of graphene

and AgNPs into the polymer matrix. The implemented hybrid strain sensor shown in Figure 3.2(g) demonstrated higher strains (maximum strain of 1000%) and sensitivity (GFs ranging from 7 to 476) than the AgNP-deposited sensors.

Due to the excellent electrical and mechanical properties, AgNWs have also been widely studied as possible conductive materials in wearable strain sensors [59]. When AgNW thin film is stretched, disconnection of the overlapped nanomaterials gradually increases, causing changes in resistance of the strain sensors [59, 90]. One major problem of the AgNW-based sensors is the weak adhesion of AgNWs on flexible polymer substrates [45, 95]. Under repeated stretching/releasing cycles, the number of detached and buckled AgNWs on the substrate increases because of the friction between the nanowires and the polymeric substrates, and thus causing an irreversible increase in resistance [45, 59]. To overcome this limitation, Amjadi et al. [59] fabricated a sandwich-structured strain sensor (see Figure 3.2(h)), i.e. AgNW thin film embedded between two layers of flexible PDMS substrates. This sandwich-structured sensor demonstrated better resistance recovery and smaller hysteresis errors during repeated stretching/releasing in comparison with the simple structured sensor (AgNWs directly deposited on the surface of PDMS).

#### (d) Microfluidic strain sensors

Although nanocomposite strain sensors demonstrate outstanding performance, the major problem is the severe hysteresis errors during the stretching/releasing cycles [63, 85]. Therefore, microfluidic sensors have emerged as an alternative stretchable strain sensor.

The microfluidic strain sensor is made of hyper-elastic elastomer with embedded microfluidic channels filled with conductive ionic liquids [63, 68–70, 84, 85, 96]. When an external force is applied to the microfluidic sensor, the microchannel is deformed resulting in a change of length and cross-sectional area of the embedded microchannel. The deformation causes a proportional variation in resistance of the conductive liquids [69, 96]. Pineda et al. [96] theoretically studied the responses of an electrofluidic sensor to the elongations using a numerical simulation and an analytical model. The theoretical analysis was in good agreement with the experimental results. Additionally, by filling eutectic Gallium Indium (eGaIn) into the microchannel, Kramer et al. [84] fabricated a strain sensor to detect the flexion of finger joints. The image of the developed sensor is displayed in Figure 3.3(a). This sensor features large strain (>350%) but shows a small sensitivity (GF: 0.36). Park et al. [97] also designed eGaIn-filled microfluidic strain sensors with different lengths, as shown in Figure 3.3(b). They were characterised with a GF approximately 3.8.

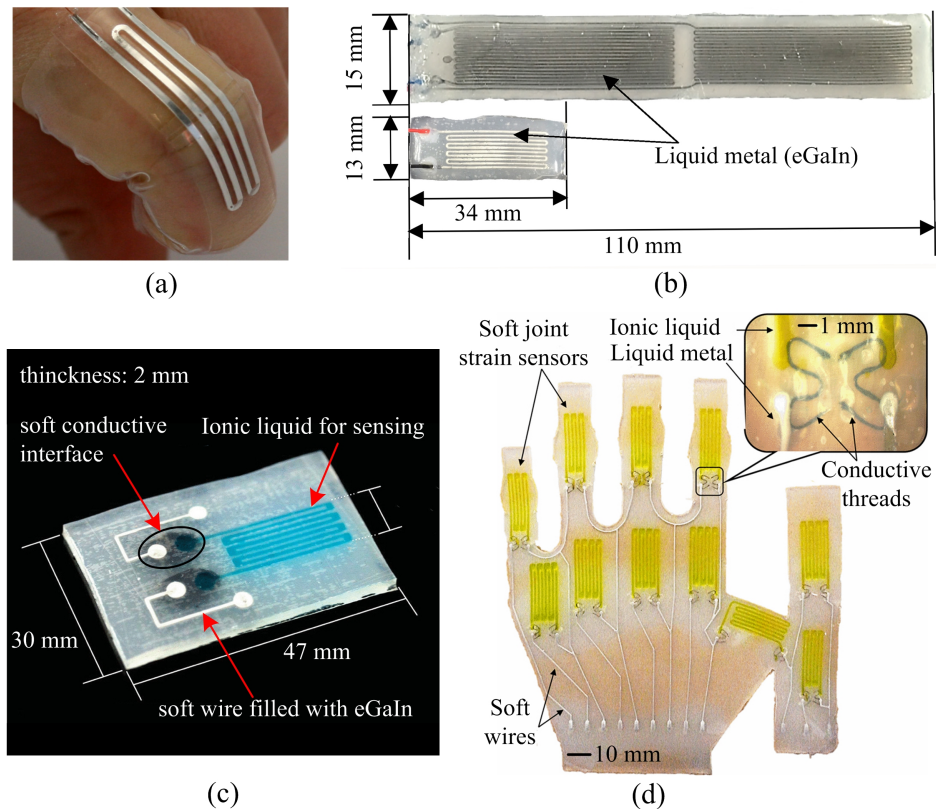


**Figure 3.3** Microfluidic strain sensors. (a) Soft strain sensor embedded with eGaIn-filled microchannel [84]. (b) Two types of eGaIn-filled microfluidic strain sensors [97]. (c) Microfluidic strain sensor filled with hybrid liquid conductors [69]. (d) Artificial skin prototype embedded with hybrid-liquid-based strain sensors [68].

Generally, microfluidic-based sensors are susceptible to electrical disturbances due to noise caused by the electrical connecting wires. To resolve these problems, Chossat et al. [69] employed two conductive liquids with different resistivity to fabricate the microfluidic sensor, one liquid for sensing and the other one with high conductivity but low piezoresistivity for wiring, as illustrated in Figure 3.3(c). Integrating 11 microfluidic sensors, they later implemented a wearable hyper-elastic artificial skin shown in Figure 3.3(d) [68]. Despite initial positive results, the authors declared that sometimes the sensing ionic liquids invaded the wire channels causing failure of the system. Additionally, an alternating current is usually applied to prevent electrolysis of the ionic solutions and polarisation of the electrodes [68, 69], making the system complicated.

A variety of wearable strain sensors have been discussed. Although they exploit different physical mechanisms they do share a number of common advantages and disadvantages as summarised below.

**Strengths:** They are flexible, stretchable, unobtrusive, light-weight and exploit simple operating principles.

**Limitations:** During the stretching/releasing cycles, they suffer from severe mechanical hysteresis and failure to recover original resistance values;

They have poor repeatability and low accuracy due to temporal signal drift;

In general, large strain sensing is inversely related to the strain sensitivity, so increasing the stretching capability of the sensor tends to compromise its sensitivity.

### 3.1.1.2 Bend Sensors

Bend sensors, also known as flex/flexion/flection sensors, angular displacement sensors, or flexible potentiometers, directly measure the amount of bend in the form of proportional variations in resistance [98]. They are generally fabricated by coating or printing carbon/polymer ink-based materials onto flexible plastic substrates such as polyimide and polyester. When the sensor bends, micro-cracks are introduced into the coated film causing the change in resistance.

Resistive bend sensors, which are currently used to monitor finger movements, are mainly commercial products. The original resistive bend sensor, marketed by Abrams Gentile Entertainment, Inc. [99], was developed specifically for use in the 'Power Glove' in 1989, the earliest motion-control accessory for home entertainment [98]. A year later, its production ceased due to the glove's imprecision and difficulty of operation [100]. Following this, several manufacturers such as Images Science Instruments, Inc. (Images SI) [101], Spectra Symbol, Corp. [102], and Flexpoint Sensor Systems, Inc. (Flexpoint SS) [103] release their own patented flexible bend sensors.

As shown in Figure 3.4(a), Images SI [104] manufactures bi-directional bend sensors with a length of 114.3 mm, which consist of a strip of resistive material sandwiched between two copper foil laminates. According to the manufacturer's specification, the sensor has a nominal resistance of 10 k $\Omega$  which decreases gradually with bending in either direction [104]. In contrast, Orenge et al. [105] reported that the piezoresistive bend sensor by Images SI showed linear increases of resistance from 4 k $\Omega$  to 16 k $\Omega$  for bending angles ranging from  $-30^\circ$  to  $180^\circ$ . Although these bend sensors were already used in glove sensing systems [106–108], they have been discontinued since 2010 by Images SI because of their low accuracy and stability.

The off-the-shelf bend sensors manufactured by Spectra Symbol are usually designed with a length of 55.9 mm or 112.2 mm, the images of which are shown in Figure 3.4(b) [109]. The sensor resistance generally demonstrates a linear dependence with the bending angle. However, a hysteresis error of approximately 14% was reported for

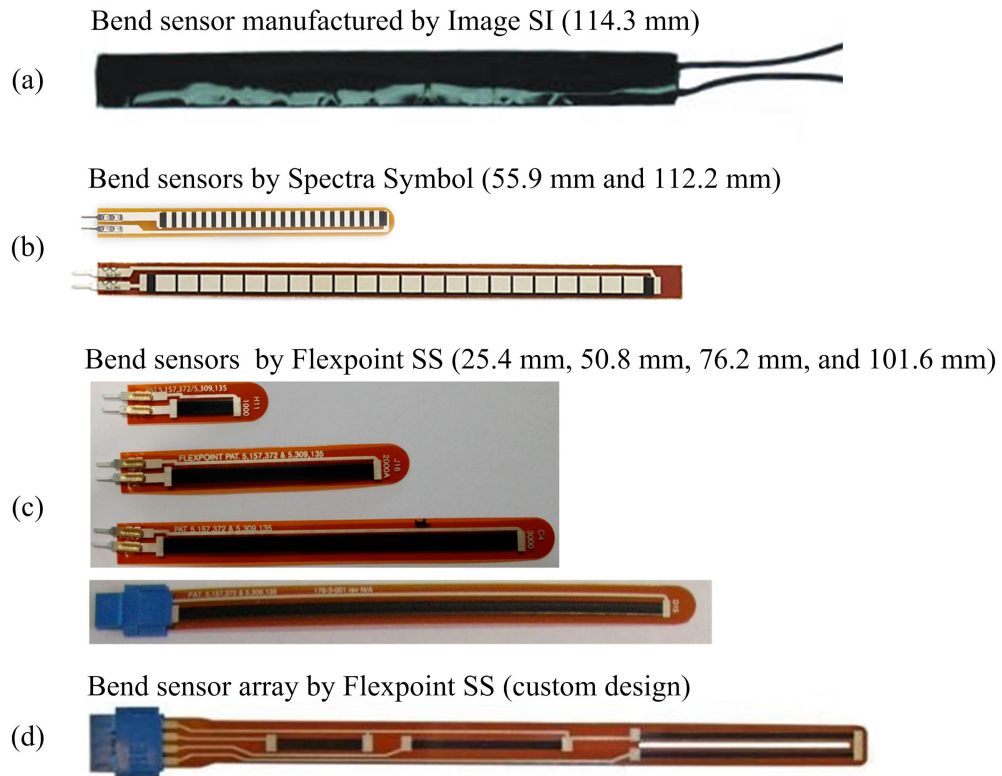


**Figure 3.4** Images of commercial bend sensors. (a) Bi-directional bend sensors manufactured by Images SI [104]. (b) Bend sensors produced by Spectra Symbol [109]. (c) Bend sensors with different lengths manufactured by Flexpoint SS [110, 111]. (d) Custom design, bend sensor array produced by Flexpoint SS [112].

the 112.2 mm sensor during bending-unbending operations in the range of  $0^\circ$  to  $90^\circ$ , much higher than the bend sensor from Flexpoint SS (about 3%) [111]. Simone and Kamper [113] investigated the sensor's time-varying behaviour, and observed a 31.8% decay of the initial resistance after bending the 112.2 mm sensor over a 3-inch tube for 30 s, almost three times higher than that of the sensors from Flexpoint SS (8.9%). Furthermore, Borghetti et al. [111] found that the sensor resistance varied from 8.2 k $\Omega$  to 13.1 k $\Omega$  when the 112.2 mm sensor was bent from  $0^\circ$  to  $90^\circ$ , i.e. a change of 4.9 k $\Omega$ ; in contrast, the bend sensor produced by Flexpoint SS produced a resistance variation of 112 k $\Omega$  for the same bending range. It can be deduced that the Flexpoint SS sensors are generally more stable and sensitive to mechanical deformations than the Spectra Symbol bend sensors.

Due to their outstanding characteristics, thin-film bend sensors produced by Flexpoint SS, are sold as proprietary 'Bend Sensors<sup>®</sup>', and they are one of the most popular sensors used in applications for tracking finger motion [114–119]. The sensors are marketed with various sizes (25.4 mm, 50.8 mm, 76.2 mm, and 101.6 mm) and different over-laminates (bare, polyester, and polyimide) as shown in Figure 3.4(c).

The active sensing geometry determines the nominal resistance of the Bend Sensors<sup>®</sup>; doubling the length or halving the width doubles the sensor resistance [120]. The polymeric over-laminated layer is designed to offer environmental protection against humidity and moisture. However, it does increase the rigidity of the Bend Sensors<sup>®</sup>. Several studies [111, 117, 121] have revealed that the sensor characteristics are affected by the over-laminate layer. This may be attributed to the increased rigidity. In 2014, Borghetti et al. [111] reported that the resistances of the polyimide, polyester, and bare bend sensors varied by about 2%, 3%, and 30% respectively, after bending at 90° for 180 s. The previous research by Oess et al. [117] also stated that the temporal signal drift of the polyester-encapsulated sensor (0.47%) was significantly smaller than that of the bare sensor (18.20%). Therefore, the sensors over-coated with polyester or polyimide are generally considered to be more stable than the bare bend sensor. To enhance the stability of the bare sensors, Gentner and Classen [116] proposed a method of gluing a thin polyvinyl chloride foil over the conductive carbon/ink layer. They obtained comparable results (the ratio of relative change in resistance being  $1.9\% \pm 1.0\%$  after staying at 60° for 50 min) with the polyester/polyimide-coated bend sensor. However, the over-laminated sensor generally yields a smaller change in resistance, and thus leading to lower sensitivity than the bare sensor [111, 121]. This was verified by the study of Saggio et al. [121] that the bare, polyester-coated, and polyimide-coated sensors showed a resistance variation of 251 k $\Omega$ , 102 k $\Omega$ , and 65 k $\Omega$  respectively when bending from 0° to 120°.

In addition to the standard designs, Flexpoint SS also supports custom designs for bespoke applications. A typical configuration for tracking finger motion is the sensor array presented by Saggio et al. [112] and shown in Figure 3.4(d). The array consisted of a unique substrate on top of which three conductive elements with different lengths were coated. This design minimises the number of electrical connection wires since the three sensing areas share the same ground wire. Figure 3.5(f) shows an instrumented wearable glove (HITEG-Glove) that employs such a sensor array [119].

The bend sensors from Flexpoint SS are commonly used to capture finger motion. Several tracking systems are shown in Figure 3.5. Shadow Monitor (see Figure 3.5(a)), designed by Simone et al. [118], was equipped with five bend Sensors<sup>®</sup> to detect finger flexion/extension. Distinct from the NeuroAssess Glove [117] (see Figure 3.5(b)), WU-Glove [116] (see Figure 3.5(c)), HITEG-Glove [119] (see Figure 3.5(f)), and Borghetti's glove shown in 3.5(d) [115], the Shadow Monitor encased individual bend sensors in a single sleeve directly glued to the finger joint being measured. This improved the measurement accuracy but also increased the overall discomfort. The Tyndall/UU glove [114], shown in Figure 3.5(e), was a flexible printed circuit board (PCB) integrated with multiple sensors including 20 resistive bend sensors, 16 triaxial accelerometers, as well

as 11 force sensors. This system was intended to facilitate the rehabilitation process for the patients with rheumatoid arthritis.

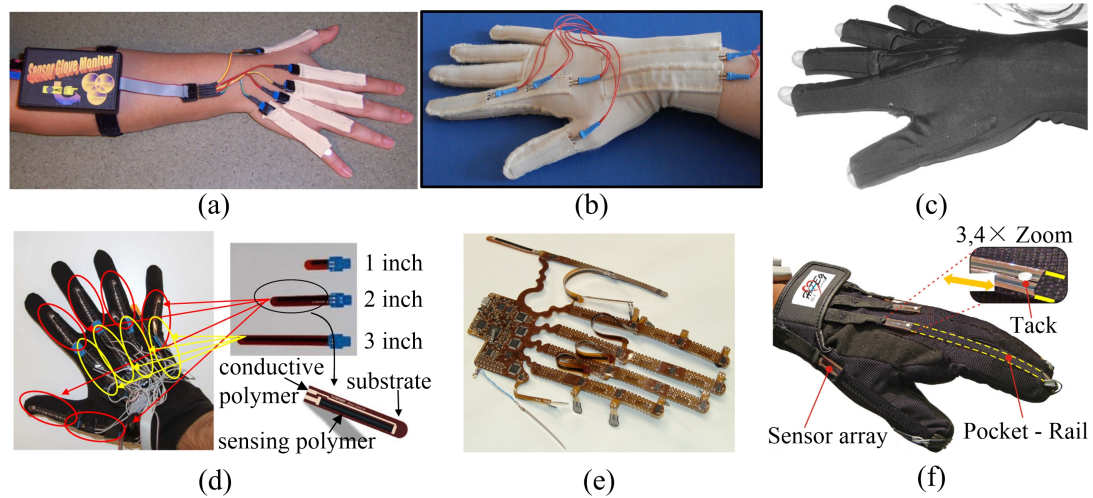


**Figure 3.5** Instrumented glove systems equipped with resistive bend sensors manufactured by Flexpoint SS. **(a)** Shadow Monitor [113, 118]. **(b)** NeuroAssess Glove [117]. **(c)** WU-Glove [116]. **(d)** Sensing glove designed by Borghetti et al. [115]. **(e)** Tyndall/UU glove (ver. 1) [114]. **(f)** HITEG-Glove [119].

Generally, ink-based commercial bend sensors are unidirectional, i.e. only sensitive to the deflections in a single direction. To achieve a bi-directional electrogoniometer, Wang et al. [122] placed two Spectra Symbol bend sensors back-to-back, and combined their outputs using a multivariate linear regression model for tracking finger flexion/extension. Flexpoint SS recently has launched bi-directional sensors by coating conductive ink on both sides of the flexible substrate, but their performance characteristics are yet to be reported.

Several other types of bend sensors have been researched for measuring finger motion as reported in the literature [123–126]. In 1996, Jurgens and Patterson [126] developed a low-cost sensor by screen printing carbon-based electrically conductive ink onto the polyester substrate. The sensor on the 0.05 mm substrate presented a repeatability of 6.5% and a variation in resistance less than 100  $\Omega$  when bending from 0° to 90°. Recently, using a peeling technique, Latessa et al. [125] developed a bi-directional flexible sensor with conductive PEDOT:PSS film, which is shown in Figure 3.6(a). This sensor demonstrated piecewise linear responses to flexion angles from -60° to 60°, but was also sensitive to microscopic strain (GF:  $17.8 \pm 4$ ). Using the same conductive material, Tongrod et al. [124] fabricated a series of bend sensor patterns (see Figure 3.6(b)) using ink-jet printing technology. The patterns with varied sensing geometries demonstrated different resistances under the same bending. However, they all showed extremely low sensitivities to angles below 20°. The study by Leigh et al. [123] presented a 3D printed bend sensing strip based on piezoresistive carbon black

filler. As shown in Figure 3.6(c), multiple sensors were embedded into the main body of a printed glove to monitor finger motion. However, the change in sensor resistance was small (less than  $600 \Omega$ ) when the fingers were fully bent. Clearly, these sensors are not as precise as the commercial bend sensors, especially the bend Sensors<sup>®</sup>.

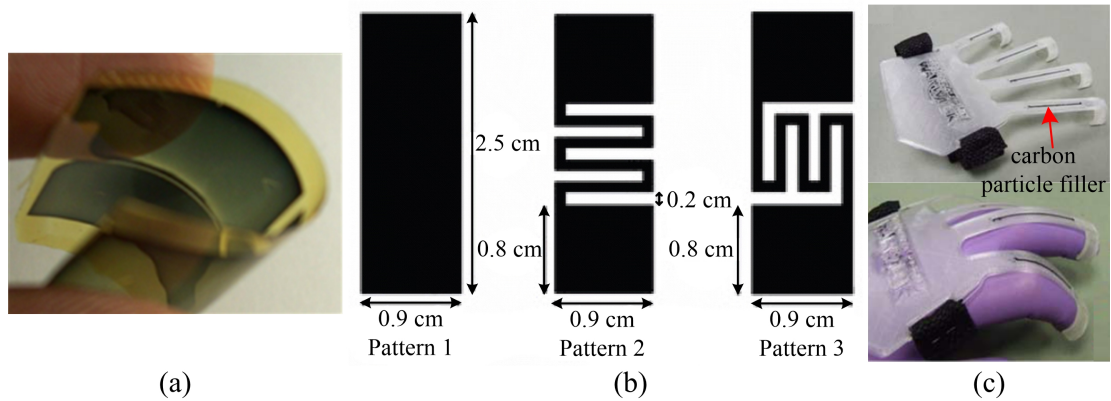


**Figure 3.6** Self-developed bend sensors. (a) PEDOT:PSS patterned bend sensor [125]. (b) Different bend sensor patterns [124]. (c) Glove cover embedded with 3D printed bend sensors [123].

The common strengths and limitations of the bend sensors are summarised below.

**Strengths:** They are highly flexible, light-weight, low-cost, and easy to operate.

**Limitations:** The commercial bend sensors are generally unidirectional, and therefore unable to detect all of the DOFs associated with finger motion;

A time-consuming calibration process is required, since bend sensors are dependent on the radius of curvature and therefore the size of the finger joint;

They are slow to respond, exhibit serious temporal drift, and suffer from significant overshoot in high speed situations;

The majority are subjected to large hysteresis errors, and fail to return to the initial state (resistance) after loading.

### 3.1.2 Optical Angle Sensors

Optical angle sensors designed for monitoring finger motion can be broadly divided into fibre optic-based sensors, optical linear encoders, LED/photodetector coupled sensors, and polarisation-based sensors.

### 3.1.2.1 Fibre-optic Sensors

Optical fibres exploit the phenomenon of total internal reflection of light. They are used extensively in long-distance telecommunications because of their reduced attenuation and higher operating bandwidths compared to wire cables. Optical fibres have also been developed as sensing units as early as 1977 [127]. Application areas include the measurement of strain, temperature, pressure, and other physical quantities. Although many studies [128–132] focus on the measurement of curvature or bending using the fibre optic-based sensors, only a few have applied this methodology to monitor the movements of articulated joints.

One popular fibre optic sensor for tracking articulation is based on an optical fibre grating which records strain and bending variations in the form of a wavelength shift. According to the period of gratings, they can be categorised into two main types: fibre Bragg grating (FBG) containing a submicron period length, and long period fibre grating (LPFG) typically having a longer period ranging from  $100\ \mu\text{m}$  to  $1000\ \mu\text{m}$  [133]. FBG sensors back-reflect particular wavelengths (also called Bragg wavelengths) and transmit all others whilst LPFG sensors couple the forward-propagating modes, i.e. only the transmission spectra to be observed.

Using a wavelength-division multiplexing technique, Silva et al. [134] fabricated a glove-shaped polymer matrix equipped with 14 reflective FBG sensors which were supplied by a curvilinear-configured single optical fibre, as shown in Figure 3.7. The gratings for each sensing unit were inscribed at intervals of  $1.84\ \text{nm}$  to ensure the accommodation of all sensors in a single fibre. The Bragg wavelength of each FBG sensor shifted in proportion to the applied strain [135]. When attached to the upper face of a standard fabric glove, the polymer structure could be used to monitor finger flexion/extension. Unfortunately, the narrow spectral bandwidths result in a low sensitivity and limited measuring range. Furthermore, additional peripherals including an optical circulator and FBG interrogator severely limits system mobility.

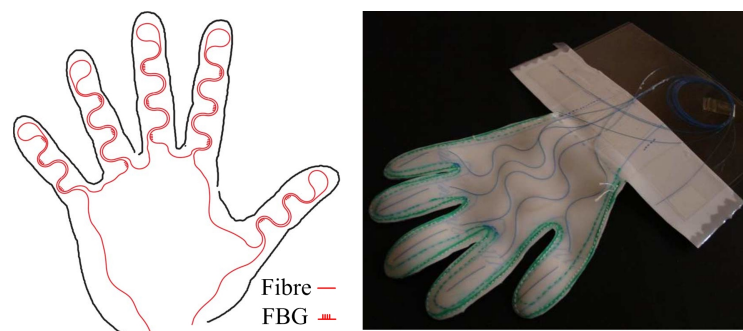


**Figure 3.7** Images of the FBG-based sensing polymer matrix [134].

The FBG sensor is inherently sensitive to both strain and temperature. Silva et al. [135] discovered that an elongation (2.5%) of the FBG sensor with the grating length of 8 mm caused the same shift (1.7 nm) in the Bragg wavelength as a 100 °C temperature change. It is therefore essential to differentiate between strain and temperature effects in order to ensure accurate strain measurements [136]. Several approaches have been proposed to overcome this problem. A straightforward method is to use a reference grating which is isolated from the applied strain and placed close to the sensing FBG [137]. An alternative solution is to adopt two superimposed FBGs with much different Bragg wavelengths, which produces different responses to the same measurands [138]. Additionally, a FBG/LPFG hybrid grating sensor was also reported to measure strain and temperature simultaneously [139]. The sensing principle was based on the principle that the LPFG element shows much higher response to temperature and a smaller response to strain compared to the FBG. Finally, a superstructure FBG was proposed to simultaneously measure the strain and temperature [140]; a superstructure FBG is a special FBG which allows the creation of equivalent phase shifts and the generation of gratings with greatly fluctuating phase and amplitude by adjusting the profile of the superstructure. These methods can separate or compensate for the temperature effect, but at the expense of increased measuring complexity.

Based on the coupling-wavelength shift, the LPFG sensing technique was also investigated for measuring finger motion, but the measurements were limited to bending angles below 45° [141]. In comparison with FBG sensors, LPFGs generally demonstrate much higher sensitivity [133]. However, the accuracy of LPFG sensors is challenged by the difficulty in measuring the exact notch wavelength since LPFG sensors work in transmission configuration producing broad bandwidth of the attenuation bands [142].

Another promising fibre optic-based sensing technique is the hetero-core structured sensor which works using light intensity modulation. As shown in Figure 3.8, the hetero-core optical fibre sensor consists of a short-length segmental fibre inserted in a transmission line fibre by means of thermal fusion splicing. The core diameter of the sensing fibre is typically 3 or 5  $\mu\text{m}$ , smaller than that of the transmission fibre (9 or 50  $\mu\text{m}$ ). According to the combined core diameters, the sensors are called 9-5-9, 9-3-9, and 50-3-50 respectively. Amongst them, the embedded 9-5-9 optical fibre sensor is most suitable for bending detection due to the relatively small optical loss at the interface boundary between the transmission fibre and the hetero-core region. When the hetero-core region is subject to macro bending, the leakage into the cladding appreciably increases, leading to changes in transmission loss [143, 144].

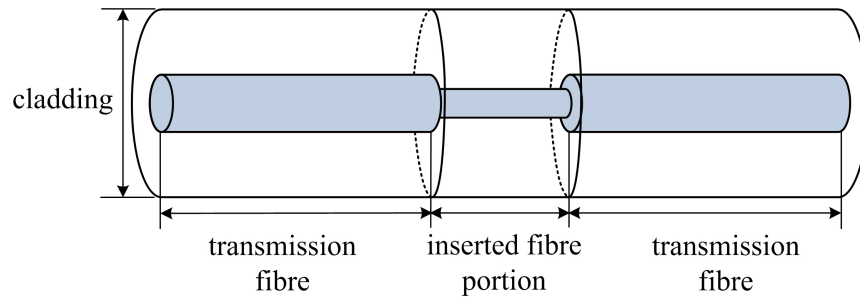


**Figure 3.8** Basic structure of hetero-core optical fibre.

Nishiyama et al. [144] investigated the characteristics of the 9-5-9 fibre sensor by mounting the sensor on to two displacement stages. The hetero-core portion was placed at the middle and the bending action was controlled by adjusting the distance between the two stages. The measured optical loss monotonically increased with the given displacement. When equipped in wearable systems in the form of a sensing jacket, a wristband, and a gait system, the hetero-core optical fibre sensors demonstrated attractive performance in recording human motion including shoulder, elbow, wrist, and knee [143]. Later, they investigated the possibility of monitoring finger flexion/extension by attaching three embedded 9-5-9 hetero-core sensors to a sensing glove [145]. As illustrated in Figure 3.9, in this sensing glove the hetero-core portion of the sensor was located on the back of the hand (initially bend), and the transmission fibre lines with two fixed terminals (point B and C) were fed through multiple short tubes stuck on the glove. When the finger flexed, the transmission fibre lines were pulled causing variations in the bending of the hetero-core portions, and thus producing different output intensity. The flexion angle of the joint was derived using the geometric relationship related to the thickness of the measured finger [145], and a calibration process is therefore required for different individuals. Due to the single-mode transmission scheme, the embedded 9-5-9 hetero-core sensors had good immunity to temperature fluctuations. However, the splicing portions between the different core diameter fibre parts may cause fragility issues for long-term use.

Plastic optical fibres (POFs) feature comparatively large core diameters (about 1 mm). In comparison with the glass/silica optical fibres, the major advantage of POF is the mechanical robustness under bending and stretching, and the low costs of manufacturing, connection and installation [146]. Due to the large attenuation and distortion, POF is commonly used for low-speed and short-distance communications. In recent years, POF sensing techniques have also attracted intense interest.

For POF-based sensors, the response sensitivity to external stimuli usually needs to be enhanced by modifying the structure of the optic fibre, such as side polishing [147], surface abrasion [148], creation of sensitive zones in the shape of teeth [149], removal

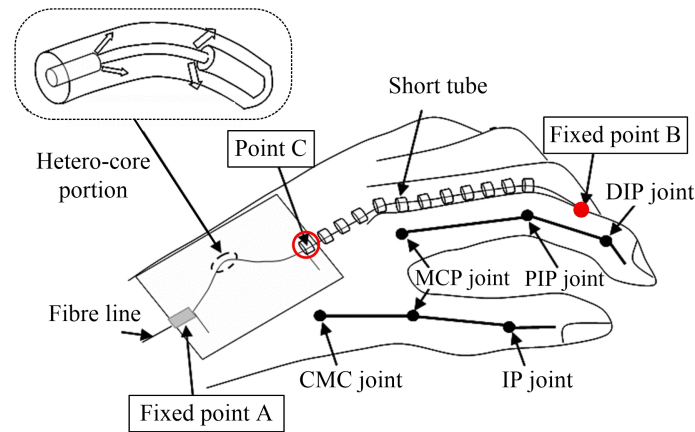


**Figure 3.9** Configuration of the embedded hetero-core fibre-optic sensor on human hand [145].

of the cladding at equal intervals [150]. Based on the modulation of light intensity, a multi-mode POF sensor was reported for strain and bending measurements [151]. Results revealed that this sensor was only capable of measuring limited strain (1.2%) and bending (0.7%). Compared with FBG-based optical sensors, POF sensors do not require complicated demodulation techniques. The majority of the reported studies focus on the applications of POF sensors in detecting knee movements [147, 149, 150].

Fujiwara et al. [152] fabricated an optical fibre transducer based on microbending attenuation. The sensor was configured with a periodical array structure as illustrated in Figure 3.10. The transducer consisted of a silica multimode fibre passing through the gaps between flexible silicone rods positioned periodically. As the user flexed his fingers, the silicone rods were stretched, and thus the optical fibre was pressed, inducing light attenuation proportional to the angular displacements. Five transducers were attached to a fabric glove for recording the movements of the index finger and the thumb. Meanwhile, a reference fibre was adopted to monitor the source stability by delivering the light directly to the charge-coupled device (CCD).

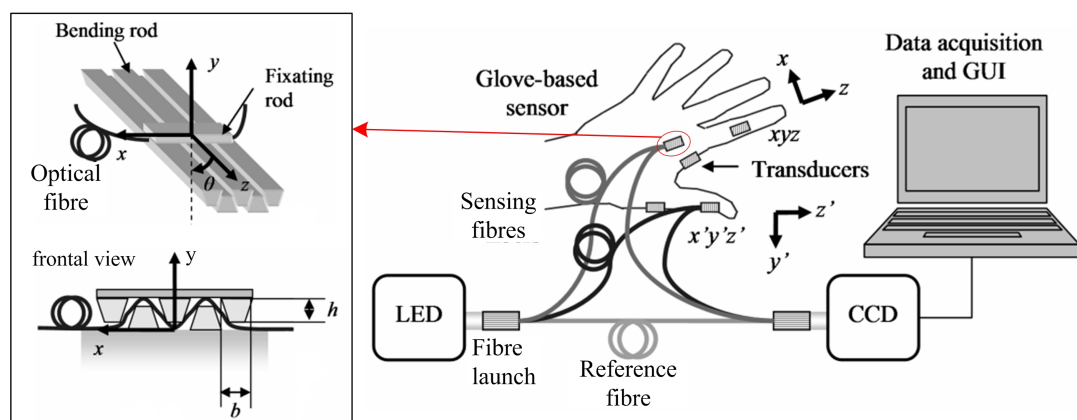


**Figure 3.10** Optical fibre bending transducer based on the microbending attenuation [152].

Other fibre optic-based sensing techniques have also been proposed to detect angular displacements, including a stress-induced birefringence fibre polarisation controller [153] and a bevelled step-index multimode fibre sensor [154]. These techniques suffer from either low measurement accuracy or limited measuring range ( $<90^\circ$ ).

The common strengths and limitations of fibre optic-based sensors are summarised below.

**Strengths:** Fibre optic-based sensors are small in size, lightweight, flexible, immune to electromagnetic interference and fast response times;

Electrical connection wires are not required during the operation;

FBG optical sensors are featured with high multiplexing capability, high stability, and low crosstalk.

**limitations:** Fibre optic-based sensors are sensitive to temperature fluctuations over time, especially the FBG-based sensors;

The stability and the reliability of the sensors based on intensity modulation are generally determined by the fluctuations in the optical power, the propagation mode of the adopted optical fibre, and undesirable bends;

The sensors based on wavelength shift, i.e. fibre grating sensors, require demodulation techniques (e.g. spectrum analyser) to separate the spectra;

Creation of structural imperfections is needed to enhance the sensitivity of the POF-based sensors.

### 3.1.2.2 Optical Linear Encoders

An optical encoder based position sensor optically recognises sequential surface patterns and then mathematically determines the position or displacement. Li et al. [27] implemented an optical linear encoder module by housing a commercial LED integrated mouse sensor (ADNS 3530 [155], Avago Technology Ltd.) and encoder strip into a customized baseplate. Using these sensing modules, they developed a finger-motion tracking device, named as SmartGlove (see Figure 3.11), to capture the flexion/extension of the MCP and PIP joints. The linear encoders recorded the displacement of the movable strips. Under the assumption that each finger joint flexed/extended around a fixed centre, the angular positions of the joints were calculated using the geometrical relationship determined by the measured displacement

and the radius of the joint. SmartGlove demonstrated a relatively high repeatability and reliability.

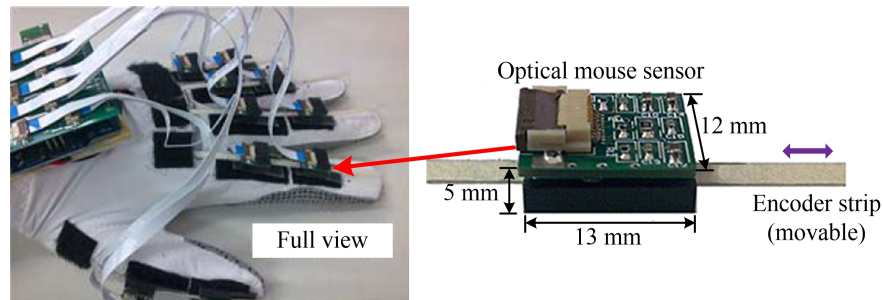


**Figure 3.11** SmartGlove integrated with ten commercial optical linear encoders [27].

Also, using the same commercial optical mouse sensor and the encoder strip, Lim et al. [156] developed a sensing goniometer to monitor the flexion of the elbow. Additionally, they also demonstrated the feasibility of using an optical linear encoder together with an accelerometer for tracking the movements of the human arm [157]. This optical linear encode consisted of an infrared emitter, a receiver, and a reflective strip. The receiver converted the light reflected off the strip into the number of pulse indicating the distance travelled as the elbow bent.

**Strengths:** Optical encoders are featured with high accuracy and high resolution.

**Limitations:** They are susceptible to surface contaminants on the encoder strips, such as dirt, oil, and dust;

The thick and wide strips may inhibit the natural finger motion.

### 3.1.2.3 LED/Photodetector Coupled Sensors

The LED/photodetector coupled sensors detect the variations in bending angles by measuring the changes in transmitted and/or reflected light intensity. The LEDs and photodetectors are usually located at opposite ends of the transmission path. In 1985, Zimmerman [158] patented an optical sensor which used a reflective interior wall within a flexible tube as the light transmission tool. The tube flexion caused a proportional decrease in the amount of light received by the photodetector. In 2009, Cavallo et al. [159] reported a LED/photodiode coupled angular sensor taking advantage of the angle-varying radiation pattern of the LED. They mounted the LED and photodiode to two contiguous phalanges of a tendon-driven robotic hand for tracking the flexion. Results indicated that this sensor had a relatively low sensitivity for the angles below  $15^\circ$ , and also suffered from ambient light interference. To improve the sensor's linearity,

later designs incorporated a mechanical component with an integration of a movable link to partly occlude the light emitted by the LED [160]. The thickness of the canal varied with the flexion of the robotic joint, causing the changes in the received light intensity. In 2014, Zhao et al. [161] measured the motion of the articulated fingers using the photoplethysmography technique, an optical method used to detect the volumetric changes of an organ. The sensor consisted of two LEDs and one photodiode which measured the slight variation in the reflected intensity after the light passed through the tissue. The outputs varied with the finger motion.

The strengths and limitations of such a sensing method can be summarised below.

**Strengths:** LED/photodetector coupled sensors have simple structures.

**Limitations:** They are prone to external light interference, limiting measurement accuracy;

The response to changes in bending angle is generally non-linear.

#### 3.1.2.4 Polarization-based Rotary Sensor

Based on Malus' law, several rotary sensors have been proposed to measure the change in rotation angle. In 1995, Albion et al. [162] patented two-phase and three-phase rotation sensors for applications in military and commercial aircraft. In the two-phase sensor, polarised light beams with their polarisation directions initially oriented at  $45^\circ$  to each other passed through a linear polariser. The three-phase sensor consisted of three light beams with a difference of  $60^\circ$  between their polarisation axes. In theory, the rotation of the linear polariser causes proportional changes in the measured light intensity. Following on from the two-phase polarisation sensing principle presented by Albion et al. [162], Barnett et al. [13], in 2002, patented a rotary motion transducer for measuring the speed, direction and displacement of a rotating shaft. In 2005, Wijntjes et al. [14] developed an optical rotary encoder in which a polariser synchronously rotated with the rotatable object, the transmitted polarised light was directed towards a plurality of analysers and photodetectors. In 2009, Li et al. [163] also passed incident light through a polarising disc mounted with four analysers for measuring the angular displacement. In 2010, Baxter and Raynor [15] proposed an optical rotary encoder using the polarisation difference imaging technique. In 2014, Ikeda et al. [164] implemented a compact optical rotary encoder which measured the rotation angle by detecting the differential light intensity of the orthogonal polarisation components.

Overall, the reported polarisation-based sensors are used either as optical rotary encoders or as the sensing units for measuring the relative rotation of two mechanical objects [13–15]. Several sensors of this kind have found application in the aircraft industry [162]. Polarisation-based optical sensors are capable of producing accurate, fast, and direct measurements for the relative rotation. In this work polarisation-based sensing has been extended to monitor real-time finger motion as described in chapters 4 to 6.

### 3.1.3 MEMS Gyroscopes and Accelerometers

Gyroscopes and accelerometers are inertia-based electronic devices that measure the orientation and/or position of an object with respect to a known starting point. A gyroscope is a freely spinning wheel mounted on two or three gimbals, which are pivoted supports allowing the rotation of the wheel about the spin axis. When rotating, the orientation of the spin axis is not affected by any tilting or rotations of the mounting, and thus gyroscopes are generally used for measuring or maintaining orientation in space. An accelerometer is a compact electromechanical unit measuring either static or dynamic acceleration along a given axis. Static forces can be used to calculate the tilt angle of an object with respect to the Earth's surface, while dynamic accelerations are useful for analysing the way that the object is vibrating or accelerating.

Although gyroscope-based tracking can offer stable and accurate orientation estimation during short-term rapid movements, a major limitation is the accumulated error which occurs during the integration of the angular velocity outputs over time [165]. Accelerometers are capable of detecting dynamic accelerations, but they are unable to distinguish between the actual dynamic acceleration and the component of Earth's gravity when the measured object accelerates in a particular direction [166]. A number of hand tracking devices have implemented accelerometers [167–169]. The *AcceleGlove* [168] uses a set of six dual-axis accelerometers mounted on the finger phalanges and the back of the hand to recognise the American Sign Language. Another glove-based prototype was equipped with two accelerometers for recording the movements of the thumb and the index finger [169]. However, these devices are only able to measure static or low-speed finger motion (i.e. flexion/extension or ABD/ADD) due to the limitation of the accelerometers.

In practical applications, many devices benefit from the combination of gyroscopes and accelerometers, i.e. inertial sensing modules. In recent years, the lightweight inertial modules are also increasingly used to measure human kinematics in clinical and rehabilitation communities [170]. Under the assumption that the human knee is a perfect hinge joint, Cooper et al. [171] positioned an inertial sensing module on either side

of the knee joint and then used Kalman filters to calculate the knee flexion/extension during dynamic activities. Using two inertial sensing modules, each containing a triaxial gyroscope and accelerometer, El-Gohary and McNames [172] combined the kinematic models of upper limb with state-space methods to continuously estimate the movements of human shoulder and elbow. Similarly, Seel et al. [173] also reported an inertial sensor-based motion tracking system for gait analysis, in which the knee flexion/extension and ankle plantar/dorsiflexion angles were investigated. In addition, Dai et al. [174] attached an inertial sensing module to the user's middle finger for capturing hand grasping. The dominant frequency and the mean range of hand grasps were calculated to assess Parkinsonian bradykinesia. Noort et al. [175] implemented a system with an integration of eleven inertial sensing modules for tracking multiple DOFs of the human hand, i.e. the movements of the left thumb, index finger, and middle finger.

The combination of gyroscopes and accelerometers improves the precision of position and orientation estimation, but the integration drift is still an obvious limitation for long-term use. Moreover, since accelerometers are incapable of detecting the motion perpendicular to the direction of the Earth's gravity, i.e. the yaw rotation, the readings of gyroscopes cannot be compensated in such situations. Therefore, inertial sensing modules are usually limited to track one or two degrees of motion trajectories [166, 171, 173, 176]. Recently, more and more studies adopt magnetometers together with inertial sensing modules to estimate the 3D motion trajectory [170, 177, 178]; magnetometers provide absolute position information by measuring the magnetic field vector surrounding the object. In this thesis, the combination of gyroscopes, accelerometers and magnetometers, is referred to as an inertial measurement unit (IMU).

In IMU-based tracking systems, gyroscopes are generally used to provide the orientation information, and accelerometers and magnetometers mostly provide complementary data to compensate the drift errors produced by the gyroscopes. Their outputs are fused by different algorithms to calculate the orientation and positions. The reported algorithms include integration, vector observation, Kalman filtering and complementary filtering, etc. [170]. Among them, the Kalman filter based fusion approaches including basic Kalman filters, extended Kalman filters, and unscented Kalman filters are favoured in estimating human motion [172].

One of the main limitations of IMU-instrumented tracking systems is their susceptibility to ferromagnetic disturbances leading to erroneous readings by the magnetometers. Several approaches were proposed to compensate for magnetic distortions, such as the modified factored quaternion algorithm [179] and the ellipsoid least-square fit algorithm

[180, 181]. Improvements were achieved but at the expense of increased computational load for the tracking system. At present, the simplest and most common way to obtain reliable measurements is to operate the IMU-based systems under controlled conditions [182–184], e.g. staying away from ferromagnetic objects.

Another challenge for IMU-based human motion capturing systems is achieving alignment of the sensors' local coordinate axes with those of the joint [173]. Despite several attempts [185, 186], it has proven very difficult to make these two coordinate frames coincident without introduction of elaborate sensor attachments. Therefore, a sensor-to-segment transformation matrix is usually required to assess human kinematics. The common approach is to perform several predefined calibration postures and/or movements. These calibration procedures significantly influence the final measurement accuracy [173, 175, 179, 184, 187].

Developments in MEMS technology has led to the miniaturisation of inertial sensing modules and IMUs to the point where it is now feasible to use them for recording human hand movements as described in the following section.

As illustrated in Figure 3.12(a), SCURRY [176], a wearable glove-like input device, included two gyroscopes packaged in the base module and four dual-axis accelerometers embedded in ring modules. The gyroscopes detected the direction of hand motion, and the accelerometers reported finger clicking. SCURRY allowed users to select a specific input character or operation using hand motion and finger clicking.

The UU/Tyndall smart glove (ver. 2) [188], as shown in Figure 3.12(b), was configured with sixteen IMUs to measure the range of finger movements. This IMU-based system could offer unbiased measurements. However, complicated data fusion and analysis were involved to determine finger movements. In this case, only the static finger flexion/extension was evaluated. The capability of this system in measuring the dynamic motion including finger flexion/extension and ABD/ADD in real time was not yet known.

Moreira et al. [180] integrated eleven IMUs with a glove to assess hand motion, which is depicted in Figure 3.12(c). Two IMUs were attached on the proximal and distal phalanges of each finger, and one IMU was located at the back of the hand. This glove system presented high stability (standard deviation  $0.13^\circ$ ), acceptable accuracy (average error  $-2.23^\circ$ ), and high reliability (intra-class correlation coefficient 0.88-0.99) but required a complicated calibration procedure including the zero-offset and temperature-based offset correction for the gyroscopes and accelerometers, and also compensation for magnetic distortions.

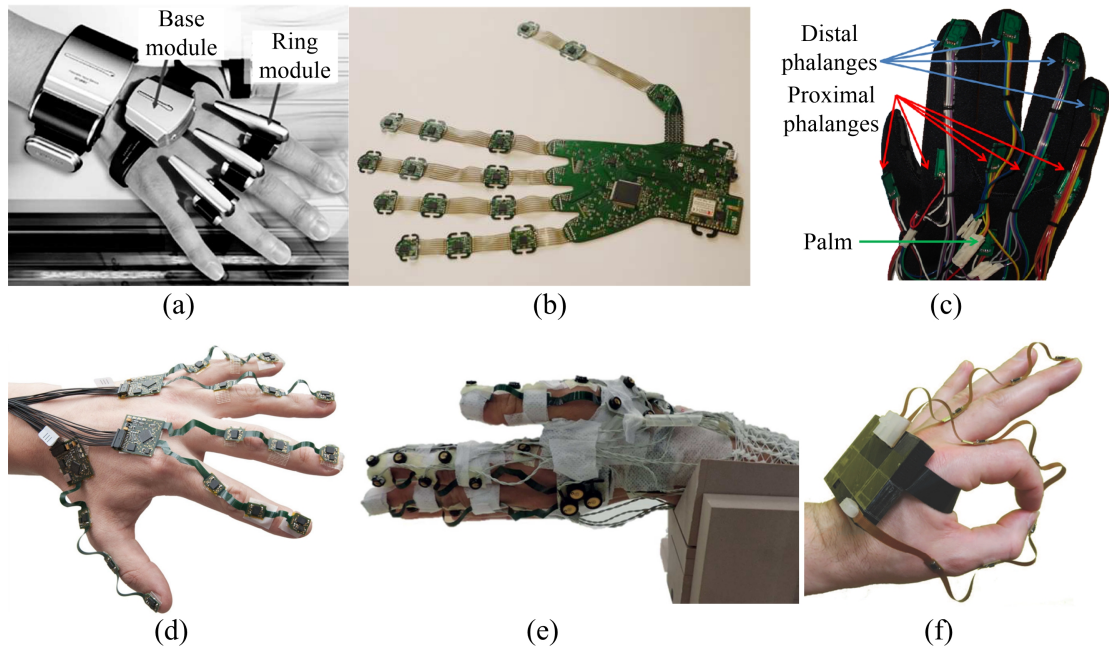


**Figure 3.12** (a) Wearable input device, SCURRY [176]. (b) The UU/Tyndall smart glove equipped with 16 IMUs [188]. (c) Motion-capture glove [180]. (d) PowerGlove equipped with multiple IMUs [184]. (e) Modified PowerGlove only equipped with gyroscopes and accelerometers [175]. (f) Hand motion tracking systems with IMU-based sensing strips [187].

The PowerGlove implemented by Kortier et al. [184] was a 3D motion tracking system for reconstructing hand motion as shown in Figure 3.12(d). In this instrumented system, two inertial sensing modules including triaxial gyroscopes and accelerometers were placed on the dorsal side of the proximal and middle phalanges of each finger, and double IMUs were deployed on the fingertip and the metacarpal. The gyroscopes were used to determine the orientation of each finger segment, while the accelerometers and magnetometers offered calibration information against the bias drifts in the estimated orientation data. Under the assumption of the kinematic chain of the articulated finger, an extended Kalman filter was designed to search the optimal trajectory assessment. Although this PowerGlove was equipped with IMUs for each finger joint, the authors only presented the dynamic flexion/extension of the thumb and the index finger at a speed no more than 116 full range finger flexions/extensions per minute. Following this research, they modified the system configuration (see Figure 3.12(e)) to include only gyroscopes and accelerometers. This can eliminate the artefacts introduced by the magnetic sensors as a result of inhomogeneous magnetic field throughout the hand when the user stays close to ferromagnetic objects [175]. The system performance was further evaluated for capturing the flexion/extension of the thumb, index and middle fingers, and the ABD/ADD and circular pointing of the index finger. Compared with a commercial motion capture device (Optotrak 3020 [189]), the system demonstrated a root mean square error ranging from  $3.3^\circ$  to  $8.4^\circ$  during the flexion/extension, ABD/ADD and circular pointing tasks of the index finger. Inconsistency was greatest for fast motion and

pointing tasks which could be related to the uncompensated offset and skin movement artefacts.

Recently, Valtin et al. [187] presented another IMU-based modular system for measuring hand motion. As showed in Figure 3.12(f), this system was placed directly on to the hand and consisted of three sensor strips and a base unit. Each sensor strip contained three IMUs for each finger and the base unit embodied a microcontroller and a 9-axis IMU. The length of the sensor strips was sufficient to accommodate stretching of the finger skin during the flexion. In contrast to the PowerGlove introduced by Kortier et al. [175, 184], this system calculated the orientation of each finger segment directly, without any assumptions on the kinematic chain.

Fang et al. [190] also implemented a data glove which was embedded with 15 IMUs. Hand gestures were estimated using linear Kalman filters under the assumption that the static magnetic field through the hand was homogeneous. Lemos et al. [191] presented IGlove, a wearable glove-based device that used four IMUs to evaluate manual dexterity on surgical simulators. Mańkowski et al. [192] described the design of a glove-like device, called CIE-DataGlove, to capture hand postures using 12 IMUs.

According to the review analysis by López-Nava and Muñoz-Meléndez [170], the majority of the inertial module based wearable systems focused on tracking human motion of upper limb or lower limb, and only a few investigated the movements of other anatomical regions including the trunk and hand/fingers. Similarly, Wang et al. [193] declared that the IMU is the most frequently used sensing technique in interactive wearable systems for monitoring upper extremity; however, most studies used IMUs to evaluate the motion of shoulder, elbow, and wrist. The lack of attention towards hand motion detection can be explained by the complicated articulation and the small sizes of the finger joints. As described in 2.1.2, there are 21 DOFs in each human hand which are only contributed by the five finger joints for local movements. Using IMUs to track all finger articulations will require complicated data fusion processes resulting in large computational overheads and thus limiting the system's real-time capability.

The following statements summarise the strengths and limitations of inertial sensors for tracking articulated motion.

**Strengths:** Inertial/IMUs-based tracking systems are capable of tracking 3D hand motion;

Inertial sensors are lightweight and non-obstructive, suitable for applications in portable devices.

**Limitations:** Calibration is required to transform the outputs from the sensing coordinate system to the joint coordinate system;

Complicated data fusion procedures cause large computation time, limits the system's real-time capability;

Gyroscopes suffer from severe accumulated drift, resulting in erroneous estimates of orientation over long periods;

Accelerometers can only determine the orientation of stationary objects with respect to the Earth's surface. Furthermore, they are incapable of sensing the motion perpendicular to the direction of the Earth's gravity, i.e. the yaw rotation;

Magnetometers are affected by distortions caused by inhomogeneous magnetic fields.

### 3.1.4 Magnetic Induction-based Sensors

Magnetic induction-based sensing techniques use a permanent magnet or electromagnet as a reference point and the hand position with respect to the magnetic source is detected by the magnetic sensor. Magnetometers which are used together with gyroscopes and accelerometers to reconstruct hand motion have been discussed in section 3.1.3. Here, we only describe magnetic sensing techniques for tracking hand trajectories.

In 2004, Kuroda et al. [194] presented a data glove named as StrinGlove for sign language recognition. This system used 24 linear inductcoders to measure the finger flexion/extension and ABD/ADD, as well as the wrist motion. The inductcoder [195] was a magnetic induction-based sensor which was composed of a ferromagnetic core moving in a conversion element, and the hand motion was recorded in the form of a phase difference.

Similarly, using magnetic induction technology, Fahn and Sun [34] constructed an instrumented system consisting of five sensing coils and ten generator coils to monitor ten finger joints. As illustrated in Figure 3.13(a), for each finger a single sensing coil was placed on the palmar side of the proximal phalange, and two magnetic flux generators were attached to the middle phalange and the metacarpal. The generator coils were energized consecutively resulting in induced electromotive forces (emfs) in the sensing coils. A geometric model was adopted to derive finger flexion angles, which were dependent on the distances between the finger joints and the magnetic generator/sensing coils. To determine these distance parameters, a two-step calibration process was required. In a subsequent study, they adopted the same sensing technique to

track the fingertip position and orientation [196]. Five sensing modules, each including two coils, were installed to five fingertips and one additional sensing coil was placed to the metacarpal of the middle finger. On each MCP joint there located two generator coils, co-centred and perpendicular to each other. This tracking system simplified the calibration process but at the expense of increased numbers of magnetic flux coils and stringent requirements on coil module installation, i.e. the coils on the each joint and fingertip required to be co-centred and perpendicular.

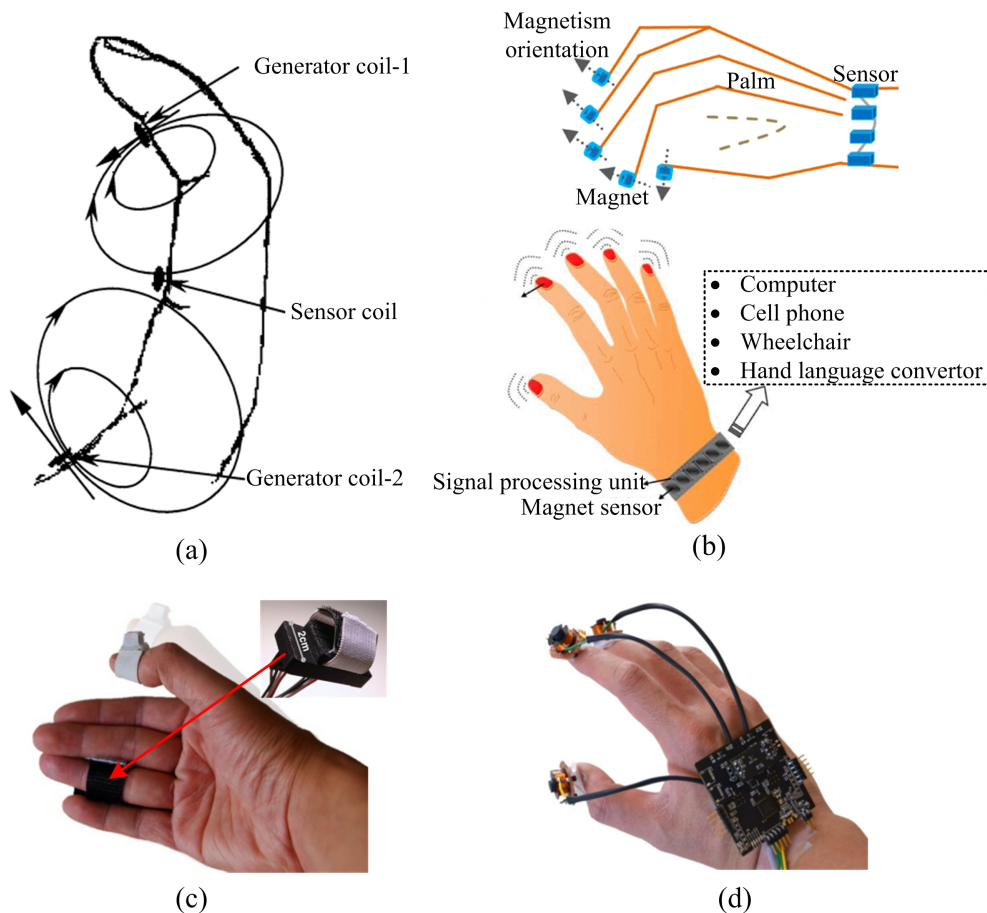


**Figure 3.13** (a) Positions of the sensing and generator coils [34]. (b) Structure of the magnetic hand tracking system [35]. (c) *uTrack*, a 3D input device [197]. (d) *Finexus*, a multiple fingertip capturing system [198].

As illustrated in Figure 3.13(b), using small permanent magnets and an electronic wristband, Ma et al. [35] implemented a hand motion tracking system for human-machine interactions. When the fingers were flexed or extended, the combined magnetic fields generated by the permanent magnets at the fingertips were captured by six two-axis commercial magneto-resistive sensors around the wristband. Finger posture could be reconstructed from the location and orientation of the fingertips calculated using a geometric model. When a subject was instructed to only move the index finger with the other fingers unchanged, the system produced motion readings with a similar trend to the commercial tracking system (Vicon [199]). However, this system was not suitable

for tracking the simultaneous motion of all fingers, since the magnetic sensors located in the wristband were sensitive to all of the magnetic fields of the permanent magnets. In a similar way, Friedman et al. [200] mounted two magnetometers at the wrist and a magnetic ring on the index finger for capturing the motion of the wrist and finger joints.

As shown in Figure 3.13(c), *uTrack* [197], a single-point input system, uses a magnetic field sensing technique to detect the relative motion between the thumb and ring finger in 3D space. A single permanent magnet was placed on to the thumb to generate a magnetic field and two triaxial magnetometers were located on the back of the ring finger with their axis aligned. In a recent study, an improved tracking system named as *Finexus* was reported (see Figure 3.13(d)). *Finexus* equipped with four magnetic sensors was capable of tracking the motion of multiple fingertips [198]. Different from *uTrack*, *Finexus* adopted a frequency-division technique to enable multipoint tracking, i.e. driving each electromagnet using alternating currents with different frequencies and then applying a band-pass filter to the outputs. Additionally, *Finexus* also featured a more extensive sensing space (volume of a sphere with a diameter of 120 mm) than that of *uTrack* (70 mm (width) × 30 mm (depth) × 60 mm (height)).

The majority of magnetic-based tracking systems only focus on fingertip positions. Their common strengths and weaknesses are summarised below.

**Strengths:** Magnetic sensing units are capable of providing precise hand positioning data.

**Limitations:** Magnetic sensors are prone to inaccuracies due to interference from the Earth's magnetic field or nearby ferromagnetic objects;

External magnetic excitation is required in magnetic tracking systems;

When monitoring multiple joints or fingertips, time-division or frequency-division multiplexing method is needed to avoid the effects of mutual induction;

Finger flexion angles are usually derived by geometric models which are related to the sensor locations and hand dimensions.

### 3.1.5 Other Sensing Techniques

Except the commonly used sensing techniques described above, other sensing techniques including capacitive sensors, inductive elements, piezoelectric sensors,

potentiometers, surface electrodes, and Kinect sensors are also reported to track finger motion. These sensing approaches are discussed briefly in the following text.

A few research groups [45, 67, 201] have investigated nanocomposite-based capacitive strain sensors for sensing articulated human motion. The literature [45] presented a parallel-plate capacitive sensor with a AgNW film embedded in the top and bottom surfaces of a polymeric substrate. Vertically aligned a CNT forest was also used to fabricate wearable piezocapacitive strain gauges [67]. Although the reported nanocomposited capacitive strain sensors could detect large tensile strain up to 50% [45, 201] and 150% [67], their GFs were no more than 1.

Inductive sensors are also used in wearable motion tracking systems. For instance, an inductive fibre meshed strain sensor was constructed to measure finger motion by Wijesiriwardana [46]. Cu wire with a diameter of 0.12 mm is knitted into lycra fabrics as sensing coils. These coil bands could be either integrated into gloves or put on as rings. This transducer avoided the intrinsic limitations of the resistive fibre-meshed sensors including performance degradation with repetitive usage, but complicated models are required to obtain the bending angles due to the simultaneous coexistence of self and mutual induction of the sensing coils.

A piezoelectric sensor produces an electric charge in response to mechanical inputs. Cha et al. [202] fabricated flexible piezoelectric sensors using polyvinylidene fluoride as the sensing material, and also integrated them with a data glove. Finger motion caused proportional variations in the sensor output voltages. The measured movements of the index finger were in good agreement with camera recordings.

Park et al. [36] used multiple linear potentiometers to detect finger motion. A wearable sensory glove was fitted with a combination of ten linear potentiometers, ten return springs, and ten flexible wires. The potentiometers and the return springs were located on the back of the hand as a compact sensing module. One terminal of each flexible wire was connected with the potentiometer and the other one was tied to the finger segments of glove. Finger flexion/extension caused movement of the corresponding flexible wire, which was measured by the potentiometer (essentially a voltage divider) in the form of electrical voltage. Finally, the joint angles were calculated by a kinematic model dependent on the dimension of the finger articulations.

The Kinect sensor, developed by Microsoft Corp. (Washington, US) [203], is an imaging device consisting of a RGB camera and infrared depth-finding sensors. In recent years, the Microsoft Kinect has attracted much attention due to its performance in tracking full-body motion. Hernoux and Chrisman [204] used the Kinect sensing system to retrieve the position of the user's hands for natural interactions in 3D virtual environments.

Bakar et al. [205] also attempted to recognise hand gestures by analysing the image frames captured by the Kinect sensor. This sensing method allows drift-free 3D motion tracking. The measured motion trajectory, however, suffered from position fluctuation due to sensor noise and occlusions. To overcome this limitation, Tian et al. [206] used an IMU and the Kinect together to estimate the 3D position of the upper limb.

EMG is another approach for tracking articulated motion. Multiple electrodes are attached to the skin to record the electrical signal produced by skeletal muscles. Finger movements activate the extrinsic flexors/extensor muscles located on the forearm, producing corresponding variations in the electrical activity [47]. Therefore, gestures can be recognised by analysing the extracted EMG patterns. This sensing approach enables the fingers to move without constraints, but the measurement accuracy is poor and also affected by the condition of the skin, e.g. the presence of sweat.

## 3.2 Hand Motion Tracking Devices

Monitoring hand motion has developed into many areas such as anthropomorphic robots [207, 208], physical therapy [114, 188] and rehabilitation [115, 193], VR [188, 209, 210], entertainment [106, 211], sign language understanding [167], human-machine communications [212], and even design and manufacturing [11]. The available hand tracking devices can be categorised into three main types: camera-based systems, EMG-based systems, and instrumented gloves, which are discussed as follows.

### 3.2.1 Camera-based Motion Capture Systems

The camera-based approach is to use single or multiple cameras to capture the scene, and then map the gestures by analysing the recorded video streams. They can be broadly divided into marker-based capturing and contour analysis. Marker-based systems place multiple dot markers strategically on the hand to track movements, while contour analysis performs hand edge and silhouette detection.

Various passive/active marker-based vision systems have been presented. In the early 1980s, the MIT Media Lab [213] developed a camera system to capture body and limb motion for real-time computer graphics animation by putting multi LEDs on a glove [12]. Later, Park and Yoon [214] also used LEDs mounted glove to capture hand gesture. In 1999, Rash et al. [215] attached 5-mm diameter retro-reflective spheres on the dorsal aspect of finger segments, and adopted three infrared cameras to record finger position

changes. Theobalt et al. [216] glued coloured reflective tape on a transparent glove for capturing the hand location of baseball athletes. To enhance the contrast between each marker, four distinct marker colours (red, yellow, blue, green) were distributed for the system. Cerveri et al. [217] configured up to 24 surface markers to estimate fine finger motion and investigated optimisation of markers position. Guskov et al. [218] introduced a wearable glove marked with numerous small colourful cloth blocks for tracking dynamic motion. Similarly, Wang et al. [219] presented a cloth glove imprinted with 20 large coloured patches, and used a single camera to capture the pattern location.

The contour tracking approach identifies hand poses without external markers, wires and cloth covers (e.g. glove). Using two cameras, Abe et al. [220] designed a 3D interface system by matching the observed hand contours with predefined gesture shapes. The literature [221–223] also reported on silhouette and edge extraction from recorded image sequences to track articulated hand motion.

Camera-based systems are generally regarded as the gold standard for tracking hand motion [121, 224]. Several commercial systems, such as the Vicon [199] and the Optitrack [225], are usually used to capture biomechanically-relevant motion and treated as a reference for other motion tracking devices. Additionally, camera-based measurement systems, especially the contour tracking devices, do not impede hand motion. However, there are several limitations which hinder their application and universality. The major limitation is that the measurement can only be performed in a restricted space determined by the position of the cameras. The subjects therefore can only stay in a confined room. Lack of portability means that the camera-based systems cannot be widely used in daily life. Secondly, image recording systems usually need to work in a special environment where the background should be uniform and obviously different from the hands or markers. Thirdly, the self-occlusion of the subjects' hands or poor image quality can lead to inaccuracies or even non-observable situations. To solve these problems, nonparametric belief propagation tracking algorithm [226], and the combination of a hierarchical filter and Bayesian filtering [221] were proposed to derive the variables related to hand position. Despite the improved performance, the measurement accuracy is still limited in poor conditions, e.g. complex lighting, cluttered background, and severe self-occlusion.

Furthermore, most camera detection devices involve complex and computation-intensive algorithms for gesture estimation, including data training, data segmentation, and template matching [223, 227, 228]. This affects the systems' capability in real-time measurements.

Lastly, commercial camera systems are costly, experiencing an exponential increase in cost with measurement accuracy.

### **3.2.2 Surface Electromyography (EMG)-based Systems**

The surface EMG-based systems measure finger motion by recording the muscle's electrical activity. Generally, multiple electrodes are located either on the user's forearm [229, 230] or at the wrist [231]. The extracted surface EMG patterns are used to recognise gestures via the processes of signal segmentation, feature extraction and classification [232]. The processed information is commonly used to manipulate the finger motion of the prosthetic hand [233–235], computer-animated virtual hands [234] and other human-computer interaction activities [236].

Generally, the EMG-based systems offer non-restrictive measurements, but they can only detect the isolated finger motion [229, 237] or limited predefined multiple-finger motion [230] due to the cross-talk phenomenon. It is a major challenge to record simultaneous and arbitrary finger motion with multiple DOFs [238]. Additionally, the quality of the finger motion reconstruction greatly depends on the number of electrodes and the spatial location [239]. In comparison with the camera-based and glove-based systems, the surface EMG tracking devices demonstrate low accuracy and poor stability in finger motion recognition [230]. Kawaguchi et al. [231] equipped 16 electrodes with a wrist-mounted sensing device which showed an averaged root-mean-square error ranging from 29° to 34° during finger motion.

### **3.2.3 Instrumented Glove Devices for Hand Motion Acquisition**

Glove-based sensing devices integrate wearable sensors with gloves/cloth covering or even directly onto the finger joints for recording hand motion. Compared with the camera-based and surface EMG-based systems, the instrumented glove devices are unaffected by finger occlusion and are able to measure multiple finger positions. These advantages make glove-based systems become the dominant devices for capturing finger movements [240]. In this work, an attempt is made to integrate the developed sensors with a glove for measuring finger motion as described in Chapter 6.

The most popular glove-based devices in the current market are CyberGlove [241], 5DT Data Glove [242], and HumanGlove [243], which offer automatic detection of hand positions for various activities. CyberGlove systems have two versions with either 18 or 22 piezo-resistive sensors to measure individual finger movements [241].

Kessler et al. [244] evaluated the characteristics of the CyberGlove equipped with 18 sensors (model CG1801) in terms of the system's sensitivity, the capability of measuring angles, and the factors affecting the measurement accuracy. 5DT Data Glove uses fibre optic-based sensors to monitor the articulated finger joints. The configurations with five and fourteen sensors are available [242]. 5DT Data Glove 5 Ultra only captures finger flexion/extension (one sensor per finger), while 5DT Data Glove 14 Ultra is designed to measure the flexion/extension of MCP and PIP joints and also the finger ABD/ADD. HumanGlove is a Bluetooth-based wireless device using Hall Effect sensors to reconstruct hand posture [243]. Dipietro et al. [8] evaluated the performance of a HumanGlove (ver. 1), and finally concluded that this glove in principle could operate as a goniometric device for dynamic recording of both finger flexion/extension and ABD/ADD. These systems, however, are relatively expensive, e.g. the 5DT Data Glove 14 Ultra is marketed at \$5495. This factor restricts their widespread use in real life applications.

Table 3.1 summarises the properties of several representative sensing systems for measuring finger motion. Although some of them can offer hand orientation and/or tactile feedback [168, 180, 184, 194, 245], only finger motion is considered here.

From Table 3.1, it is obvious that the majority of the tracking systems integrate multiple sensing units with a glove or a hand-shaped cover for measuring finger movements. This integration method simplifies the sensor attachment, facilitates the donning and removing of the system for individuals, and also offers improved comfort in comparison with the approach by directly securing sensors on to the finger's skin. The wearable hand motion tracking systems can be used in various applications such as VR, rehabilitation, animation, human-machine interaction, sign language understanding, and remote operation. However, the majority of the tracking devices require a separate calibration process for each individual, since the adopted sensors are highly dependent on the dimension of the finger joint. The calibration is critical to determining the system performance and can take minutes to complete [118, 152].

Furthermore, finger flexion/extension tracking has attracted much more attention than the detection of finger ABD/ADD. For monitoring finger flexion/extension, one-DOF sensors are commonly used in wearable glove-based devices. However, the measurement accuracy is usually adversely affected when monitoring two-DOF finger joints, e.g. the MCP joints. The main reason is that finger ABD/ADD and flexion/extension do not occur in isolation [24] leading to unwanted deformations of the flexion sensors. For example, the spaces between adjacent fingers generally decrease when fingers curl into the palm.

**Table 3.1** Summary of glove-based devices.

Devices	Sensors	Sensor attachment	Recorded finger motion	Applications	Calibration
CyberGlove * [241]	18 or 22 resistive bend sensors	glove	Flexion/extension and ABD/ADD	Animation, VR, digital prototyping, biomechanics, medical and military training	Required
5DT Data Glove * [242]	5 or 14 fibre optics based sensors	glove	Flexion/extension (the MCP and/or PIP joints), and ABD/ADD	Animation and other motion capture applications	Required
HumanGlove (ver. 1) * [8]	20 Hall effect sensors	glove	Flexion/extension and ABD/ADD	Rehabilitation, robotics, and VR	Required
KPF-based sensing glove [26]	5 KPF strain sensors	glove	Flexion/extension (the MCP joints of middle/little fingers, the PIP joint of the ring finger), and ABD/ADD (the thumb/little finger)	Rehabilitation, robotic teleoperation, and entertainment	Required
Wireless smart glove [59]	5 AgNW strain sensors	glove	Flexion/extension (PIP joints)	VR	Required
Artificial skin [68]	11 microfluidic strain sensors	hand cover	Flexion/extension, and ABD/ADD (thumb)	Motion capture applications	Required

Continued on next page

Table 3.1 – continued from previous page

Devices	Sensors	Sensor attachment	Recorded finger motion	Applications	Calibration
SIGMA glove [107]	18 bend sensors from Images SI	glove	Flexion/extension and ABD/ADD	Clinical	Required
Shadow Monitor [118]	5 bend sensors from Flexpoint SS	directly on finger digits	Flexion/extension (each MCP joint)	Healthcare	Required (8 min per person)
WU-Glove [116]	14 bend sensors from Flexpoint SS	glove	Flexion/extension (MCP and PIP joints), and the ABD/ADD	Widespread use in research, clinical, and Rehabilitation	Required (10 s)
NeuroAssess Glove [117]	6 bend sensors from Flexpoint SS	glove	Flexion/extension (the thumb and index finger)	Clinical practice and rehabilitation	No
Sensing glove designed by Borghetti et al. [115]	10 bend sensors from Flexpoint SS	glove	Flexion/extension (the MCP and PIP joints)	Sign language recognition, tele-diagnosis, and VR	Required
HITEG-Glove [119]	4 bend sensor arrays and 2 discrete sensors from Flexpoint SS	glove	Flexion/extension	Rehabilitation	unknown

Continued on next page

Table 3.1 – continued from previous page

Devices	Sensors	Sensor attachment	Recorded finger motion	Applications	Calibration
DAGLOVE [245]	10 bend sensors from Spectral Symbol	glove	Flexion/extension (the MCP and PIP/DIP joints)	Teleoperation	unknown
SmartGlove [27]	10 optical linear encoders	glove	Flexion/extension	Animation	Required
Sensing glove designed by Fujiwara [152]	5 optical fibre sensors	glove	Flexion/extension (the thumb and index finger), and ABD/ADD (index finger)	HCI	Required (~1 min)
Soft sensing system developed by Park [97]	7 microfluidic sensors	directly on finger joints	Flexion/extension and ABD/ADD of the thumb/index finger	VR and Rehabilitation	Required
Magnetic induction based glove [34]	5 magnetic sensing coils and 10 generator coils	directly on finger phalanges	Flexion/extension (the MCP and PIP joints)	HCI	Required
StrinGlove [194]	24 inductcoders	glove	Flexion/extension and ABD/ADD	Sign language recognition	Required

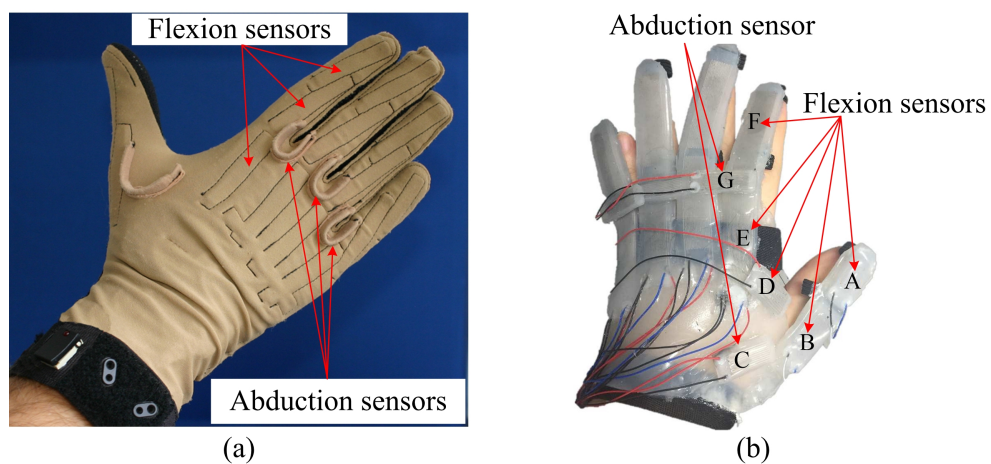
Continued on next page

Table 3.1 – continued from previous page

Devices	Sensors	Sensor attachment	Recorded finger motion	Applications	Calibration
AcceleGlove [168]	6 dual-axis accelerometers	Directly on finger phalanges	Flexion/extension or ABD/ADD	Sign language recognition	unknown
PowerGlove by Kortier [184]	20 pairs of gyroscopes and accelerometers, and 10 magnetometers	directly on finger phalanges	Dynamic assessment for the flexion/extension (thumb/index finger) and the ABD/ADD (index finger)	Kinematic analysis	Required
Modified PowerGlove [175]	11 pairs of gyroscopes and accelerometers	Directly on finger phalanges	Flexion/extension (thumb, index, middle fingers), and ABD/ADD and circumduction (index finger)	3D finger kinematics	Required
Motion-capture glove [180]	11 IMUs	glove	Flexion/extension and ABD/ADD	Rehabilitation and animation	Required
GESTO [29]	11 IMUs	glove	Flexion/extension and ABD/ADD	VR	Required

*Note:* In the first column, the devices with their names followed by ‘\*’ are commercial systems, and the others are instruments under research. In the column labelled as ‘Recorded finger motion’, ‘ABD/ADD’ stands for finger abduction/adduction. The column, named as ‘Applications’, lists the main applications reported in the literature for each system. The abbreviations of ‘VR’ and ‘HCI’ denote virtual reality and human-computer interaction respectively.

Currently, only a few glove systems are able to measure two-DOF finger movements. One method is the use of inertial sensing modules or IMUs that can provide 3D information of hand motion including finger ABD/ADD. The major drawback is the accumulated integral error and the large computation time required for data fusion processes. An alternative method is to use multiple one-DOF flexible sensors. As shown in Figure 3.14, the flexion/extension sensors are usually placed on the finger joints of interest, and the ABD/ADD sensors are attached to the dorsal surface of the proximal phalanges of adjacent fingers either in an arched configuration (Figure 3.14(a)) or in a straight line (Figure 3.14(b)). The arched sensing structure for measuring the finger ABD/ADD is favoured in the glove-based sensing systems, such as CyberGlove [241], 5DT Data Glove 14 Ultra [242], WU-Glove [116], and Tyndall/UU [114].



**Figure 3.14** Sensor configurations in glove-based systems. (a) CyberGlove II [241], in which the abduction sensors are in an arched configuration. (b) Soft strain sensor based system [97], in which the abduction sensor was attached to the proximal phalanges of adjacent fingers in a straight line.

However, with the approaches shown in Figure 3.14, reliable ABD/ADD readings can only be obtained when the adjacent fingers have similar flexion, otherwise twisting/elongation of the ABD/ADD sensors by pure flexion motion can occur leading to inaccurate and unreliable readings. Additionally, gestures, such as crossed fingers, deteriorate the measurement accuracy of both finger flexion/extension and ABD/ADD when one-DOF sensors are used for recording the motion of the two-DOF MCP joints. These problems are further explained in Figure 3.15, in which the ABD/ADD sensor is simplified as a red straight bar and the flexion/extension sensors are represented using green bars. Clearly, the ABD/ADD sensor is elongated with the flexion of only the index finger (see Figure 3.15(b)); when the index finger crosses over the middle finger, both the flexion/extension and the ABD/ADD sensors deform and fail to detect the actual finger motion, as shown in Figure 3.15(c).

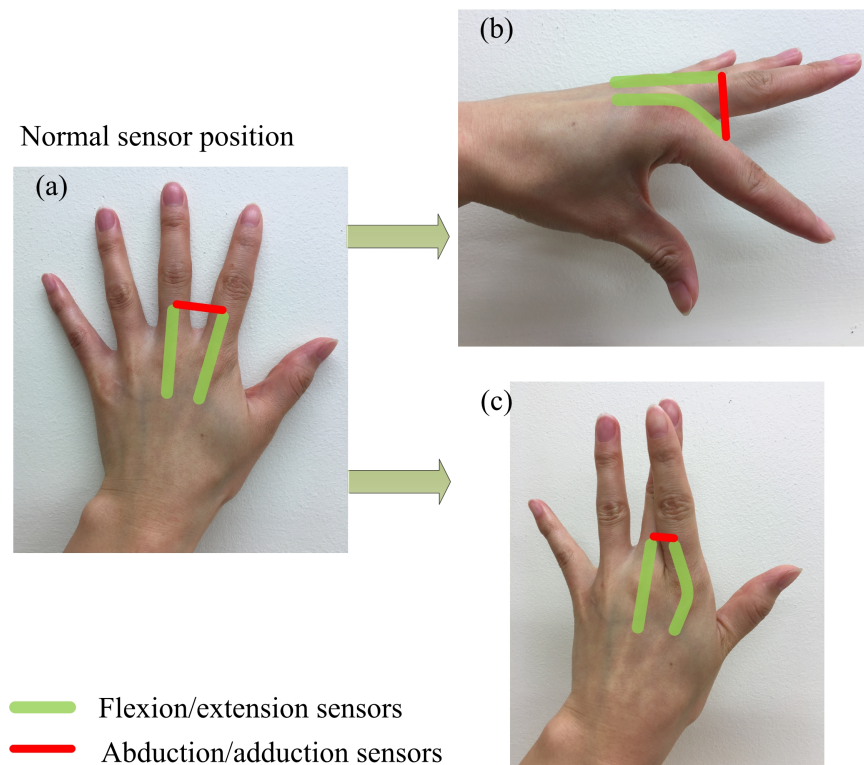


**Figure 3.15** Problems of using one-DOF flexible sensors to track the movements of two-DOF joints. (a) Normal sensor position. (b) Finger flexion/extension without ABD/ADD. (c) Crossed finger gesture.

Recently some approaches are reported to tackle the crosstalk problem. Kim et al. [246] identified the optimal locations of the single-axis sensors for properly measuring the two-DOF CMC joint motion. During the measurements of thumb motion, this approach reduced the amount of crosstalk, but the estimated errors were still large, i.e. more than  $5^\circ$ . Moreover, Park et al. [97] applied decoupling algorithms to the signal from the microfluidic strain sensors; the algorithms were based on the projected triangle formed by the joint position. Experimental results showed the root-mean-square errors of the measured motion of the two-DOF joints were still larger than those of the one-DOF joints.

Both finger flexion/extension and ABD/ADD are important parameters for finger kinematics. The majority of studies to date only consider finger flexion and extension, but accurate information on finger ABD/ADD is essential for areas such as medical diagnostics and rehabilitation. Accurate and simultaneous monitoring of two-DOF motion in human hand joints is an area underexplored in current glove-based systems. Therefore, one of the major objectives in this work is to find an effective solution to this problem.

### 3.3 Summary

A literature survey regarding the various sensing techniques and the instrumented systems for tracking articulated hand motion is given in this chapter. The performance of each type of sensor are briefly presented and their common advantages and disadvantages are summarised. For discussion, the available motion tracking systems are mainly divided into three categories: camera-based systems, EMG-based devices, and glove-based systems. Due to the unique features, glove-instrumented devices have become the dominant devices for capturing hand motion. Certain limitations of the sensing capabilities of the current glove-instrumented devices are highlighted which need to be addressed.

The polarisation-based sensing method provides a direct measurement of angle, as opposed to other types of flexure sensor, which generally use indirect methods such as electrical resistance or capacitance changes converted to angles using a trigonometrical conversion model. Additionally, the polarisation-based technique offers high measurement accuracy and a fast response time. Therefore, a polarisation-based method was considered an ideal choice as the sensing technique in this research.

## **Chapter 4**

# **Electro-optical Goniometric Sensor Design and Experimental Methods**

Inspired by the articulated structure of finger joints, three electro-optical goniometric sensors based on Malus' law were developed and investigated for tracking finger motion. These electro-optical sensors were designed with different capabilities, so as to measure different types of finger joints. 3D printing technology was used to manufacture the sensors, making the sensor configurations compact. In this chapter, the operating principle, the sensor fabrication, the experimental set-up for sensor characterisation, the signal processing approach, and the developed software will be described.

### **4.1 Electro-optical Goniometric Sensor Design**

Three distinct sensors were developed in this work utilising a single-axis sensor design (sensor#1 and sensor#2) and a two-axis goniometric sensor (sensor#3). The operating principle and the manufacture of these three sensors are described in this section.

#### **4.1.1 Operating Principle of the Electro-optical Goniometric Sensors**

The operating principle of all three electro-optical sensors were based on Malus' law, i.e. detecting the change in rotation by analysing the attenuation of polarised light transmitted through a linear polarising film. The three sensors differed from each other in the configuration and number of sensing components.

The schematic diagram of sensor#1 is shown in Figure 4.1. This sensor has a single transmission pathway which is referred to as a channel in this thesis. The sensor consists of two linear polarising films that rotate relative to each other. The unpolarised light passed through the first polariser and was attenuated by the second polariser, also known as the analyser. The dash-dot lines represent the transmission axes of the polariser and the analyser. According to the coordinate system illustrated in Figure 4.1, the incident light was polarised in the direction of  $\theta_{110}$  to the negative z-axis after travelling through the linear polariser. After that, the polarised light was partly blocked and only the components parallel to the analyser's transmission axis were transmitted to the photodiode, a light-sensitive semiconductor device which converted the incident light to a flow of electric charge.

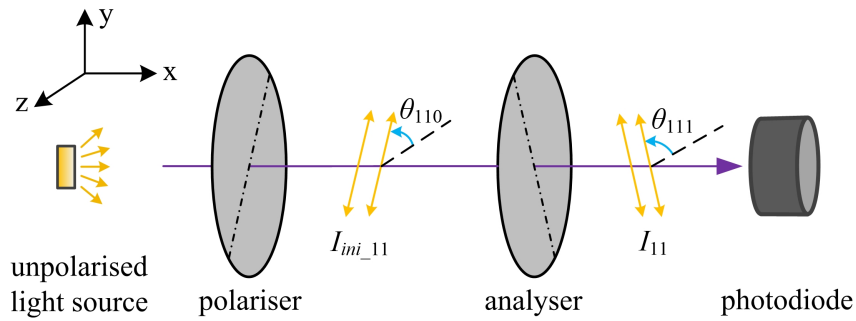


**Figure 4.1** The schematic diagram of sensor#1, a basic single-axis sensor.

Supposing the polarising film is perfect, the intensity of the polarised light passing through the analyser,  $I_{11}$ , can be computed using equation (4.1) according to Malus' Law which is described in 2.2.2.

$$I_{ij} = I_{ini\_ij} \cos^2(\delta_{ij}) = I_{ini\_ij} \cos^2(\theta_{ij1} - \theta_{ij0}) \quad (4.1)$$

where the subscripts  $i$  and  $j$  denote the label of the electro-optical sensor and the sensing channel to be measured respectively. The parameter  $I_{ini\_ij}$  represents the initial polarised light intensity in the channel  $j$  of the goniometric sensor labelled as  $i$ . The parameter  $\delta_{ij}$  denotes the angle between the direction of the light's initial polarisation and the analyser's transmission axis, i.e. the difference between  $\theta_{ij0}$  and  $\theta_{ij1}$ .

For sensor#1, the subscripts both  $i$  and  $j$  equal one in equation (4.1). It can be found that the final luminous intensity is proportional to the intersection angle of the transmission axes of the polariser and the analyser. The photodiode shown in Figure 4.1 can linearly convert the received light intensity into an electric current  $i_{11}$ , which can be estimated by equation (4.2).

$$i_{ij} = k_{ij}I_{ij} = k_{ij}I_{ini\_ij} \cos^2(\delta_{ij}) = m_{ij} \cos^2(\delta_{ij}) \quad (4.2)$$

where the parameter  $k_{ij}$  is a constant dependent on the performance of the employed photodiode, and  $m_{ij}$  is the product of  $k_{ij}$  and  $I_{ini\_ij}$ .

According to equation (4.2), the angular rotation can be obtained by measuring the output current. In this case, the measuring range of sensor#1 is  $90^\circ$ , which is adequate for tracking the entire range of flexion and extension of the DIP joints ( $< 90^\circ$ ). However, certain finger joints can perform movements in excess of  $90^\circ$ , e.g. the PIP joints (up to  $135^\circ$ ) and in this case, sensor#1 is insufficient for tracking such finger activities. To solve this problem, sensor#2, an improvement on the single-axis goniometric sensor, was developed.

As illustrated in Figure 4.2, sensor#2 consists of a single visible light source, a linear polariser  $PL_{20}$ , two thin-film analysers  $AL_{2j}$  ( $j = 1, 2$ ), and two photodiodes  $PD_{2j}$ . Passing through  $PL_{20}$ , the light was polarised in the direction of the transmission axis (the dash-dot line) at an angle  $\theta_{20}$  to the negative z-axis and then split into two separate channels ( $CH_{2j}$ ). Each channel had its own analyser and photodiode, so that the incident polarised light was analysed and recorded in the form of an electric current.  $CH_{21}$  and  $CH_{22}$  were arranged symmetrically around the central line of the light source, producing simultaneous outputs.

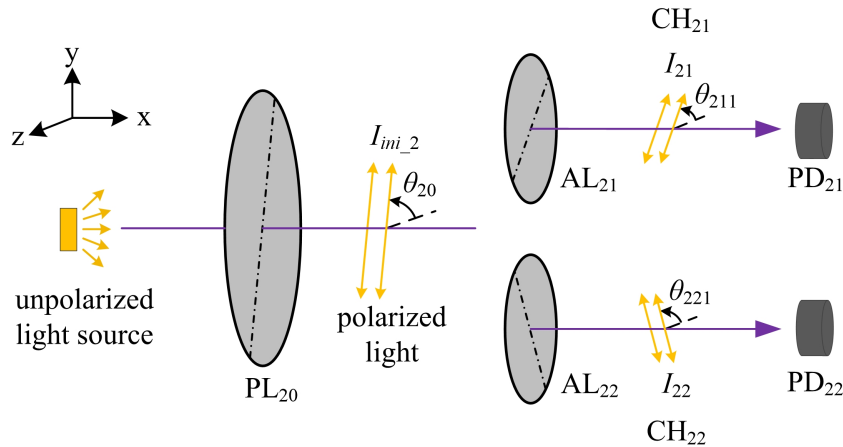


**Figure 4.2** The schematic diagram of sensor#2, an improved single-axis sensor.  $PL_{20}$  represents a linear polariser.  $AL_{2j}$  and  $PD_{2j}$  represent the linear analyser and the photodiode in the channel  $CH_{2j}$  ( $j = 1, 2$ ), respectively.

The two channels of sensor#2 transmitted the polarised light in the same way as that of sensor#1. In each channel, the light intensity received by the photodiode obeys equation (4.1) and the converted electric current follows equation (4.2). In these two equations, the subscript  $i$  denoting the label of the electro-optical sensor equals two, and

the channel number  $j$  can be one or two. The parameters  $I_{ini\_21}$  and  $I_{ini\_22}$  in equation (4.1) represent the amount of the polarised light initially entering CH<sub>21</sub> and CH<sub>22</sub> respectively; in theory they are half the value of  $I_{ini\_2}$  shown in Figure 4.2 due to the symmetrical structure of the two sensing channels.

The analysers AL<sub>21</sub> and AL<sub>22</sub> were oriented with their transmission axes set at 40°. This arrangement enables CH<sub>21</sub> and CH<sub>22</sub> to produce different simultaneous outputs, since the polarised light entering the two channels comes from the same source. To ensure that at least one channel will be operating in the region with maximum sensitivity and linearity, the oriented angle should be in the range 40° to 50° because the cosine squared function demonstrates a high linearity in the region of 20° to 70°.

The simultaneous outputs of the two sensing channels of sensor#2 were combined to determine the angular displacement. This expanded the measuring range to 180° and also improved the sensitivity. The data fusion method will be described in detail in section 4.2.3.

Sensor#2 had an improved measuring range in comparison with sensor#1, but both single-axis sensors were only capable of measuring finger movements in one plane. Finger articulations by MCP joints can perform motion in two planes including flexion/extension, ABD/ADD, as well as circumduction. Therefore, another electro-optical sensor, i.e. sensor#3, with two rotational axes, was developed to monitor two-DOF joint motion.

The operating principle of sensor#3 is illustrated in Figure 4.3. This design is comprised of four symmetrical optical channels (CH<sub>3j</sub>,  $j = 1, 2, 3,$  and 4). The unpolarised light source provided visible light for all four channels. Each channel included a linear polariser PL<sub>3j</sub>, a thin-film analyser AL<sub>3j</sub>, and a photodiode PD<sub>3j</sub>, operated in the same way as sensor#1. The received light intensity  $I_{3j}$  and the output current of the photodiode obeyed equations (4.1) and (4.2) respectively. In such a case, the subscript  $i$  in these two equations equals three and  $j$  denoting the channel number is an integer ranging from 1 to 4.

According to the coordinate system defined in Figure 4.3, CH<sub>31</sub> and CH<sub>33</sub> were oriented along the x-axis. Their simultaneous outputs were fused to determine finger flexion/extension. Supposing that the transmission axes of the polarisers PL<sub>31</sub> and PL<sub>33</sub> were in the same direction, the analysers AL<sub>31</sub> and AL<sub>33</sub> were initially oriented with their transmission axes at a fixed angle to each other in the range 40° to 50°. This was the same as sensor#2.

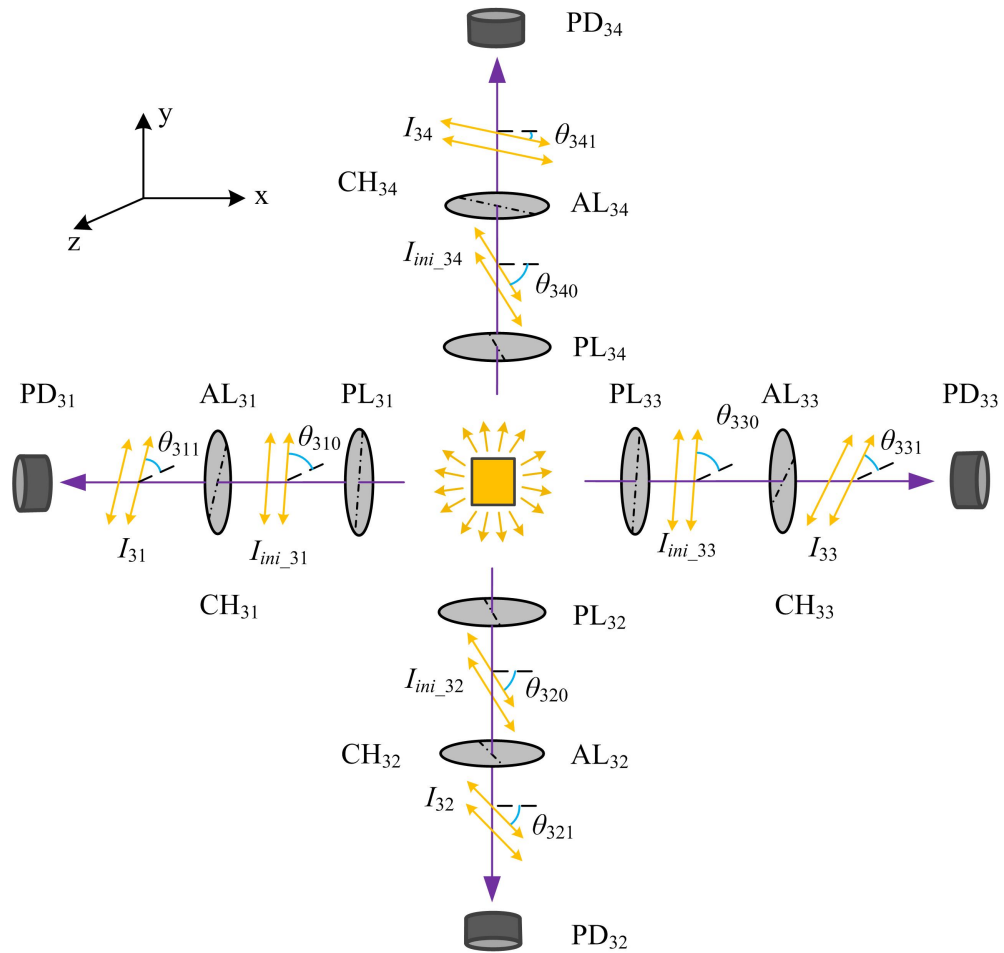


**Figure 4.3** The schematic diagram of sensor#3, a two-axis electro-optical goniometric sensor.  $PL_{3j}$ ,  $AL_{3j}$ , and  $PD_{3j}$  represent a linear polariser, a linear analyser and a photodiode in the channel  $CH_{3j}$  ( $j = 1, 2, 3,$  and  $4$ ), respectively.

In Addition,  $CH_{32}$  and  $CH_{34}$  located along the y-axis were designed for recording the finger ABD/ADD movements. They were configured and operated in the same way as  $CH_{31}$  and  $CH_{33}$ .

#### 4.1.2 Sensor Models for 3D Printing and Integrated Goniometric Sensors

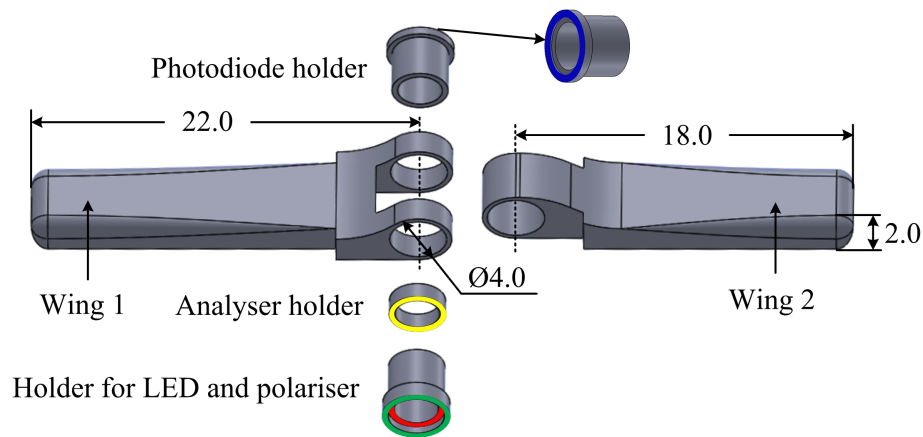
Using 3D printing technology, the electro-optical sensors were all designed with compact hinge configurations. The 3D models for the three sensors were modelled in SolidWorks 2015 [247]. The assembly models are shown in Figure 4.4(a), Figure 4.5(a), and Figure 4.6(a), and the details of the technical designs are presented in Appendix A. Each sensor had two wings for attachment to the finger segments, and a housing (holder) for integration of the electronic and optical components. The length of the sensor wings can be made bespoke to suit different finger sizes.

The sensor framework was manufactured by an EnvisionTEC's Perfactory Mini Multi Lens 3D Printer (EnvisionTEC, Inc., Dearborn, US) [248]. This printer uses the state of art Digital Light Processing technology to produce fine details with a resolution capability of 32  $\mu\text{m}$ . The nanoparticle-filled resin RCP30 (EnvisionTEC, Inc., Dearborn, US) [249] was chosen as the 3D printing material due to its outstanding features including superior stiffness, opaque appearance, and suitability for building parts at very high resolution.

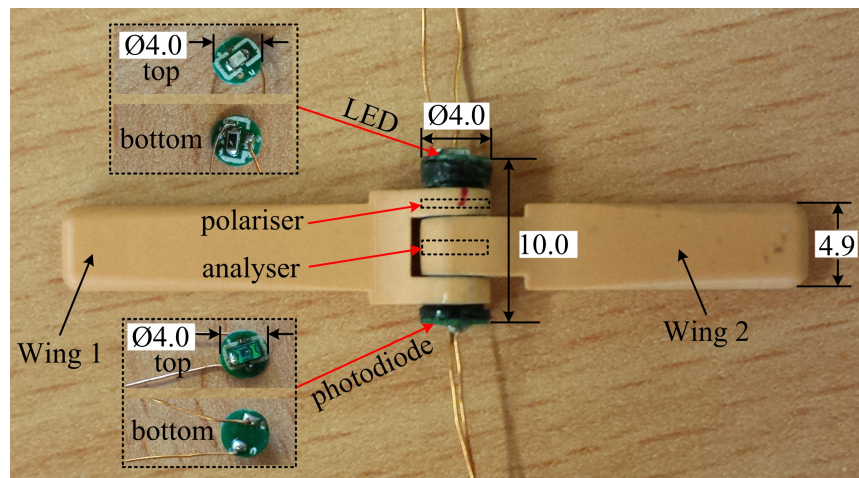
According to the operating principle described in 4.1.1, the light source, linear polarisers, analysers, and photodiodes are required for all three electro-optical sensors. The surface mounted LED (KPG-1608ZGC, Farnell element14, Leeds, UK) [250], with a dominant wavelength of 525 nm, was chosen as the visible light source due to its small dimension (1.6 mm  $\times$  0.8 mm  $\times$  0.25 mm) and the high luminous intensity (400 millicandelas). The thin-film linear polarisers and analysers were made from commercial polarising sheet (Edmund Optics Ltd., York, UK) [251], with an extinction ratio of 9000:1 and high transmission from 450 nm to 700 nm. This high contrast polarising film with a thickness of 0.18 mm can be cut to any size. The photodiode (TEMD6200FX01, Farnell element14, Leeds, UK) [252] with a peak spectral sensitivity at 540 nm was employed to detect the resultant light intensity. Its operating wavelength range matched that of the LED and the polarising film. The photodiode also featured a high response speed (rise time and fall time about 150 ns), low dark current ( $< 5$  nA), low diode capacitance (typically 60 pF when the reverse voltage is 0 V), and small dimensions (2 mm  $\times$  1.25 mm  $\times$  0.85 mm).

The goniometric sensors worked in the visible region, it was therefore necessary to eliminate the influence of ambient light. The 3D printing material RCP30, was opaque and partially blocked the ambient light. Non-reflective, black Aluminum foil tape (AT205 [253], Thorlabs Inc., Ely, UK) was used to block the remaining ambient light (not included in the figures for clarity).

As shown in Figure 4.4, sensor#1 had an overall length of 40.0 mm, a width of approximately 10.0 mm, and a height of 4.0 mm; i.e. dimensions suitable for most adults' fingers. Several separate holders ( housings) were designed for the electronic and the optical components. The green, red, and yellow surfaces of the holders shown in Figure 4.4(a) were for the attachment of the LED, the linear polariser, and the thin-film analyser respectively. The photodiode was fixed to the blue surface of the Photodiode holder, facing opposite to the LED. In fact, the LED and the photodiode were soldered onto separate double-layered circular PCB with a thickness of 0.4 mm and a diameter of 4 mm, as shown in Figure 4.4(b).



(a)



(b)

**Figure 4.4** Sensor#1, a single-axis electro-optical sensor with a measuring range of  $90^\circ$ . All units are in millimetres. (a) The 3D model design; (b) the images of the complete sensor and the PCBs for the LED and photodiode.

Finally, the holders for the LED, the polariser, and the photodiode were glued to Wing 1 and the holder for the analyser was fixed inside Wing 2. A rotation between Wing 1 and Wing 2 causes the same rotational change between the polariser and the analyser. The wings were attached to the dorsal surfaces of adjoining phalanges and rotated in unison with the joint rotation during finger flexion or extension.

The 3D model and the photograph of sensor#2 are displayed in Figure 4.5. The overall length of this sensor was 40.0 mm, width 8.0 mm and height 4.5 mm. The design, shown in Figure 4.5(a), was similar to that of sensor#1 except for embedded internal chambers inside the holders. This enabled all of the components including the LED, linear polariser, analysers and photodiodes to be integrated directly without the use of PCB boards. In Figure 4.5(a), the red surface and the green space (inside the holder) were designed for the linear polariser and the visible LED respectively. Parallel channels, each consisting of an analyser/photodiode pair, were symmetrically housed inside the

holder embedded inside Wing 2. A baffle plate (purple part in Wing 2) was located in the central plane of the holder to prevent light in one channel interfering with the other channel. Furthermore, the holder section that passes the electrical wiring to the photodiodes also forms part of the hinge mechanism.

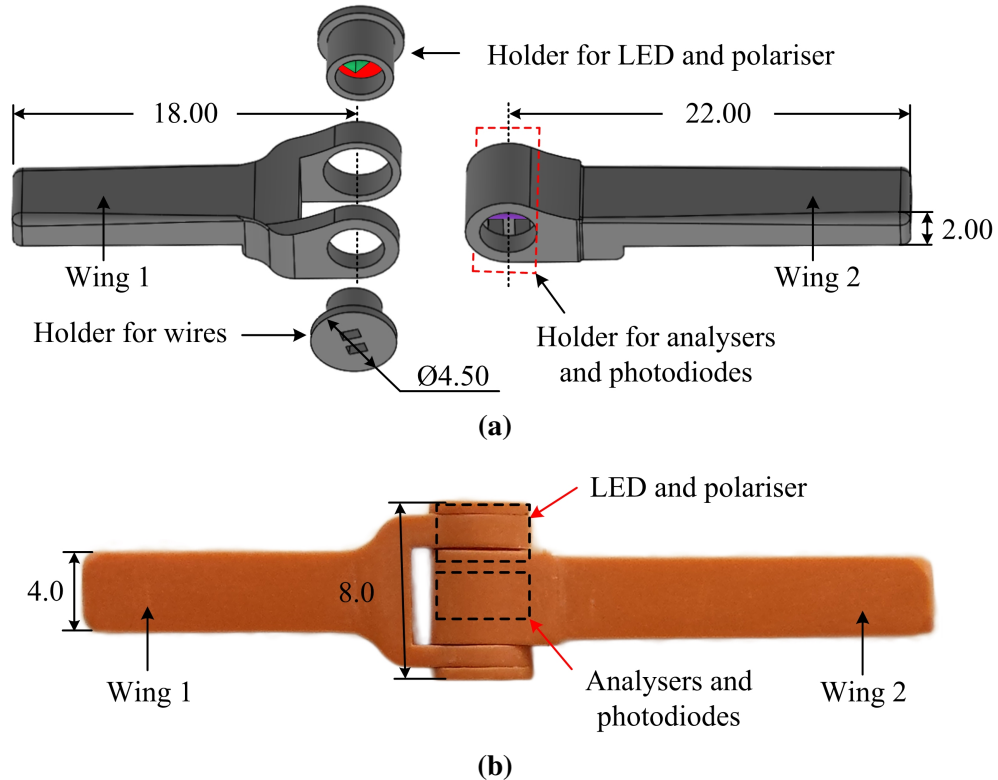


**Figure 4.5** Sensor#2, a single-axis electro-optical sensor with improved measuring capability. All units are in millimeters. (a) The 3D model design; (b) a photograph of the integrated sensor.

As shown in Figure 4.5(b), the holder for the LED and polariser together with the electrical wire holder were glued so that they followed the rotation of Wing 1. When the two wings rotate relatively, the angle between the polariser and the analysers also changes, leading to variations in the output intensities of the two channels. This compact design enabled tracking of the larger range motion typically seen in PIP joints.

The two-axis goniometric sensor (sensor#3) used an alternative hinge structure. As shown in Figure 4.6(a), the LEDs and linear polarisers, for four channels, were located inside a cross-shaped holder which was optically aligned with the analysers and photodiodes in the two wing sections. In each channel, the green, red, yellow, and blue surfaces were for the location of the LED, the linear polariser, the thin-film analyser, and the photodiode respectively. Not all component locations are visible in Figure 4.6(a) but a detailed technical drawing of sensor#3 can be found in Appendix A.

Figure 4.6(b) shows an image of the integrated two-axis optical goniometric sensor. When the sensor wings are aligned, the horizontal line along CH<sub>31</sub> and CH<sub>33</sub> is defined

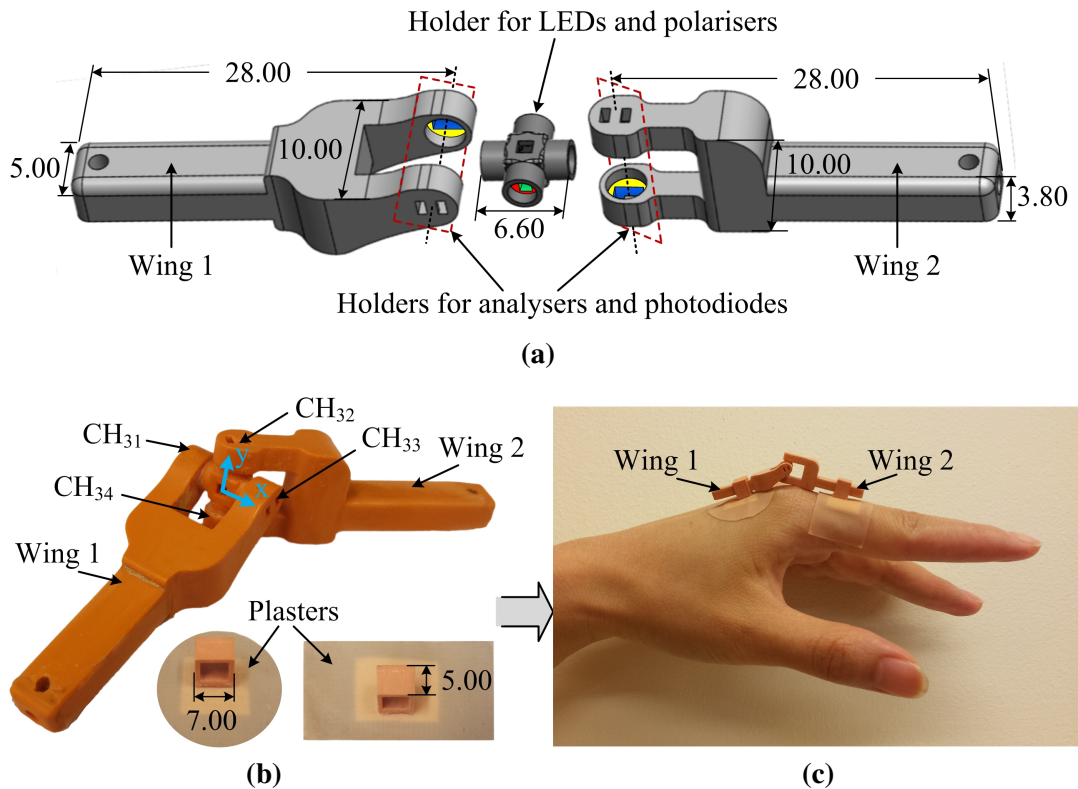


**Figure 4.6** Sensor#3, a two-axis goniometric sensor. All units are in millimetres. (a) The 3D model design; (b) a photograph of the integrated sensor and the two rectangular hollow parts glued on the adhesive plasters; (c) an example of the sensor's placement on the MCP joint of the left index finger.

as the x-axis and the vertical line along CH<sub>32</sub> and CH<sub>34</sub> as the y-axis. This sensor prototype had an overall width of 10 mm, height of 10 mm and a length of 56 mm.

An example of sensor#3 attached to the MCP joint of the index finger is shown in Figure 4.6(c). The two rectangular components, glued on to adhesive plasters, were placed on the metacarpal and the proximal phalanx of the left index finger. The sensor wings were inserted into the rectangular parts, enabling them to slide in response to finger movements. When the index finger flexes or extends, the rotation of the wings occurs about the x-axis of the sensor. Similarly, ABD/ADD motion causes sensor rotation about the y-axis. Finger circumduction is also possible using recorded output data from both rotation directions.

## 4.2 Motorised Measurement System and Software Design to Investigate Sensor Characteristics

An automated measurement apparatus controlled under LabVIEW was implemented to investigate the sensor performance. In the following, an overview of the measurement system is given, including the conditioning circuitry, the data processing method, and the software.

### 4.2.1 Measurement System Overview

To reduce human operating errors and improve measurement consistency, an automated experimental set-up was built to assess the performance of the goniometric sensors. The block diagram and the system photograph are shown in Figure 4.7 and Figure 4.8, respectively.

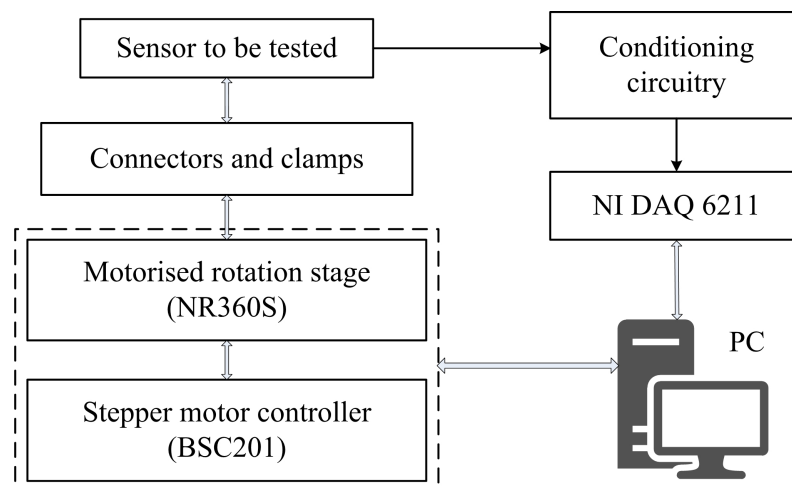


**Figure 4.7** The block diagram of the automated measurement apparatus. Under the drive of the controller BS201, the motorised stage NR360S is used to adjust the rotation speed and angle. The sensor is connected to the rotation stage by the clamps. The sensor outputs are conditioned, acquired, and stored in the PC.

A 360° continuous motorised rotation stage (NR360S [254]) in combination with a stepper motor actuator from Thorlabs Inc. (Ely, UK) [255] was employed to control the rotation angles and speeds. The two-phase hybrid stepper motor provided an accuracy of 5 arcmin (about 0.1°) and a maximum speed of 50°/s when driven by the micro-stepping motor controller (BSC201 [256]). The single channel stepper motor controller offered 409600 microsteps per revolution. This motor controller contained a full suite of software support tools which allowed immediate control of all settings and operations. ActiveX interfacing technology enabled programmable equivalents of the

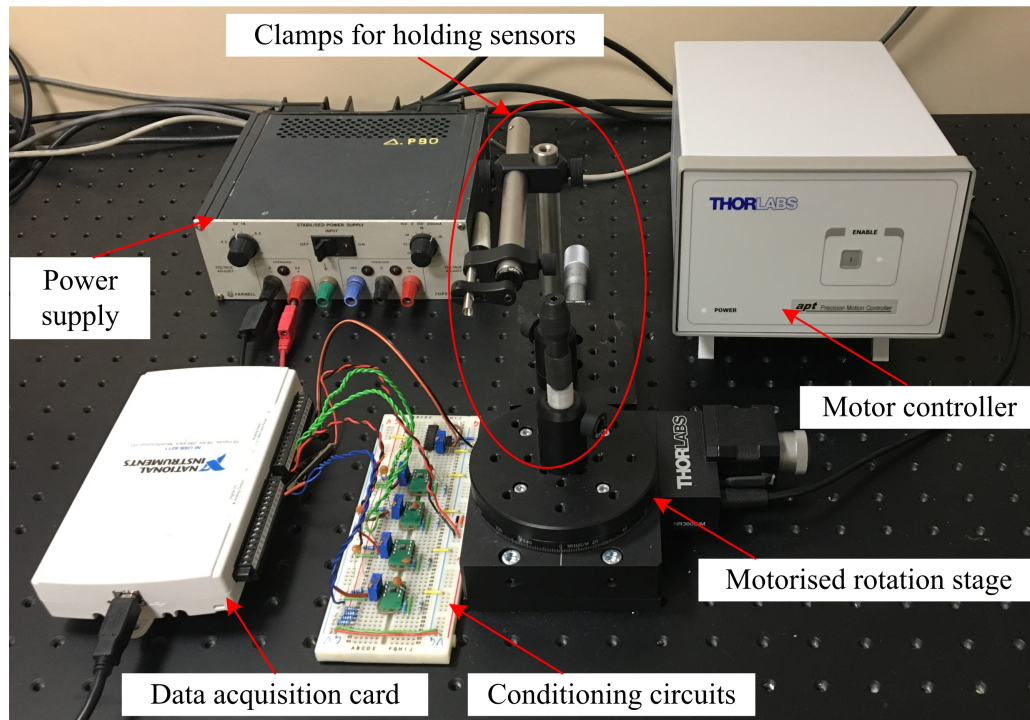


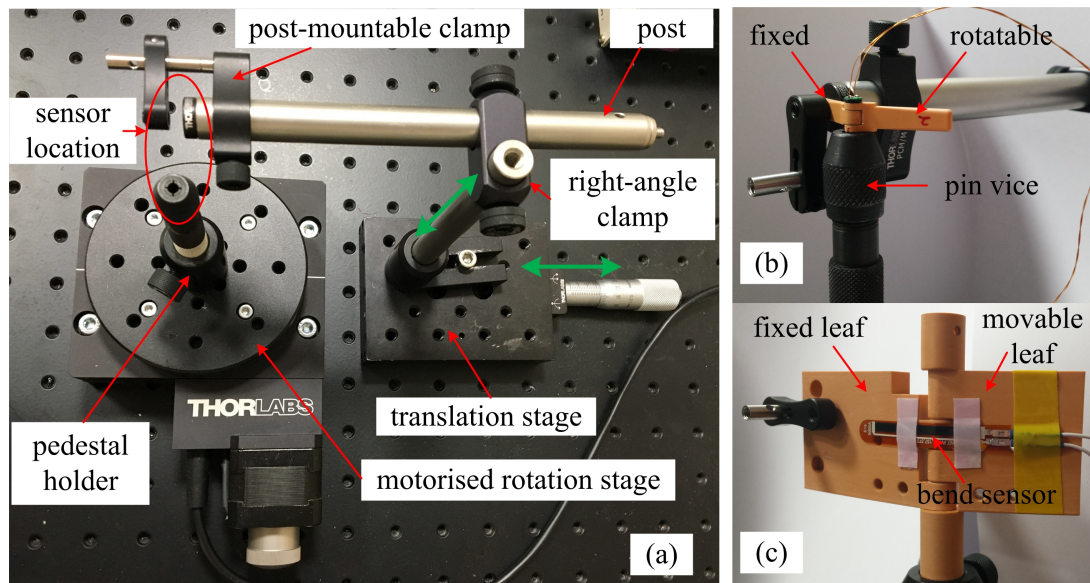
**Figure 4.8** The photograph of the automated measurement apparatus.

parameter settings for a wide range of software development environments including LabVIEW [257], MATLAB [258], and Visual C++ [259]. In this work, all activities were controlled using ActiveX in LabVIEW, and signal acquisition using a National Instruments (NI) data acquisition card (USB-6211, National Instruments Corp., Austin, US [260]). This data acquisition (DAQ) device having one 16-bit analog-to-digital converter provides a resolution of  $153 \mu\text{V}$  and an absolute accuracy of  $1410 \mu\text{V}$  with the input range from  $-5\text{V}$  to  $5\text{V}$ .

Output signals were passed through conditioning circuitry prior to data acquisition. As shown in Figure 4.8, the surface-mounted amplifiers, for the optical sensors, were PCB mounted on to breakout boards, and the complete conditioning circuitry was built using a standard prototyping breadboard. Although not implemented in this work, manufacturing the conditioning circuitry as a complete PCB should reduce effects due to parasitic capacitance and electrical noise interference. The conditioning circuits are described in section 4.2.2.

As shown in Figure 4.8, clamps (in the red circle) were used to hold the sensor under test, to enable the sensor to follow the motor's rotation. The lateral view of the holders and clamps is displayed in Figure 4.9(a). The translation stage adjusted the position of the post along the horizontal direction, and the right-angle clamp controlled the vertical location. A post-mountable clamp with a flat base adapter was used to clamp the sensor

wing, and the pedestal holder fixed to the central aperture of the rotation stage supported the sensor holder.



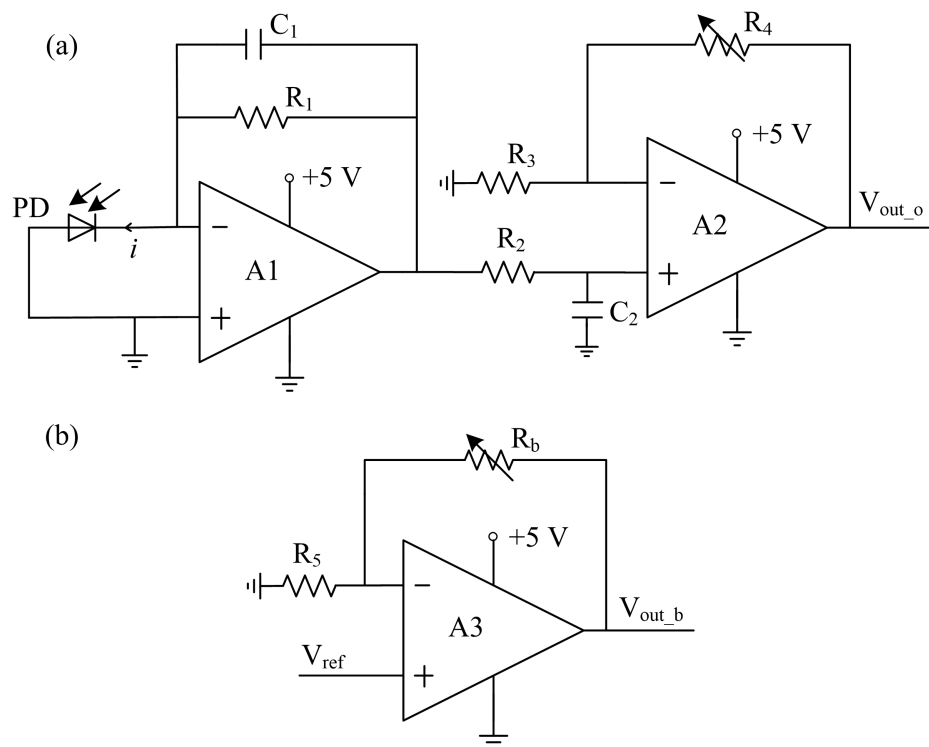
**Figure 4.9** (a) Photograph of the mechanical set-up for holding sensors; (b) the method to hold the electro-optical goniometric sensor; (c) the approach to fix the commercial bend sensor.

Figure 4.9(b) shows the method used to fix the single-axis goniometric sensor. A pin vice, mounted vertically on the pedestal holder shown in Figure 4.9(a), held the electro-optical sensor in place. For the single-axis sensors, i.e. sensor#1 and sensor#2, Wing 2 was fixed rigidly by the post-mountable clamp, whilst Wing 1 was allowed to rotate under the control of the motorised stage. For the dual-axis sensor, sensor#3, the performance along each axis were assessed separately using the same rotation stage. To evaluate the rotation about the x-axis, Wing 2 was clamped rigidly and Wing 1 was allowed to move. Similarly, Wing 1 was clamped and Wing 2 was rotatable during the testing for the rotation about the y-axis.

As stated in Chapter 3, the commercial resistive bend sensors from Flexpoint SS have been widely utilised in glove-based systems for detecting hand motion due to their flexibility, low cost, and light weight. Such a bend sensor without any overlamination film was evaluated using the automated measurement system. This acted as a reference point for comparison with the electro-optical goniometric sensors. The dimensions of the bend sensor was  $50.80 \text{ mm} \times 7.00 \text{ mm} \times 0.16 \text{ mm}$ , as shown in Figure 3.4(c), and it was fixed according to the method described by Saggio [261]. As shown in Figure 4.9(c), it was inserted into two plastic sleeves attached to the surface of the plastic hinge with the conductive ink layer facing away from the hinge surface. One leaf of the hinge was fixed and the other was free to follow the rotation of the motor. In this work, the radius of curvature of the hinge was 8.5 mm.

### 4.2.2 Sensor Signal Conditioning Circuitry Design

The electro-optical sensors produce a changing electrical current and the bend sensor a change in electrical resistance in response to rotation. Signal conditioning is required to convert these responses into voltage, since DAQ systems that measure voltage are more readily available. In this work, the sensing data was acquired using the NI USB-6211. The circuit diagrams for a single channel of the electro-optical sensors and the bend sensor are shown in Figure 4.10(a) and (b) respectively.



**Figure 4.10** The conditioning circuits. (a) The current-to-voltage converter for a single channel of the optical sensors,  $R_2=3\text{ M}\Omega$ ,  $R_3=820\ \Omega$ ,  $C_1=3.3\text{ pF}$ ,  $C_2=0.1\ \mu\text{F}$ ,  $R_1=3.3\text{ M}\Omega$  (sensor#2 and sensor#3) or  $6.6\text{ M}\Omega$  (sensor#1); (b) the resistance-to-voltage converter for the bend sensor,  $V_{ref}=0.5\text{ V}$ ,  $R_5=39\text{ k}\Omega$ , and  $R_b$  represents the sensor resistance.

A photodiode is a PN junction or PIN structure. It produces a photocurrent when the light is absorbed in the junction's depleted region. The photocurrent flows from cathode to anode outside the diode, opposite to the direction of the current in a normal diode or LED. A photodiode typically operates in photovoltaic mode or photoconductive mode. In photovoltaic mode, the photodiode is zero biased and the converted voltage is linearly dependent on the incident radiation. For photoconductive mode, an external reverse bias is usually applied to the photodiode, which improves the speed of response but also directly increases the dark current (current that is generated in the absence of light). This produces more electronic noise than the photovoltaic circuit mode. The total current through the photodiode is the sum of the dark leakage current and the

photocurrent. Zero dark current results in maximum sensitivity of the device [262]. In low-frequency applications and low-level light detections, photovoltaic mode generally outperforms photoconductive mode. For this reason, photovoltaic mode was chosen as the mode of operation in this work.

As shown in Figure 4.10(a), the operation of the photodiode (PD) eliminates the dark current and linearly converts the received light intensity to electric current  $i$ . The resistor  $R_1$  determines the gain. The feedback capacitor  $C_1$  is used to compensate for the photodiode junction capacitance and the input capacitance of the amplifier, preventing unstable operation. Meanwhile, the parallel combination of  $R_1$  and  $C_1$  together also determine the frequency response of the circuit. The signal is initially amplified by the feedback resistor  $R_1$ , and then modulated further by a second-stage amplifier with a low-pass filter. Finally, the output voltage can be obtained by equation (4.3).

$$V_{out_o} = \frac{iR_1}{1 + j\omega C_1 R_1} \left(1 + \frac{R_4}{R_3}\right) \approx iR_1 \left(1 + \frac{R_4}{R_3}\right) \quad (4.3)$$

where the parameter  $\omega$  is the angular frequency presented in radians per second and the symbol  $j$  expresses the phase shift between the voltage and the current.

For the three electro-optical sensors, the signal generated in each channel is conditioned using the circuit shown in Figure 4.10(a). The circuit utilises a dual, high speed, CMOS operational amplifier LTC6244HVIMS8#PBF [263] (Farnell element14, Leeds, UK) featured with a low input offset voltage ( $<100 \mu\text{V}$ ), low input bias current (1 pA at  $25^\circ\text{C}$ ), low input capacitance (3.5 pF in differential mode), low noise, and high slew rate (40 V/ $\mu\text{s}$ ).

By substituting the expression for  $i$  (equation (4.2)) into equation (4.3), the output voltage in the sensing channel can be calculated using equation (4.4). In theory, the output voltage is 0 V when the relative rotation angle between the polariser and the analyser located in the same channel is  $90^\circ$ . However, a non-zero constant voltage  $a_{ij}$  may appear due to the amplifier's offset current and imperfect light extinction of the polarising film. Therefore, the measured voltage obeys equation (4.4).

$$V_{out_{ij}} = m_{ij} \cos^2 \delta_{ij} R_1 \left(1 + \frac{R_4}{R_3}\right) + a_{ij} = n_{ij} \cos^2 \delta_{ij} + a_{ij} \quad (4.4)$$

where the subscripts  $i$  and  $j$  denote the label of the electro-optical sensor and the channel being measured respectively. The parameter  $n_{ij}$  is a constant of proportionality

determined by the amplification factor. The parameter  $a_{ij}$  is a constant voltage value; in ideal conditions, it equals 0.

Therefore, the rotation angle in one period (i.e.  $180^\circ$ ) of the optical sensors can be derived by the following equation.

$$\delta_{ij} = \begin{cases} \arccos \sqrt{(V_{out\_ij} - a_{ij})/n_{ij}} & (0^\circ < \delta_{ij} \leq 90^\circ) \\ -\arccos \sqrt{(V_{out\_ij} - a_{ij})/n_{ij}} & (-90^\circ < \delta_{ij} \leq 0^\circ) \end{cases} \quad (4.5)$$

As shown in Figure 4.10(b), a non-inverting operational amplifier circuit was designed for use with the bend sensor. The quadruple low-noise operational amplifier TLC2274CNE4 (Farnell element14, Leeds, UK) [264] was used exhibiting a high slew rate ( $3.6 \text{ V}/\mu\text{s}$ ). The symbol  $R_b$  represents the sensor resistance and  $R_5$  is a constant resistance for determining the output range.  $V_{ref}$  is a reference voltage applied to the positive input. Equation (4.6) was used to compute the output voltage of the commercial bend sensor.

$$V_{out\_b} = V_{ref} \left(1 + \frac{R_b}{R_5}\right) \quad (4.6)$$

### 4.2.3 Weighted-average Fusion Method for Multichannel Signal Data

As described in section 4.1, a two-channel methodology was employed for both sensor#2 and sensor#3. The simultaneous output data would be fused to determine the actual rotation angle. As expressed in equation (4.4), the output voltage of each channel is proportional to the square of the cosine of the rotation angle. To explain the data fusion method, two cosine squared output signals ( $y_1$  and  $y_2$ ) with a certain phase difference ( $\varphi$ ), mathematically represented in equation (4.7) are thereby introduced.

$$\begin{aligned} y_1 &= k_1 \cos^2 \beta_1 + b_1 \\ y_2 &= k_2 \cos^2 \beta_2 + b_2 = k_2 \cos^2(\beta_1 + \varphi) + b_2 \end{aligned} \quad (4.7)$$

where the parameters  $k_1$  and  $k_2$  denote the peak-to-peak amplitude of the output,  $b_1$  and  $b_2$  representing the constant offset values, and  $\beta_1$  and  $\beta_2$  denoting the rotation or

bending angles in degrees. The parameters  $k_1$  ( $k_2$ ),  $b_1$  ( $b_2$ ) and  $\beta_1$  ( $\beta_2$ ) in equation (4.7) correspond to the parameters  $n_{ij}$ ,  $a_{ij}$  and  $\delta_{ij}$  in equation (4.4), respectively. According to the operating principle of sensor#2 and sensor#3, the parameter  $\varphi$  can be any value ranging from  $40^\circ$  to  $50^\circ$ .

For simplification, a special case is taken as an example. The parameters,  $k_1$ ,  $k_2$ ,  $b_1$ , and  $b_2$ , are assigned with a same value of one volt, and the phase difference  $\varphi$  is assigned with  $45^\circ$ . The variable  $\beta_1$  is specified with a series of values between  $-90^\circ$  and  $90^\circ$  with an equal space of  $0.5^\circ$  to calculate the output signals using MATLAB. The computed signals  $y_1$  and  $y_2$  are plotted in Figure 4.11.

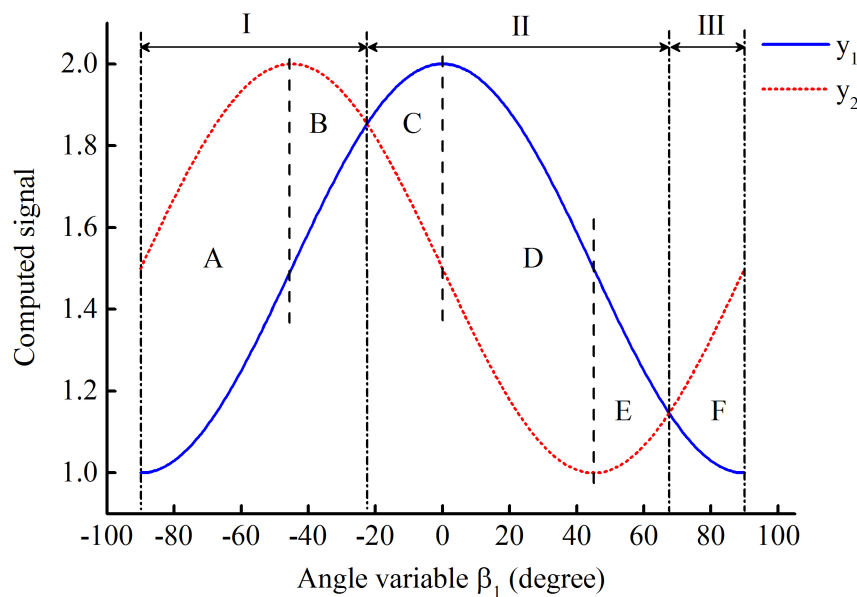


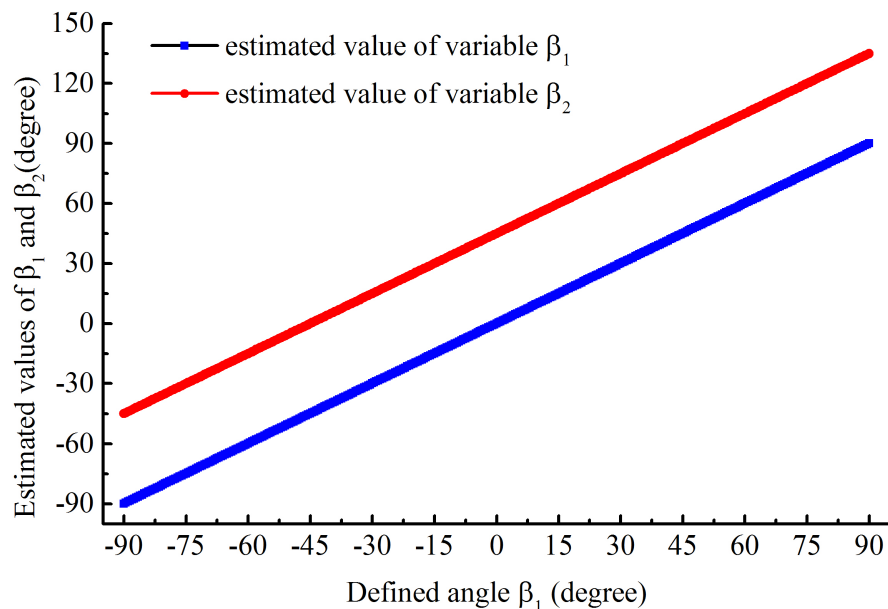
**Figure 4.11** The simulated signals ( $y_1$  and  $y_2$ ) with the same amplitude but a phase difference of  $45^\circ$ . They are proportional to the square of the cosine of the angle variable  $\beta_1$ . The signals can be divided into three regions: I, II, and III according to the output amplitudes, and they can be further divided into six subregions (A-F) based on the angular position with the maximum or minimum output.

As shown in Figure 4.11, the amplitude of the two signals can be divided into three regions: I, II, and III. In region I and region III, the values of  $y_1$  are smaller in comparison with  $y_2$ , while the opposite is true in region II. According to the angular positions with the maximum or minimum value, these three regions can be further split into six subregions (A-F). According to equation (4.5),  $\beta_1$  and  $\beta_2$  in each subregion can be calculated using the mathematical expressions listed in Table 4.1.

Figure 4.12 shows the angular positions which are derived from the two signals using the expressions in Table 4.1. Clearly, both  $\beta_1$  and  $\beta_2$  are successfully derived in the range from  $-90^\circ$  to  $90^\circ$ . The difference between them is  $45^\circ$  at any point, which is consistent with the initial setting.

**Table 4.1** Calculation of the angular positions of the two simulated signals.

Region	Estimated value of $\beta_1$	Estimated value of $\beta_2$	
I	subregion A	$-\arccos(\sqrt{(y_1 - b_1)/k_1})$	$-\arccos(\sqrt{(y_2 - b_2)/k_2})$
	subregion B	$-\arccos(\sqrt{(y_1 - b_1)/k_1})$	$\arccos(\sqrt{(y_2 - b_2)/k_2})$
	subregion C	$-\arccos(\sqrt{(y_1 - b_1)/k_1})$	$\arccos(\sqrt{(y_2 - b_2)/k_2})$
II	subregion D	$\arccos(\sqrt{(y_1 - b_1)/k_1})$	$\arccos(\sqrt{(y_2 - b_2)/k_2})$
	subregion E	$\arccos(\sqrt{(y_1 - b_1)/k_1})$	$\arccos(-\sqrt{(y_2 - b_2)/k_2})$
III	subregion F	$\arccos(\sqrt{(y_1 - b_1)/k_1})$	$\arccos(-\sqrt{(y_2 - b_2)/k_2})$

**Figure 4.12** The angle variables calculated using the simulated output signals and the mathematical model.

Since  $y_1$  and  $y_2$  are presented digitally, the sensitivity of these two signals, i.e. the change in output for unit input, can be computed using equation (4.8).

$$S_i(N_i) = k_i(\cos^2(N_i + P_i) - \cos^2(N_i)) \quad (i = 1, 2) \quad (4.8)$$

where the subscript  $i$  denotes the signal label, e.g. the calculation for  $y_1$  when  $i$  equals one.  $N_i$  is the current angle and  $P_i$  is the step size.  $S_i(N_i)$  represents the incremental sensitivity of signal  $y_i$  at the angle of  $N_i$ . Here  $P_i$  is assigned with a value of  $0.5^\circ$  which is same to the step size used to generate  $y_i$ .

The computed incremental sensitivities of  $y_1$  and  $y_2$  are shown in Figure 4.13. It can be found that the sensitivity of the two signals varies with the angular position. The absolute value of the sensitivity of  $y_1$  is maximum ( $8.7 \text{ mV}/0.5^\circ$ ) at  $\pm 45^\circ$  and becomes  $0 \text{ mV}/0.5^\circ$  at  $\pm 90^\circ$  and  $0^\circ$ . For the ease of description, the region with sensitivity greater than  $5.5 \text{ mV}/0.5^\circ$  is defined as sensitive region and otherwise as insensitive region. At the angle ranging from  $-70^\circ$  to  $-20^\circ$  and from  $20^\circ$  to  $70^\circ$ ,  $y_1$  is just operated in the sensitive region while  $y_2$  does work in the insensitive region at some positions (i.e.  $-55^\circ$  to  $-35^\circ$  and  $35^\circ$  to  $55^\circ$ ). In the range of  $-90^\circ$  to  $-70^\circ$ ,  $-20^\circ$  to  $20^\circ$ , and  $70^\circ$  to  $90^\circ$ ,  $y_1$  falls into the insensitive region at some points whilst  $y_2$  performs in the sensitive region. The setting of the phase difference (i.e.  $45^\circ$ ) between  $y_1$  and  $y_2$  ensures that at least one signal works in the sensitive region for the angle spreading  $180^\circ$ .

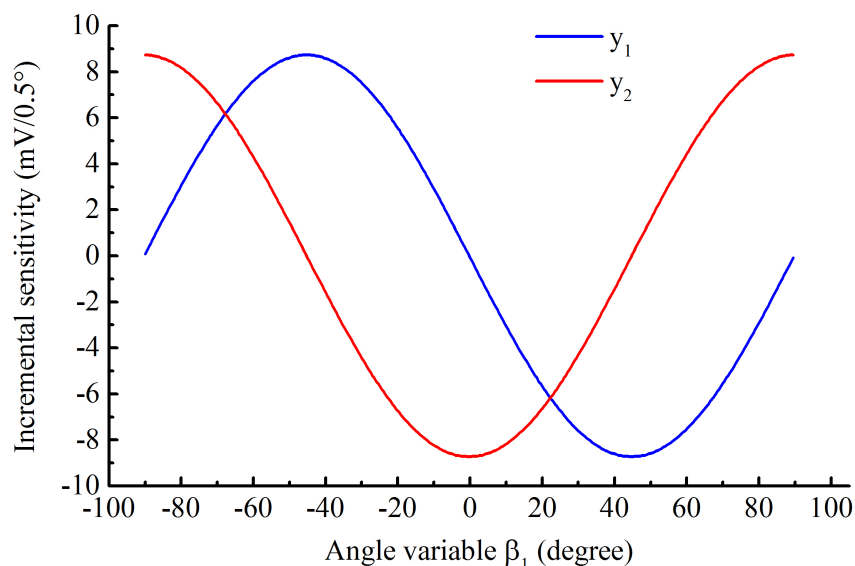


**Figure 4.13** Incremental sensitivity for  $0.5^\circ$  steps.

To improve the sensitivity, the angles derived from the two output signals are fused to determine the angular position by a weighted average method. Variable weighting is

applied to each signal taking into account the angular dependency of their sensitivities. Higher weights are applied when the sensitivity of the signal is maximum, i.e. near to the angle of  $45^\circ$ . Therefore, the final angle  $\beta$  can be computed by equation (4.9).

$$\beta = w_1\beta_1 + w_2(\beta_2 - \varphi)$$

$$w_1 = \left(1 - \frac{|y_1 - h_1|}{|y_1 - h_1| + |y_2 - h_2|}\right)^n \quad (4.9)$$

$$w_2 = 1 - w_1$$

where  $w_1$  and  $w_2$  denote the allocated different weights for the two signals  $y_1$  and  $y_2$ , respectively. The symbol  $h_1$  represents the value of  $y_1$  when  $\beta_1$  equals  $45^\circ$  and  $h_2$  is the value of  $y_2$  with  $\beta_2$  equal to  $45^\circ$  in equation (4.7). The parameter  $n$  is determined by the nonlinear least squares regression based on the experimental dataset for the optimal angle estimation. In this example,  $n$  equals one for the computed dataset represented in Figure 4.11.

Unlike the single signal example, it is very difficult to determine the incremental sensitivity after applying the data fusion method to the two signals ( $y_1$  and  $y_2$ ). According to equation (4.9), when either  $y_1$  or  $y_2$  works in the insensitive region, the angle  $\beta$  will be largely determined by the signal operating in the sensitive region. When they both work in the sensitive region, the angle  $\beta$  is almost equally determined by the two signals. The sensitive region is usually treated as a linear part. For this reason, the sensitivity can be approximated as the slope of  $y_1$  or  $y_2$  in the sensitive region, i.e.  $8\text{mV}/0.5^\circ$ , after applying the data fusion approach to the dataset shown in Figure 4.11.

Additionally, the angle  $\beta$  in equation (4.9) is dominantly determined by the linear part (i.e. the sensitive region) of the two signals, and thereby the fused output can be regarded as linear.

#### 4.2.4 Software for Measurement System Control and Sensor Data Acquisition

As stated in 4.2.1, both the rotating stage and the signal acquisition are controlled using LabVIEW programming. To fully characterise the sensor, three distinct investigations were conducted; (1) assessment of static and dynamic characteristics, (2) evaluation of the data fusion approach, and (3) the capability of the sensor in monitoring finger motion.

The programming methodology is described below, and the LabVIEW programs can be found in Appendix B.

#### 4.2.4.1 Virtual Instrument for Investigation of Sensor Characteristics

Characterisation of the sensor included linearity, repeatability, stability and dynamic responses. All measurements under static conditions were controlled in a similar way using LabVIEW. The simplified block diagram is shown in Figure 4.14. After initialisation, the motorised stage and sensor rotated to a specific position according to the first element in the angle sequence. Following this, the configured DAQ virtual channels started to acquire the output voltage of the sensor, and then the data were saved to a file in the PC. These processes executed in a loop to test the sensor at different angular positions. The iteration stopped when the rotation stage reached the position defined by the last element in the angle sequence. Finally, the rotation stage was deactivated and all DAQ tasks were stopped and cleared.

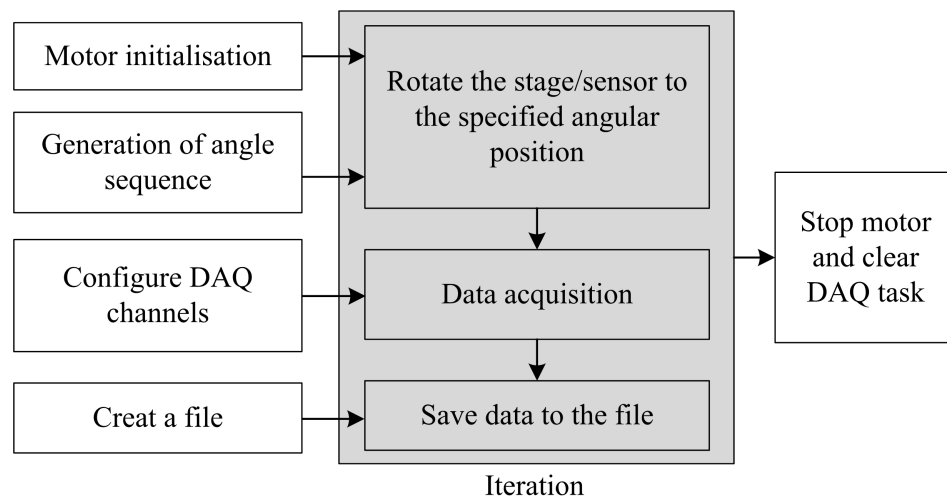


**Figure 4.14** The simplified LabVIEW block diagram for evaluating the sensor's static characteristics. The iterative actions included motor rotation, data acquisition, data display and storage.

Different angle sequences were created using LabVIEW code for testing the sensor linearity, repeatability, and stability. For instance, a sequence of equally spaced angle points were generated for the linearity assessment by controlling the parameters, such as the start and finish positions, and the angle intervals. Data sampling at each angle was also determined by setting the sampling rate and sampling time. The LabVIEW programs for generating these angular positions are listed in Appendix B (SubVI: C & E).

The method for performing dynamic measurements is illustrated in Figure 4.15. Rotation tasks and data acquisition were synchronised to measure the sensor's dynamic responses. The synchronisation signal, initiated rotation of the motor stage, registered the motor's real-time position and acquired the sensor output. The motorised stage stopped rotating when it arrived at the specified angle.

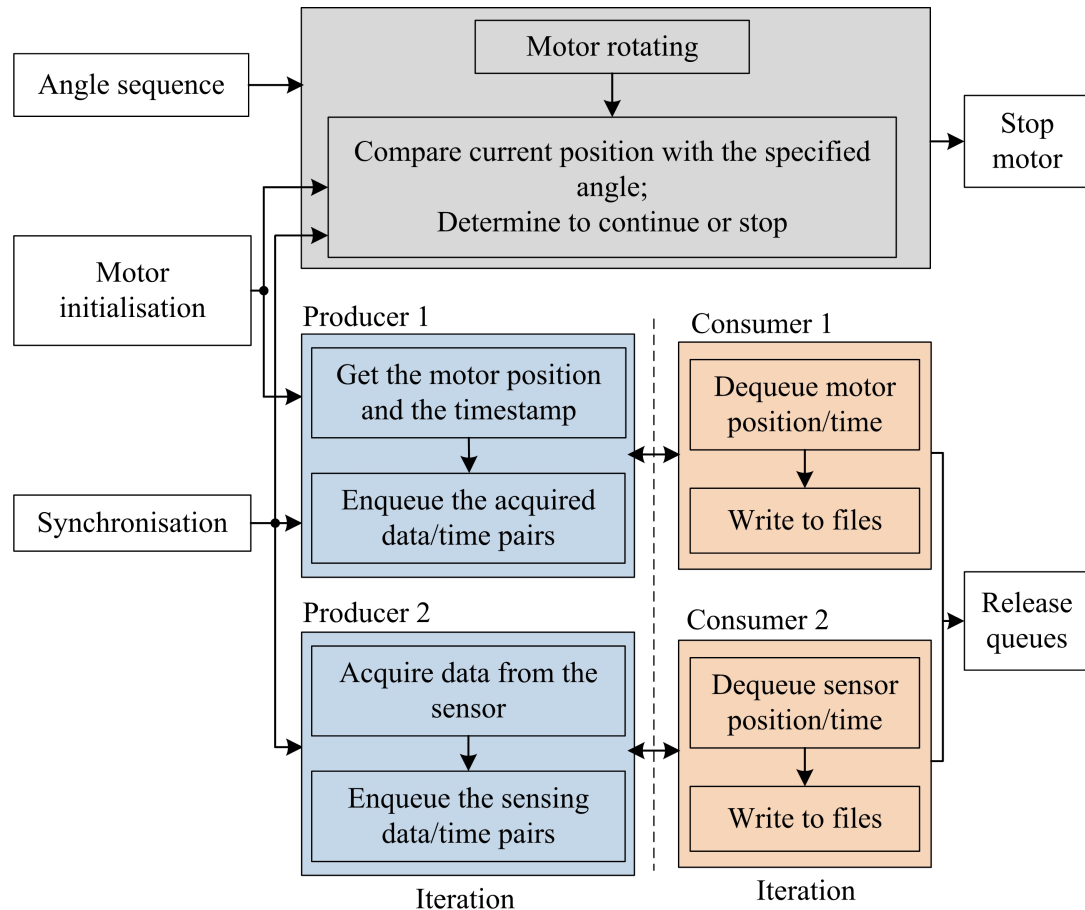


**Figure 4.15** The simplified LabVIEW block diagram for evaluating the sensor dynamic responses. The motorised stage keeps rotating continuously until it reaches to the specified angular position. Synchronous to the motor's rotation, the data acquisition and processing of the motor's trajectory and the sensor outputs are performed in two producer/consumer loops.

The acquisition, processing, and storage of the motor's trajectory and the sensor's outputs were executed in two producer/consumer patterns. The producer/consumer pattern contains two major components and share a common buffer used as a data queue. The producer generates data and puts them into the queue for later processing, and the consumer is then free to remove the data from the queue at any time in the future. This pattern can efficiently decouple the processes that produce and consume data at different rates. In this application, the motor's position and the sensor's output and the corresponding timestamp were acquired in the producer loops, and the data storage as well as the waveform display was dealt with by the consumer loops.

Figure 4.16 shows the graphical user interface (LabVIEW front panel) for evaluating the sensor's static and dynamic characteristics. It mainly included four subpanels: A1, B1, C1, and D1. A1 displayed the virtual control panel of the motorised rotation stage, B1 for setting the parameters of the stage, C1 showing the sensor output waveforms, and D1 for selecting the measurement to be made and adjusting the test settings.

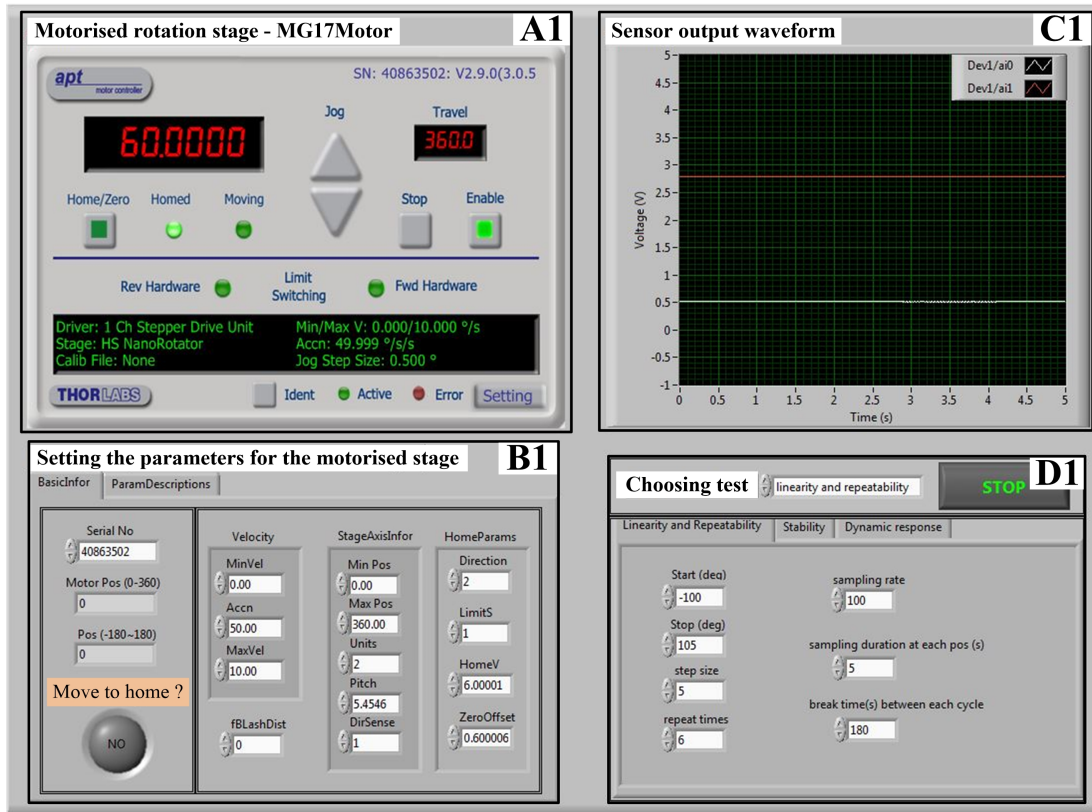


**Figure 4.16** The LabVIEW graphical user interface for testing sensor characteristics.

In the active control panel of the motorised stage (A1), the current operating states (e.g. the motor position, the range of travel, and the specified settings) and a series of control buttons were displayed, so that the user can manually interact with the rotation controller units through this panel. This Virtual Instrument (VI), however, used the software functions based on the ActiveX interfacing technology to set all parameters and to control the motor operations automatically. The parameters including the rotational velocity and acceleration can be adjusted in B1, and thus the user does not need to change anything in the control panel of the motorised rotation system. Before taking measurements, the user can also choose to send the motor to the home position where the counter is reset to zero degrees by clicking the 'Move to home?' button located in B1. In D1, the tab control including three pages: Linearity and Repeatability, Stability, and Dynamic response will switch to the corresponding page according to the selected test. In each tab page the parameters can be altered to generate a sequence of rotating angles for the measurement to be carried out. The sensor output voltages were graphically

displayed in C1. The number of the plots shown in the waveform chart can be adjusted; two plots were displayed in the graphical user interface as shown in Figure 4.16.

#### 4.2.4.2 Virtual Instrument for Evaluating the Data Fusion Method

This VI is used to evaluate the data fusion approach employed by the multi-channel optical goniometric sensors, i.e. sensor#2 and sensor#3. The simplified block diagram of the LabVIEW VI is shown in Figure 4.17.

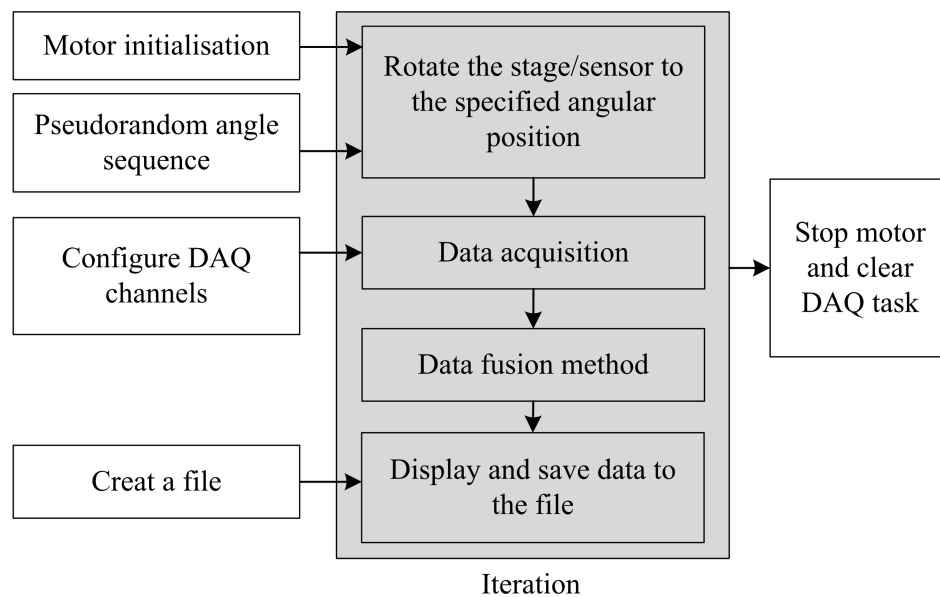


**Figure 4.17** The simplified LabVIEW block diagram for evaluating the data fusion method. A sequence of uniformly distributed pseudorandom angle values is generated to control the system rotation. After the motor moves to the specific angle, the sensor data acquisition and processing is performed.

To simulate finger motion, uniformly distributed pseudorandom angles were generated and applied to the motorised stage. As for previous measurements, the motor rotation, data acquisition, and data processing were performed in sequence and repeated continuously for all specified angular positions. The sensor outputs acquired by the NI DAQ were fused by the weighted average approach which was achieved using a MATLAB script in LabVIEW. The motion trajectories recorded by the sensor were displayed in the LabVIEW front panel.

Figure 4.18 shows the corresponding user interface. It contained four subpanels: A2, B2, C2, and D2. The subpanels A2 and B2 presented the virtual control panel and the parameter settings for the rotation stage, respectively. All the parameters of the motorised stage were adjusted in B2. In C2, the user can select the investigation to be made and trigger the Stop event for the measurement. D2 displayed the difference

between the position of the rotation stage and the angular result derived from the output voltage of each sensing channel. The result after applying the weighted average fusion method was also demonstrated in D2.

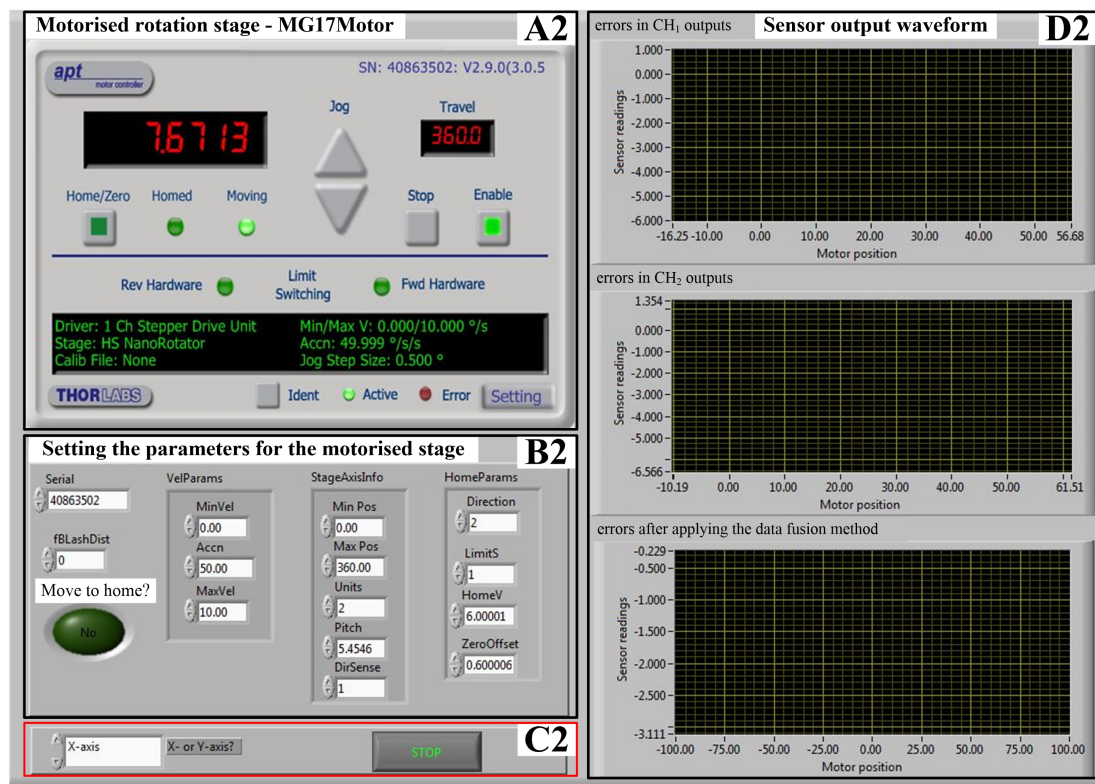


**Figure 4.18** The user interface for evaluating the efficiency of the data fusion method for sensor#2 and sensor#3.

#### 4.2.4.3 Virtual Instrument for Monitoring Finger Motion

To evaluate the bend sensor and all three optical sensors for monitoring finger motion, a LabVIEW VI has been developed. Appropriate finger joints were selected according to each sensor's specific measuring capabilities. Sensor#1 was used to track the motion of the DIP joint, sensor#2 and the bend sensor to monitor the PIP joint, and sensor#3 to record the movements of the MCP joint. It was not possible to mount each sensor simultaneously on to the finger due to space restrictions caused by overlapping wings. This problem can be easily overcome by reducing the length of the sensor wings in future designs.

During finger motion, video frames were also recorded using a single-camera system as a reference point; video recording is commonly regarded as the gold standard for monitoring articulated motion. In this research, the camera was mounted 300 mm above a table on which the user's hand was placed during the measurements and the

focal plane of the camera was kept parallel to the table top. The camera provides 1080 pixel high-definition video recording when operating at 60 frames per second. Multiple markers were made onto the electro-optical sensors and their location is discussed in Chapter 6. The camera system recorded the trajectories of the markers during the measurements.

As shown in Figure 4.19, the user starts by selecting the finger joint to be measured, and then the camera-based system and the sensor data acquisition are triggered simultaneously. For the camera system, the video is kept recording until the measurement is finished. For each sensor or sensor pair, the data acquisition occurs in the producer loop, and the data processing and analysis take place in the consumer loop. In the consumer loop, the output voltages of the sensors are converted to angles based on the voltage-to-angle relationships; both sensor#2 and sensor#3 require data fusion processing. In addition, the user is allowed to define the zero-degree position of the finger joints. The subsequent finger motion is then assessed and mathematically described with respect to the defined zero point.

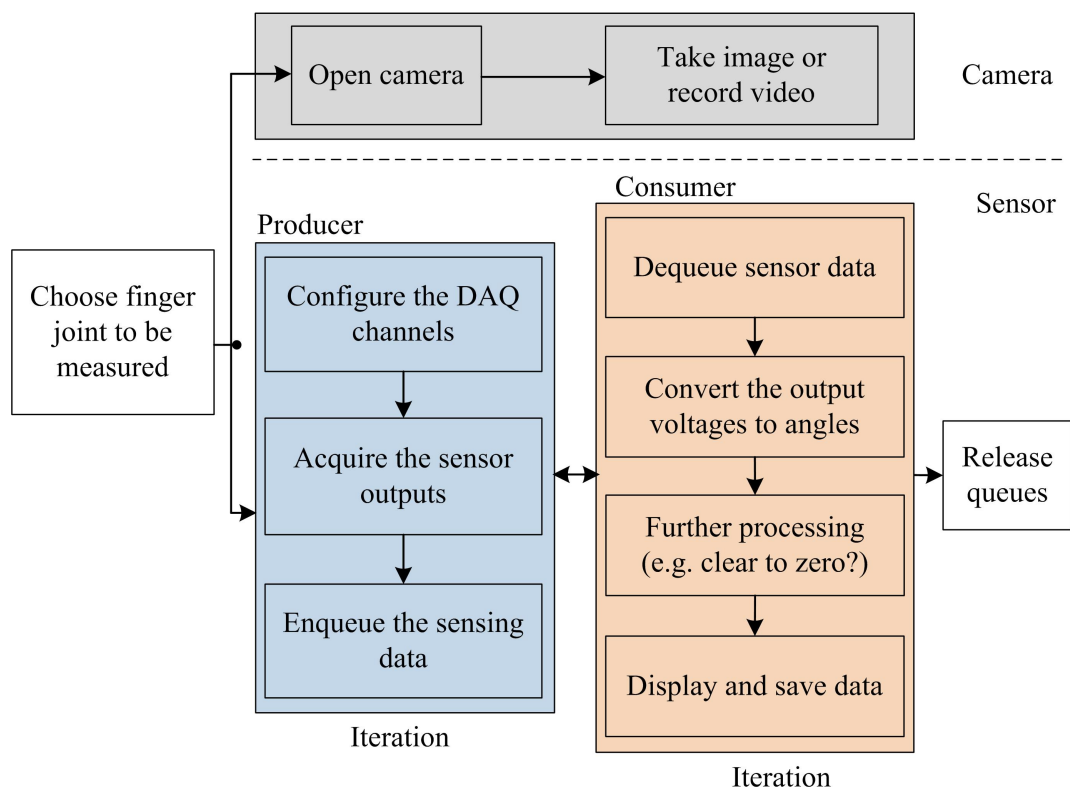


**Figure 4.19** The simplified LabVIEW block diagram for monitoring finger motion. After the confirmation of the finger joint to be measured, the sensor output acquisition and the data processing are triggered in the producer and consumer loops, respectively; meanwhile, the single-camera system also starts to record the finger movements.

This research took the left index finger as an example to investigate the sensors' capability. Figure 4.20 shows the graphical user interface for monitoring the finger

motion. The user interface is divided into three subpanels: A3, B3 and C3. The image of a left hand with highlighted index finger joints is displayed in A3. At the beginning of the measurements, the user needs to select the finger joint to be measured. After the selection, the grey circular shape located on the chosen joint turns green. The subpanel B3 includes a tab control which consists of three pages: DIP: Sensor#1, PIP: Sensor#2 and bend sensor, and MCP: Sensor#3. According to the selected finger joint, the tab pages switch automatically. The motion of the recorded finger joint is demonstrated in the corresponding tab page. In Figure 4.20, the PIP joint is selected; the grey circular shape on the PIP joint in A3 changes to green and the tab control in B3 turns to the page named as *PIP: Sensor#2 and bend sensor*. C3 allows the user to set the current hand gesture as the zero-degree position, adjust the sensor's parameters and terminate the measurements at any time.

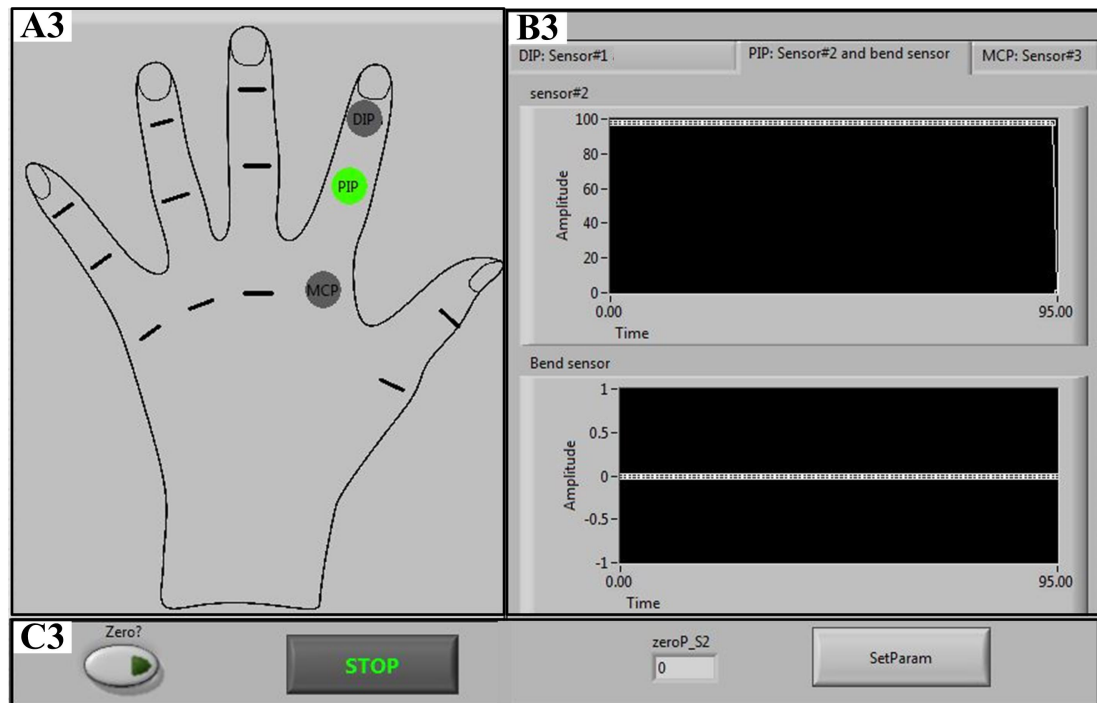


**Figure 4.20** The user interface for monitoring finger motion.

## 4.3 Summary

Based on Malus' law, three electro-optical goniometric sensors with compact configurations were developed. Sensor#1 was designed with one sensing channel and a measuring range of  $90^\circ$ . Sensor#2 was created with a single rotation axis but had two sensing channels producing simultaneous outputs. Sensor#3 featured two rotation axes each having two channels. A weighted-average fusion method was introduced to process the output of sensor#2 and sensor#3, which enabled these two sensors to detect

---

a range of  $180^\circ$  and also improved the sensor sensitivity. The distinctive features make the three electro-optical sensors suitable for monitoring different finger joints. A commonly used commercial bend sensor was chosen as a reference point for the developed sensors. To investigate the sensor performance, an automated measurement system consisting of the motorised rotation stage, conditioning circuitry and data acquisition system was built. Meanwhile, LabVIEW programs were also coded to control the system and data acquisition.

# Chapter 5

## Sensor Static and Dynamic Characteristics

The performance of the three electro-optical sensors and the commercial bend sensor are investigated using the automated measurement apparatus discussed in Chapter 4. In this chapter, their static characteristics including linearity, hysteresis, repeatability, stability, and accuracy are assessed. The dynamic response was studied using sensor#1 and compared with the bend sensor.

### 5.1 Sensor Static Characteristics

The static measurements for the three electro-optical sensors and the bend sensor were all carried out under the same conditions. The motor rotated at  $10^\circ/\text{s}$  (clockwise and anticlockwise directions), the sensor data was sampled at 100 Hz, and all measurements were conducted at room temperature.

A separate Cartesian coordinate system is defined for each sensor type. For the optical sensors, alignment of wings is defined as  $0^\circ$ ; and for the commercial bend sensor, the natural flat position is defined as  $0^\circ$ .

#### 5.1.1 Performance of the Single-axis Electro-optical Sensor

The static characteristics of sensor#1, including linearity, hysteresis, repeatability, and temporal stability, are evaluated and presented as follows.

### 5.1.1.1 Voltage-to-Angle Relationship

To investigate the voltage-to-angle relationship, sensor#1 was rotated through angles ranging from  $-20^\circ$  to  $100^\circ$  and then back to  $-20^\circ$  with increments of  $5^\circ$ . For each angle setting, up to 500 samples were taken. This process was repeated five times with an interval of three minutes between each cycle. At each angular position, the data obtained in the five repeated tests were averaged and plotted in Figure 5.1.

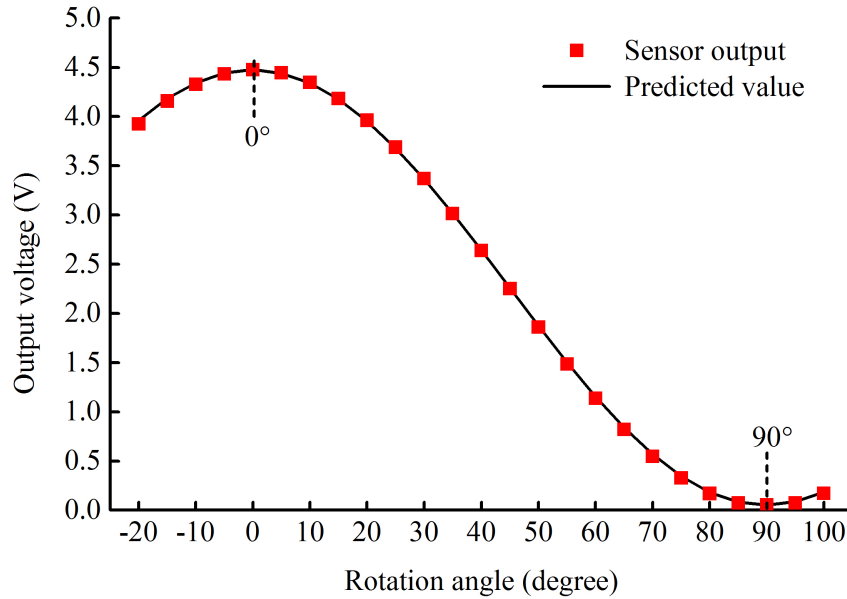


**Figure 5.1** The voltage-to-angle relationship of sensor#1 in the range of  $-20^\circ$  to  $100^\circ$ .

According to the descriptions in Chapter 4, the output voltages of sensor#1 would follow the mathematical model presented in equation (4.4), in which the subscripts  $i$  and  $j$  equal one. Trust-region-reflective least square algorithm was applied to determine the parameters  $n_{11}$  and  $a_{11}$ , and the fitted function is shown in equation (5.1).

$$V_{out\_11} = 4.423 \cos^2(\delta_{11}) + 0.052 = 4.423 \cos^2(\delta + 0.1) + 0.052 \quad (5.1)$$

where the variable  $\delta_{11}$  represents the relative orientation of the transmission axes of the polariser and the analyser, and the variable  $\delta$  denotes the motor's angular position ranging from  $-20^\circ$  to  $100^\circ$ , i.e. the position of sensor#1. The value 0.1 indicates that the transmission axes of the two polarising films are closely aligned when sensor#1 is at  $0^\circ$ .

Using equation (5.1), the predicted output of sensor#1 is plotted in Figure 5.1. It can be seen that the measured output voltages of sensor#1 are consistent with the predicted values. The absolute value of the deviation from the predicted values is 0.1% - 13.3%,

averaged as 2.3%. The deviation greater than 5.0% occurs at the angles ranging from 80° to 100° where the sensitivity is close to zero as analysed in 4.2.3.

According to Malus' law, the output voltage should be 0 V when the transmission axes of the polarising films are perpendicular to each other. However, an offset voltage of 0.052 V existed in the outputs of sensor#1, as shown in Figure 5.1 and equation (5.1). This may be caused by several reasons including limited polariser quality, misalignment of the two pieces of polarising film, the input bias current of the amplifier, and interference from the ambient light.

The polarising film features an extinction ratio of 9000:1, equivalent to the ratio of the percentage light transmission for parallel (36%) and crossed polarisers (0.004%). The polariser and the analyser of sensor#1 were located inside two separate 3D printed holders and great effort was made to correctly align the polarising films. The maximum measured output of sensor#1 is 4.48 V, and thus the offset voltage due to the above extinction ratio should be around 0.5 mV which is much smaller than the detected offset voltage (52 mV). Therefore, the polarising film is not the main reason for this offset value.

The input bias current sensor#1's amplifier, i.e. the average of the current entering the terminals of the amplifier, is typically about 1 pA at 25 °C. Passing through the conditioning circuitry, this current can be converted to a voltage of about 0.12 mV. Clearly, the input bias current of the amplifier is not a key factor leading to the offset voltage either.

As described in Chapter 4, two approaches are taken to avoid the influence of the ambient light: the use of the opaque printing material and the coverage of the non-reflective black Aluminium foil tape to the optical sensors. Furthermore, all the light sources including the fluorescent lamp in the lab room were turned off during the measurements of sensor characteristics. Therefore, the influence of the ambient light can be ignored.

The visible LED source of sensor#1 typically offers a high luminous intensity about 400 millicandelas when driven by a current of 20 mA. The LED is located at a distance of 6.50 mm from the photodiode. The unpolarised light emitted by the LED can be possibly transmitted through the sensor wall via a series of reflection and refraction, and finally hit the photodiode. Furthermore, the integration gaps of sensor#1 can also facilitate the transmission of the visible light.

According to the above analysis, the unwanted internal reflection of the visible light emitted by the LED source can be the main reason for the detected offset voltage, which

will be further discussed in 5.1.3.1. All the measured outputs shifted up by an equal value, and thus the offset voltage does not affect the measurement performance of sensor#1.

### 5.1.1.2 Hysteresis Analysis

By averaging the data acquired in the five repeated measurements, the sensor outputs for clockwise and anticlockwise rotations were obtained as shown in Figure 5.2.

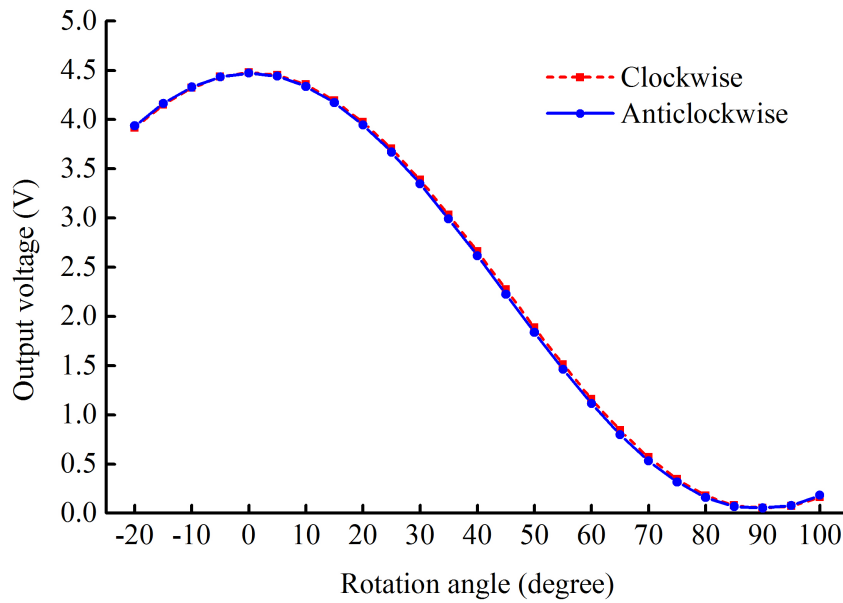


**Figure 5.2** The clockwise and anticlockwise outputs of sensor#1 for the rotations ranging from  $-20^\circ$  to  $100^\circ$ .

Clearly, the two output curves presented in Figure 5.2 almost coincide. At each testing angle, only slight differences between them can be observed. For numerical description of the hysteresis magnitude, the equation defined in the literature [63, 265] is employed to quantify the hysteresis errors.

$$DH(\phi) = \frac{\Delta V(\phi)}{V_{max} - V_{min}} \times 100\% \quad (5.2)$$

where  $\Delta V(\phi)$  denotes the difference between the sensor outputs in the clockwise and anticlockwise directions at a given angle  $\phi$ . The parameters  $V_{max}$  and  $V_{min}$  are the maximum and the minimum output voltages of the sensor of interest, respectively.

The calculated results showed the hysteresis of sensor#1 was no more than 1.1% for the range  $-20^\circ$  to  $100^\circ$ . The hysteresis errors may be due to tolerance limits of the 3D printing process. The friction between the contact surfaces of the rotating parts together

with manufacturing limitations may lead to differences in the mechanical clockwise and anticlockwise rotations. Additionally, the sensor wing was designed to lie perpendicular to the rotation axis and deviations from this configuration may also be a factor.

### 5.1.1.3 Repeatability Evaluation

As mentioned in 5.1.1.1, the bidirectional measurements for sensor#1 were repeated five times under identical conditions. For each rotation cycle, the output voltages measured at the same angular position were averaged. The results for the five tests are displayed in Figure 5.3.

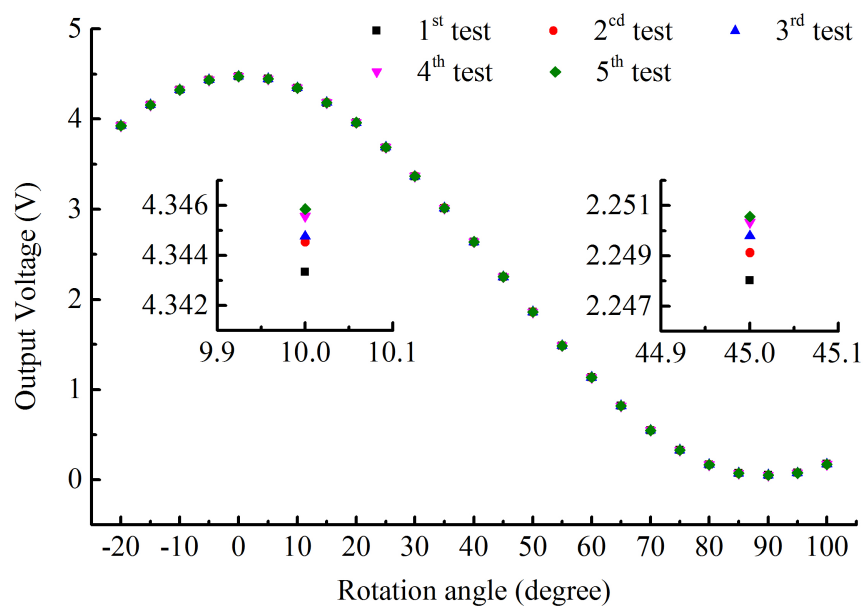


**Figure 5.3** The output voltages of sensor#1 during the five repeated rotation tests in the range of  $-20^\circ$  to  $100^\circ$ . The readings at  $10^\circ$  and  $45^\circ$  are enlarged as examples.

Sensor#1 produced similar readings at each angle during the repeated tests. The enlarged view of measurements taken at  $10^\circ$  and  $45^\circ$ , insets displayed in Figure 5.3, shows a maximum difference less than 4 mV, significantly smaller than the output signals (4.345 V at  $10^\circ$  and 2.250 V at  $45^\circ$ ). For the tested angles, the relative standard deviation (RSD), i.e. the ratio of the standard deviation to the mean value, is no more than 0.8%, with an average of 0.1%. The large RSD occurs at the angular positions ranging from  $80^\circ$  to  $100^\circ$ , which can be explained by the uncertainty of the measurement system ( $\pm 5$  mV) and the low sensitivity in this region.

Numerous different quantitative indices exist for the evaluation of sensor repeatability. The Statistical Range (SR), i.e. the difference between the highest and the lowest measured angles, and the standard deviation (SD) are frequently used for repeatability assessment of sensors used in glove-based systems [8, 27, 116, 118, 119, 266]. For

comparison purposes, the same statistical approach is adopted for this work, however it should be noted that the measurements reported here were obtained under more controlled conditions compared to the hand model data reported in the literature. Since the effective measuring range of sensor#1 is limited to  $90^\circ$ , only rotations in the range  $0^\circ$  to  $90^\circ$  are considered. According to equations (5.2) and (4.5), the output data presented in Figure 5.3 are converted to angular positions in degrees. The computed sensor angles versus the rotation stage angles are plotted in Figure 5.4.

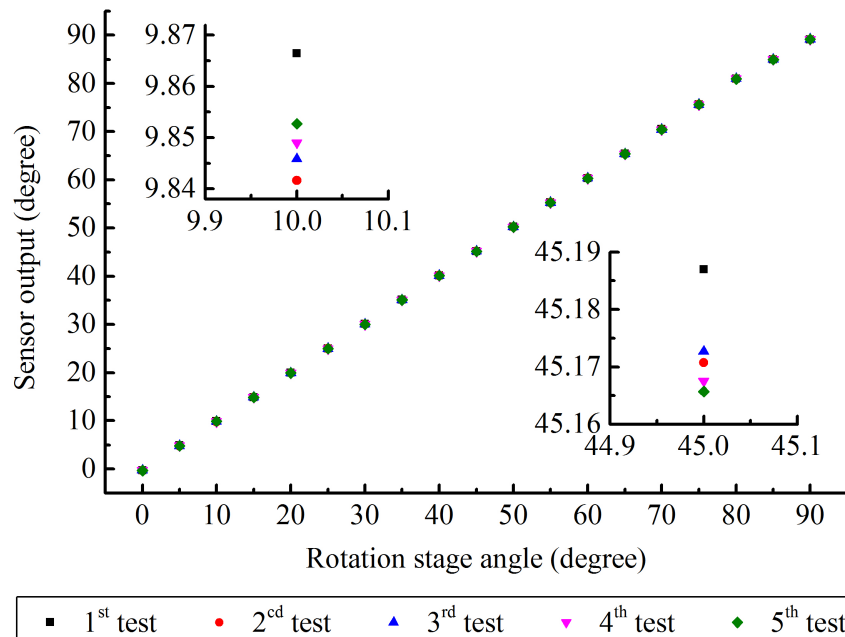


**Figure 5.4** The rotation angles derived from the output voltages of sensor#1 during the five repeated tests in the range of  $0^\circ$  to  $90^\circ$ . The results at  $10^\circ$  and  $45^\circ$  are enlarged as examples.

The spread in output data over five measurement cycles is shown in the insets in Figure 5.4. In these examples, the maximum spread is less than  $0.03^\circ$  for measurements at  $10^\circ$  and  $45^\circ$ .

At each position, the difference between the highest and lowest derived angles, i.e. the SR of sensor#1, was computed. The average values of SR and SD, computed over all angles in the range  $0^\circ$  to  $90^\circ$ , are  $0.03^\circ$  and  $0.01^\circ$ , respectively. This is much smaller than the results of the fibre optic sensor (SR:  $5.60^\circ$ , SD:  $2.30^\circ$ ) [266], Hall Effect sensor (SR:  $6.65^\circ$ , SD:  $2.14^\circ$ ) [8], optical linear encoder (SR:  $3.29^\circ$ , SD:  $3.06^\circ$ ) [27], and resistive bend sensor (SR:  $3.25^\circ$ , SD:  $1.07^\circ$ ) [119], which were integrated into gloves or supports and investigated by using real hand models. The less controlled conditions, i.e. mounting on real hands, are likely to exaggerate repeatability values for the reported sensors; the sensor repeatability under laboratory conditions were not reported. Sensor#1, with much higher repeatability albeit under ideal conditions, shows great promise as a sensory element for future glove-based systems.

Furthermore, with respect to the predefined rotation angles, sensor#1 demonstrates a mean absolute error (MAE) of  $0.28^\circ$ ; all errors fall within  $\pm 0.94^\circ$ . The insets in Figure 5.4 show that the sensor angles differ from the predefined rotations  $10^\circ$  and  $45^\circ$  by no more than  $-0.16^\circ$  and  $0.19^\circ$ , respectively. Therefore, it can be deduced that sensor#1 is also featured with a high measurement accuracy.

#### 5.1.1.4 Sensor Stability

The sensor stability was assessed by fixing the bending angle and measuring changes in the output over an extended period of time. In the test, sensor#1 was rotated to a specific bending angle, and then remained at that position for 180 minutes during which the output data was continuously acquired. The sensor stability was investigated at rotation angles of  $30^\circ$ ,  $45^\circ$ ,  $60^\circ$ , and  $90^\circ$ . The data was sampled at 100 Hz, generating a data set of 1,080,000 points at each angle. To reduce the amount of the samples, the raw data was averaged per second, i.e. every 100 data points. The change in sensor output at angular positions of  $30^\circ$ ,  $45^\circ$ ,  $60^\circ$ , and  $90^\circ$  is displayed in Figure 5.5 along with the average output voltage and the range of variation values. The results in Figure 5.5 show that the outputs of sensor#1 generally remain constant at the investigated angular positions. Over the maximum measurement period of 180 min, the variations in the output amplitudes are small (2.4-3.8 mV). The voltage variations at  $30^\circ$  (3.4 mV),  $45^\circ$  (3.8 mV), and  $60^\circ$  (3.1 mV) all correspond to an angular change of  $0.05^\circ$ . The small voltage variation at  $90^\circ$  (2.4 mV) causes a change in the angular reading about  $1.34^\circ$ ; this can be explained by the extremely low sensitivity which is close to zero at  $90^\circ$ .

The observed variations can be possibly explained by the change in ambient temperature, the stability of the power supply, and the thermal effect of the electronic components including the LED light source and the photodiode. However, all the measurements were carried out at room temperature ( $25^\circ\text{C}$ ), and thus the change in ambient temperature cannot be the main reason. For the power supplied to sensor#1 (+5 V), it showed a decrease of 6 mV when measured over 180 min using NI USB 6211. This would cause a reduction of approximately 0.07 mA in the forward current of the LED, and thereby causing proportional changes in the luminous intensity (about 1.4 millicandela in theory). Consequently, the measured outputs would show a decreasing trend during the measurements. Furthermore, the thermal effect of the electronic components may also contribute to the variations in the sensor outputs. According to the manufacturer's datasheet, the luminous intensity of the LED decreases with an increase in temperature. As the LED gradually heated up, the luminous intensity of the visible light would decrease, leading to a reduction in the photocurrent generated by the photodiode, and thus the output voltages would decline.

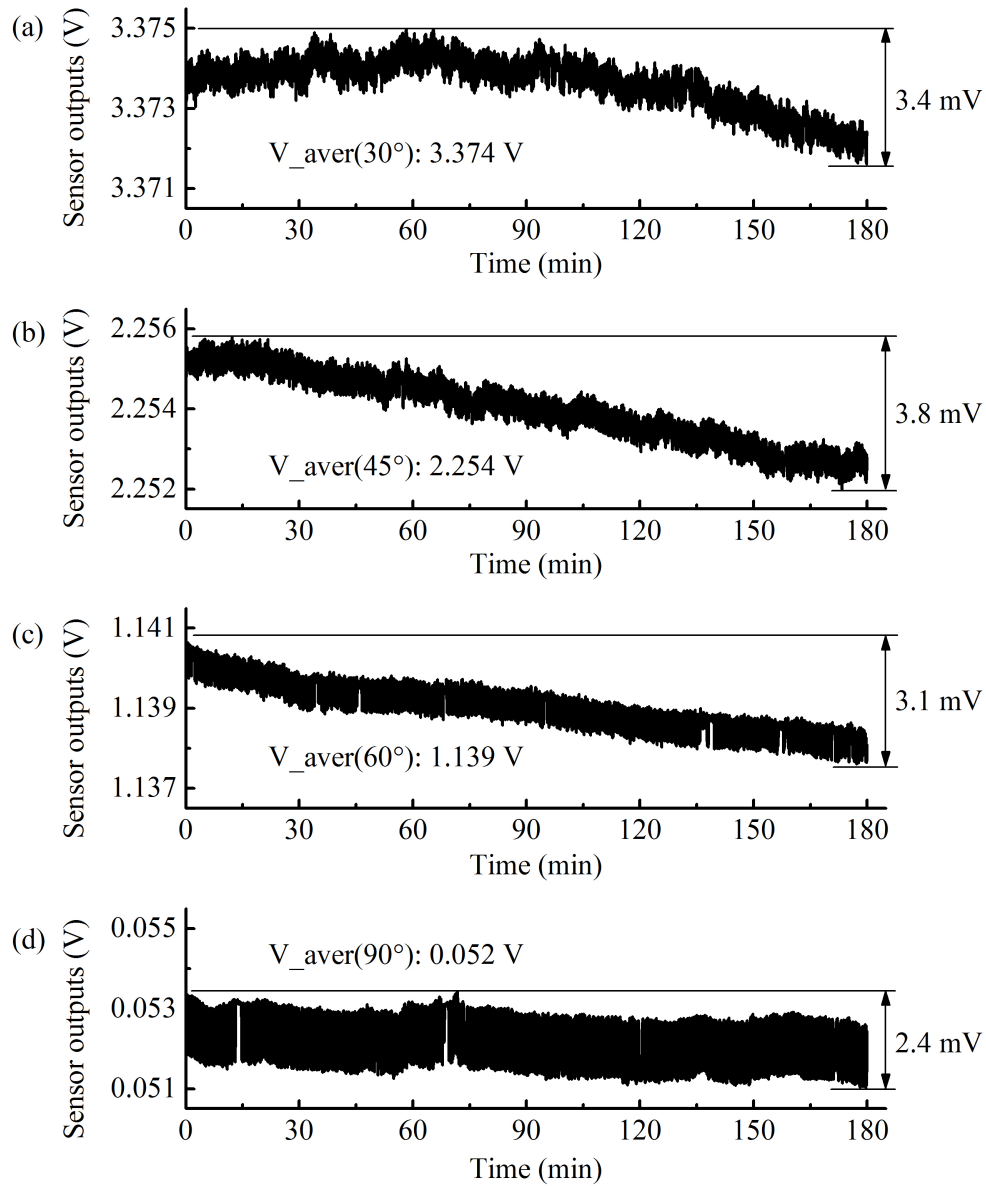


**Figure 5.5** The outputs of sensor#1 at different rotating angles over 180 minutes. **(a)** is the sensor output at the rotation angle of  $30^\circ$ ; **(b)** for  $45^\circ$ ; **(c)** for  $60^\circ$ ; and **(d)** for  $90^\circ$ .  $V_{\text{aver}}(\delta)$  represents the averaged output reading of sensor#1 at the angular position  $\delta$  ( $\delta=30^\circ, 45^\circ, 60^\circ$ , and  $90^\circ$ ).

The sensor output at  $30^\circ$ ,  $45^\circ$ ,  $60^\circ$ , and  $90^\circ$  all demonstrated random fluctuations of 1-2 mV which can be regarded as the electronic noise. This is a reduced number due to the averaging applied to the raw data.

## 5.1.2 Performance of the Single-axis Electro-optical Sensor Using Data Fusion Approach

The static characteristics of sensor#2, including linearity, hysteresis errors, and repeatability, are presented and analysed in the following. The sensor performance obtained for random angle testing is also discussed.

### 5.1.2.1 Voltage-to-Angle Relationship

As described in Chapter 4, to expand the measuring range, sensor#2 was designed with two sensing channels. The measurements followed the same procedures as for sensor#1 but carried out in the range of  $-90^\circ$  to  $110^\circ$ . During the measurements, the two channels  $CH_{21}$  and  $CH_{22}$  were sampled simultaneously. The output voltages of both channels are shown in Figure 5.6.

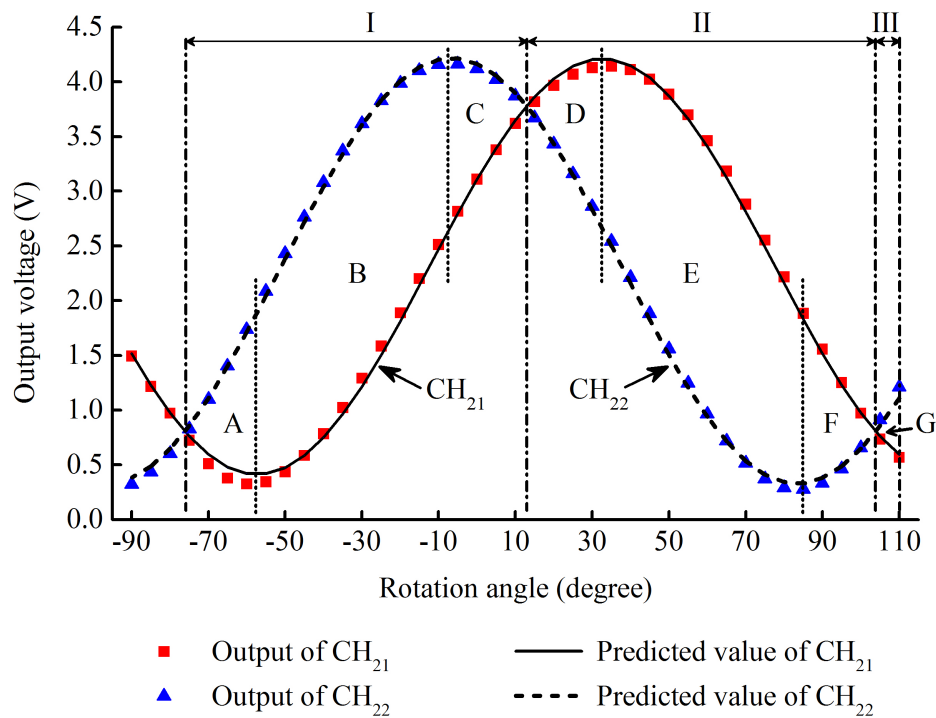


**Figure 5.6** The voltage-to-angle relationship of the two sensing channels of sensor#2 ( $CH_{21}$  and  $CH_{22}$ ) in the range of  $-90^\circ$  to  $110^\circ$ .

The output voltages of  $CH_{21}$  and  $CH_{22}$  follow closely the model values predicted by equation (4.4), in which the subscript  $i$  equals 2 and  $j$  being 1 or 2. Based on the data set shown in Figure 5.6, trendline functions were fitted for the two channels and presented in equation (5.3).

$$V_{out\_21} = 3.799 \cos^2(\delta_{21}) + 0.412 = 3.799 \cos^2(\delta - 32.6) + 0.412 \quad (5.3)$$

$$V_{out\_22} = 3.889 \cos^2(\delta_{22}) + 0.328 = 3.899 \cos^2(\delta + 6.9) + 0.328$$

where the variable  $\delta_{21}$  represents the relative rotation of the polariser's and analyser's transmission axes in CH<sub>21</sub>, and  $\delta_{22}$  is the variation happened in CH<sub>22</sub>, respectively. The variable  $\delta$  denotes the angular position of the motorised stage and sensor#2. The value  $-32.6^\circ$  indicates the analyser's orientation relative to the polariser's transmission axis in CH<sub>21</sub> when the motorised stage and sensor#2 are at the zero position, and  $6.9^\circ$  occurring in CH<sub>22</sub>. Since the light entering into CH<sub>21</sub> and CH<sub>22</sub> are polarised in the same direction, the phase shift ( $39.5^\circ$ ) in these two channels indicates the difference between the analysers' orientation, basically meeting the design requirement ( $40^\circ$ - $50^\circ$ ). Additionally, the differences between the coefficients of the two fitted functions may be due to inconsistencies in fabrication and differences due to tolerances of the electronic components in the conditioning circuits.

Using equation (5.3), the theoretical outputs for CH<sub>21</sub> and CH<sub>22</sub> are computed and also plotted in Figure 5.6. Clearly, the measured outputs of the two sensing channels are consistent with their predicted values at each angular position. The average deviations from the predicted values are  $\pm 3.9\%$  for CH<sub>21</sub> and  $\pm 3.7\%$  for CH<sub>22</sub>. These numbers are greater than the average deviation of sensor#1 ( $\pm 2.3\%$ ), which may be caused by the challenging fabrication of sensor#2 due to the more complicated design. The deviations are greatest at the positions close to the maximum and the minimum outputs, which can be explained by the small sensitivities at these angular positions.

### 5.1.2.2 Hysteresis Error

The performance of sensor#2 was investigated for both clockwise and anticlockwise directions. For each channel, the bidirectional outputs were obtained by averaging the data measured over five repetitions.

As shown in Figure 5.7, both CH<sub>21</sub> and CH<sub>22</sub> produce consistent responses during clockwise and anticlockwise rotations. There are small deviations near the maxima and minima amounting to less than 0.06 V.

Using equation (5.2), the hysteresis of sensor#2 were quantified as 1.8% for CH<sub>21</sub> and 1.5% for CH<sub>22</sub>, higher than the hysteresis performance with sensor#1 (1.1%). This can

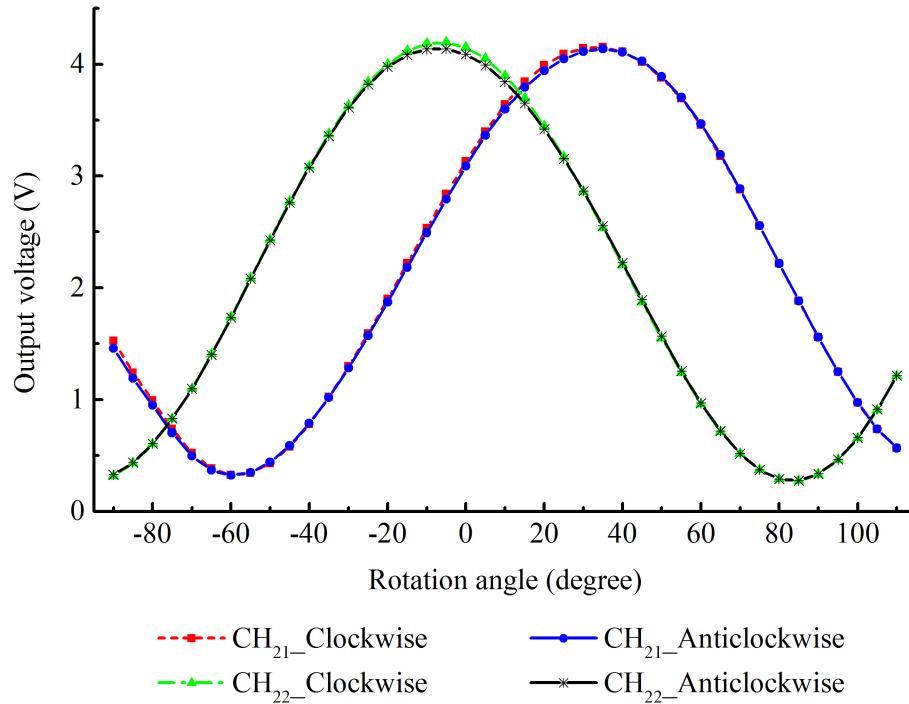


**Figure 5.7** The clockwise and anticlockwise output voltages of the two sensing channels of sensor#2. CH<sub>21</sub>\_Clockwise and CH<sub>21</sub>\_Anticlockwise represent the outputs of CH<sub>21</sub> when sensor#2 rotates from -90° to 110°, and then back to -90°. Similarly, CH<sub>22</sub>\_Clockwise and CH<sub>22</sub>\_Anticlockwise represent the corresponding readings of CH<sub>22</sub>.

be explained by the complicated mechanical design and the difficulty of integration of sensor#2.

### 5.1.2.3 Repeatability Analysis

Figure 5.8 and Figure 5.9 shows the outputs of the two sensing channels of sensor#2, i.e. CH<sub>21</sub> and CH<sub>22</sub>, respectively. Over five tests, both channels generated similar outputs at each angular position.

As the examples shown in the insets in Figure 5.8 and Figure 5.9, CH<sub>21</sub> shows variations in the voltage no more than 0.060 V at -10° and 0.004 V at 55°, and CH<sub>22</sub> demonstrates fluctuations of less than 0.015 V at both -10° and 55°. These variations are small in comparison with the measured output values at the two rotation positions.

For any angle in the range -90° to 110°, the RSD values in CH<sub>21</sub> and CH<sub>22</sub> are no more than 1.6% and 2.0%, respectively. The average RSD is 0.5% in both CH<sub>21</sub> and in CH<sub>22</sub>. These two sensing channels demonstrate comparable performance during the repeated tests. In comparison with sensor#1 (0.1%), the two channels of sensor#2 show much higher RSD. This is related to the difficulty of fabrication of sensor#2 and the wide

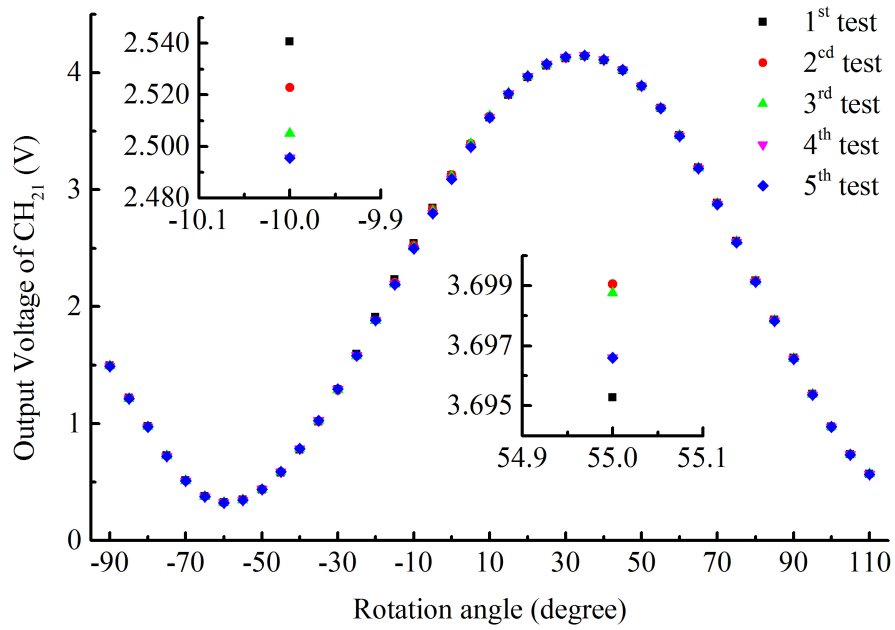


**Figure 5.8** The output readings of CH<sub>21</sub> of sensor#2 during the five repeated measurements in the range of -90° to 110°. The readings at -10° and 55° are enlarged as examples.

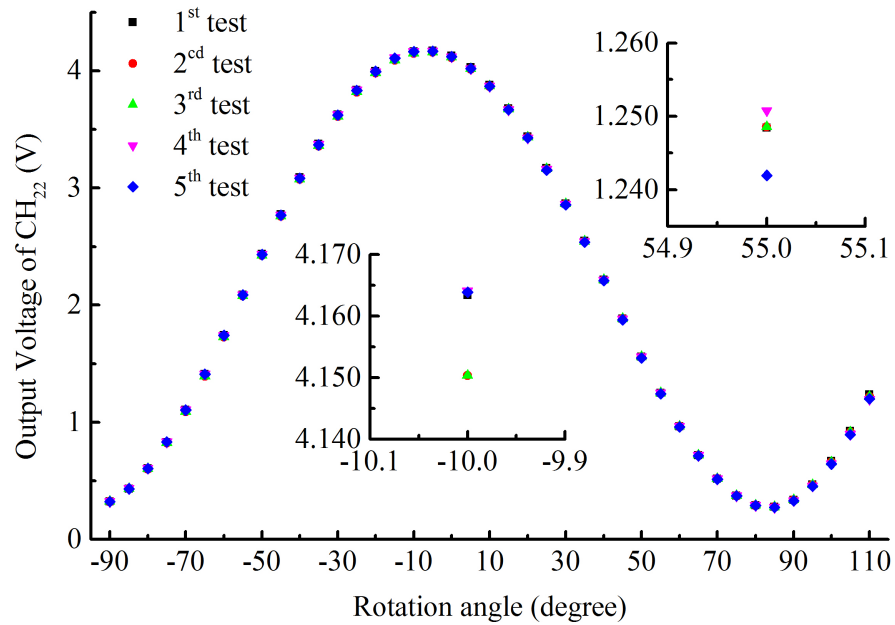


**Figure 5.9** The output readings of CH<sub>22</sub> of sensor#2 during the five repeated measurements in the range of -90° to 110°. The readings at -10° and 55° are enlarged as examples.

testing angle range (200° for sensor#2 and 120° for sensor#1) including more regions with low sensitivity.

The SR and SD together are used to quantitatively evaluate the repeatability of sensor#2. For consistency, the rotation angles of sensor#2 were measured simultaneously from

the output voltages of CH<sub>21</sub> and CH<sub>22</sub>. For these measurements, a range of -70° to 110° was investigated to replicate the ROM of a PIP joint.

By comparing the output amplitudes of the two sensing channels, voltage readings are divided into three regions: I, II, & III, as shown in Figure 5.6. In region I and region III, the outputs of CH<sub>21</sub> are smaller than the ones of CH<sub>22</sub>, while it is opposite in region II. These three regions are further divided into seven subregions: A – G, according to the angular position with the maximum or minimum output. The expressions listed in Table 4.1 are applied to derive the rotation angles based on the dataset presented in Figure 5.8 and Figure 5.9. Finally, the derived angles in CH<sub>21</sub> and CH<sub>22</sub> are combined together by using the data fusion approach introduced in 4.2.3. From the five tests, the fused rotation angles are displayed in Figure 5.10.

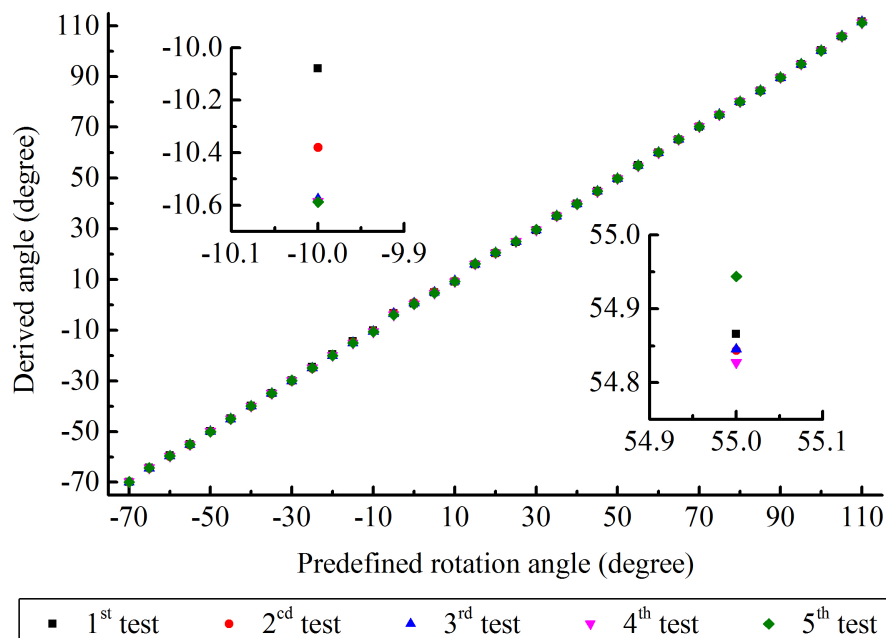


**Figure 5.10** The rotation angles derived from the outputs of sensor#2 for the five repeated tests in the range of -70° to 110°.

The insets in Figure 5.10 indicate that during the five tests the sensor output vary no more than 0.51° and 0.12° at the position of -10° to 55°, respectively. For each investigated angle, the difference between the highest and the lowest derived values, i.e. the SR, over five measurement cycles are computed. The value of SR ranges from 0.05° to 0.69°, with an average of 0.24°. SD is also calculated which is spreading from 0.03° to 0.28° and averaged as 0.10°.

#### 5.1.2.4 Random Angle Testing to Evaluate the Performance of the Single-axis Sensor after Applying Data Fusion Method

This investigation further evaluated the efficiency of the data fusion method of sensor#2. One hundred uniformly distributed pseudorandom numbers ranging from  $-70^\circ$  to  $110^\circ$  were generated in MATLAB to simulate finger motion. Measurements were carried out successively, i.e. sensor#2 rotated from one measurement position to the next, with five hundred samples recorded at each angle. These operations and data processing were controlled using LabVIEW as described in 4.2.4.2.

The differences between the output angles of each channel and the defined rotation angles are plotted in Figure 5.11. The output of sensor#2 after applying the data fusion method is also presented.

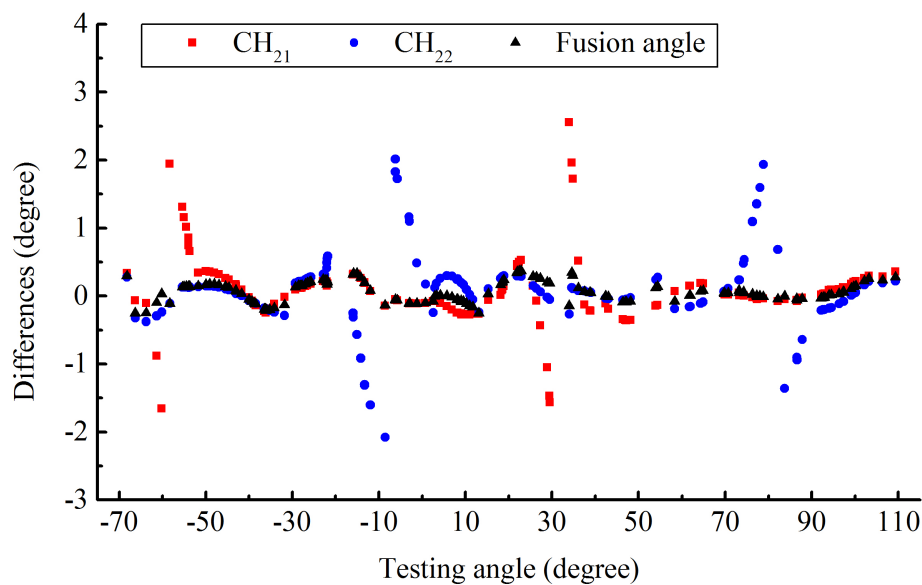


**Figure 5.11** The differences between the measured readings of sensor#2 and the predefined pseudorandom testing angle for the range of  $-70^\circ$  to  $110^\circ$ .

For  $CH_{21}$  and  $CH_{22}$ , the majority of the output angles differ from the test angles by  $\pm 0.5^\circ$ . However, the differences are larger at angles in the range  $-65^\circ$  to  $-50^\circ$  and from  $25^\circ$  to  $35^\circ$  for  $CH_{21}$  (up to  $2.6^\circ$ ), and in the range  $-15^\circ$  to  $0^\circ$  and  $75^\circ$  to  $90^\circ$  for  $CH_{22}$  (about  $2.1^\circ$ ). This can be explained by the small sensitivities in these regions, at which the sensing channels produce outputs close to the minimum or the maximum values (see Figure 5.6). Additionally, the uncertainty of the measurement system ( $\pm 5$  mV) can also be a factor causing such errors, since the detectable change in the rotation angle is limited to  $2^\circ$  at the least sensitive point. The result obtained by fusing the readings from  $CH_{21}$  and  $CH_{22}$  shows significantly smaller ( $\pm 0.4^\circ$ ) sensing errors, in comparison with the outputs measured in a single channel. The MAE is  $0.29^\circ$  and  $0.34^\circ$  in  $CH_{21}$  and

CH<sub>22</sub>, respectively, and this decreases to 0.13° after applying the data fusion approach. Clearly, the proposed data fusion method improves the measurement accuracy and also reduces the influence of the uncertainty of the measurement system. Furthermore, this investigation verifies that sensor#2 is capable of detecting rotations over a 180° range.

### 5.1.3 Performance of the Two-axis Electro-optical Sensor Using Data Fusion Method

The static performance of sensor#3, including the linearity, hysteresis, repeatability, and the improvements of measurement accuracy after applied the data fusion approach are studied and presented as follows.

#### 5.1.3.1 Voltage-to-Angle Relationship

Sensor#3 is designed with two rotational axes, i.e. defined as the x-axis and the y-axis in this investigation. The performance about these two axes was investigated separately using the motorised system which performs movements in a single plane. For the rotations about the x-axis, data from CH<sub>31</sub> and CH<sub>33</sub> were acquired simultaneously. This operation was repeated for CH<sub>32</sub> and CH<sub>34</sub> when sensor#3 was rotated about the y-axis. The measurements about each rotational axis were carried out in clockwise and anticlockwise directions and repeated five times.

The voltage-to-angle relationship for CH<sub>31</sub> and CH<sub>33</sub> was averaged over five cycles and is plotted in Figure 5.12. Similarly, the sensing performance about the y-axis for CH<sub>32</sub> and CH<sub>34</sub>, is presented in Figure 5.13.

In theory, the output voltages of the four sensing channels of sensor#3 should follow the regression model described in equation (4.4), in which the subscript  $i$  equals 3 and the channel number  $j$  being 1, 2, 3, or 4. According to the data set presented in Figure 5.12 and Figure 5.13, the estimated regression functions for the four channels CH<sub>3 $j$</sub>  is given by equation (5.4).

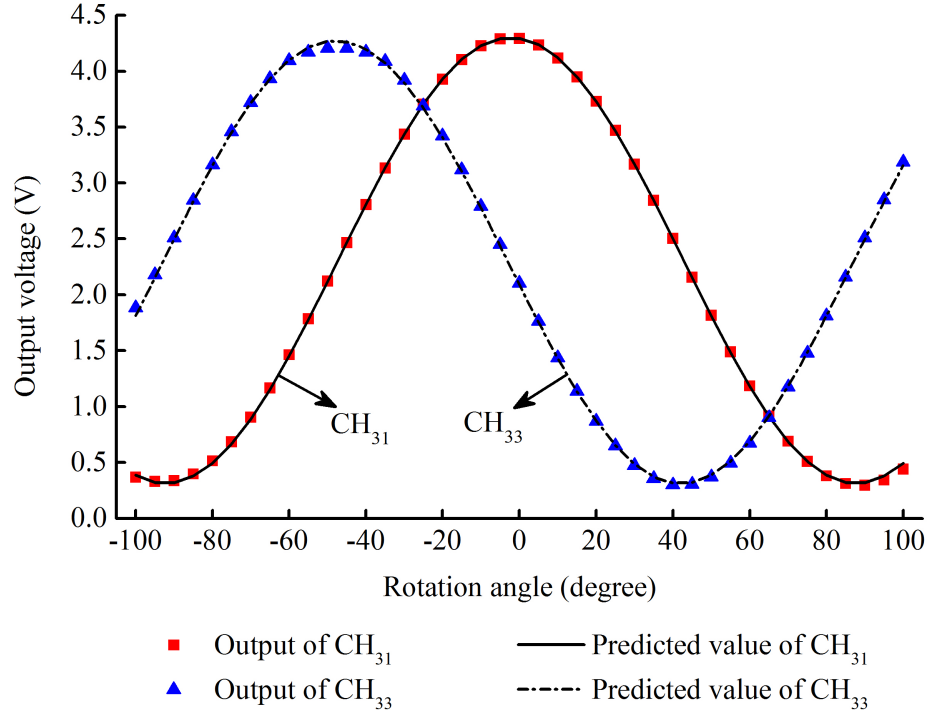


**Figure 5.12** The voltage-to-angle relationship of CH<sub>31</sub> and CH<sub>33</sub> of sensor#3 for the rotations about the x-axis in the range of -100° to 100°.

$$\begin{aligned}
 V_{out\_31} &= 3.985 \cos^2(\delta_{31}) + 0.316 = 3.985 \cos^2(\delta_x + 2.3) + 0.316 \\
 V_{out\_33} &= 3.958 \cos^2(\delta_{33}) + 0.314 = 3.958 \cos^2(\delta_x + 48.0) + 0.314 \\
 V_{out\_32} &= 3.895 \cos^2(\delta_{32}) + 0.291 = 3.895 \cos^2(\delta_y + 0.2) + 0.291 \\
 V_{out\_34} &= 3.878 \cos^2(\delta_{34}) + 0.274 = 3.878 \cos^2(\delta_y + 45.3) + 0.274
 \end{aligned}
 \tag{5.4}$$

where the variable  $\delta_{3j}$  ( $j=1, 2, 3,$  and  $4$ ) denote the relative rotation angle between the polariser and the analyser in CH<sub>3j</sub>. The variables  $\delta_x$  and  $\delta_y$  denote the angular position of the motorised stage, i.e. the rotation in degrees of sensor#3 about the x-axis and the y-axis, respectively.

As shown in equation (5.4), the phase difference between the outputs of CH<sub>31</sub> and CH<sub>33</sub> is 45.7° (48.0 minus 2.3), and the phase of the outputs of CH<sub>32</sub> shifts from that of CH<sub>34</sub> by 45.1° (45.3 minus 0.2). These differences are in accordance with the original design intention. The other coefficients of the four regression functions are close to each other, which implies similar performance of the four channels. The slight difference may

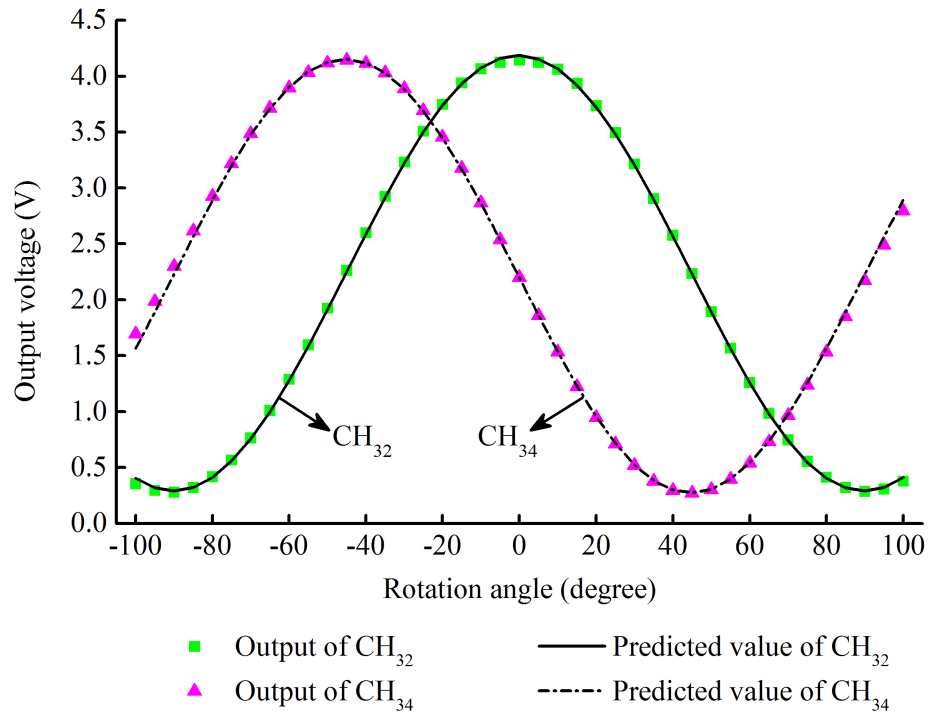


**Figure 5.13** The voltage-to-angle relationship of CH<sub>32</sub> and CH<sub>34</sub> of sensor#3 for the rotations about the y-axis in the range of  $-100^\circ$  to  $100^\circ$ .

be caused by inconsistencies in the conditioning circuits and the fabrication, the latter being hand built.

Using equation (5.4), the theoretical outputs of the four sensing channels of sensor#3 were calculated. The predicted output curves for CH<sub>31</sub> and CH<sub>33</sub> are plotted in Figure 5.12 and the ones for CH<sub>32</sub> and CH<sub>34</sub> are displayed in Figure 5.13. The output voltages measured in the four channels of sensor#3 are consistent with the predicted values at each angular position. The average deviations from the predicted values are  $\pm 1.6\%$  in CH<sub>31</sub>,  $\pm 1.2\%$  in CH<sub>33</sub>,  $\pm 1.5\%$  in CH<sub>32</sub>, and  $\pm 1.3\%$  in CH<sub>34</sub>. They are all smaller than the average deviations of sensor#1 ( $\pm 2.3\%$ ) and sensor#2 ( $\pm 3.9\%$  for CH<sub>21</sub> and  $\pm 3.7\%$  for CH<sub>22</sub>). This can be related to the more integrated 3D design of sensor#3, i.e. the holders for the electronic and optical components directly located inside the sensor wings. Unlike sensor#2, each sensing channel of sensor#3 is designed with one physical channel without sharing any source. This configuration may be also a factor.

In addition, the four sensing channels all produce a voltage offset of about 0.30 V, which is similar to that of sensor#2 (0.33 V, see Figure 5.6), but much greater than the value of sensor#1 (0.05 V, see Figure 5.1). According to the analysis in 5.1.1.1, the unwanted internal reflections of the visible light emitted by the LED should be the main reason for the measured offset voltages.

For all three electro-optical sensors, identical LEDs were used and driven under the same current, thus it can be assumed that the same unpolarised light intensity was emitted by the light source into each sensing channel. According to the inverse-square law, i.e. the intensity is inversely proportional to the square of the distance from the light source, the offset voltage caused by the unwanted internal reflections of the visible light can be mathematically formulated using the following equation:

$$V \propto ki \propto kI \propto \frac{k}{r^2} \quad (5.5)$$

where the parameter  $i$  represents the output current generated by the photodiode, and  $k$  is the amplification factor determined by the conditioning circuit. The parameter  $I$  denotes the intensity of the unpolarised light received by the photodiode, and  $r$  is the distance between the LED and the photodiode.

According to the conditioning circuitry and the 3D technical design, the parameters  $k$  and  $r$  for each optical sensor is listed in Table 5.1. The value of the parameter  $k$  represented the total amplification factor in the conditioning circuit.

**Table 5.1** The amplification factor  $k$  and the distance  $r$  between the LED and the photodiode for the three electro-optical goniometric sensors.

Parameters	sensor#1	sensor#2	sensor#3
amplification factor $k$	$1.23 \times 10^8$	$2.28 \times 10^7$	$2.11 \times 10^7$
distance $r$ (mm)	6.50	1.15	1.20

By substituting the parameters listed in Table 5.1 into equation (5.5), the calculation shows that the voltage caused by the unwanted internal reflection in sensor#3 should be 0.8 times that of sensor#2 and also 5.0 times the amount in sensor#1. In fact, the measured offset voltage in sensor#3 (0.30 V) is 0.9 times as great as that in sensor#2 (0.33 V, see Figure 5.6), and about 5.8 times the amount in sensor#1 (0.05 V, see Figure 5.1). The calculated results closely match the ratio of the offset voltages measured in the three sensors. This further verifies that the unwanted internal reflection of the visible light is the main reason for the measured offset voltage.

### 5.1.3.2 Hysteresis Analysis

Figure 5.14 and Figure 5.15 show the bidirectional performance of sensor#3 to the rotations about the x-axis and the y-axis, respectively. As can be seen, there was no obvious hysteresis behaviour in the output curves of all four channels.

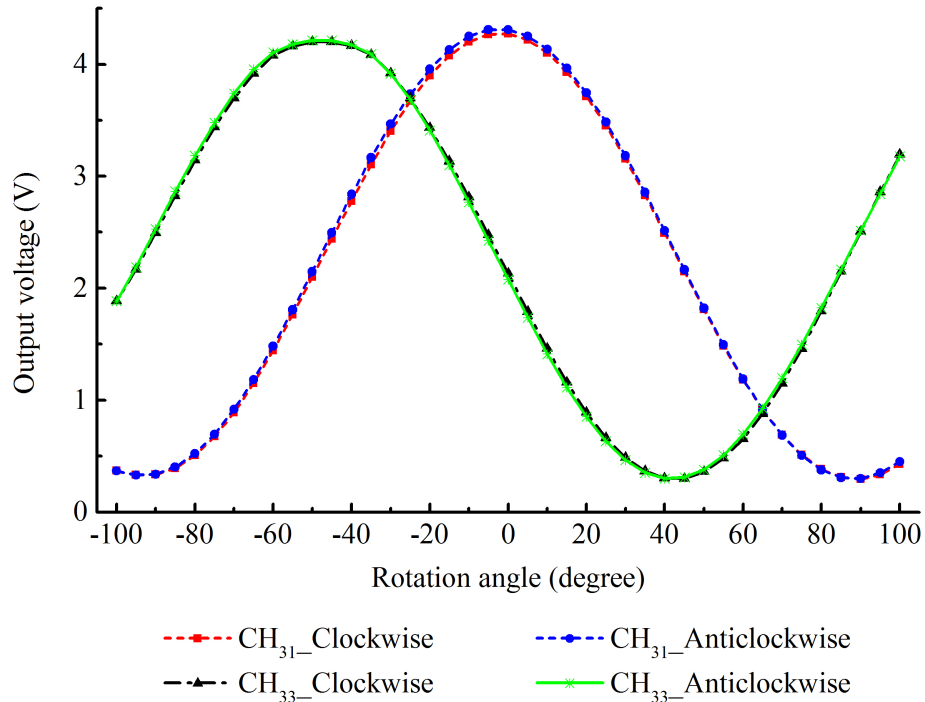


**Figure 5.14** The outputs of sensor#3 for the clockwise and the anticlockwise rotations about the x-axis. CH<sub>31</sub>\_Clockwise and CH<sub>31</sub>\_Anticlockwise represent the outputs of CH<sub>31</sub> when sensor#3 rotates from -100° to 100°, and then back to -100°. Similarly, CH<sub>33</sub>\_Clockwise and CH<sub>33</sub>\_Anticlockwise represent the corresponding readings of CH<sub>33</sub>.

Equation (5.2) was used to quantify the hysteresis error of sensor#3. For bidirectional rotations about the x-axis, CH<sub>31</sub> demonstrates 1.6% hysteresis and CH<sub>33</sub> shows 1.4% hysteresis. For clockwise and anticlockwise rotations about the y-axis, the hysteresis errors are 1.9% in CH<sub>32</sub> and 1.7% in CH<sub>34</sub>. Clearly, all four sensing channels of sensor#3 exhibit similar hysteresis effects which are comparable to sensor#2 (1.8% for CH<sub>21</sub> and 1.5% for CH<sub>22</sub>) but greater than sensor#1 (1.1%). This can be explained by the more complicated 3D design of sensor#2 and sensor#3 compared with sensor#1.

### 5.1.3.3 Repeatability Analysis

As stated in 5.1.3.1, the measurements were repeated five times for the rotations about the x-axis and also the y-axis. The outputs measured in each channel of sensor#3 are shown in Figure 5.16.

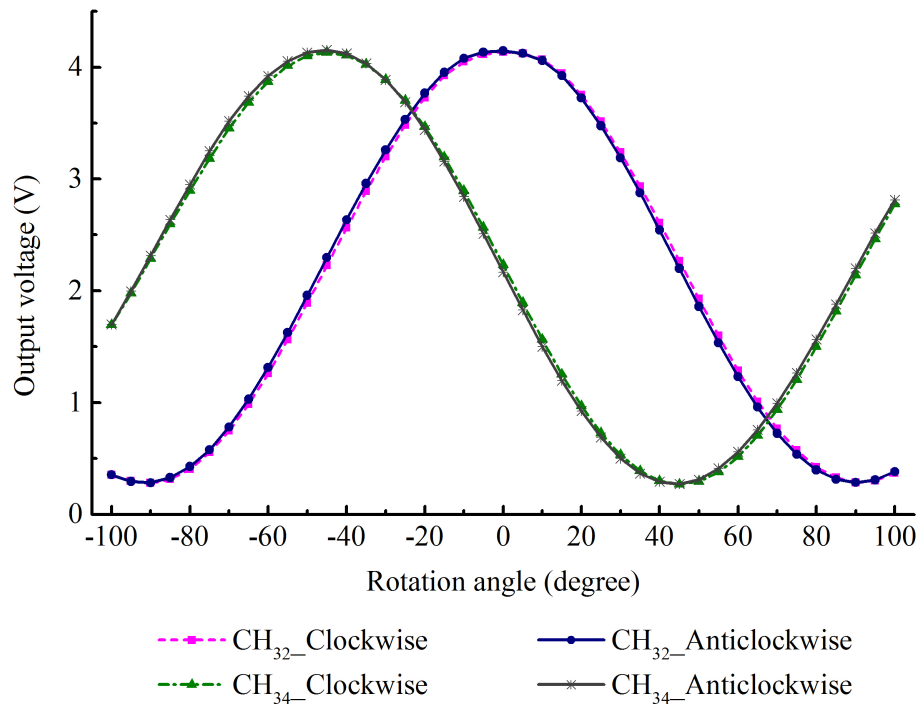


**Figure 5.15** The outputs of sensor#3 for the clockwise and the anticlockwise rotations about the y-axis. CH<sub>32</sub>\_Clockwise and CH<sub>32</sub>\_Anticlockwise represent the outputs of CH<sub>32</sub> when sensor#3 rotates from -100° to 100°, and then back to -100°. Similarly, CH<sub>34</sub>\_Clockwise and CH<sub>34</sub>\_Anticlockwise represent the corresponding readings of CH<sub>34</sub>.

Generally, at each angular position, the four sensing channels all demonstrate small variations in the output voltages during the repeated tests. The readings at 35° are taken as examples and shown in the insets in Figure 5.16. As displayed in Figure 5.16(a) and (b), when the measurement system was rotated to 35° about the x-axis, the readings of CH<sub>31</sub> vary no more than 0.040 V, and the variations in the outputs of CH<sub>33</sub> are less than 0.004 V during the five measurements. Similarly, for the rotation about the y-axis the maximum changes in the outputs of CH<sub>32</sub> and CH<sub>34</sub> are 0.040 V and 0.004 V respectively (see insets in Figure 5.16(c) and (d)). These variations are all relatively small with respect to the overall signal values.

Overall, for the investigated angle range, the RSD values are no more than 0.8% for CH<sub>31</sub>, 0.6% for CH<sub>33</sub>, 1.1% for CH<sub>32</sub>, and 0.6% for CH<sub>34</sub>. The averaged RSD is as small as 0.4% for CH<sub>31</sub>, 0.2% for CH<sub>33</sub>, 0.6% for CH<sub>32</sub>, and 0.4% for CH<sub>34</sub>.

As for sensor#1 and sensor#2, the SR and SD were also used to evaluate the repeatability of sensor#3. According to the derivation method presented in Table 4.1, the measured outputs were converted to rotation angles. By applying the data fusion approach, the signal obtained in CH<sub>31</sub> and CH<sub>33</sub> were combined to determine the angle about the x-axis, and the combination of CH<sub>32</sub> and CH<sub>34</sub> for evaluating the angle about the y-axis. Since the x-axis and the y-axis of sensor#3 are designed to monitor the flexion/extension

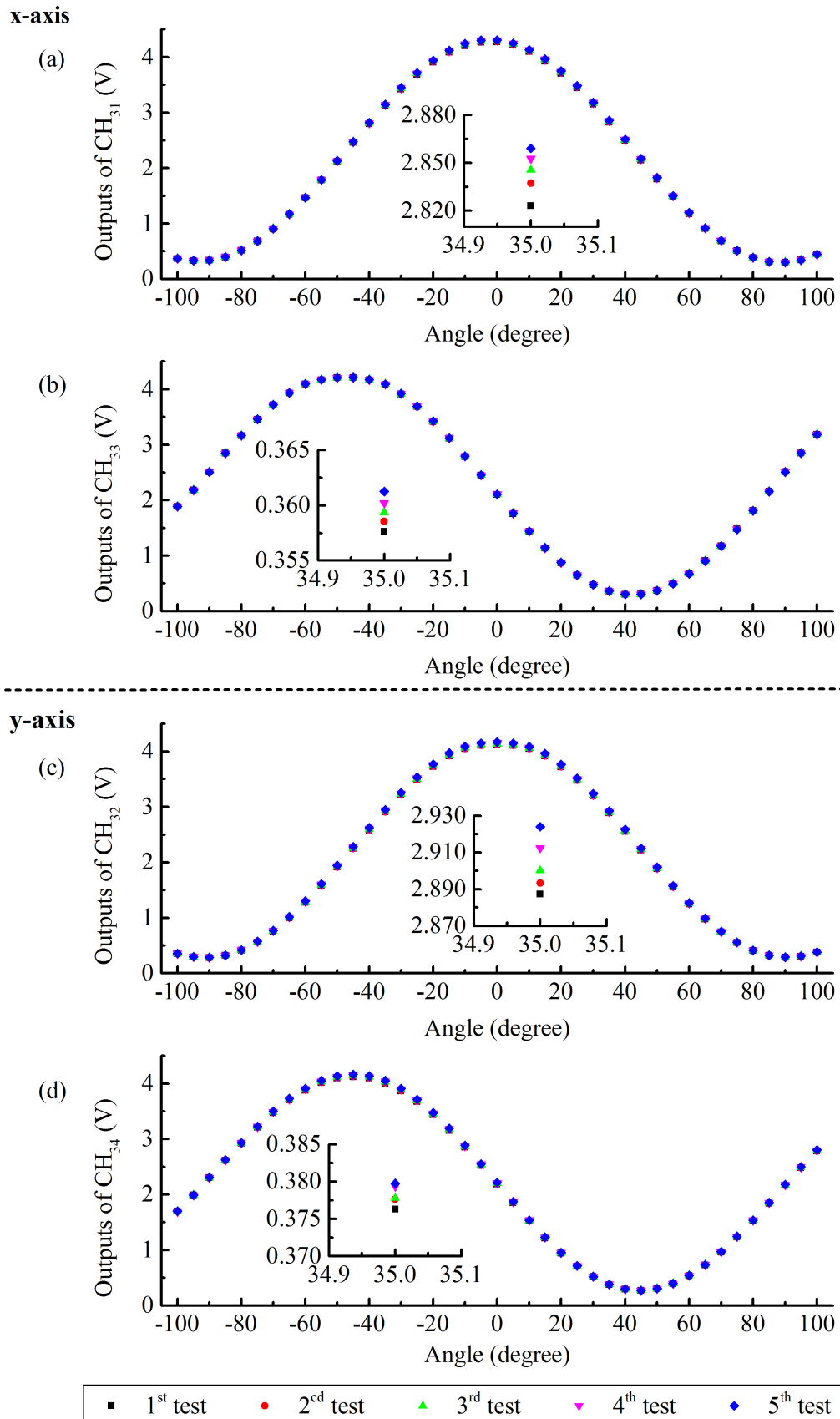


**Figure 5.16** The measured results of sensor#3 during the five repeated tests. (a) Outputs of  $\text{CH}_{31}$ ; (b) outputs of  $\text{CH}_{33}$ ; (c) outputs of  $\text{CH}_{32}$ ; (d) outputs of  $\text{CH}_{34}$ . For each channel, the reading at  $35^\circ$  are enlarged as an example.

and ABD/ADD of MCP joints, respectively, the measured voltages are converted to appropriate ranges. For x-axis rotations, a range of  $-80^{\circ}$  to  $100^{\circ}$  is used and for the y-axis,  $-90^{\circ}$  to  $90^{\circ}$ . The results are presented in Figure 5.17 and Figure 5.18.

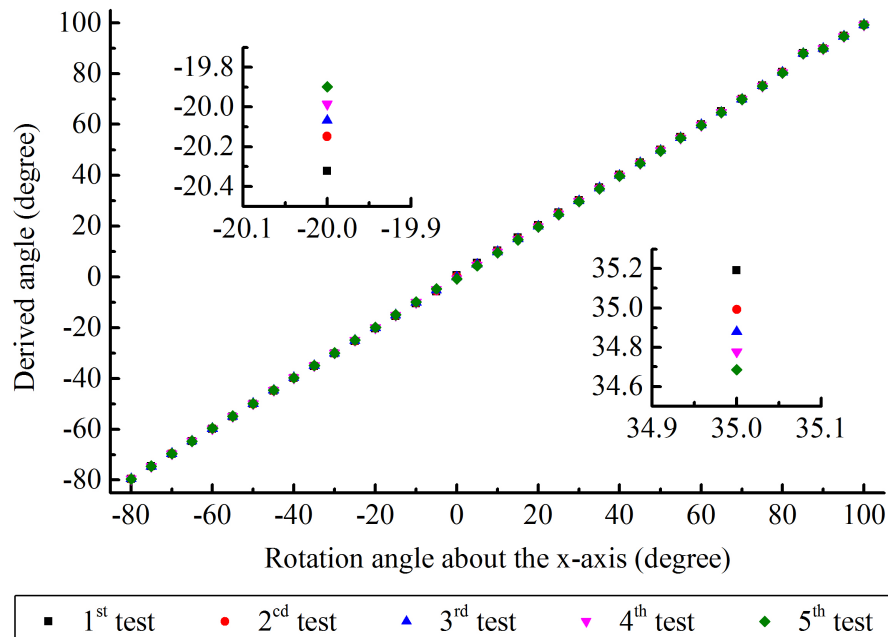


**Figure 5.17** The rotation angles derived from the outputs of CH<sub>31</sub> and CH<sub>33</sub> of sensor#3 for the five repeated tests about the x-axis in the range of  $-80^{\circ}$  to  $100^{\circ}$ . The readings at  $-20^{\circ}$  and  $35^{\circ}$  are enlarged as examples.

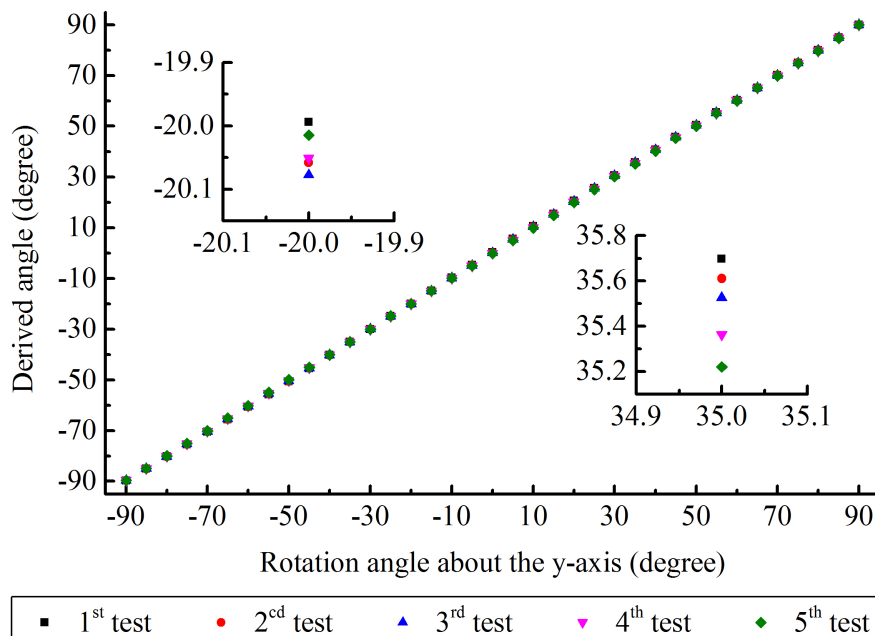


**Figure 5.18** The rotation angles derived from the outputs of CH<sub>32</sub> and CH<sub>34</sub> of sensor#3 for the five repeated tests about the y-axis in the range of  $-90^{\circ}$  to  $90^{\circ}$ . The readings at  $-20^{\circ}$  and  $35^{\circ}$  are enlarged as examples.

The insets in Figure 5.17 indicates that the variations in the derived angles from the x-axis are less than  $0.6^{\circ}$  at the angular positions of  $-20^{\circ}$  and  $35^{\circ}$ . For the rotations about

the y-axis, sensor#3 shows changes in the angular readings less than  $0.2^\circ$  at  $-20^\circ$  and  $0.6^\circ$  at  $35^\circ$ .

For each test angle, the difference between the highest and lowest derived angles (i.e. SR) over the five measurement cycles was computed for rotations about the two axes. Among them, the maximum SR is  $1.36^\circ$  for rotations about the x-axis and  $0.79^\circ$  for the y-axis. About the x-axis, the SR and SD average  $0.39^\circ$  and  $0.15^\circ$  respectively; for rotations about the y-axis, the mean SR and SD are  $0.34^\circ$  and  $0.14^\circ$  respectively. Therefore, sensor#3 demonstrates similar repeatability to rotations about the x-axis and y-axis.

#### 5.1.3.4 Random Angle Testing to Investigate the Performance of the Two-axis Sensor after Data Fusion Process

The random rotation test was made on sensor#3 in order to investigate the sensor performance after applying the data fusion method. Using MATLAB functions, one hundred uniformly distributed pseudorandom numbers were generated to simulate finger motion. The angular data in the range of  $-80^\circ$  to  $100^\circ$  was used to simulate the motion of a MCP finger joint in flexion/hyperextension, and the range was changed to  $-90^\circ$  to  $90^\circ$  for the simulation of ABD/ADD movements. During the measurements, sensor#3 rotated from one angular position to the next, with 500 samples recorded at each angle. The angular readings obtained by CH<sub>31</sub> and CH<sub>33</sub> were fused for x-axis rotations and similarly the outputs of CH<sub>32</sub> and CH<sub>34</sub> fused for y-axis monitoring. The measurement errors with respect to the defined rotation angles are shown in Figure 5.19.

Figure 5.19 shows that the tracked angles using sensor#3 exhibit lower error differences for the weighted average method. For individual channels, larger sensing errors occur at the angular positions with small sensitivity, i.e. when the channel outputs are close to the minimum or maximum value. For instance, in comparison with the other measurement positions, CH<sub>31</sub> generates much greater differences (up to  $3.28^\circ$ ) at the angles ranging from  $-10^\circ$  to  $10^\circ$  and  $80^\circ$  to  $100^\circ$ . At these angular positions, CH<sub>31</sub> produces output voltages close to the maximum or minimum value, which can be seen in Figure 5.12.

For the rotations about the x-axis, CH<sub>31</sub> and CH<sub>33</sub> demonstrate a MAE of  $0.77^\circ$  and  $0.58^\circ$ , respectively, whilst the fused results present a much smaller MAE of  $0.25^\circ$ . When sensor#3 measured the rotations about the y-axis, the computed MAE is  $0.33^\circ$  in CH<sub>32</sub> and  $0.44^\circ$  in CH<sub>34</sub>, and decreases down to  $0.19^\circ$  after the data fusion processing. Therefore, the weighted average method greatly enhances the measurement results, and the overall MAE of sensor#3 is no more than  $0.25^\circ$ .

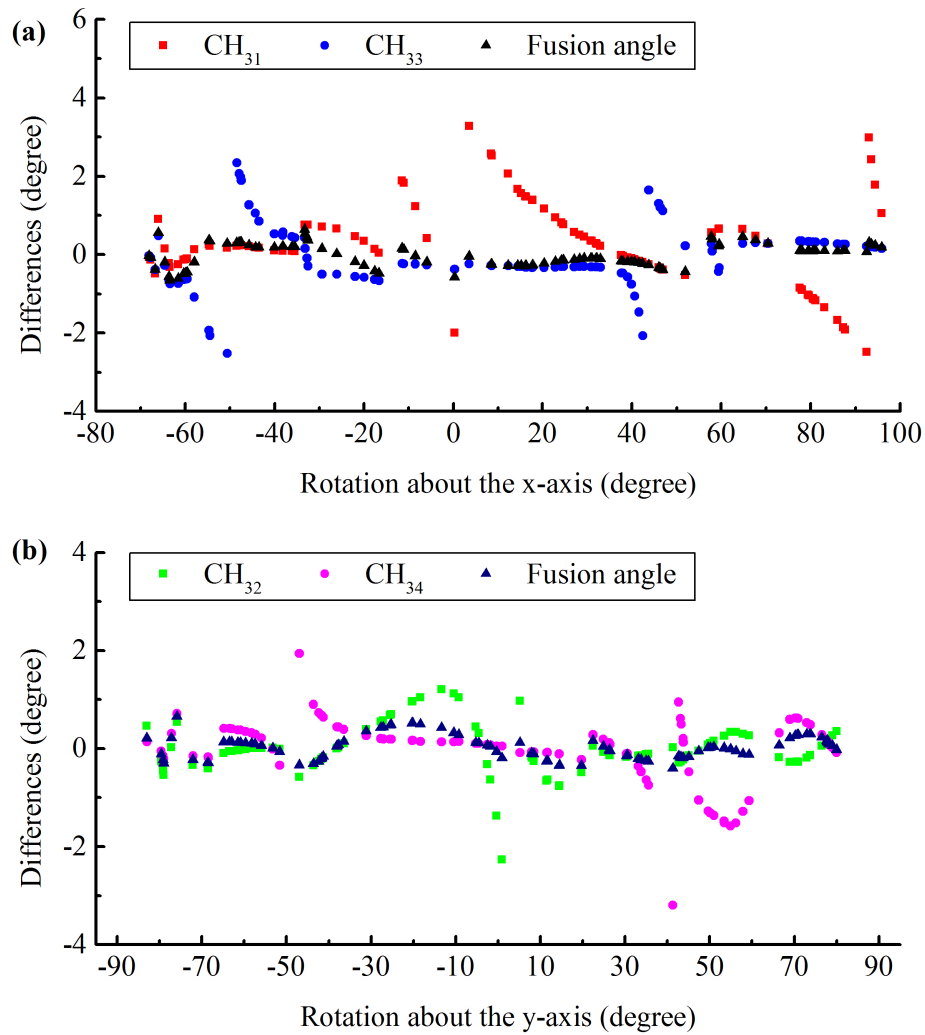


**Figure 5.19** The differences between the measured angular outputs of sensor#3 and the predefined pseudorandom testing angles spanning 180°. **(a)** The results for the rotations about the x-axis; **(b)** the results for the rotations about the y-axis.

### 5.1.4 Performance of the Commonly Used Commercial Resistive Bend Sensor

The 50.8-mm commercial bend sensor from Flexpoint SS was evaluated as a reference point for the developed electro-optical sensors. The investigations include the sensor linearity, hysteresis errors, repeatability, and stability.

#### 5.1.4.1 Linearity of the Bend Sensor

Following the same measurement procedure as sensor#1, the commercial bend sensor was evaluated from -20° to 100°, and then back to -20° with increments of 5°. For each

angle setting, up to 500 data points were acquired. This process was repeated five times under the same conditions.

The voltage-to-angle relationship of the bend sensor is plotted in Figure 5.20. The bend sensor showed unidirectional behaviour, i.e. only able to respond to positive bending angles. The subsequent regression analysis was only conducted on samples obtained at angles ranging from  $0^\circ$  to  $100^\circ$ . As shown in equation (5.6), for flexion below  $20^\circ$  a linear function is used to express the relationship between the output voltage and the bending angle. A second-degree polynomial function is adopted for the flexion no less than  $20^\circ$ . This equation possesses high adjusted R-squared value (0.9989) and small residual sum of squares (0.0252), indicating a good model fit.

$$V_b = \begin{cases} 0.00061\delta + 0.7984, & 0 \leq x < 20 \\ 0.00049\delta^2 - 0.0127\delta + 0.8477, & x \geq 20 \end{cases} \quad (5.6)$$

where the variable  $\delta$  denotes the bending angle in degrees, and  $V_b$  denotes the output voltage of the commercial bend sensor.

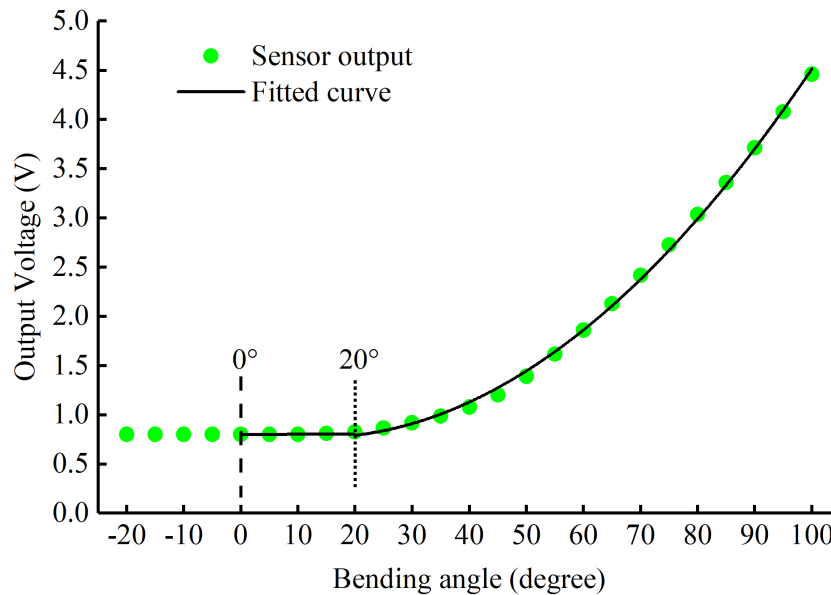


**Figure 5.20** The voltage-to-angle relationship of the commercial bend sensor in the flexion range of  $-20^\circ$  to  $100^\circ$ .

Although an obvious increase in the sensor output could be observed with increasing bending angle ( $>30^\circ$ ), the bend sensor demonstrates insensitivity to small flexion angles under  $20^\circ$ . This observation is consistent with results reported in the literature [111, 117, 121, 267, 268]. To enhance the sensor linearity, several solutions were reported by other research groups including the use of modulation circuits [116, 269] and the optimisation of the sensing geometry by cutting some parts of the conductive

coating [267, 270]. These approaches failed to improve sensor linearity. In this work the bend sensor was unmodified during the measurements.

The insensitivity of the bend sensor to small flexions and its unidirectional nature is likely to limit the monitoring of finger movements, e.g. the finger hyperextension and small flexion.

#### 5.1.4.2 Hysteresis Error

The measurements for the commercial bend sensor were carried out in clockwise and anticlockwise directions. The sensor responses to the bidirectional motion are displayed in Figure 5.21.

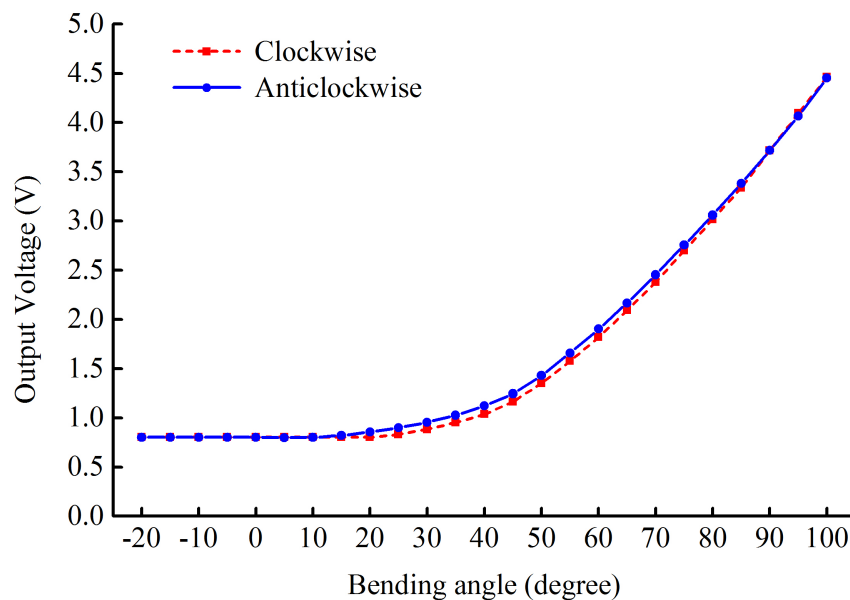


**Figure 5.21** The outputs of the commercial bend sensor during clockwise and anticlockwise flexion ranging from  $-20^\circ$  to  $100^\circ$ .

It can be found that this bend sensor demonstrates obvious hysteresis errors during the clockwise-anticlockwise movements, especially at angles ranging from  $15^\circ$  to  $85^\circ$ . Using equation (5.2), the hysteresis error of this bend sensor is quantified as 2.3%. In the literature [111], Borghetti et al. reported much greater hysteresis (about 12.5%) for a bare bend sensor from Flexpoint SS; the sensor had a length of 101.6 mm, twice the length of the bend sensor tested in this work. These results can be explained by the viscoelastic effects of the polymeric matrix.

### 5.1.4.3 Repeatability

Figure 5.22 shows the output of the bend sensor measured over five tests. As can be observed, at each angular position the bend sensor produces similar readings during the repeated measurements. For instance, the variations in the sensor outputs are less than 3 mV at 30° and 40 mV at 85° (see insets in Figure 5.22). Over the five measurements, the bend sensor demonstrates RSD less than 0.5%, with an average of 0.2% for flexions in the range -20° to 100°.

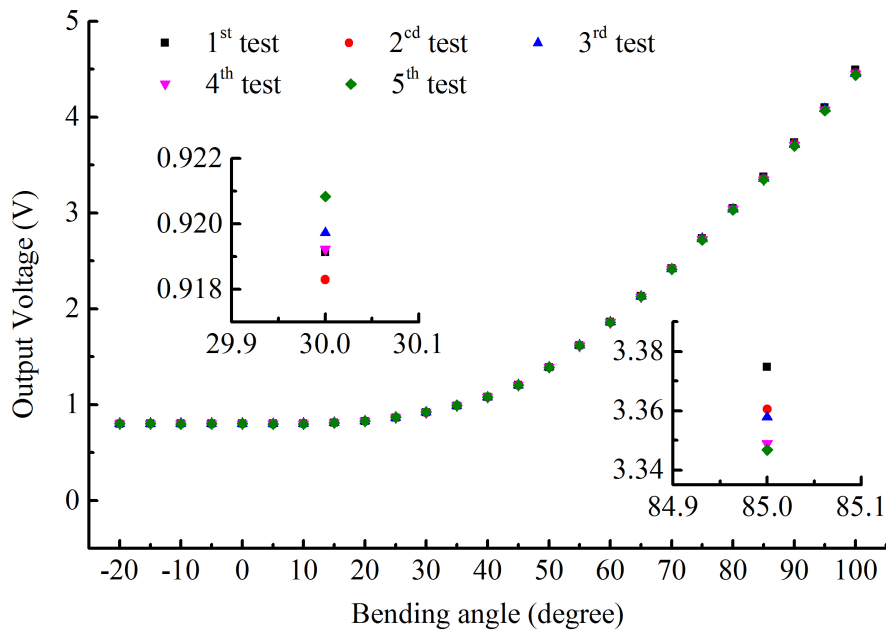


**Figure 5.22** The output readings of the commercial bend sensor for the five repeated measurements in the range of -20° to 100°.

Using the trendline function shown in equation (5.6), the flexion angles of the bend sensor were derived from the measured voltages. Due to the unidirectional property, here only the outputs measured at positive angles were processed and converted. The derived flexion angles are displayed in Figure 5.23.

As shown in Figure 5.23, the angles derived from the output voltages of the bend sensor differed slightly from each other at the same testing position. The insets show that the variations are much smaller (less than 0.2° at 30° and 0.6° at 85°) compared to the amount of sensor flexion. In the flexion range of interest, the bend sensor demonstrates SR no more than 0.66°, with an average of 0.23°. During the five tests, the mean SD is only 0.09°. Overall, this commercial bend sensor demonstrates a high repeatability under identical testing conditions.

However, the measurement accuracy is greatly dependent on the flexion state. A straight line representing the ideal outputs, i.e. the values identical to the input flexion angles, is

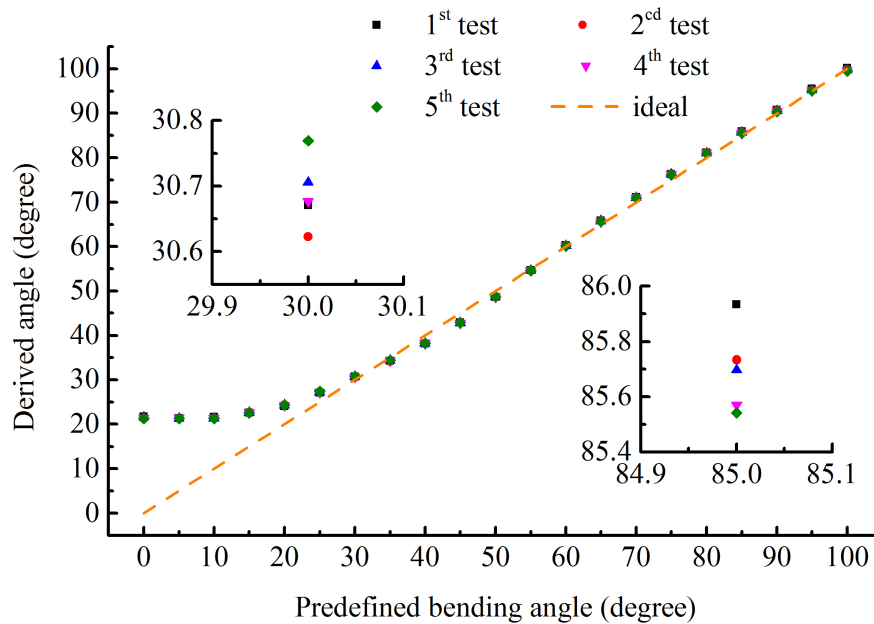


**Figure 5.23** The flexion angles derived from the outputs of the commercial bend sensor for the five repeated tests in the range of  $0^\circ$  to  $100^\circ$ . The orange dashed line represents the ideal sensor outputs, i.e. the derived sensor angles equal to the predefined flexion.

plotted in Figure 5.23 (see the orange dashed line). Clearly, the measured angle deviates from the ideal output at bending angles less than  $20^\circ$  making the bend sensor unsuitable for measuring small flexions. For the movements ranging from  $25^\circ$  to  $100^\circ$ , the bend sensor demonstrates a MAE of  $0.94^\circ$  with respect to the rotation angle of the motorised stage; all errors fall within  $\pm 2.21^\circ$ .

#### 5.1.4.4 Temporal Stability Evaluation

As with the investigation for sensor#1, the bend sensor was made to monitor static angles, set by the motorised stage, equal to  $30^\circ$ ,  $45^\circ$ ,  $60^\circ$ , and  $90^\circ$ , successively. When the system rotated to each specific position, the bend sensor was static for up to 180 minutes during which the sensor data was continuously acquired at a rate of 100 Hz.

The outputs of the bend sensor at the flexion angles of  $30^\circ$ ,  $45^\circ$ ,  $60^\circ$ , and  $90^\circ$  are presented in Figure 5.24. The overall variation at each flexion is indicated on the right-hand side of the figure.

The bend sensor shows an increase in signal drift with increased flexion angles, i.e. 19.4 mV to 176.0 mV with the flexion increasing from  $30^\circ$  to  $90^\circ$ . In all cases, the drift is negative resulting in a reduced signal amplitude. The rate of decrease is greatest over the first 30 min and then slows down. According to the voltage-to-angle relationship

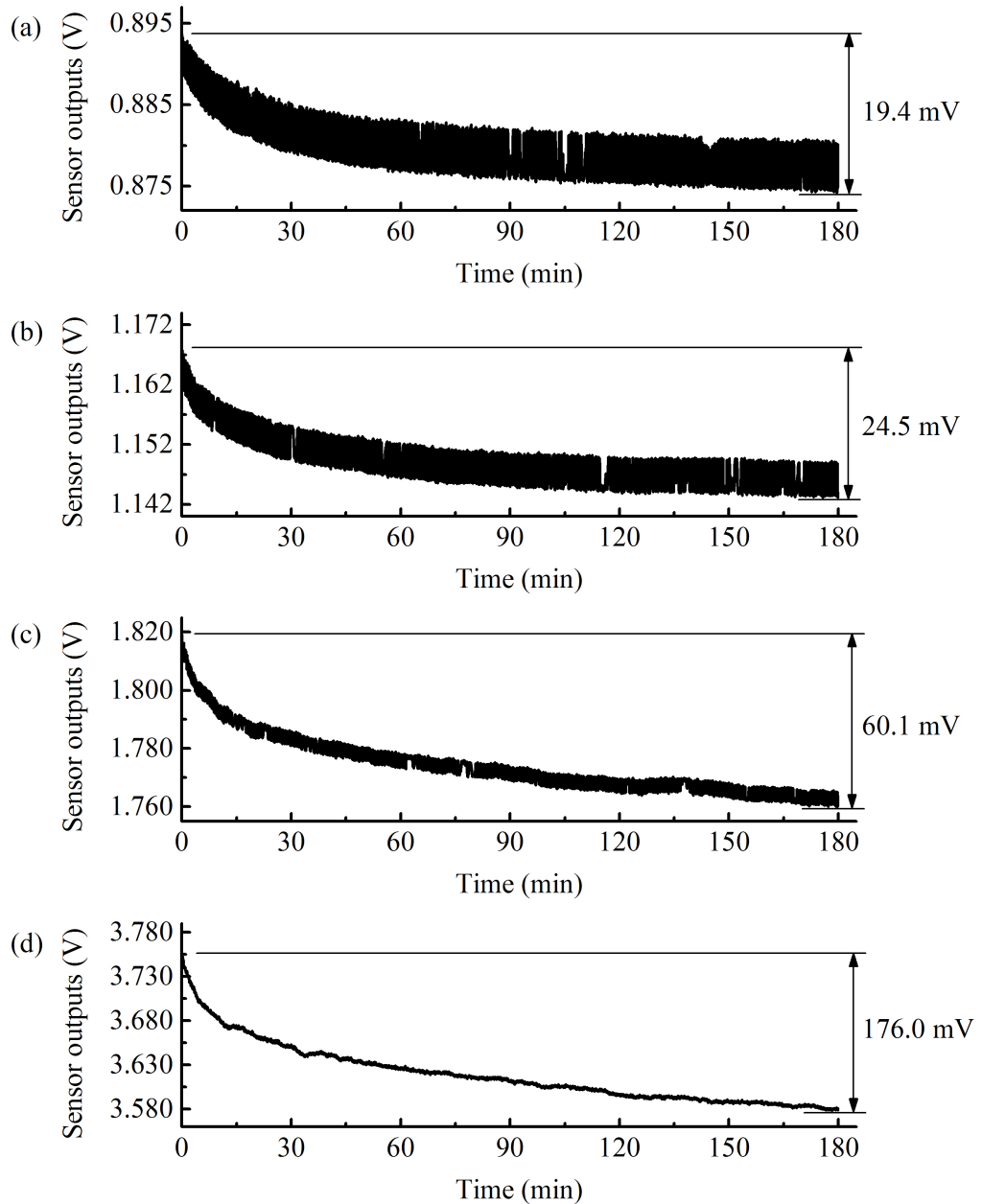


**Figure 5.24** The outputs of the commercial bend sensor at different bending angles over 180 minutes. **(a)** is the sensor outputs with the flexion angle of  $30^\circ$ ; **(b)** for  $45^\circ$ ; **(c)** for  $60^\circ$ ; and **(d)** for  $90^\circ$ .

shown in equation (5.6), the signal drift of the bend sensor was converted into angular variation. The drift at  $30^\circ$ ,  $45^\circ$ ,  $60^\circ$ , and  $90^\circ$  corresponds to a flexion change of  $1.20^\circ$ ,  $0.79^\circ$ ,  $1.32^\circ$ , and  $2.37^\circ$  respectively. They are much larger than the angular variation of sensor#1 ( $0.05^\circ$  at  $30^\circ$ ,  $45^\circ$ ,  $60^\circ$ , and  $1.33^\circ$  at  $90^\circ$ ).

As shown in equation (5.7), the drift ratio, i.e. the relative change in output, was computed to quantitatively assess the sensor stability.

$$DR(\phi) = \frac{V_t(\phi) - V_{ini}(\phi)}{V_{ini}(\phi)} \times 100\% \quad (5.7)$$

where  $DR(\phi)$  denotes the drift ratio at the angle  $\phi$ . For a given angle  $\phi$ , the parameters  $V_{ini}(\phi)$  and  $V_t(\phi)$  represent the initial voltage output and the output at time  $t$ , respectively.

The drift ratio was calculated for the bend sensor at flexion positions of  $30^\circ$ ,  $45^\circ$ ,  $60^\circ$ , and  $90^\circ$ . The same operations were also performed on sensor#1 for comparison. The raw data was averaged per minute, i.e. every 6000 data points, to smooth the curves. The computed results are displayed in Figure 5.25. At each bending state, the values of the percentage drift after 10 min, 30 min, 60 min, 120 min, and 180 min (T1-T5) are also superimposed on the drift curve in Figure 5.25.

Results in Figure 5.25 show that sensor#1 demonstrates significantly less drift compared to the bend sensor over the maximum measurement period of 180 minutes. In the case of the commercial bend sensor, there is a clear increase in signal drift with increased flexion, i.e. 1.5% to 4.4% with bending from  $30^\circ$  to  $90^\circ$ . In contrast, the drift values of sensor#1 are much smaller; the absolute values are close to zero irrespective of the bending angle. The large drift ratio of sensor#1 at  $90^\circ$  is a consequence of the low output signal amplitude (about 0.05 V). Small fluctuations including the electronic noise in output voltages lead to large drift ratio values. The increased drift in the bend sensor is, however, indicative of some form of structural relaxation and increases significantly at larger bend angles.

### 5.1.5 Comparison of Sensor Static Characteristics

Table 5.2 summarises the static characteristics of the three electro-optical sensors together with the commercial bend sensor. The performance data of wearable sensors reported by other research groups is also included.

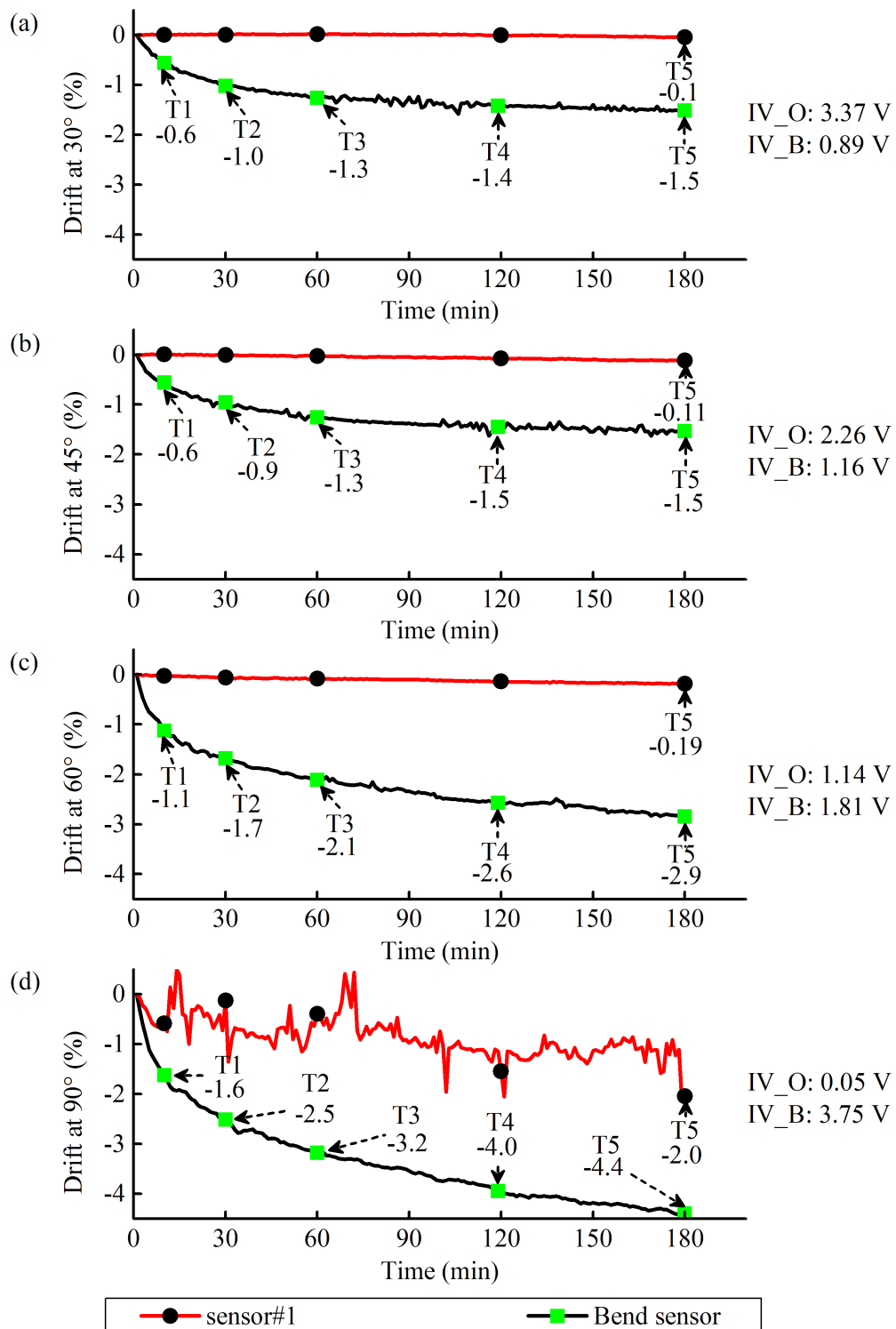


**Figure 5.25** Drift ratios of the commercial bend sensor and the developed optical sensor (sensor#1) at different bending angles over 180 minutes: (a) is the result with the flexion angle of 30°; (b) for 45°; (c) for 60°; (d) for 90°. IV\_O represents the initial voltage reading of sensor#1 at the corresponding angular position, and IV\_B is for the commercial bend sensor.

**Table 5.2** Comparison of the sensor static characteristics.

Sensors	Linearity	Sensitivity	Hysteresis	Repeatability		Stability	MAE	Depend on joint size	Measuring ability	
				Mean SR	Mean SD					
Electro-optical sensors	sensor#1	nonlinear $\propto \cos^2 \theta$	71.0 mV/° (linear part)	1.1%	0.03°	0.01°	stable	0.28°	no	90° single axis
	sensor#2	near linear	60.7 mV/°	1.8%	0.24°	0.10°	stable	0.13° (Fusion)	no	180° single axis
	x-axis	near linear	63.0 mV/°	1.6%	0.39°	0.15°	stable	0.25° (Fusion)	no	180° two axes
	sensor#3 y-axis	near linear	62.0 mV/°	1.9%	0.34°	0.14°	stable	0.19° (Fusion)	no	
Bend sensor from Flexpoint SS (tested in this thesis)	piecewise linear	10.7 mV/° (20°-40°) 57.3 mV/° (>40°)	2.3%	0.23°	0.09°	severe drift	0.94° (25°-100°)	yes	above 20° single axis	
Commercial bend sensor from Spectra Symbol [111]	almost linear	56 $\Omega$ /°	14.0%	\	\	25% at 90° after 3 min	\	yes	single axis	

Continued on next page

Table 5.2 – continued from previous page

Sensors	Linearity	Sensitivity	Hysteresis	Repeatability		Stability	MAE	Depend on joint size	Measuring ability
				Mean SR	Mean SD				
Ink-based resistive strain sensor [65]	nonlinear	GF: $3.8 \pm 0.6$ (loading portion)	>10.0%	\	\	severe drift	\	yes	~400% strain single axis
Carbon nanotubes based strain sensor [51]	nonlinear	GF: 0.82 (strain<40%) GF: 0.06 (strain>60%)	\	\	\	3.0% (creep up)	\	yes	~280% strain single axis
AgNP based stretchable strain sensor [58]	linear	GF: 2.05	1.5% (strain: 0-20%)	\	\	1.5% after 1h (strain: 10%)	\	yes	tension: 20% compression: ~3.6%
FBG sensor [134]	nonlinear	\	\	\	\	\	max: $2.00^\circ$ (0-90°)	yes	\
Single-mode optical fibre sensor [153]	nonlinear	\	\	\	\	\	$1.36^\circ$	yes	$90^\circ$
Embedded hetero-core fibre-optic sensor [145]	linear	\	\	\	$0.88^\circ$	\	\	yes	$97.2^\circ$

Continued on next page

Table 5.2 – continued from previous page

Sensors	Linearity	Sensitivity	Hysteresis	Repeatability		Stability	MAE	Depend on joint size	Measuring ability
				Mean SR	Mean SD				
Potentiometer [36]	linear	\	\	\	\	\	0.65°	yes	\
Fibre optic sensor (DataGlove)* [266]	\	\	\	5.60°	2.30°	\	\	\	\
Hall effect sensor (HumanGlove)* [8]	\	\	\	6.65°	2.14°	\	\	\	\
Optical linear encoder (SmartGlove)* [27]	linear	\	\	3.29°	3.06°	\	1° (encoder)	yes	\
Commerical bend sensor (WU Glove)* [116]	linear, after modification	\	\	4.96°	1.59°	-1.9±1.0% at 60° after 50 min	\	yes	\
Commerical bend sensor (Shadow Monitor)* [118]	nonlinear	variable	\	3.36°	1.05°	\	\	yes	\
Commerical bend sensor (HITEG-Glove)* [119]	nonlinear	variable	\	3.25°	1.07°	\	\	yes	\

*Note:* In the first column, the marker ‘\*’ indicates that the repeatability of the sensors/sensing gloves were obtained using real hands. ‘\’ means the literature did not report the corresponding performance index. The SR, i.e. Statistical Range, is the difference of the highest and the lowest measured angles at the same position, and the abbreviation SD represents the standard deviation of the outputs. The MAE is abbreviation of mean average error.

As shown in Table 5.2, sensor#1 is nonlinear, producing output voltages proportional to the cosine squared of the rotation angle. The outputs can be regarded as near linear when the rotation angle, i.e. the relative orientation of the polariser and the analyser, is in the range of  $20^\circ$  to  $70^\circ$ . In such linear regions, sensor#1 demonstrates a sensitivity of 71.0 mV/degree. According to the description in 4.2.3, after applying the data fusion method, sensor#2 and sensor#3 can be regarded as near linear sensors. Their sensitivity is approximated as 60.7 mV/ degree and 62.0 mV/ degree. The bend sensor tested in this thesis exhibits a comparable sensitivity (57.3 mV/degree) when the flexion angle is above  $40^\circ$ . The sensitivity of these sensors can be further increased by adjusting the amplification factor of the conditioning circuits. For other sensors reported in the literature, the majority also demonstrated nonlinear response to the change in rotation/flexion. In some cases, their sensitivities are expressed differently, e.g. as a GF, therefore a direct comparison cannot be made with the electro-optical goniometric sensors.

The commercial bend sensor tested in this work demonstrates much smaller hysteresis (2.3%) than the sensor manufactured by Spectra Symbol (14.0%) [111] and also the ink-based resistive strain sensor ( $>10.0\%$ ) [65]. However, this hysteresis error is still greater than that of the three electro-optical sensors ( $<1.9\%$ ).

SR and SD are used to assess the sensor repeatability. From Table 5.2, it can be observed that sensor#2, sensor#3, and the commercial bend sensor present comparable repeatability under identical conditions, with sensor#1 displaying the best results. This might be related to the simpler structural design of sensor#1. Sensor#2 and sensor#3 have more complicated design, increasing the level of difficulty in sensor fabrication, and thus leading to slightly reduced performance. Other sensors, including fibre optic-based sensors, Hall Effect sensors, optical linear encoders, and commercial bend sensors, show much higher SR and SD. However, their repeatability was obtained under less controlled conditions, i.e. mounted on real hands via gloves or supports. This is likely to produce significantly worse repeatability compared to the ideal conditions used in our measurements. Despite this, the HITEG-Glove, Shadow Monitor, and WU glove, adopting bend sensors from Flexpoint SS, are more repeatable than the Hall Effect and fibre optic-based glove systems. Therefore, the optical sensors developed as part of this work, with repeatability comparable to the bend sensor from Flexpoint SS under ideal conditions, show great promise as sensory elements for future glove-based systems.

In terms of sensor stability, the electro-optical sensors outperform the commercial bend sensors [43, 111, 116] and the reported strain sensors [51, 58, 65]. As shown in Figure 5.5 and Figure 5.25, sensor#1 generally shows constant drift errors (2.4-3.8 mV) irrespective of the rotation angle. In contrast, the bend sensor manufactured by

Flexpoint SS exhibits increasing drift with the increased flexion angle (see Figure 5.24 and Figure 5.25). To enhance the sensor stability, Gentner et al. [116] glued a polyvinyl chloride foil over the sensitive material layer of the bend sensor from Flexpoint SS. Results showed the sensor outputs could creep up by about 1.9% after remaining at 60° flexion for 50 min, which is still significantly greater than the variation in the outputs of the electro-optical sensors, e.g. sensor#1 changed by only 0.1%. In addition, it was reported that the resistive bend sensor manufactured by Spectra Symbol showed incredible drift (25%) when kept at 90° after 3 min [111].

The three electro-optical sensors demonstrates similar mean absolute errors with respect to the angular positions of the motorised system. The errors ( $\leq 0.28^\circ$ ) are much smaller than the commercial bend sensor tested in this work ( $0.94^\circ$ ), the FBG sensor (max:  $2.00^\circ$ ) [134], the single-mode optic fibre-based sensor (root-mean-square error:  $1.36^\circ$ ) [153], the linear potentiometer ( $0.65^\circ$ ) [36], and optical encoders ( $1.00^\circ$ ) [27]. The result of the commercial bend sensor only involves the sensor outputs at the angles ranging from 25° to 100°, since large errors occur at small flexion angles due to its non-linearity (see Figure 5.23).

Furthermore, most of the sensors listed in Table 5.2 are dependent on the radius of curvature, i.e. the size of the finger joint. For instance, the 50.8-mm bend sensor from Flexpoint SS demonstrated a resistance of 500 k $\Omega$  when bent to 90° around a rod with a diameter of 6 mm, and double this resistance in the case of a 12-mm diameter pin [121]. Therefore, time-consuming calibration is required for monitoring fingers of different sizes. In contrast, the developed optical sensors are not affected by different joint sizes in principle.

For the measuring ability, as shown in Table 5.2, the sensors reported by other research groups [51, 58, 65, 134, 145, 153] are mainly single-axis, which are usually used to measure finger flexion/extension in one plane. Additionally, some sensors can only capture the movements in a limited range, e.g. the single-mode ( $90^\circ$ ) [153] and the embedded hetero-core optic fibre-based sensors ( $97.2^\circ$ ) [145], which is not enough for tracking the entire motion of several finger joints, e.g. the PIP joints. For strain sensors, their abilities in measuring finger flexion are largely determined by the joint size and their stretchability. Although the commercial bend sensor from Flexpoint SS is capable of monitoring flexion in a wide range, it is unidirectional and insensitive to flexion angles below 20° (see Figure 5.20). This limits the accurate measurements of finger motion. The three developed electro-optical sensors have different features, suitable for different finger joints. Sensor#1 is single-axis and capable of tracking motion in 90°, and thus it can be used to record the real-time movements of DIP joints. Sensor#2 has an expanded measuring span ( $180^\circ$ ), which can be adopted for detecting the motion of

PIP joints in one plane. Sensor#3 is designed with two rotational axes, and each axis has a wide measurement range of  $180^\circ$ . These properties enable sensor#3 to monitor two-DOF finger joints, e.g. the MCP joint.

Overall, the developed electro-optical sensors demonstrate high sensitivity, high stability, great repeatability, low hysteresis, small mean absolute errors with respect to the defined rotation angles, and also wide measuring range. These properties demonstrate great potential of the goniometric sensors for accurately tracking finger motion.

## **5.2 Evaluation of the Dynamic Responses of the Electro-optical Goniometric Sensor and the Commercial Bend Sensor**

As stated in 5.1, the developed optical sensors demonstrated promising static characteristics for detecting angular position. Here, the dynamic performance of the optical sensors will be investigated and compared. Since each channel of sensor#2 and sensor#3 works in the same way to sensor#1, sensor#1 is mainly discussed and compared with the commercial bend sensor.

The dynamic characteristics of sensor#1 and the bend sensor were evaluated by using the motorised stage in continuous mode. In this test, the motor performed rotations at the maximum angular acceleration of  $70^\circ/s^2$  allowed by the experimental apparatus. The sensor data was acquired at a rate of 10 kHz in synchronisation with the motor controller.

As shown in Figure 5.20, the commercial bend sensor showed approximately linear performance with a sensitivity of  $57 \text{ mV}/^\circ$  above  $40^\circ$  whereas sensor#1 was most sensitive for angles between  $20^\circ$  to  $70^\circ$  (see Figure 5.1). Therefore, their responses in the range from  $40^\circ$  to  $70^\circ$  were investigated where both sensors possess a high sensitivity.

The motor acceleration and the test range limit the maximum speed of the motor to  $45.8^\circ/s$ , and thereby the sensor responses were investigated at different rotation speeds of  $15^\circ/s$ ,  $25^\circ/s$ ,  $35^\circ/s$ , and  $45^\circ/s$ . The measurement procedure involved increasing the angle from  $40^\circ$  to  $70^\circ$  and then back again to  $40^\circ$  at the specific rotation speed. A two-second delay was included at the beginning and end of each cycle. This process was repeated for five cycles.

During the measurements, the motorised stage moved after receiving a command from the motor controller and then returned a confirmatory message back to the controller. Time delays associated with this communication are not provided by the manufacturer. Therefore, in this work it is reasonable to assume that the communication time delays are small in comparison to the rotation speeds used to simulate joint movement.

Figure 5.26 shows the dynamic responses of both sensor#1 and the commercial bend sensor. Sensor#1 exhibits identical behaviour to that of the motorised rotation stage, effectively providing an instantaneous response relative to the speeds investigated here (15, 25, 35, 45°/s). In contrast, the bend sensor exhibits an initial time delay followed by a complicated response consisting of a negative to positive time delay transition. There was also clearly a problem with mechanical hysteresis with the bend sensor where the final reading did not return to the starting value. It can be declared that the optical sensor possesses a dynamic response superior to the commercial bend sensor under the test velocities investigated here.

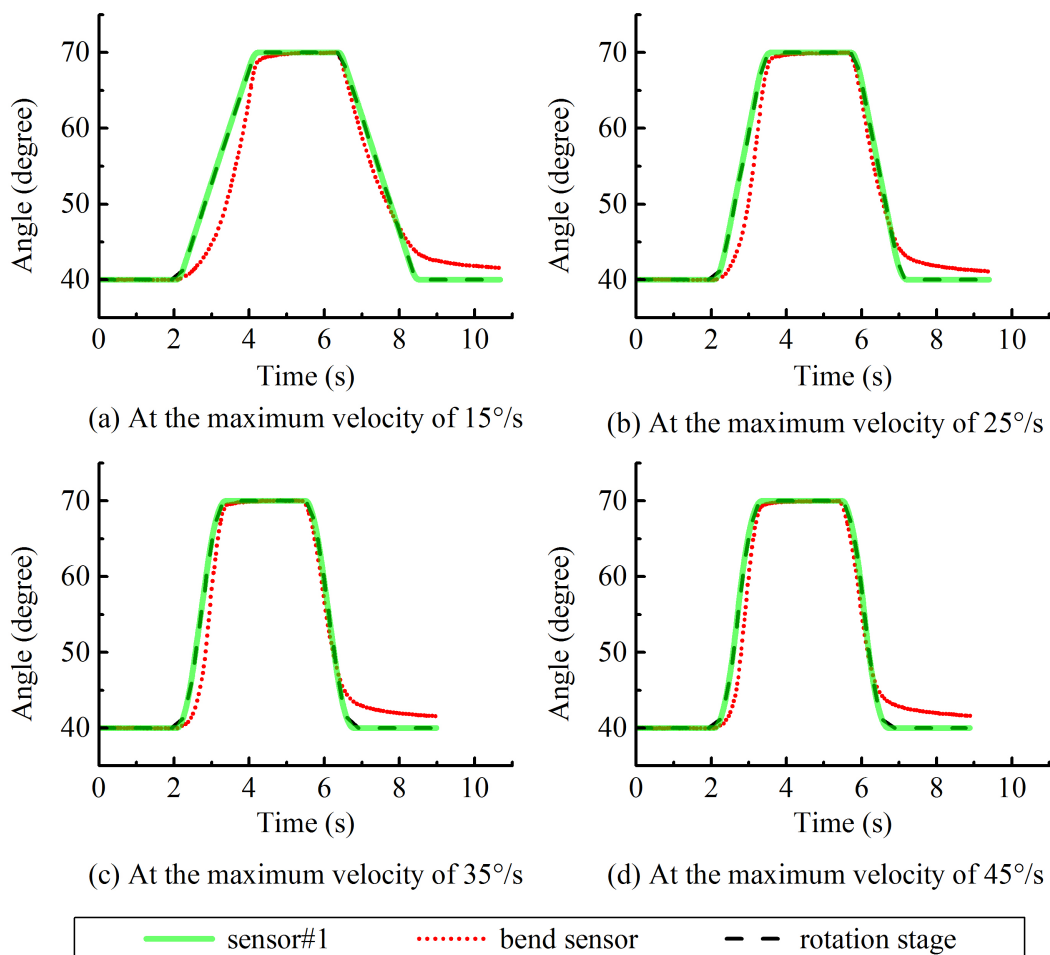


**Figure 5.26** Dynamic performance of sensor#1 and the commercial bend sensor at different rotation speeds. Sensor performance at the maximum velocity: (a) for 15°/s; (b) for 25°/s; (c) for 35°/s; (d) for 45°/s.

In the measurement systems for the bend sensor, only the conditioning circuitry, sensor attachment method, and also the sensor itself differed from those of sensor#1. These factors could possibly explain the difference between their dynamic responses.

In the conditioning circuitry, different amplifiers were used for the bend sensor and sensor#1. For the bend sensor, the amplifier with a settling time of  $2.6 \mu\text{s}$  was used. The amplifier adopted for sensor#1 has a settling time of  $0.535 \mu\text{s}$ . The short settling time cannot account for the difference in the sensor responses. Additionally, the capacitor  $C_2$  in the conditioning circuit shown in Figure 4.10(a) was removed for sensor#1 to eliminate the delay introduced by the filters during this experiment. Other components, i.e. the resistors, cannot cause long time delay for both sensors. So the conditioning circuitry cannot be regarded as a major factor for the obvious delay phenomenon in the bend sensor's response.

Secondly, sensor#1 and the bend sensor were attached to the motorised rotation stage using different methods Figure 4.9(b) and (c). The friction generated between the sensors and the clamps/supports could possibly affect the sensor performance. For sensor#1, the friction problem can be ignored, because the sensor wing was tightly held by a pin vice powered by the stepper motor. However, the friction between the hinge supporter, the plastic sleeve, and the sensor itself (see Figure 4.9(c)) could work on the bend sensor during the unloading period (i.e. back to  $40^\circ$  from  $70^\circ$ ), even though it does not greatly affect the bend sensor during the flexion (i.e. moving towards  $70^\circ$ ) because of the pull from the motor. During the unloading period, the sensor strip could be bent due to frictional forces when it was pushed inside the sleeve, which can explain the response of the bend sensor from  $70^\circ$  towards  $40^\circ$  (see the decline stage in Figure 5.26).

Thirdly, the delay phenomenon of the bend sensor can be related to the material relaxation time and the inherent attributes. However, currently there is no reported information about the material behaviour and the dynamic performance of the bend sensor manufactured by Flexpoint SS.

## 5.3 Summary

In comparison with the commercial bend sensor and also the reported nanocomposite strain sensors, optical fibre-based sensors, potentiometers, etc., the three electro-optical goniometric sensors all demonstrated higher sensitivity, more stable responses, lower hysteresis, smaller sensing errors, and wider measuring range. Furthermore, during the dynamic measurement the electro-optical goniometric sensor successfully tracked

---

the continuous rotations of the motorised stage whilst the commercial bend sensor demonstrated a large time delay and a failure to return to the start reading. The excellent performance of the developed electro-optical sensors reveals their great potential as sensory units for tracking articulated finger motion.

## **Chapter 6**

# **Electro-optical Goniometric Sensors for Tracking Finger Motion**

In this chapter, the capability of the developed goniometric sensors for tracking finger motion is discussed. Sensor#1 was used to capture the movements of the DIP joint of the index finger, sensor#2 for the PIP joint, and sensor#3 for the MCP joint. Furthermore, the 50.8-mm bend sensor manufactured by Flexpoint SS was also evaluated for monitoring finger movements, but only for the PIP joint due to the limitations discussed previously. During the measurements, video/photograph was recorded using a single-camera system as a reference point.

### **6.1 The DIP Joint Motion Detection Using the Single-axis Electro-optical Sensor**

As discussed in 5.1.5, sensor#1 is suitable for measuring the movements of the DIP finger joints. To evaluate its capability, sensor#1 was used to record the flexion/extension of the DIP joint of a healthy left index finger.

#### **6.1.1 Sensor Attachment to Finger DIP Joint**

As shown in Figure 6.1(a), sensor#1 was attached to a left handed nylon glove for tracking the DIP joint of the index finger. Since the skin elongates with finger flexion, two plastic sleeves were used to assist with sensor attachment. The lateral view (Figure 6.1(b)) shows how the wings of sensor#1 were inserted into the sleeves and fixed, using

adhesive plasters, to the distal and middle phalanxes. This enabled the sensor's wings to slide in response to finger flexion/extension. An elastic fibre, not illustrated in Figure 6.1 for clarity, was used to cover sensor#1 to keep the sensor wings close to the finger during finger motion.

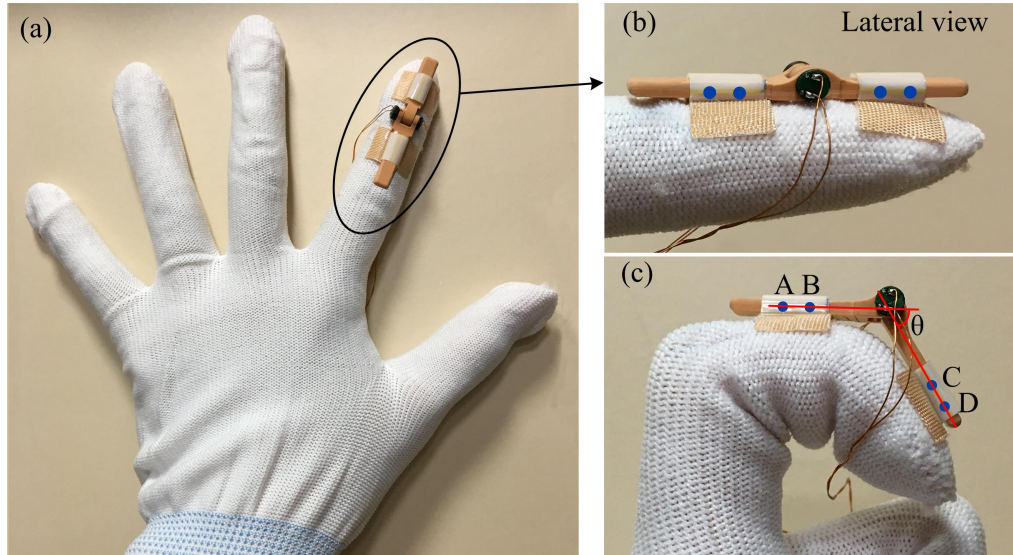


**Figure 6.1** The attachment of sensor#1 to a left handed nylon glove (the DIP joint of the index finger) and the motion estimation method using video sequences. (a) The front view of sensor attachment; (b) the lateral view of sensor attachment; (c) the video-based method used to estimate finger movements. The four blue markers (A-D) are put for the video recordings.

Additionally, four blue dots (A, B, C, and D) were marked onto the plastic sleeves (see Figure 6.1(b) and (c)) to facilitate video recording. As shown in Figure 6.1(c), superimposing a straight (red) line through the centre of the two dots on each sleeve, indicates the direction of the sensor's wing. Therefore, the relative position of the sensor wings, i.e. the flexion angle of the DIP joint ( $\theta$ ), can be obtained by analysing the trajectories of the two straight lines.

### 6.1.2 Monitoring Flexion and Extension of the DIP Joint

The left hand was initially placed flat on a table with fingers open, where was recorded as  $0^\circ$  flexion. The fingers of the hand were then clenched except for the index finger which remained straight. After this, index finger was bent and then straightened for seven repetitions. The motion was measured by sensor#1 at a sampling rate of 60 Hz and captured by the camera system at 60 frames per second.

During the measurements, the participant performed flexion/extension with the lateral side of the index finger close to a flat support which was perpendicular to the axis of

the camera lens; and hence it can be assumed that the plane of the finger motion was parallel to the focal plane of the camera.

The measured movements of the PIP joint are presented in Figure 6.2. The video curve (dotted line) was obtained by analysing the trajectories of the four blue markers on sensor#1. A software application called Tracker (ver. 4.97) [271] was used to automatically track the markers' position relative to the top left corner of the video image. It works by creating a template image of each blue marker and then searching each frame for the best match to that template in a user-defined rectangular search area. The best match is the one with the highest match score which is inversely proportional to the sum of the square of the RGB differences between the defined template and match pixels. Finally, the angle between each marker pair for every frame was computed as the flexion of the finger DIP joint. The uncertainty of this tracking method is about  $\pm 1.0^\circ$  which is mainly caused by the variation in the marker position estimation.

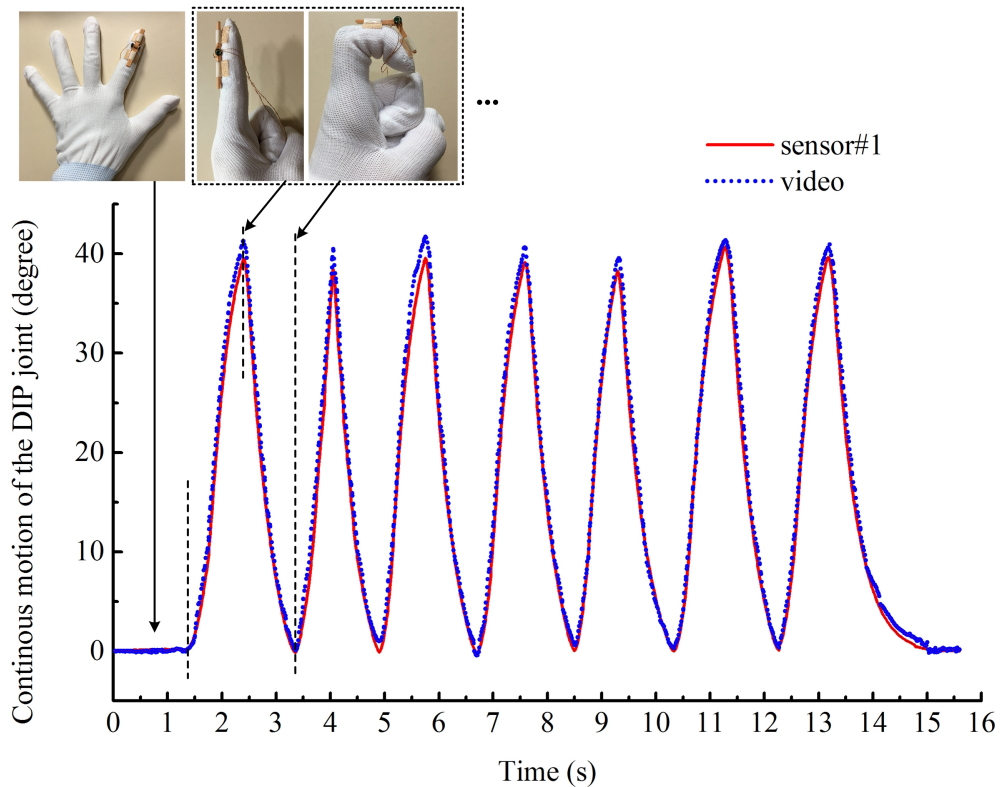


**Figure 6.2** The continuous flexion and extension of the DIP joint of the index finger. The actions in the dotted box were repeated continuously.

As shown in Figure 6.2, the traces provided by both sensor#1 and the video data are consistent, with an average absolute difference of  $1.0^\circ$  over all data points. However, at maximum flexion (around  $40^\circ$ ), the difference is greatest at around  $3.5^\circ$ . This may be due to a number of reasons including separation between the sensor wing and the DIP joint, the misalignment between the marker plane and the camera's focal plane,

estimation errors caused by blurred frames in the recorded video, and the measurement uncertainty of the video curve estimation.

## 6.2 Measurement of the PIP joint Motion Using the Single-axis Sensor with Data Fusion Method

Sensor#2 is characterised with a single rotational axis and a wide measurement range of  $180^\circ$ , which is sufficient for recording the entire ROM of the one-DOF PIP joints. To assess the capability of sensor#2 for tracking finger motion, the goniometric sensor was attached to the PIP joint of the left index finger. The 50.8-mm commercial bend sensor, tested in Chapter 5, was used as a comparison. During the measurements, the degree of the flexion/extension was recorded as positive values while hyperextension was registered as negative values. A position with the hand flat on the table was defined as  $0^\circ$  flexion.

### 6.2.1 Sensor Attachment to Finger PIP Joint

As shown in Figure 6.3(a), both sensor#2 and the bend sensor were attached simultaneously to the same finger but on separate overlapping gloves. Sensor#2 was attached to a separate nylon layer which was sewn on the glove, and the commercial bend sensor was placed directly on the glove just below the goniometric sensor, i.e. sensor#2. The red triangle mark shown in Figure 6.3(a) indicates the location of the electrical connectors of the bend sensor. As shown in Figure 6.3(b), the commercial bend sensor was inserted into two plastic sleeves glued on the glove. The end with the electrical connectors was fixed whereas the other end was able to slide freely in unison with the flexion and extension of the PIP joint. As shown in Figure 6.3(c), the wings of sensor#2 were inserted into two rectangular 3D printed parts which were placed over the middle and proximal phalanxes of the index finger. The rectangular parts could keep the sensor wings close to the finger phalanxes during the flexion/extension. Additionally, blue markers (A, B, and C) were put onto the two rectangular parts and the centre of sensor#2, and located in the same plane for recording video frames. These markers lined up when the sensor wings were straight. In this arrangement, the angle determined by the three markers with the vertex at marker B can be treated as the degree of finger flexion.

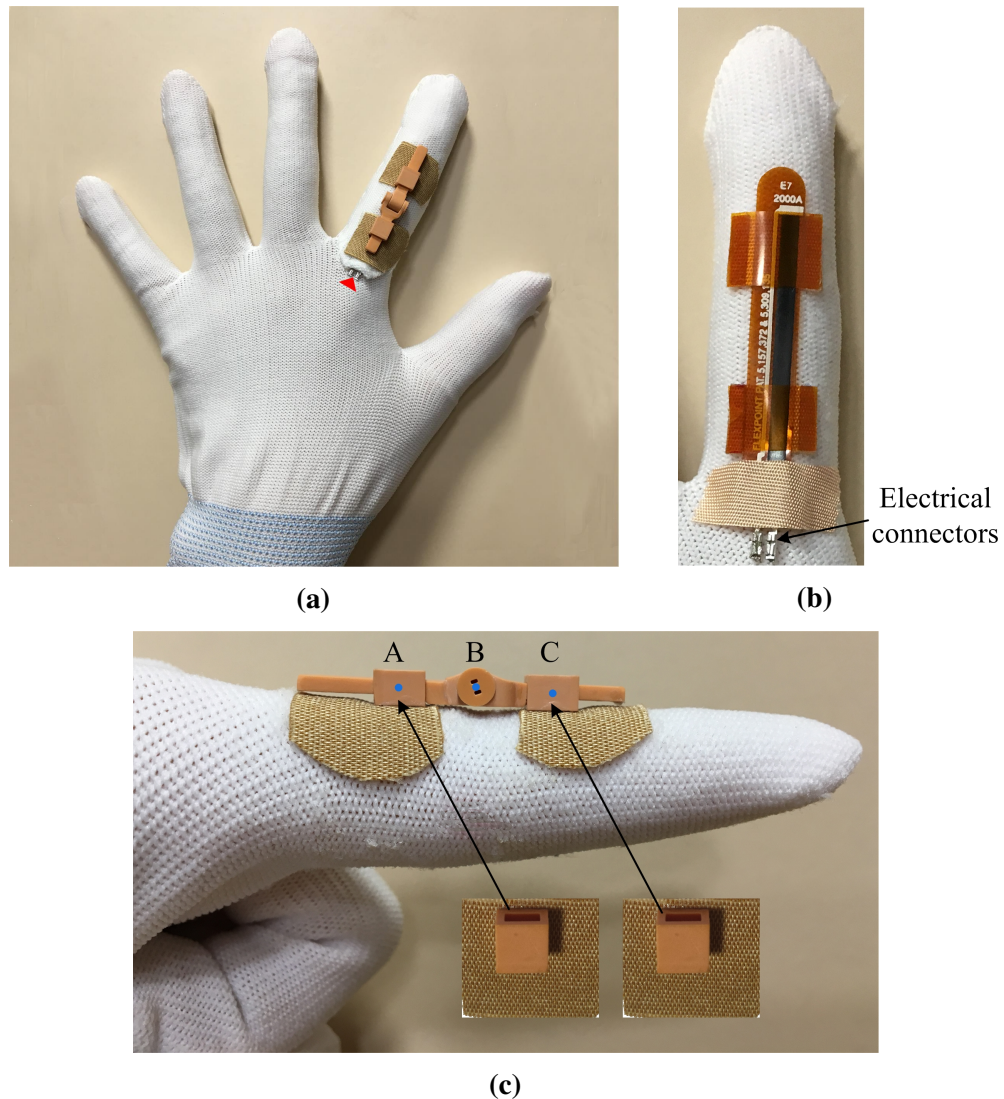


**Figure 6.3** Examples of the sensors' attachment to the left handed nylon glove, (a) red mark indicating the location of the commercial bend sensor, which was embedded under sensor#2; (b) attachment detail of the commercial bend sensor, on the dorsal surface of the PIP joint; (c) attachment detail of sensor#2, above the dorsal surface of the PIP joint of the left index finger.

### 6.2.2 Measuring Flexion and Extension of the PIP Joint

Since the bend sensor manufactured by Flexpoint SS [103] is highly dependent on the radius of curvature, i.e. the joint size, calibration was necessary prior to data collection. The instrumented glove was placed on the left hand and then the index finger was gradually flexed to different positions from  $0^\circ$  flexion. At each position, the flexion angle of the PIP joint was measured using a digital angle ruler [272] which has a measurement accuracy of  $0.3^\circ$  and a resolution of  $0.1^\circ$ ; meanwhile, the output voltage of the bend sensor was also recorded. Using the measured angle-voltage pairs, a second-degree polynomial function was fitted for calibrating the bend sensor.

After the calibration process, the hand's posture returned to the initial gesture, i.e. hand flat on the table with fingers open. Following this, the fingers were made to form a clenched fist quickly, before returning to the initial state again. Each posture was kept for a few seconds. This procedure was repeated continuously for six cycles, i.e. a series of six flexion and extension movements. The outputs of sensor#2 and the commercial bend sensor were acquired simultaneously. Photographs were taken to record finger positions at the minimum and maximum flexion as a reference point; the angular motion of the PIP joint was assessed by calculating the angle formed by the three blue markers (see Figure 6.3(c)).

Figure 6.4 displays the measured flexion and extension of the PIP joint. Sensor#2 demonstrates faster response speed and higher stability than the commercial bend sensor.

During the fast transition between the flat fingers and the clenched fist, the bend sensor exhibited an evident overshoot. The readings then gradually reduced for the remaining clenched fist period. A similar performance was also observed when only the bend sensor was used thus eliminating the influence of sensor#2 as a factor for the overshoot. Furthermore, similar examples of overshoot and instability were reported in the literature for bend sensors, from Flexpoint SS, used to monitor fast flexion [116, 119]. In contrast, sensor#2 produces fast and stable responses to the sudden flexion/extension.

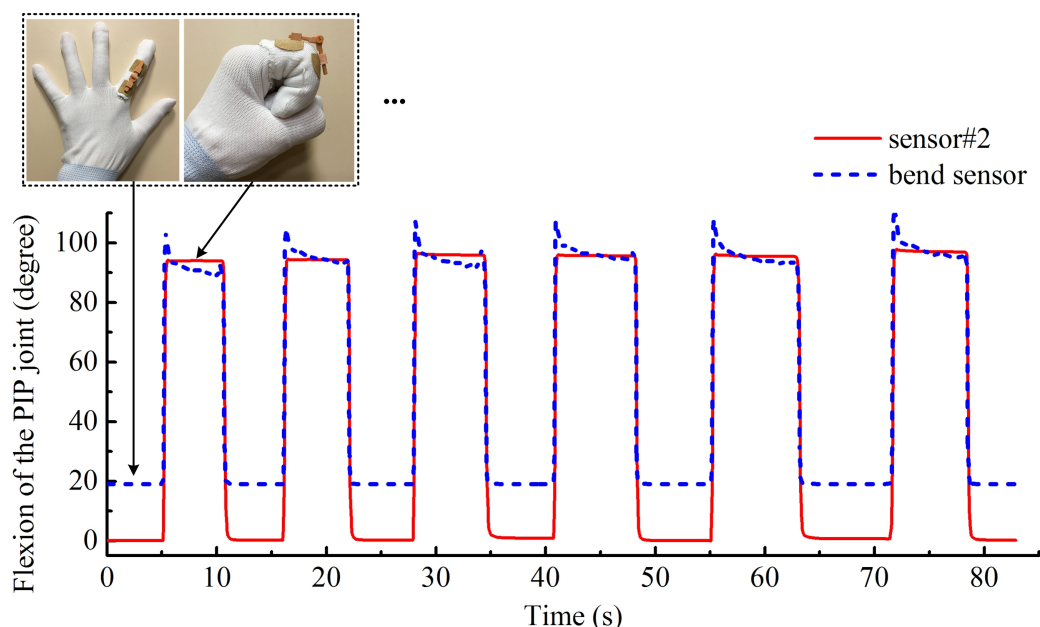


**Figure 6.4** The flexion and extension of the PIP joint of the left index finger recorded by sensor#2 and the commercial bend sensor. The actions in the dotted box were repeated continuously.

For the clenched fist, the outputs of sensor#2 average  $95.5^\circ$ , comparable to the reading of  $96.3^\circ$  for measurements obtained from photographs. At the state of  $0^\circ$  flexion,

sensor#2 produces an average output of  $0.2^\circ$  whilst the bend sensor generates a reading of  $19.0^\circ$ . The large error of the bend sensor can be explained by its non-linearity at small flexions, which is verified in 5.1.4.

Another measurement was carried out to investigate the sensor capability of tracking continuous finger flexion/extension. Both sensor#2 and the commercial bend sensor were used to measure such motion simultaneously. For comparison, a video was also recorded using the single-camera system.

Starting from  $0^\circ$  flexion, the hand was clenched using all fingers except the index finger, i.e. keeping the index finger flat on the table. The index finger was then bent into the clenched fist position before returning to the flat state. This was repeated six times.

The continuous finger motion recorded by the three sensing techniques is displayed in Figure 6.5. The video trace was obtained by calculating the angle defined by the three blue markers on sensor#2 also using the software application called Tracker (ver. 4.97) [271]. In Tracker, the autotracker tool was used to track the trajectories of all three markers and the protractor tool (resolution  $0.1^\circ$ ) was adopted to measure the angle

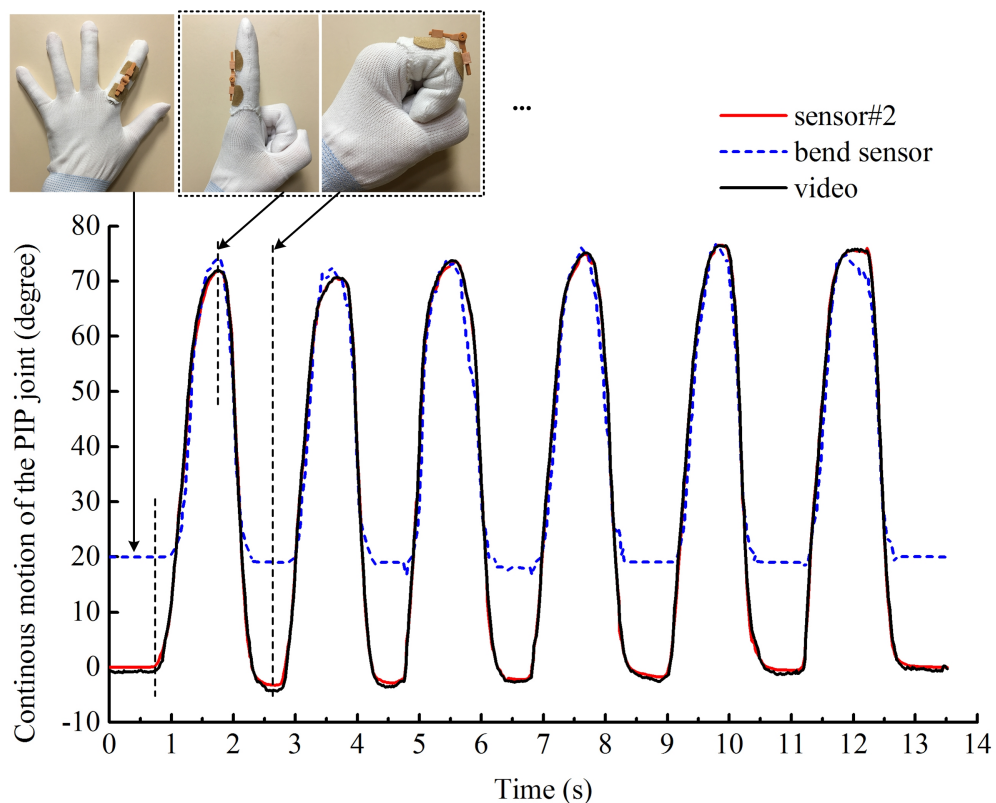


**Figure 6.5** The dynamic motion of the PIP joint of the left index finger recorded by sensor#2, the commercial bend sensor, and the video camera. The actions in the dotted box were repeated continuously over six cycles.

determined by the location of three markers with the vertex at marker B (see Figure 6.3(c)).

As shown in Figure 6.5, sensor#2 demonstrates angular readings close to the recorded video curve, with an absolute difference no more than  $2.4^\circ$  and a mean absolute error  $0.6^\circ$ . In contrast, the commercial bend sensor fails to measure the finger flexion below  $20^\circ$ . In the detectable range ( $>20^\circ$ ), the bend sensor exhibits a mean absolute error of  $3.4^\circ$  (relative to the video reference points), which is much larger than that of sensor#2.

Overall, sensor#2 outperforms the commercial bend sensor in terms of stability, response speed, and measurement accuracy, and shows great potential for monitoring hand movements in real time.

## 6.3 Motion Detection of the MCP Joints

To assess the capability for monitoring the motion of two-DOF finger joints, sensor#3 was attached to the dorsal surface of the MCP joint of the index finger in a similar fashion to that shown in Figure 4.6(c). In contrast to the glove-mounted sensor#1 and sensor#2, sensor#3 was attached to the left index finger. This was necessary because the glove fitting on the back of the hand was poor compared to the finger segments. This direct attachment method avoids errors caused by the motion of the glove relative to the hand.

Sensor#3 was used to measure flexion/extension, ABD/ADD, simultaneous flexion/extension and ABD/ADD, and circumduction of the MCP joint. During these measurements, the arm was maintained in a relaxed state by resting it on a table. The position with the hand flat was defined as  $0^\circ$  flexion/extension, and with the fingers closed as  $0^\circ$  ABD/ADD. The measurement results are described as follows.

### 6.3.1 Flexion and Extension of the Index MCP Joint

The hand was initially placed flat on the table with fingers closed. A fist was formed by rapidly bending the fingers and maintaining this posture for a few seconds before extending the fingers to maximum hyperextension. This procedure was repeated continuously for five cycles. During testing, the fingers (except the thumb) were always kept close to each other so that ABD/ADD was  $0^\circ$ . Photographs were taken to record finger positions at their maximum flexion and hyperextension as a reference. For

example, the angular motion of the left index finger was assessed by measuring the angle subtended by the markers running along the proximal phalange of the index finger and those on the back of the hand, as illustrated in Figure 6.6.

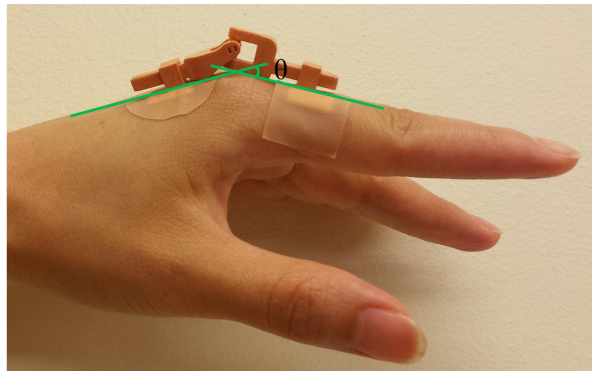


**Figure 6.6** The method to estimate the flexion angle of the MCP joint.

Figure 6.7 shows the output response of sensor#3 to alternating finger flexion and extension. The positive readings represent index finger flexion or extension, and the negative angles indicate hyperextension. Variations in shape and width of the waveform are due to variations in hand movements and periods of inactivity respectively.

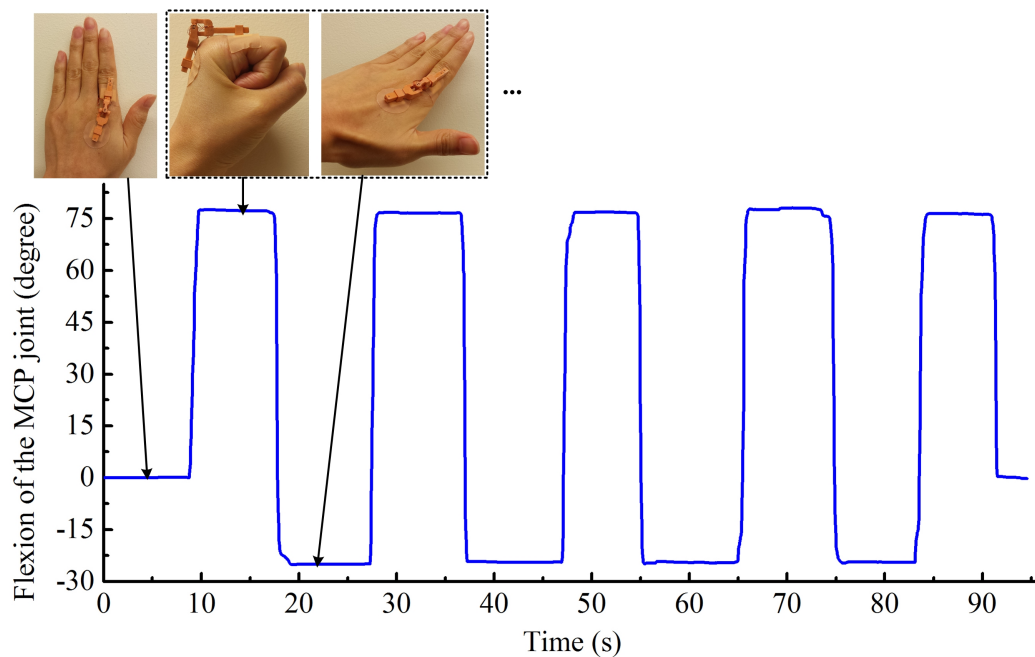


**Figure 6.7** The flexion and extension of the MCP joint of the left index finger. Fingers repeated the actions in the dotted box continuously, and finally returned to the initial state.

For this particular test subject, the electro-optical sensor recorded a maximum finger flexion of  $78.5^\circ$  when the hand was clenched into a fist, and a maximum hyperextension of  $25.1^\circ$ . This compares to readings of  $80.7^\circ$  and  $22.9^\circ$  for measurements obtained from the photographic analysis.

### 6.3.2 Abduction and Adduction of the Index MCP Joint

This test involved measuring ABD/ADD, starting with an open hand posture. Whilst maintaining the index finger in the same position, the other fingers were made to curl towards the palm. This was followed by moving the index finger to its maximum position of ABD and then ADD, staying at each position for several seconds. The index finger was kept fully extended during these movements.

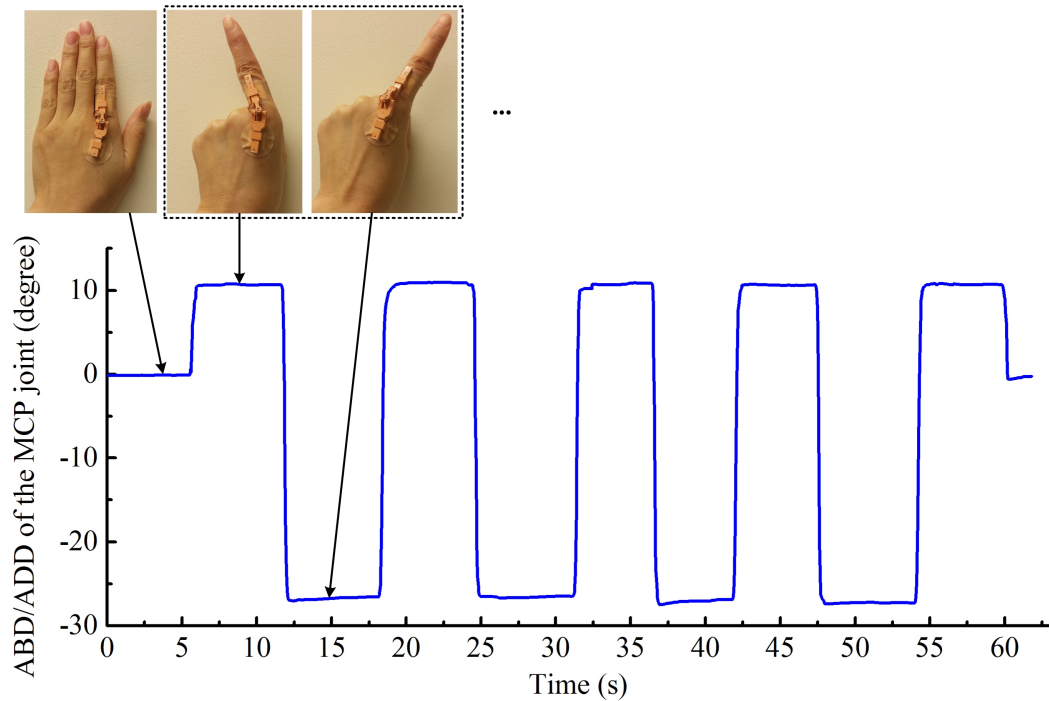


**Figure 6.8** The abduction and adduction of the MCP joint of the participant's index finger. The fingers repeated the actions in the dotted box continuously, and finally returned to the initial state.

Figure 6.8 shows the capability of sensor#3 to track finger ABD/ADD. The readings are positive for motion left of the finger midline, and negative to the right. For this study, the measured maximum ABD/ADD for the left and right sides are  $11.0^\circ$  and  $27.5^\circ$  respectively and this compares with readings of  $12.5^\circ$  and  $30.2^\circ$  obtained photogrammetrically. As seen with the flexion and extension measurements, the sensing channels of sensor#3 for ABD/ADD monitoring have excellent dynamic response.

### 6.3.3 Simultaneous Flexion/Extension and Abduction/Adduction of the Index MCP Joint

Simultaneous finger flexion/extension and ABD/ADD was also investigated. Initially, the hand was laid flat on the table with fingers closed, i.e.  $0^\circ$  flexion/extension and  $0^\circ$  ABD/ADD. Keeping this initial gesture for about 1 second, the fingers were then spread apart whilst the hand remained flat on the table. The fingers were then clenched before extending to maximum hyperextension and ABD. This action was performed repeatedly for eight cycles before returning to the initial gesture as shown in Figure 6.9. Compared to actions with zero ABD, simultaneous finger flexion and ADD led to higher readings, whilst finger extension and ABD led to a reduction in reading amplitude. These changes are consistent with the biomechanical interdependencies of the hand. The positive peak values in Figure 6.9 coincided with maximum finger flexion and ADD, i.e. the clenched gesture. The negative peaks corresponded with maximum hyperextension and ABD.

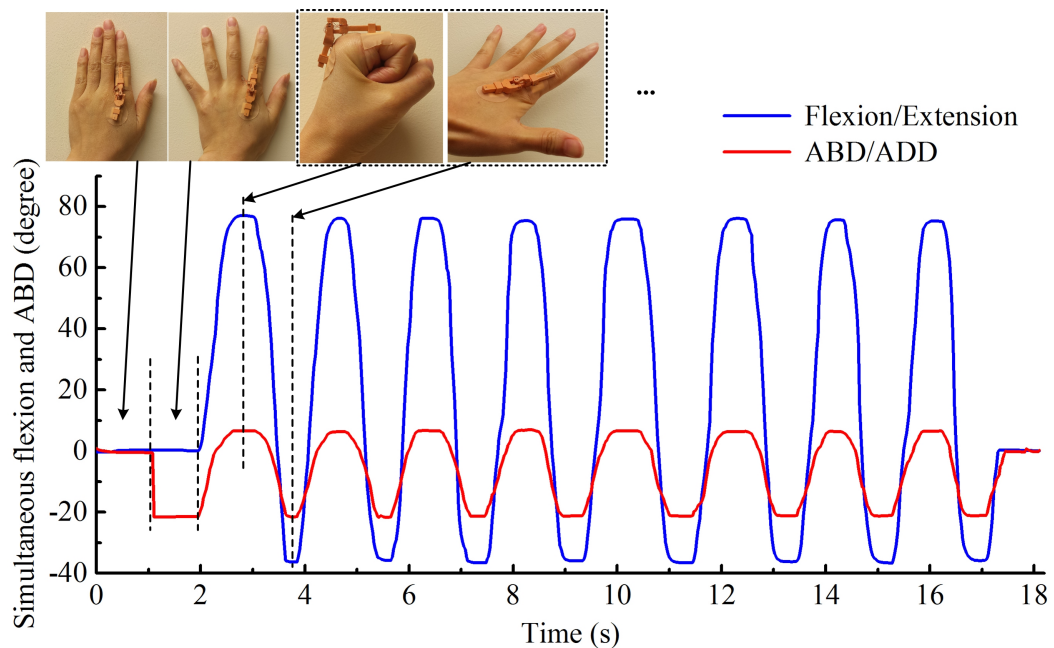


**Figure 6.9** The simultaneous movements of the flexion/extension and ABD/ADD of the MCP joint of the index finger. The actions in the dotted box were repeated continuously.

For this test, the maximum captured flexion is  $77.1^\circ$ . The hyperextension is up to  $37.2^\circ$ , much greater than the  $25.1^\circ$  measured in Figure 6.7 for hyperextension without ADD. This is because in general, less hyperextension occurs when the four fingers are closed together. Additionally, the maximum ABD/ADD left and right of the finger midline is  $7.1^\circ$  and  $21.8^\circ$  respectively. Due to the continuous movements of the fingers, it was difficult to take photographs or videos using the single-camera system during this testing. However, the promising results shown in Figure 6.9 reveal that the optical sensor has the ability to track finger flexion/extension and ABD/ADD simultaneously.

### 6.3.4 Circumduction of the Index MCP Joint

The final investigation looked at finger circumduction. In this case, the index finger moved to maximum hyperextension starting from the origin ( $0^\circ$  flexion/extension and  $0^\circ$  ABD/ADD) while clenching the remaining fingers. The tip of the index finger was then made to execute a clockwise circular motion which included positions of maximum ABD/ADD, i.e. circumduction.

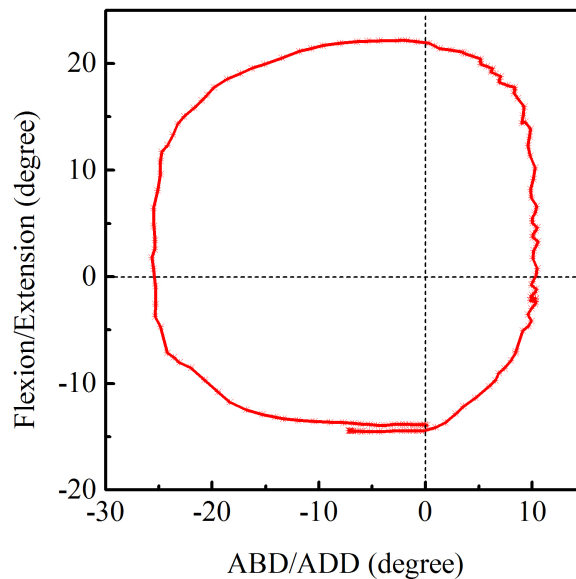


**Figure 6.10** The circumduction of the MCP joint of the index finger.

Figure 6.10 shows the clockwise trajectory of the left index finger when tracked by sensor#3. During circumduction, the MCP joint exhibited four movement types. Starting from maximum hyperextension (negative reading), the MCP joint executed: flexion-ABD, flexion-ADD, extension-ABD, and extension-ADD, before returning to the initial start point. The single-camera method used in this work was not capable of monitoring dynamic finger circumduction. Figure 6.10 indicates that this type of optical sensing has great potential for tracking the circumduction of the MCP joints. Finger circumduction enables circular pointing and is essential for applications such as virtual reality and entertainment. Sensor#3 would be ideally suited to applications in these areas.

## 6.4 Summary

The three electro-optical goniometric sensors discussed in this section demonstrated that collectively, they have the capability to capture the full range of articulation of the human finger. Sensor#1 successfully recorded the continuous flexion/extension

of the DIP joint of the index finger. Sensor#2 demonstrated a mean absolute error of  $0.6^\circ$  with respect to video recordings used to monitor the movements of the PIP joint; in contrast, the commercial bend sensor commonly used in glove-based systems showed inferior performance particularly for flexions below  $20^\circ$ . Sensor#3 produced outstanding performance when tracking MCP joint motion including flexion/extension, ABD/ADD and circumduction.

# Chapter 7

## Conclusion and Future Work

This chapter summarises the research work presented in this thesis, discusses the limitations of the developed goniometric sensors, and suggests directions for future work.

### 7.1 Conclusions

This work was concerned with the development and evaluation of novel goniometric sensors for measuring rotation angles and their applications in tracking hand kinematics including the motion of the DIP, PIP, and MCP joints. The main contributions of this research include: i) exploitation of the polarisation-based sensing method for tracking human hand kinematics; ii) development of a one-axis sensor with a wide-angle measurement capability; iii) design of a single sensing unit for the two-DOF finger joints.

According to the investigations and research achievements, the following conclusions can be drawn.

- This is the first time a polarisation-based sensing technique has been used for monitoring human hand kinematics. Using 3D printing technology, three electro-optical goniometric sensors were developed. They featured different measurement capabilities suitable for monitoring the different types of human finger joints.
- Sensor#1 measures the rotation angle by analysing the attenuation of light transmitted through linear polarising films. The output voltages in proportion to

the cosine squared rotation angles are consistent with the theoretically predicted values, showing an average difference of  $\pm 2.32\%$ . Sensor#1 has a single rotation axis, and is capable of measuring motion ranging from  $0^\circ$  to  $90^\circ$ . These features make sensor#1 suitable for monitoring the movements of the DIP joints with one DOF.

- Sensor#2 provides a wide measurement range of  $180^\circ$ , sufficient for tracking the entire ROM of hinged finger joints, e.g. the PIP joints ( $120^\circ$ - $150^\circ$ ). Sensor#2 is designed with two sensing channels along a single axis, to produce simultaneous outputs. In the two channels, the analysers are initially oriented with their transmission axes at about  $40^\circ$  to each other. Since the analysers receive the incident light polarised in the same direction, this arrangement ensures that at least one channel operates in the region with the maximum sensitivity and linearity. Furthermore, by comparing the output amplitudes of the two channels, the effective measurement range of sensor#2 is expanded to  $180^\circ$ . In fact, the oriented angle can be any value ranging from  $40^\circ$  to  $50^\circ$ , since the cosine squared function has high linearity in the range of  $20^\circ$  to  $70^\circ$ .
- Sensor#3 features two measurement axes; this is unique in designing a single sensing element for the two-DOF finger joints. Each axis of sensor#3 contains two sensing channels arranged and operated in a similar way to that of sensor#2. Each axis is capable of measuring the rotations spanning  $180^\circ$ , and the measurement result is accurate to  $\pm 0.25^\circ$  under laboratory conditions. The promising characteristics make sensor#3 overcome the limitations seen in other sensing techniques for capturing real-time motion of finger joints with two DOFs.
- For sensor#2 and sensor#3, a weighted average method is proposed to combine the simultaneous outputs of the sensing channels. Variable weight is applied to each channel taking into account the angular dependency of their sensitivity; more weight is applied when the channel sensitivity is high. During the random angle testing, the maximum errors of the two sensing channels (CH<sub>21</sub> and CH<sub>22</sub>) of sensor#2 are  $\pm 2.55^\circ$  and  $\pm 2.08^\circ$ , respectively, whilst the maximum error decreases to  $\pm 0.37^\circ$  after fusing the outputs of the two channels. The data fusion processing also reduces the overall mean absolute error of sensor#3 down to  $0.25^\circ$  for rotations about the x-axis and y-axis. It can be deduced that the data fusion method significantly enhances the measurement output of sensor#2 and sensor#3.
- Compared with the commercial bend sensor from Flexpoint SS, the electro-optical sensors developed in this work demonstrate superior characteristics

in terms of accuracy, repeatability, stability, measurement range, as well as dynamic response. The measurement accuracy of the electro-optical sensors is also much higher than that of the optical fibre and potentiometer based technologies. The compact hinged configurations enable the electro-optical sensors to track the physical bending angles directly. Their independence of the radius of curvature avoids time-consuming calibration procedures, making them ideal for integration into a glove-based system for tracking hand movements. The electro-optical sensors were attached to the dorsal surface of the finger for tracking articulated motion. This is consistent with standard clinical practice using manual goniometers.

- The use of opaque printing material and non-reflective black Aluminium foil in the construction of the optical sensors avoided problems due to interference from ambient light sources. Observed offset voltages were attributed to internal reflections of light emitted by the LED source picked up by the photodiode. For each sensor, the output values measured at different rotation angles shifted by equal amounts. Therefore, the offset voltage does not affect the sensor's overall performance.
- Sensor#1 was attached to the left index finger's DIP joint via a nylon glove for tracking continuous flexion/extension. It demonstrates a mean absolute error of  $1.0^\circ$  in reference to measurements obtained from video recordings. It can be concluded that sensor#1 has great potential for accurately tracking the motion of DIP finger joints.
- Sensor#2 was used to capture the flexion and extension of the PIP joint of the index finger. When the finger quickly flexes or extends, sensor#2 produces stable, fast, and accurate responses, with a mean absolute error of  $0.6^\circ$  with reference to the results obtained from video recordings. In contrast, the commercial bend sensor manufactured by Flexpoint SS exhibits an obvious overshoot error. Additionally, the bend sensor exhibits non-linearity for finger flexions below  $20^\circ$ . It can be seen that sensor#2 outperforms the popular commercial bend sensor when monitoring finger motion. The excellent performance reveals the capability of sensor#2 for tracking the movements of one-DOF PIP joints.
- When attached to the MCP joint of the index finger, the two-axis goniometric sensor (sensor#3) successfully tracked complex finger motion in real time, including flexion/extension, ABD/ADD and circumduction. Sensor#3 achieves angular measurements within  $2.7^\circ$  of the reference values obtained from video recordings. The promising results verify the capability of sensor#3 for tracking two-DOF finger motion.

Under laboratory conditions, the designed goniometric sensors demonstrated promising and attractive characteristics. The results for tracking the motion of the DIP, PIP, and MCP joints of the left index finger demonstrate the sensors' capabilities. Furthermore, these sensors have the potential to be fabricated with other dimensions for monitoring other joints in the human body, e.g. ankle, wrist, and knee.

## 7.2 Future Directions

The work presented in this thesis describes an effective sensing method to track hand motion. Several potential directions for future work have been identified and discussed below.

Each electro-optical goniometric sensor developed in this research needs at least one LED as the light source. Dozens of LEDs will be required when multiple sensors are configured in a glove to track the motion of all finger joints. This will consume excessive energy and also require many electrical wires for connection. To reduce the number of LEDs, a possible way is using optical fibres to transmit the light emitted by a single LED for multiple goniometric sensors.

In this work, the LED is driven by a constant-voltage circuit, i.e. using an ordinary load-limiting resistor and a power supply (+5 V). The voltage fluctuations and temperature changes can cause disproportional variations in the current passing through the LED, and then result in unstable light intensity. This problem can be tackled by driving LED light sources with a regulated constant-current circuit, which is more resistant to changes in the supply voltage. Therefore, the stability of the electro-optical goniometric sensors can be improved.

Additionally, the goniometric sensors working in the visible region are susceptible to ambient light interference. In this work, several methods including testing the sensors in a dark laboratory room have been implemented to avoid such influence. However, it is impossible to operate the sensors under these conditions in practice. Supplying an alternating current to modulate LED intensity together with a high-pass filter for conditioning the outputs may solve this issue. This approach can also eliminate the constant output offset voltage mainly caused by the unwanted internal reflection.

Moreover, further studies are required to investigate the sensors' capabilities of tracking finger motion, such as the effects of temperature variation, sensor adaptability to measure other finger joints, simultaneous measurements of multiple finger joints, and performance on different hand sizes. Only when these have been achieved can the

---

sensors be considered capable for integration with a glove or suitable support to provide an accurate motion tracking system. The potential of the goniometric sensors for monitoring other joints in the human body, e.g. ankle, knee, wrist, and shoulder, and the application in tendon-driven robotic hands can also be explored in the future.

# Bibliography

- [1] HealthDay News (2014 May 04), “4 in 10 people will suffer arthritic hands over lifetime.” [Online]. Available: <https://consumer.healthday.com/senior-citizen-information-31/misc-arthritis-news-41/4-in-10-people-will-suffer-arthritic-hands-over-lifetime-722378.html> (accessed on Apr. 03, 2018).
- [2] D. M. Avery, C. M. Rodner, and C. M. Edgar, “Sports-related wrist and hand injuries: a review,” *J. Orthop. Surg. Res.*, vol. 11, p. 99, Sept. 2016.
- [3] Economic News (2016 Nov. 10), *Nonfatal Occupational Injuries and Illnesses Requiring Days Away From Work*, Bureau of Labor Statistics, Washington, DC, USA. [Online]. Available: <https://www.bls.gov/news.release/osh2.htm> (accessed on Apr. 03, 2018).
- [4] Y. E. van Kooij, A. Fink, M. W. Nijhuis-van der Sanden, and C. M. Speksnijder, “The reliability and measurement error of protractor-based goniometry of the fingers: A systematic review,” *J. Hand Ther.*, to be published.
- [5] M. Dutton, “The examination and evaluation,” in *Orthopaedic Examination, Evaluation, and Intervention*, 2nd ed. New York, NY, USA: McGraw-Hill, 2009, ch. 8, sec. 1. [Online]. Available: [http://highered.mheducation.com/sites/0071474013/student\\_view0/index.html](http://highered.mheducation.com/sites/0071474013/student_view0/index.html)
- [6] V. Macionis, “Reliability of the standard goniometry and diagrammatic recording of finger joint angles: A comparative study with healthy subjects and non-professional raters,” *BMC Musculoskelet. Disord.*, vol. 14, p. 17, Jan. 2013.
- [7] Patterson Medical Ltd., *Assessment Tools*, Nottingham, UK. [Online]. Available: [https://www.pattersonmedical.co.uk/Supplies/ProductFamilyDetails/PIF\\_A4418](https://www.pattersonmedical.co.uk/Supplies/ProductFamilyDetails/PIF_A4418) (accessed on: Sept. 28 2017).
- [8] L. Dipietro, A. M. Sabatini, and P. Dario, “Evaluation of an instrumented glove for hand-movement acquisition,” *J. Rehabil. Res. Dev.*, vol. 40, no. 2, pp. 179–189, Mar./Apr. 2003.
- [9] B. Ellis and A. Bruton, “A study to compare the reliability of composite finger flexion with goniometry for measurement of range of motion in the hand,” *Clin. Rehabil.*, vol. 16, no. 5, pp. 562–570, Aug. 2002.
- [10] Danmic Global LLC., *Rolyan Finger/Toe Goniometer Tight-Fitting Hinge*, San Jose, CA, USA. [Online]. Available: <http://www.danmicglobal.com/524417.aspx> (accessed on Apr. 03, 2018).

- [11] L. Dipietro, A. M. Sabatini, and P. Dario, "A survey of glove-based systems and their applications," *IEEE Trans. Syst., Man, Cybern. C (Appl. Rev.)*, vol. 38, no. 4, pp. 461–482, Jul. 2008.
- [12] D. J. Sturman and D. Zeltzer, "A survey of glove-based input," *IEEE Comput. Graph. Appl.*, vol. 14, no. 1, pp. 30–39, Jan. 1994.
- [13] D. Barnett, "Optical resolver and method of use," U.S. Patent 20 020 125 412 A1, Mar. 11, 2002.
- [14] G. Wijntjes and C. Markos, "Non-contact optical polarization angle encoder," U.S. Patent 20 050 002 032 A1, Nov. 6, 2002.
- [15] P. Baxter and J. Raynor, "Rotary encoders," U.S. Patent 7 777 879, Aug. 17, 2010.
- [16] N. Palastanga and R. Soames, "The upper limb," in *Anatomy and Human Movement: Structure and Function*, 6th ed., R. Demetriou-Swanwick and S. Davies, Eds. China: Churchill Livingstone Elsevier, 2012, ch. 2, pp. 48–51, 161–183.
- [17] M. R. Villarreal, "Bones of the human hand." [Online]. Available: [https://commons.wikimedia.org/wiki/File%3AScheme\\_human\\_hand\\_bones-en.svg](https://commons.wikimedia.org/wiki/File%3AScheme_human_hand_bones-en.svg) (accessed on: Apr. 01, 2018).
- [18] N. Palastanga and R. Soames, "Introduction," in *Anatomy and Human Movement: Structure and Function*, 6th ed., R. Demetriou-Swanwick and S. Davies, Eds. China: Churchill Livingstone Elsevier, 2012, ch. 1, pp. 18–20.
- [19] OpenStax College, "Types of synovial joints." [Online]. Available: [https://commons.wikimedia.org/wiki/File%3A909\\_Types\\_of\\_Synovial\\_Joints.jpg](https://commons.wikimedia.org/wiki/File%3A909_Types_of_Synovial_Joints.jpg) (accessed on: Apr. 01, 2018).
- [20] K. S. Saladin, "Joints," in *Human Anatomy*, 2nd ed., C. H. Wheatley and K. A. Queck, Eds. New York, NY, USA: Michelle Watnick, 2008, ch. 9, pp. 243–248.
- [21] C. N. Henley, "Motion of the fingers, thumb, and wrist – language of hand and arm surgery series." [Online]. Available: <http://noelhenley.com/532/motion-of-the-fingers-thumb-and-wrist-language-of-hand-and-arm-surgery-series/> (accessed on: Sept. 28, 2017).
- [22] A. Hollister, W. L. Buford, L. M. Myers, D. J. Giurintano, and A. Novick, "The axes of rotation of the thumb carpometacarpal joint," *J. Orthop. Res.*, vol. 10, no. 3, pp. 454–460, May 1992.
- [23] W. P. Cooney, M. J. Lucca, E. Y. Chao, and R. L. Linscheid, "The kinesiology of the thumb trapeziometacarpal joint," *J. Bone Joint Surg. Am.*, vol. 63, no. 9, pp. 1371–1381, Dec. 1981.
- [24] J. Lee and T. L. Kunii, "Model-based analysis of hand posture," *IEEE Comput. Graph. Appl.*, vol. 15, no. 5, pp. 77–86, Sept. 1995.
- [25] Y. Wu and T. S. Huang, "Hand modeling, analysis and recognition," *IEEE Signal Process. Mag.*, vol. 18, no. 3, pp. 51–60, Sept. 2001.
- [26] S. Ciotti, E. Battaglia, N. Carbonaro, A. Bicchi, A. Tognetti, and M. Bianchi, "A synergy-based optimally designed sensing glove for functional grasp recognition," *Sensors*, vol. 16, no. 6, p. 811, Jun. 2016.

- [27] K. Li, I. M. Chen, S. H. Yeo, and C. K. Lim, "Development of finger-motion capturing device based on optical linear encoder," *J. Rehabil. Res. Dev.*, vol. 48, no. 1, p. 69, 2011.
- [28] J. J. Kuch and T. S. Huang, "Vision based hand modeling and tracking for virtual teleconferencing and telecollaboration," in *Proc. 5th IEEE Int. Conf. Computer Vision*, Cambridge, MA, USA, 1995, pp. 666–671.
- [29] T. L. Baldi, S. Scheggi, L. Meli, M. Mohammadi, and D. Prattichizzo, "GESTO: A glove for enhanced sensing and touching based on inertial and magnetic sensors for hand tracking and cutaneous feedback," *IEEE Trans. Human-Mach. Syst.*, to be published.
- [30] S. Cobos, M. Ferre, M. S. Uran, J. Ortego, and C. Pena, "Efficient human hand kinematics for manipulation tasks," in *2008 IEEE/RSJ Int. Conf. Intelligent Robots and Systems*, Nice, France, pp. 2246–2251.
- [31] J. Lin, Y. Wu, and T. S. Huang, "Modeling the constraints of human hand motion," in *Proc. Workshop Human Motion*, Los Alamitos, CA, USA, 2000, pp. 121–126.
- [32] F. C. Chen, A. Favetto, M. Mousavi, E. P. Ambrosio, S. Appendino, A. Battezzato, D. Manfredi, F. Pescarmona, and B. Bona, "Human hand: Kinematics, statics and dynamics," in *41st Int. Conf. Environmental Systems*, Portland, OR, USA, 2011, pp. 17–21.
- [33] R. Degeorges, J. Parasie, D. Mitton, N. Imbert, J. N. Goubier, and F. Lavaste, "Three-dimensional rotations of human three-joint fingers: an optoelectronic measurement. Preliminary results," *Surg. Radiol. Anat.*, vol. 27, no. 1, pp. 43–50, Mar. 2005.
- [34] C. S. Fahn and H. Sun, "Development of a data glove with reducing sensors based on magnetic induction," *IEEE Trans. Ind. Electron.*, vol. 52, no. 2, pp. 585–594, Apr. 2005.
- [35] Y. Ma, Z. Mao, W. Jia, C. Li, J. Yang, and M. Sun, "Magnetic hand tracking for human-computer interface," *IEEE Trans. Magn.*, vol. 47, no. 5, pp. 970–973, May 2011.
- [36] Y. Park, J. Lee, and J. Bae, "Development of a wearable sensing glove for measuring the motion of fingers using linear potentiometers and flexible wires," *IEEE Trans. Ind. Informat.*, vol. 11, no. 1, pp. 198–206, Feb. 2015.
- [37] E. Hecht, "Electromagnetic theory, photons, and light," in *Optics*, 5th ed., M. Borthakur and V. Tiwari, Eds. England, UK: Pearson Education Ltd., 2017, ch. 3, pp. 45–57.
- [38] E. Hecht, "Polarization," in *Optics*, 5th ed., M. Borthakur and V. Tiwari, Eds. England, UK: Pearson Education Ltd., 2017, ch. 8, pp. 338–344.
- [39] Edmund Optics Inc., "Introduction to polarization," Barrington, NJ, USA, Appl. Note, 2015. [Online]. Available: <https://www.edmundoptics.com/resources/application-notes/optics/introduction-to-polarization/>
- [40] Thorlabs, Inc., *Nanoparticle Linear Film Polarizer*, Ely, UK. [Online]. Available: [https://www.thorlabs.com/newgrouppage9.cfm?objectgroup\\_id=752](https://www.thorlabs.com/newgrouppage9.cfm?objectgroup_id=752) (accessed on Dec. 05, 2017).

- [41] T. Erdogan, "Understanding polarization," Semrock Inc., New York, NY, USA, Tech. Rep. [Online]. Available: <https://www.semrock.com/understanding-polarization.aspx>
- [42] A. Macleod, "Thin film polarizers and polarizing beam splitters," *SVC Bull.*, 2009.
- [43] L. Wang, T. Meydan, and P. Williams, "Design and evaluation of a 3-D printed optical sensor for monitoring finger flexion," *IEEE Sensors J.*, vol. 17, no. 6, pp. 1937–1944, Mar. 2017.
- [44] L. Wang, T. Meydan, and P. I. Williams, "A two-axis goniometric sensor for tracking finger motion," *Sensors*, vol. 17, no. 4, p. 770, Apr. 2017.
- [45] F. Xu and Y. Zhu, "Highly conductive and stretchable silver nanowire conductors," *Adv. Mater.*, vol. 24, no. 37, pp. 5117–5122, Jul. 2012.
- [46] R. Wijesiriwardana, "Inductive fiber-meshed strain and displacement transducers for respiratory measuring systems and motion capturing systems," *IEEE Sensors J.*, vol. 6, no. 3, pp. 571–579, Jun. 2006.
- [47] W. G. Darling, K. J. Cole, and G. F. Miller, "Coordination of index finger movements," *J. Biomech.*, vol. 27, no. 4, pp. 479–491, Apr. 1994.
- [48] A. V. Alaferdov, R. Savu, T. A. Rackauskas, S. Rackauskas, M. A. Canesqui, D. S. De Lara, G. O. Setti, E. Joanni, G. M. De Trindade, U. B. Lima *et al.*, "A wearable, highly stable, strain and bending sensor based on high aspect ratio graphite nanobelts," *Nanotechnology*, vol. 27, no. 37, p. 375501, Sept. 2016.
- [49] H. O. Michaud, J. Teixidor, and S. P. Lacour, "Soft flexion sensors integrating stretchable metal conductors on a silicone substrate for smart glove applications," in *2015 28th IEEE Int. Conf. Micro Electro Mechanical Systems (MEMS)*, Estoril, Portugal, pp. 760–763.
- [50] H. O. Michaud, L. Dejace, S. De Mulatier, and S. P. Lacour, "Design and functional evaluation of an epidermal strain sensing system for hand tracking," in *2016 IEEE/RSJ Int. Conf. Intelligent Robots and Systems (IROS)*, Daejeon, South Korea, 2016, pp. 3186–3191.
- [51] T. Yamada, Y. Hayamizu, Y. Yamamoto, Y. Yomogida, A. Izadi-Najafabadi, D. N. Futaba, and K. Hata, "A stretchable carbon nanotube strain sensor for human-motion detection," *Nat. Nanotechnol.*, vol. 6, no. 5, pp. 296–301, Mar. 2011.
- [52] J. H. Kong, N. S. Jang, S. H. Kim, and J. M. Kim, "Simple and rapid micropatterning of conductive carbon composites and its application to elastic strain sensors," *Carbon*, vol. 77, pp. 199–207, Oct. 2014.
- [53] X. Xiao, L. Yuan, J. Zhong, T. Ding, Y. Liu, Z. Cai, Y. Rong, H. Han, J. Zhou, and Z. Wang, "High-strain sensors based on ZnO nanowire/polystyrene hybridized flexible films," *Adv. Mater.*, vol. 23, no. 45, pp. 5440–5444, Oct. 2011.
- [54] S. H. Bae, Y. Lee, B. K. Sharma, H. J. Lee, J. H. Kim, and J. H. Ahn, "Graphene-based transparent strain sensor," *Carbon*, vol. 51, pp. 236–242, Jan. 2013.

- [55] X. Li, P. Sun, L. Fan, M. Zhu, K. Wang, M. Zhong, J. Wei, D. Wu, Y. Cheng, and H. Zhu, "Multifunctional graphene woven fabrics," *Sci. Rep.*, vol. 2, p. 395, May 2012.
- [56] J. Li, S. Zhao, X. Zeng, W. Huang, Z. Gong, G. Zhang, R. Sun, and C. Wong, "Highly stretchable and sensitive strain sensor based on facilely prepared three-dimensional graphene foam composite," *ACS Appl. Mater. Interfaces*, vol. 8, no. 29, pp. 18 954–18 961, Jul. 2016.
- [57] C. Yan, J. Wang, W. Kang, M. Cui, X. Wang, C. Y. Foo, K. J. Chee, and P. S. Lee, "Highly stretchable piezoresistive graphene–nanocellulose nanopaper for strain sensors," *Adv. Mater.*, vol. 26, no. 13, pp. 2022–2027, Apr. 2014.
- [58] J. Lee, S. Kim, J. Lee, D. Yang, B. C. Park, S. Ryu, and I. Park, "A stretchable strain sensor based on a metal nanoparticle thin film for human motion detection," *Nanoscale*, vol. 6, no. 20, pp. 11 932–11 939, Aug. 2014.
- [59] M. Amjadi, A. Pichitpajongkit, S. Lee, S. Ryu, and I. Park, "Highly stretchable and sensitive strain sensor based on silver nanowire–elastomer nanocomposite," *ACS nano*, vol. 8, no. 5, pp. 5154–5163, Apr. 2014.
- [60] S. Chen, Y. Wei, X. Yuan, Y. Lin, and L. Liu, "A highly stretchable strain sensor based on a graphene/silver nanoparticle synergic conductive network and a sandwich structure," *J. Mater. Chem. C*, vol. 4, no. 19, pp. 4304–4311, Apr. 2016.
- [61] Y. Yu, Y. Luo, A. Guo, L. Yan, Y. Wu, K. Jiang, Q. Li, S. Fan, and J. Wang, "Flexible and transparent strain sensors based on super-aligned carbon nanotube films," *Nanoscale*, vol. 9, no. 20, pp. 6716–6723, Apr. 2017.
- [62] Y. Wang, J. Cheng, Y. Xing, M. Shahid, H. Nishijima, and W. Pan, "Stretchable platinum network-based transparent electrodes for highly sensitive wearable electronics," *Small*, vol. 13, no. 27, p. 1604291, Jul. 2017.
- [63] S. G. Yoon, H. J. Koo, and S. T. Chang, "Highly stretchable and transparent microfluidic strain sensors for monitoring human body motions," *ACS Appl. Mater. Interfaces*, vol. 7, no. 49, pp. 27 562–27 570, Nov. 2015.
- [64] M. Amjadi and I. Park, "Carbon nanotubes-EcoFlex nanocomposite for strain sensing with ultra-high stretchability," in *2015 28th IEEE Int. Conf. Micro Electro Mechanical Systems (MEMS)*, Estoril, Portuga, 2015, pp. 744–747.
- [65] J. T. Muth, D. M. Vogt, R. L. Truby, Y. Mengüç, D. B. Kolesky, R. J. Wood, and J. A. Lewis, "Embedded 3D printing of strain sensors within highly stretchable elastomers," *Adv. Mater.*, vol. 26, no. 36, pp. 6307–6312, Jun. 2014.
- [66] S. Ryu, P. Lee, J. B. Chou, R. Xu, R. Zhao, A. J. Hart, and S. G. Kim, "Extremely elastic wearable carbon nanotube fiber strain sensor for monitoring of human motion," *ACS Nano*, vol. 9, no. 6, pp. 5929–5936, Jun. 2015.
- [67] U. H. Shin, D. W. Jeong, S. M. Park, S. H. Kim, H. W. Lee, and J. M. Kim, "Highly stretchable conductors and piezocapacitive strain gauges based on simple contact-transfer patterning of carbon nanotube forests," *Carbon*, vol. 80, pp. 396–404, Dec. 2014.

- [68] J. B. Chossat, Y. Tao, V. Duchaine, and Y. L. Park, "Wearable soft artificial skin for hand motion detection with embedded microfluidic strain sensing," in *2015 IEEE Int. Conf. Robotics and Automation (ICRA)*, Seattle, WA, USA, pp. 2568–2573.
- [69] J. B. Chossat, Y. L. Park, R. J. Wood, and V. Duchaine, "A soft strain sensor based on ionic and metal liquids," *IEEE Sensors J.*, vol. 13, no. 9, pp. 3405–3414, Sept. 2013.
- [70] F. L. Hammond, Y. Mengüç, and R. J. Wood, "Toward a modular soft sensor-embedded glove for human hand motion and tactile pressure measurement," in *2014 IEEE/RSJ Int. Conf. Intelligent Robots and Systems*, Chicago, IL, USA, 2014, pp. 4000–4007.
- [71] S. J. Park, J. Kim, M. Chu, and M. Khine, "Highly flexible wrinkled carbon nanotube thin film strain sensor to monitor human movement," *Adv. Mater. Technol.*, vol. 1, no. 5, p. 1600053, Aug. 2016.
- [72] A. Tognetti, F. Lorussi, G. Dalle Mura, N. Carbonaro, M. Pacelli, R. Paradiso, and D. De Rossi, "New generation of wearable goniometers for motion capture systems," *J. Neuroeng. Rehabil.*, vol. 11, p. 56, Apr. 2014.
- [73] F. Lorussi, E. P. Scilingo, M. Tesconi, A. Tognetti, and D. De Rossi, "Strain sensing fabric for hand posture and gesture monitoring," *IEEE Trans. Inf. Technol. Biomed.*, vol. 9, no. 3, pp. 372–381, Sept. 2005.
- [74] E. P. Scilingo, F. Lorussi, A. Mazzoldi, and D. De Rossi, "Strain-sensing fabrics for wearable kinaesthetic-like systems," *IEEE Sensors J.*, vol. 3, no. 4, pp. 460–467, Aug. 2003.
- [75] N. Carbonaro, A. Greco, G. Anania, G. Dalle Mura, R. Tognetti, P. Scilingo, and D. De Rossi, "Unobtrusive physiological and gesture wearable acquisition system: A preliminary study on behavioral and emotional correlations," in *1st Int. Conf. Global Health Challenges*, Venice, Italy, 2012, pp. 88–92.
- [76] M. Stoppa and A. Chiolerio, "Wearable electronics and smart textiles: A critical review," *Sensors*, vol. 14, no. 7, pp. 11 957–11 992, Jul. 2014.
- [77] E. Jespersen and M. R. Neuman, "A thin film strain gauge angular displacement sensor for measuring finger joint angles," in *Proc. Annu. Int. Conf. IEEE Engineering in Medicine and Biology Society*, vol. 2, New Orleans, LA, USA, 1988, p. 807.
- [78] H. O. Michaud, J. Teixidor, and S. P. Lacour, "Soft metal constructs for large strain sensor membrane," *Smart Mater. Struct.*, vol. 24, no. 3, p. 035020, Feb. 2015.
- [79] C. Mattmann, F. Clemens, and G. Tröster, "Sensor for measuring strain in textile," *Sensors*, vol. 8, no. 6, pp. 3719–3732, Jun. 2008.
- [80] N. Lu, C. Lu, S. Yang, and J. Rogers, "Highly sensitive skin-mountable strain gauges based entirely on elastomers," *Adv. Funct. Mater.*, vol. 22, no. 19, pp. 4044–4050, Oct. 2012.
- [81] W. Yuan, Q. Zhou, Y. Li, and G. Shi, "Small and light strain sensors based on graphene coated human hairs," *Nanoscale*, vol. 7, no. 39, pp. 16 361–16 365, Oct. 2015.

- [82] M. Amjadi, A. Pichitpajongkit, S. Ryu, and I. Park, "Piezoresistivity of Ag NWs-PDMS nanocomposite," in *2014 IEEE 27th Int. Conf. Micro Electro Mechanical Systems (MEMS)*, San Francisco, CA, USA, pp. 785–788.
- [83] A. C. Yuen, A. A. Bakir, N. N. Z. M. Rajdi, C. L. Lam, S. M. Saleh, and D. H. Wicaksono, "Proprioceptive sensing system for therapy assessment using cotton fabric-based biomedical microelectromechanical system," *IEEE Sensors J.*, vol. 14, no. 8, pp. 2872–2880, Aug. 2014.
- [84] R. K. Kramer, C. Majidi, R. Sahai, and R. J. Wood, "Soft curvature sensors for joint angle proprioception," in *2011 IEEE/RSJ Int. Conf. Intelligent Robots and Systems*, San Francisco, CA, USA, 2011, pp. 1919–1926.
- [85] Y. L. Park, B. R. Chen, and R. J. Wood, "Design and fabrication of soft artificial skin using embedded microchannels and liquid conductors," *IEEE Sensors J.*, vol. 12, no. 8, pp. 2711–2718, Aug. 2012.
- [86] A. Tognetti, R. Bartalesi, F. Lorussi, and D. De Rossi, "Body segment position reconstruction and posture classification by smart textiles," *Trans. Inst. Measurement Control*, vol. 29, no. 3-4, pp. 215–253, Aug. 2007.
- [87] C. T. Huang, C. L. Shen, C. F. Tang, and S. H. Chang, "A wearable yarn-based piezo-resistive sensor," *Sens. Actuator A: Phys.*, vol. 141, no. 2, pp. 396–403, Feb. 2008.
- [88] R. Wijesiriwardana, T. Dias, and S. Mukhopadhyay, "Resistive fibre-meshed transducers," in *Proc. IEEE 7th Int. Symp. Wearable Computers*, White Plains, NY, USA, 2003, pp. 200–209.
- [89] D. De Rossi, F. Carpi, F. Lorussi, A. Mazzoldi, E. Scilingo, and A. Tognetti, "Electroactive fabrics for distributed, conformable and interactive systems," in *Proc. IEEE Sensors 2002*, vol. 2, Orlando, FL, USA, pp. 1608–1613.
- [90] M. Amjadi, K. U. Kyung, I. Park, and M. Sitti, "Stretchable, skin-mountable, and wearable strain sensors and their potential applications: A review," *Adv. Funct. Mater.*, vol. 26, no. 11, pp. 1678–1698, Mar. 2016.
- [91] National Instruments, Corp., "Strain gauge measurement – a tutorial," Austin, Texas, United States, Appl. Note 078, 1998. [Online]. Available: [http://elektron.pol.lublin.pl/elekp/ap\\_notes/NI\\_AN078\\_Strain\\_Gauge\\_Meas.pdf](http://elektron.pol.lublin.pl/elekp/ap_notes/NI_AN078_Strain_Gauge_Meas.pdf)
- [92] F. Lorussi, S. Galatolo, and D. E. De Rossi, "Textile-based electrogoniometers for wearable posture and gesture capture systems," *IEEE Sensors J.*, vol. 9, no. 9, pp. 1014–1024, Sept. 2009.
- [93] P. T. Gibbs and H. Asada, "Wearable conductive fiber sensors for multi-axis human joint angle measurements," *J. Neuroeng. Rehabil.*, vol. 2, p. 7, Mar. 2005.
- [94] M. K. Shin, J. Oh, M. Lima, M. E. Kozlov, S. J. Kim, and R. H. Baughman, "Elastomeric conductive composites based on carbon nanotube forests," *Adv. Mater.*, vol. 22, no. 24, pp. 2663–2667, Jun. 2010.
- [95] S. De, T. M. Higgins, P. E. Lyons, E. M. Doherty, P. N. Nirmalraj, W. J. Blau, J. J. Boland, and J. N. Coleman, "Silver nanowire networks as flexible, transparent, conducting films: Extremely high DC to optical conductivity ratios," *ACS Nano*, vol. 3, no. 7, pp. 1767–1774, Jun. 2009.

- [96] F. Pineda, F. Bottausci, B. Icard, L. Malaquin, and Y. Fouillet, "Using electrofluidic devices as hyper-elastic strain sensors: Experimental and theoretical analysis," *Microelectron. Eng.*, vol. 144, pp. 27–31, Aug. 2015.
- [97] W. Park, K. Ro, S. Kim, and J. Bae, "A soft sensor-based three-dimensional (3-D) finger motion measurement system," *Sensors*, vol. 17, no. 2, p. 420, Feb. 2017.
- [98] G. Saggio, F. Riillo, L. Sbernini, and L. R. Quitadamo, "Resistive flex sensors: A survey," *Smart Mater. Struct.*, vol. 25, no. 1, p. 013001, Dec. 2015.
- [99] Bloomberg L.P., "Company overview of abrams gentile entertainment, inc." [Online]. Available: <https://www.bloomberg.com/research/stocks/private/snapshot.asp?privcapId=995949> (accessed on Sept. 13, 2017).
- [100] ABC News (2008 May 19), "Backwards compatible - the Power Glove." [Online]. Available: <http://www.abc.net.au/tv/goodgame/stories/s2248843.htm> (accessed on Sept. 30, 2017).
- [101] Images Scientific Instruments, Inc., Staten Island, NY, USA. [Online]. Available: <http://www.imagesco.com/> (accessed on Sept. 30, 2017).
- [102] Spectra Symbol Corp., Salt Lake City, UT, USA. [Online]. Available: <http://www.spectrasymbol.com/> (accessed on Sept. 30, 2017).
- [103] Flexpoint Sensor Systems, Inc., Draper, UT, USA. [Online]. Available: <http://www.flexpoint.com/> (accessed on Sept. 30, 2017).
- [104] Images Scientific Instruments, Inc., *Two-Directional Bi-Flex Sensors*, Staten Island, NY, USA. [Online]. Available: <http://www.imagesco.com/sensors/flex-sensor.html> (accessed on Sept. 30, 2017).
- [105] G. Orengo, G. Saggio, S. Bocchetti, and F. Giannini, "Evaluating strain sensor performance for motion analysis," in *Proc. Int. Conf. Biomedical Electronics and Devices*, Rome, Italy, 2011, pp. 244–249.
- [106] G. Costantini, M. Todisco, and G. Saggio, "A wireless glove to perform music in real time," in *Proc. 8th WSEAS Int. Conf. Applied Electromagnetics, Wireless and Optical Communications*, Penang, Malaysia, 2010, pp. 58–60.
- [107] N. W. Williams, J. M. T. Penrose, C. M. Caddy, E. Barnes, D. R. Hose, and P. Harley, "A goniometric glove for clinical hand assessment: Construction, calibration and validation," *J. Hand Surg. Br.*, vol. 25, no. 2, pp. 200–207, Apr. 2000.
- [108] G. Saggio, M. De Sanctis, E. Cianca, G. Latessa, F. De Santis, and F. Giannini, "Long term measurement of human joint movements for health care and rehabilitation purposes," in *2009 1st Int. Conf. Wireless Communication, Vehicular Technology, Information Theory and Aerospace & Electronic Systems Technology*, Aalborg, Denmark, 2009, pp. 674–678.
- [109] SparkFun Electronics, *Flex/Force Sensor*, Niwot, CO, USA. [Online]. Available: <https://www.sparkfun.com/categories/143> (accessed on Sept. 30, 2017).
- [110] G. Saggio, L. Bianchi, S. Castelli, M. B. Santucci, M. Fraziano, and A. Desideri, "In vitro analysis of pyrogenicity and cytotoxicity profiles of flex sensors to be used to sense human joint postures," *Sensors*, vol. 14, no. 7, pp. 11 672–11 681, Jul. 2014.

- [111] M. Borghetti, E. Sardini, and M. Serpelloni, "Evaluation of bend sensors for limb motion monitoring," in *2014 IEEE Int. Symp. Medical Measurements and Applications*, Lisboa, Portugal, 2014, pp. 1–5.
- [112] G. Saggio, "Bend sensor arrays for hand movement tracking in biomedical systems," in *2011 4th IEEE Int. Workshop Advances in Sensors and Interfaces (IWASI)*, Savelletri di Fasano, Italy, pp. 51–54.
- [113] L. K. Simone and D. G. Kamper, "Design considerations for a wearable monitor to measure finger posture," *J. Neuroeng. Rehabil.*, vol. 2, p. 5, Mar. 2005.
- [114] B. O'Flynn, J. Torres, J. Connolly, J. Condell, K. Curran, and P. Gardiner, "Novel smart sensor glove for arthritis rehabilitation," in *Proc. 2013 IEEE Int. Conf. Body Sensor Networks*, Cambridge, MA, USA, pp. 1–6.
- [115] M. Borghetti, E. Sardini, and M. Serpelloni, "Sensorized glove for measuring hand finger flexion for rehabilitation purposes," *IEEE Trans. Instrum. Meas.*, vol. 62, no. 12, pp. 3308–3314, Dec. 2013.
- [116] R. Gentner and J. Classen, "Development and evaluation of a low-cost sensor glove for assessment of human finger movements in neurophysiological settings," *J. Neurosci. Methods*, vol. 178, no. 1, pp. 138–147, Mar. 2009.
- [117] N. P. Oess, J. Wanek, and A. Curt, "Design and evaluation of a low-cost instrumented glove for hand function assessment," *J. Neuroeng. Rehabil.*, vol. 9, p. 2, Jan. 2012.
- [118] L. K. Simone, N. Sundarajan, X. Luo, Y. Jia, and D. G. Kamper, "A low cost instrumented glove for extended monitoring and functional hand assessment," *J. Neurosci. Methods*, vol. 160, no. 2, pp. 335–348, Mar. 2007.
- [119] G. Saggio, "A novel array of flex sensors for a goniometric glove," *Sens. Actuator A: Phys.*, vol. 205, pp. 119–125, Jan. 2014.
- [120] Flexpoint Sensor Systems, Inc., "Mechanical application design guide," Design guide, 2015. [Online]. Available: <http://www.flexpoint.com/media-resources/mechanical-data-sheets/>
- [121] G. Saggio, A. Pallotti, L. Sbernini, V. Errico, and F. Di Paolo, "Feasibility of commercial resistive flex sensors for hand tracking applications," *Sensors Transducers*, vol. 201, no. 6, pp. 17–26, Jun. 2016.
- [122] P. T. Wang, C. E. King, A. H. Do, and Z. Nenadic, "A durable, low-cost electrogoniometer for dynamic measurement of joint trajectories," *Med. Eng. Phys.*, vol. 33, no. 5, pp. 546–552, Jun. 2011.
- [123] S. J. Leigh, R. J. Bradley, C. P. Purssell, D. R. Billson, and D. A. Hutchins, "A simple, low-cost conductive composite material for 3D printing of electronic sensors," *PLoS ONE*, vol. 7, no. 11, p. e49365, Nov. 2012.
- [124] N. Tongrod, S. Lokavee, N. Watthanawisuth, A. Tuantranont, and T. Kerdcharoen, "Design and development of data glove based on printed polymeric sensors and zigbee networks for human–computer interface," *Disabil. Rehabil. Assist. Technol.*, vol. 8, no. 2, pp. 115–120, Mar. 2013.
- [125] G. Latessa, F. Brunetti, A. Reale, G. Saggio, and A. Di Carlo, "Piezoresistive behaviour of flexible PEDOT:PSS based sensors," *Sens. Actuators B: Chem.*, vol. 139, no. 2, pp. 304–309, Jun. 2009.

- [126] J. Jurgens and P. Patterson, "Development and evaluation of an inexpensive sensor system for use in measuring relative finger positions," *Med. Eng. Phys.*, vol. 19, no. 1, pp. 1–6, Jan. 1997.
- [127] T. G. Giallorenzi, J. A. Bucaro, A. Dandridge, G. Sigel, J. H. Cole, S. C. Rashleigh, and R. G. Priest, "Optical fiber sensor technology," *IEEE Trans. Microw. Theory Techn.*, vol. 30, no. 4, pp. 472–511, Apr. 1982.
- [128] J. M. Williams, I. Haq, and R. Y. Lee, "Dynamic measurement of lumbar curvature using fibre-optic sensors," *Med. Eng. Phys.*, vol. 32, no. 9, pp. 1043–1049, Nov. 2010.
- [129] M. Zawawi, S. O’Keeffe, E. Lewis, and K. O’Sullivan, "Extrinsic optical fibre bending sensor for spine monitoring," in *Proc. IEEE Sensors 2015*, Busan, South Korea, 2015, pp. 1–4.
- [130] J. Madrigal, D. Barrera, J. Hervás, H. Chen, and S. Sales, "Directional curvature sensor based on long period gratings in multicore optical fiber," in *2017 25th Optical Fiber Sensors Conference (OFS)*, Jeju, South Korea, pp. 1–4.
- [131] H. Gong, X. Yang, K. Ni, C. Zhao, and X. Dong, "An optical fiber curvature sensor based on two peanut-shape structures modal interferometer," *IEEE Photon. Technol. Lett.*, vol. 26, no. 1, pp. 22–24, Jan. 2014.
- [132] W. N. MacPherson, M. J. Gander, R. McBride, J. D. C. Jones, P. M. Blanchard, J. G. Burnett, A. H. Greenaway, B. Mangan, T. A. Birks, J. C. Knight *et al.*, "Remotely addressed optical fibre curvature sensor using multicore photonic crystal fibre," *Opt. Commun.*, vol. 193, no. 1, pp. 97–104, Jun. 2001.
- [133] A. Taghipour, A. Rostami, M. Bahrami, H. Baghban, and M. Dolatyari, "Comparative study between LPFG- and FBG-based bending sensors," *Opt. Commun.*, vol. 312, pp. 99–105, Feb. 2014.
- [134] A. F. da Silva, A. F. Gonçalves, P. M. Mendes, and J. H. Correia, "FBG sensing glove for monitoring hand posture," *IEEE Sensors J.*, vol. 11, no. 10, pp. 2442–2448, Oct. 2011.
- [135] A. F. da Silva, A. F. Gonçalves, L. A. de Almeida Ferreira, F. M. M. Araújo, P. M. Mendes, and J. H. Correia, "PVC smart sensing foil for advanced strain measurements," *IEEE Sensors J.*, vol. 10, no. 6, pp. 1149–1155, Jun. 2010.
- [136] B. Lee, "Review of the present status of optical fiber sensors," *Opt. Fiber Technol.*, vol. 9, no. 2, pp. 57–79, Apr. 2003.
- [137] M. G. Xu, J. L. Archambault, L. Reekie, and J. P. Dakin, "Thermally-compensated bending gauge using surface-mounted fibre gratings," *Int. J. Optoelectron.*, vol. 9, no. 3, pp. 281–283, 1994.
- [138] M. G. Xu, J. L. Archambault, L. Reekie, and J. P. Dakin, "Discrimination between strain and temperature effects using dual-wavelength fibre grating sensors," *Electron. Lett.*, vol. 30, no. 13, pp. 1085–1087, Jun. 1994.
- [139] H. J. Patrick, G. M. Williams, A. D. Kersey, J. R. Pedrazzani, and A. M. Vengsarkar, "Hybrid fiber Bragg grating/long period fiber grating sensor for strain/temperature discrimination," *IEEE Photon. Technol. Lett.*, vol. 8, no. 9, pp. 1223–1225, Sept. 1996.

- [140] B. O. Guan, H. Y. Tam, X. M. Tao, and X. Y. Dong, "Simultaneous strain and temperature measurement using a superstructure fiber Bragg grating," *IEEE Photon. Technol. Lett.*, vol. 12, no. 6, pp. 675–677, Jun. 2000.
- [141] C. A. Perez-Ramirez, D. L. Almanza-Ojeda, J. N. Guerrero-Tavares, F. J. Mendoza-Galindo, J. M. Estudillo-Ayala, and M. A. Ibarra-Manzano, "An architecture for measuring joint angles using a long period fiber grating-based sensor," *Sensors*, vol. 14, no. 12, pp. 24 483–24 501, Dec. 2014.
- [142] M. Deng, C. P. Tang, T. Zhu, and Y. J. Rao, "Highly sensitive bend sensor based on Mach-Zehnder interferometer using photonic crystal fiber," *Optics Communications*, vol. 284, no. 12, pp. 2849–2853, Mar. 2011.
- [143] M. Nishiyama, H. Sasaki, and K. Watanabe, "Performance characteristics of wearable embedded hetero-core fiber sensors for unconstrained motion analyses," *Trans. Soc. Instrum. Control Engr.*, vol. 43, no. 12, pp. 1075–1081, Dec. 2007.
- [144] M. Nishiyama, H. Sasaki, and K. Watanabe, "A deformation sensitive pad-structure embedded with hetero-core optic fiber sensors," *Sens. Actuator A: Phys.*, vol. 136, no. 1, pp. 205–211, 2007.
- [145] M. Nishiyama and K. Watanabe, "Wearable sensing glove with embedded hetero-core fiber-optic nerves for unconstrained hand motion capture," *IEEE Trans. Instrum. Meas.*, vol. 58, no. 12, pp. 3995–4000, Dec. 2009.
- [146] L. Bilro, N. Alberto, J. L. Pinto, and R. Nogueira, "Optical sensors based on plastic fibers," *Sensors*, vol. 12, no. 9, pp. 12 184–12 207, Sept. 2012.
- [147] L. Bilro, J. G. Oliveira, J. L. Pinto, and R. N. Nogueira, "A reliable low-cost wireless and wearable gait monitoring system based on a plastic optical fibre sensor," *Meas. Sci. Technol.*, vol. 22, no. 4, p. 045801, Mar. 2011.
- [148] A. Babchenko and J. Maryles, "A sensing element based on 3D imperfected polymer optical fibre," *J. Opt. A: Pure Appl.*, vol. 9, no. 1, pp. 1–5, Nov. 2006.
- [149] D. Z. Stupar, J. S. Bajic, L. M. Manojlovic, M. P. Slankamenac, A. V. Joza, and M. B. Zivanov, "Wearable low-cost system for human joint movements monitoring based on fiber-optic curvature sensor," *IEEE Sensors J.*, vol. 12, no. 12, pp. 3424–3431, Dec. 2012.
- [150] S. G. Kim, K. W. Jang, W. J. Yoo, S. H. Shin, S. Cho, and B. Lee, "Feasibility study on fiber-optic goniometer for measuring knee joint angle," *Opt. Rev.*, vol. 21, no. 5, pp. 694–697, Sept. 2014.
- [151] K. S. C. Kuang, W. J. Cantwell, and P. J. Scully, "An evaluation of a novel plastic optical fibre sensor for axial strain and bend measurements," *Meas. Sci. Technol.*, vol. 13, no. 10, pp. 1523–1534, Sept. 2002.
- [152] E. Fujiwara, M. F. M. dos Santos, and C. K. Suzuki, "Flexible optical fiber bending transducer for application in glove-based sensors," *IEEE Sensors J.*, vol. 14, no. 10, pp. 3631–3636, Oct. 2014.
- [153] M. Donno, E. Palange, F. Di Nicola, G. Bucci, and F. Ciancetta, "A new flexible optical fiber goniometer for dynamic angular measurements: Application to human joint movement monitoring," *IEEE Trans. Instrum. Meas.*, vol. 57, no. 8, pp. 1614–1620, Aug. 2008.

- [154] G. I. Jung, J. S. Kim, T. H. Lee, J. H. Choi, H. B. Oh, A. H. Kim, G. M. Eom, J. H. Lee, S. C. Chung, J. R. Park *et al.*, “Development of an optical fiber sensor for angular displacement measurements,” *Biomed. Mater. Eng.*, vol. 24, no. 1, pp. 771–780, 2014.
- [155] Avago Technology Ltd., *ANDS 3530 Low Power LED Integrated Slim Mouse Sensor*, San Jose, CA, USA. [Online]. Available: <https://media.digikey.com/pdf/Data%20Sheets/Avago%20PDFs/ADNS-3530.pdf> (accessed on Apr. 05, 2018).
- [156] C. K. Lim, Z. Luo, I. M. Chen, and S. H. Yeo, “A low cost wearable optical-based goniometer for human joint monitoring,” *Front. Mech. Eng.*, vol. 6, no. 1, pp. 13–22, Mar. 2011.
- [157] C. K. Lim, Z. Q. Luo, I. M. Chen, and S. H. Yeo, “Wearable wireless sensing system for capturing human arm motion,” *Sens. Actuator A: Phys.*, vol. 166, no. 1, pp. 125–132, Mar. 2011.
- [158] T. G. Zimmerman, “Optical flex sensor,” U.S. Patent 4 542 291 A, Sep. 17, 1985.
- [159] A. Cavallo, G. De Maria, C. Natale, and S. Pirozzi, “Optoelectronic joint angular sensor for robotic fingers,” *Sens. Actuator A: Phys.*, vol. 152, no. 2, pp. 203–210, Jun. 2009.
- [160] G. Palli and S. Pirozzi, “Optical sensor for angular position measurements embedded in robotic finger joints,” *Adv. Robot.*, vol. 27, no. 15, pp. 1209–1220, Jun. 2013.
- [161] S. Zhao, Y. Ozturk, and K. S. Moon, “Wireless photoplethysmograph knuckle sensor system for measuring finger motions,” in *2014 Int. Symp. Optomechatronic Technologies*, Seattle, WA, USA, pp. 205–209.
- [162] N. Albion, R. F. Asmar, R. W. Huggins, G. E. Miller, and C. R. Porter, “Optical angle sensor using polarization techniques,” U.S. Patent 5 424 535 A, Jun. 13, 1995.
- [163] W. Li, X. Lu, and Y. Lin, “Novel absolute displacement sensor with wide range based on Malus law,” *Sensors*, vol. 9, no. 12, pp. 10 411–10 422, Dec. 2009.
- [164] S. Ikeda, E. Higurashi, T. Suga, and T. Oguchi, “Miniaturized polarization sensors integrated with wire-grid polarizers,” in *2014 Int. Conf. Electronics Packaging*, Toyama, Japan, pp. 376–379.
- [165] G. Ligorio, E. Bergamini, I. Pasciuto, G. Vannozzi, A. Cappozzo, and A. M. Sabatini, “Assessing the performance of sensor fusion methods: Application to magnetic-inertial-based human body tracking,” *Sensors*, vol. 16, no. 2, p. 153, Jan. 2016.
- [166] K. Hirose, H. Doki, and A. Kondo, “A measurement method of the 2DOF joint angles and angular velocities using inertial sensors,” in *2012 Proc. SICE Annu. Conf.*, Akita, Japan, 2012, pp. 366–371.
- [167] J. L. Hernandez-Rebollar, N. Kyriakopoulos, and R. W. Lindeman, “A new instrumented approach for translating American Sign Language into sound and text,” in *Proc. 6th IEEE Int. Conf. Automatic Face and Gesture Recognition*, Seoul, South Korea, 2004, pp. 547–552.

- [168] J. L. Hernandez-Rebollar, N. Kyriakopoulos, and R. W. Lindeman, "The AcceleGlove: A whole-hand input device for virtual reality," in *Proc. ACM SIGGRAPH 2002 Conf. Abstracts and Applications*, San Antonio, TX, USA, p. 259.
- [169] F. A. Dwiputra, B. Achmad *et al.*, "Accelerometer-based recorder of fingers dynamic movements for post-stroke rehabilitation," *Int. J. Adv. Sci., Eng. Inf. Technol.*, vol. 7, no. 1, pp. 299–304, 2017.
- [170] I. H. López-Nava and A. Muñoz-Meléndez, "Wearable inertial sensors for human motion analysis: A review," *IEEE Sensors J.*, vol. 16, no. 22, pp. 7821–7834, Nov. 2016.
- [171] G. Cooper, I. Sheret, L. McMillian, K. Siliverdis, N. Sha, D. Hodgins, L. Kenney, and D. Howard, "Inertial sensor-based knee flexion/extension angle estimation," *J. Biomech.*, vol. 42, no. 16, pp. 2678–2685, Feb. 2009.
- [172] M. El-Gohary and J. McNames, "Shoulder and elbow joint angle tracking with inertial sensors," *IEEE Trans. Biomed. Eng.*, vol. 59, no. 9, pp. 2635–2641, Sept. 2012.
- [173] T. Seel, J. Raisch, and T. Schauer, "IMU-based joint angle measurement for gait analysis," *Sensors*, vol. 14, no. 4, pp. 6891–6909, Apr. 2014.
- [174] H. Dai, H. Lin, and T. C. Lueth, "Quantitative assessment of parkinsonian bradykinesia based on an inertial measurement unit," *Biomed. Eng. Online*, vol. 14, p. 68, Jul. 2015.
- [175] J. C. van den Noort, H. G. Kortier, N. van Beek, D. H. Veeger, and P. H. Veltink, "Measuring 3D hand and finger kinematics - a comparison between inertial sensing and an opto-electronic marker system," *PLoS ONE*, vol. 11, no. 11, p. e0164889, Nov. 2016.
- [176] Y. S. Kim, B. S. Soh, and S. G. Lee, "A new wearable input device: SCURRY," *IEEE Trans. Ind. Electron.*, vol. 52, no. 6, pp. 1490–1499, Dec. 2005.
- [177] H. G. Kortier, J. Antonsson, H. M. Schepers, F. Gustafsson, and P. H. Veltink, "Hand pose estimation by fusion of inertial and magnetic sensing aided by a permanent magnet," *IEEE Trans. Neural Syst. Rehabil. Eng.*, vol. 23, no. 5, pp. 796–806, Sept. 2015.
- [178] C. M. N. Brigante, N. Abbate, A. Basile, A. C. Faulisi, and S. Sessa, "Towards miniaturization of a MEMS-based wearable motion capture system," *IEEE Trans. Ind. Electron.*, vol. 58, no. 8, pp. 3234–3241, Aug. 2011.
- [179] I. Prayudi and D. Kim, "Design and implementation of IMU-based human arm motion capture system," in *2012 IEEE Int. Conf. Mechatronics and Automation*, Chengdu, China, pp. 670–675.
- [180] A. H. Moreira, S. Queirós, J. Fonseca, P. L. Rodrigues, N. F. Rodrigues, and J. L. Vilaça, "Real-time hand tracking for rehabilitation and character animation," in *2014 IEEE 3rd Int. Conf. Serious Games and Applications for Health (SeGAH)*, Rio de Janeiro, Brazil, pp. 1–8.
- [181] Y. Choi, K. Yoo, S. J. Kang, B. Seo, and S. K. Kim, "Development of a low-cost wearable sensing glove with multiple inertial sensors and a light and fast orientation estimation algorithm," *J. Supercomput.*, pp. 1–14, Aug. 2016.

- [182] S. Fantozzi, A. Giovanardi, D. Borra, and G. Gatta, "Gait kinematic analysis in water using wearable inertial magnetic sensors," *PLoS ONE*, vol. 10, no. 9, p. e0138105, Sept. 2015.
- [183] P. Picerno, A. Cereatti, and A. Cappozzo, "Joint kinematics estimate using wearable inertial and magnetic sensing modules," *Gait Posture*, vol. 28, no. 4, pp. 588–595, Nov. 2008.
- [184] H. G. Kortier, V. I. Sluiter, D. Roetenberg, and P. H. Veltink, "Assessment of hand kinematics using inertial and magnetic sensors," *J. Neuroeng. Rehabil.*, vol. 11, p. 70, Apr. 2014.
- [185] K. Kawano, S. Kobashi, M. Yagi, K. Kondo, S. Yoshiya, and Y. Hata, "Analyzing 3D knee kinematics using accelerometers, gyroscopes and magnetometers," in *2007 IEEE Int. Conf. System of Systems Engineering*, San Antonio, TX, USA, pp. 1–6.
- [186] K. Liu, T. Liu, K. Shibata, and Y. Inoue, "Ambulatory measurement and analysis of the lower limb 3D posture using wearable sensor system," in *2009 Int. Conf. Mechatronics and Automation*, Changchun, China, pp. 3065–3069.
- [187] M. Valtin, C. Salchow, T. Seel, D. Laidig, and T. Schauer, "Modular finger and hand motion capturing system based on inertial and magnetic sensors," *Current Directions Biomed. Eng.*, vol. 3, no. 1, pp. 19–23, Mar. 2017.
- [188] B. O'flynn, J. T. Sanchez, J. Connolly, J. Condell, K. Curran, P. Gardiner, and B. Downes, "Integrated smart glove for hand motion monitoring," in *Proc. 6th Int. Conf. Sensor Device Technologies and Applications*, Venize, Italy, 2015.
- [189] Northern Digital Inc. (NDI), *Optotrak 3020*, Ontario, Canada. [Online]. Available: <https://www.ndigital.com/msci/products/optotrak-certus/> (accessed on Sept. 30, 2017).
- [190] B. Fang, F. Sun, H. Liu, and D. Guo, "A novel data glove for fingers motion capture using inertial and magnetic measurement units," in *2016 IEEE Int. Conf. Robotics and Biomimetics (ROBIO)*, Qingdao, China, pp. 2099–2104.
- [191] J. D. Lemos, A. M. Hernandez, and G. Soto-Romero, "An instrumented glove to assess manual dexterity in simulation-based neurosurgical education," *Sensors*, vol. 17, no. 5, p. 988, Apr. 2017.
- [192] T. Mańkowski, J. Tomczyński, and P. Kaczmarek, "CIE-DataGlove, a multi-IMU system for hand posture tracking," in *Proc. Int. Conf. Automation 2017*, Warsaw, Poland, pp. 268–276.
- [193] Q. Wang, P. Markopoulos, B. Yu, W. Chen, and A. Timmermans, "Interactive wearable systems for upper body rehabilitation: A systematic review," *J. Neuroeng. Rehabil.*, vol. 14, p. 20, Mar. 2017.
- [194] T. Kuroda, Y. Tabata, A. Goto, H. Ikuta, M. Murakami *et al.*, "Consumer price data-glove for sign language recognition," in *Proc. 5th Int Conf. Disability, Virtual Reality Associated Technologies*, Oxford, UK, 2004, pp. 253–258.
- [195] Encoder Technology, LLC., "A discussion of encoder technology's converter and impedance detector technology," Units 5 & 6 Leatherhead Ind. Est, Leatherhead, Tech. Rep., 2000. [Online]. Available: <https://www.encoder-technology.com/>

- [196] C. S. Fahn and H. Sun, "Development of a fingertip glove equipped with magnetic tracking sensors," *Sensors*, vol. 10, no. 2, pp. 1119–1140, Jan. 2010.
- [197] K. Y. Chen, K. Lyons, S. White, and S. Patel, "uTrack: 3D input using two magnetic sensors," in *Proc. 26th Annu. ACM Symp. User Interface Software and Technology*, St. Andrews, UK, 2013, pp. 237–244.
- [198] K. Y. Chen, S. N. Patel, and S. Keller, "Finexus: Tracking precise motions of multiple fingertips using magnetic sensing," in *Proc. 2016 CHI Conf. Human Factors in Computing Systems*, San Jose, CA, USA, 2016, pp. 1504–1514.
- [199] Vicon Motion Systems Ltd., Centennial, CO, USA. [Online]. Available: <https://www.vicon.com/> (accessed on Sept. 30, 2017).
- [200] N. Friedman, J. B. Rowe, D. J. Reinkensmeyer, and M. Bachman, "The manometer: A wearable device for monitoring daily use of the wrist and fingers," *IEEE J. Biomed. Health Inform.*, vol. 18, no. 6, pp. 1804–1812, Nov. 2014.
- [201] S. Yao and Y. Zhu, "Wearable multifunctional sensors using printed stretchable conductors made of silver nanowires," *Nanoscale*, vol. 6, pp. 2345–2352, Dec. 2014.
- [202] Y. Cha, J. Seo, J. S. Kim, and J. M. Park, "Human–computer interface glove using flexible piezoelectric sensors," *Smart Mater. Struct.*, vol. 26, no. 5, p. 057002, Apr. 2017.
- [203] Microsoft Corp., *Kinect for Xbox One*, Washington, DC, USA. [Online]. Available: <https://www.xbox.com/en-GB/xbox-one/accessories/kinect> (accessed on Sept. 30, 2017).
- [204] F. Hernoux and O. Christmann, "A seamless solution for 3D real-time interaction: Design and evaluation," *Virtual Reality*, vol. 19, no. 1, pp. 1–20, Mar. 2015.
- [205] M. Z. A. Bakar, R. Samad, D. Pebrianti, M. Mustafa, and N. R. H. Abdullah, "Finger application using K-Curvature method and Kinect sensor in real-time," in *2015 Int. Symp. Technology Management and Emerging Technologies (ISTMET)*, Langkawai Island, Malaysia, pp. 218–222.
- [206] Y. Tian, X. Meng, D. Tao, D. Liu, and C. Feng, "Upper limb motion tracking with the integration of IMU and Kinect," *Neurocomputing*, vol. 159, pp. 207–218, Jul. 2015.
- [207] H. Mnyusiwalla, P. Vulliez, J. P. Gazeau, and S. Zeghloul, "A new dexterous hand based on bio-inspired finger design for inside-hand manipulation," *IEEE Trans. Syst., Man, Cybern., Syst.*, vol. 46, no. 6, pp. 809–817, Jun. 2016.
- [208] G. Gerboni, A. Diodato, G. Ciuti, M. Cianchetti, and A. Menciassi, "Feedback control of soft robot actuators via commercial flex bend sensors," *IEEE/ASME Trans. Mechatronics*, vol. 22, no. 4, pp. 809–817, Aug. 2017.
- [209] G. Saggio, G. Latessa, F. De Santis, L. Bianchi, L. R. Quitadamo, M. G. Marciani, and F. Giannini, "Virtual reality implementation as a useful software tool for e-health applications," in *Proc. 2009 IEEE Int. Symp. a World of Wireless, Mobile and Multimedia Networks & Workshops*, Kos, Greece, pp. 1–6.

- [210] F. W. B. Li, R. W. H. Lau, and F. F. C. Ng, "VSculpt: A distributed virtual sculpting environment for collaborative design," *IEEE Trans. Multimedia*, vol. 5, no. 4, pp. 570–580, Dec. 2003.
- [211] K. Mitobe, T. Kaiga, T. Yukawa, T. Miura, H. Tamamoto, A. Rodgers, and N. Yoshimura, "Development of a motion capture system for a hand using a magnetic three dimensional position sensor," in *33th Int. Conf. and Exhibition Computer Graphics and Interactive Techniques (SIGGRAPH2006 Research Posters)*, Boston, MA, USA, p. 102.
- [212] G. J. Grimes, "Digital data entry glove interface device," U.S. Patent 4 414 537 A, Nov. 8, 1983.
- [213] MIT Media Lab, Cambridge, MA, USA. [Online]. Available: <https://www.media.mit.edu/> (accessed on Sept. 30, 2017).
- [214] J. Park and Y.-L. Yoon, "LED-Glove based interactions in multi-modal displays for teleconferencing," in *16th Int. Conf. Artificial Reality and Telexistence-Workshops*, Hangzhou, China, 2006, pp. 395–399.
- [215] G. S. Rash, P. P. Belliappa, M. P. Wachowiak, N. N. Somia, and A. Gupta, "A demonstration of the validity of a 3-D video motion analysis method for measuring finger flexion and extension," *J. Biomech.*, vol. 32, no. 12, pp. 1337–1341, Dec. 1999.
- [216] C. Theobalt, I. Albrecht, J. Haber, M. Magnor, and H.-P. Seidel, "Pitching a baseball: Tracking high-speed motion with multi-exposure images," in *Proc. 31st Int. Conf. Computer Graphics and Interactive Techniques (SIGGRAPH '04)*, Los Angeles, CA, USA, 2004, pp. 540–547.
- [217] P. Cerveri, E. De Momi, N. Lopomo, G. Baud-Bovy, R. M. L. Barros, and G. Ferrigno, "Finger kinematic modeling and real-time hand motion estimation," *Ann. Biomed. Eng.*, vol. 35, no. 11, pp. 1989–2002, Nov. 2007.
- [218] I. Guskov, S. Klibanov, and B. Bryant, "Trackable surfaces," in *Proc. 2003 ACM SIGGRAPH/Eurographics Symp. Computer Animation*, San Diego, CA, USA, pp. 251–257.
- [219] R. Y. Wang and J. Popović, "Real-time hand-tracking with a color glove," in *ACM Transactions on Graphics (TOG) - Proc. ACM SIGGRAPH 2009*, vol. 28, no. 3, New Orleans, LA, USA, p. 63.
- [220] K. Abe, H. Saito, and S. Ozawa, "Virtual 3-D interface system via hand motion recognition from two cameras," *IEEE Trans. Syst., Man, Cybern. A, Syst., Humans*, vol. 32, no. 4, pp. 536–540, Jul. 2002.
- [221] B. Stenger, A. Thayananthan, P. H. Torr, and R. Cipolla, "Model-based hand tracking using a hierarchical Bayesian filter," *IEEE Trans. Pattern Anal. Mach. Intell.*, vol. 28, no. 9, pp. 1372–1384, Sept. 2006.
- [222] M. Donoser and H. Bischof, "Real time appearance based hand tracking," in *2008 19th Int. Conf. Pattern Recognition*, Tampa, FL, USA, pp. 1–4.
- [223] C. S. Lee, S. Y. Chun, and S. W. Park, "Tracking hand rotation and various grasping gestures from an IR camera using extended cylindrical manifold embedding," *Comput. Vis. Image Underst.*, vol. 117, no. 12, pp. 1711–1723, Dec. 2013.

- [224] H. Zhou and H. Hu, "Human motion tracking for rehabilitation - a survey," *Biomed. Signal Proces. Control*, vol. 3, no. 1, pp. 1–18, Jan. 2008.
- [225] OptiTrack, London, UK. [Online]. Available: <https://optitrack.com/> (accessed on Sept. 30, 2017).
- [226] E. B. Sudderth, M. I. Mandel, W. T. Freeman, and A. S. Willsky, "Distributed occlusion reasoning for tracking with nonparametric belief propagation," in *Proc. Advances in Neural Information Processing Systems (NIPS 2004)*, Vancouver, BC, Canada, pp. 1369–1376.
- [227] Y. Zhu, G. Xu, and D. J. Kriegman, "A real-time approach to the spotting, representation, and recognition of hand gestures for human–computer interaction," *Comput. Vis. Image Underst.*, vol. 85, no. 3, pp. 189–208, Mar. 2002.
- [228] R. Rosales, V. Athitsos, L. Sigal, and S. Sclaroff, "3D hand pose reconstruction using specialized mappings," in *Proc. 8th IEEE Int. Conf. Computer Vision*, vol. 1, Vancouver, BC, Canada, 2001, pp. 378–385.
- [229] R. J. Smith, F. Tenore, D. Huberdeau, R. Etienne-Cummings, and N. V. Thakor, "Continuous decoding of finger position from surface EMG signals for the control of powered prostheses," in *30th Annu. Int. Conf. IEEE Engineering in Medicine and Biology Society*, Vancouver, BC, Canada, 2008, pp. 197–200.
- [230] Y. Huang and H. Liu, "Performances of surface EMG and ultrasound signals in recognizing finger motion," in *2016 9th Int. Conf. Human System Interactions (HSI)*, Portsmouth, UK, pp. 117–122.
- [231] J. Kawaguchi, S. Yoshimoto, Y. Kuroda, and O. Oshiro, "Estimation of finger joint angles based on electromechanical sensing of wrist shape," *IEEE Trans. Neural Syst. Rehabil. Eng.*, vol. 25, no. 9, pp. 1409–1418, Sept. 2017.
- [232] X. Chen, X. Zhang, Z. Zhao, J. Yang, V. Lantz, and K. Wang, "Multiple hand gesture recognition based on surface EMG signal," in *2007 1st Int. Conf. Bioinformatics and Biomedical Engineering*, Wuhan, China, pp. 506–509.
- [233] A. Hiraiwa, K. Shimohara, and Y. Tokunaga, "EMG pattern analysis and classification by neural network," in *Proc. IEEE Int. Conf. Systems, Man and Cybernetics*, Cambridge, MA, USA, 1989, pp. 1113–1115.
- [234] N. P. Reddy and V. Gupta, "Toward direct biocontrol using surface EMG signals: Control of finger and wrist joint models," *Med. Eng. Phys.*, vol. 29, no. 3, pp. 398–403, Apr. 2007.
- [235] C. Ishii, "Recognition of finger motions for myoelectric prosthetic hand via surface EMG," in *Advances in Mechatronics*, H. Martinez-Alfaro, Ed. Croatia: InTech, 2011, ch. 8. [Online]. Available: <https://www.intechopen.com/books/advances-in-mechatronics/recognition-of-finger-motions-for-myoelectric-prosthetic-hand-via-surface-emg>
- [236] M. R. Ahsan, M. I. Ibrahimy, O. O. Khalifa *et al.*, "EMG signal classification for human computer interaction: A review," *Eur. J. Sci. Res.*, vol. 33, no. 3, pp. 480–501, Jan. 2009.
- [237] J. Kawaguchi, S. Yoshimoto, M. Imura, and O. Oshiro, "Finger joint angle estimation from electrical contact resistance," *Electron. Commun. Japan*, vol. 100, no. 6, pp. 35–44, Jun. 2017.

- [238] L. Pan, D. Zhang, J. Liu, X. Sheng, and X. Zhu, "Continuous estimation of finger joint angles under different static wrist motions from surface EMG signals," *Biomed. Signal Process. Control*, vol. 14, pp. 265–271, Nov. 2014.
- [239] M. Gazzoni, N. Celadon, D. Mastrapasqua, M. Paleari, V. Margaria, and P. Ariano, "Quantifying forearm muscle activity during wrist and finger movements by means of multi-channel electromyography," *PLoS ONE*, vol. 9, no. 10, p. e109943, Oct. 2014.
- [240] U. Çulha and F. Iida, "Enhancement of finger motion range with compliant anthropomorphic joint design," *Bioinspir. Biomim.*, vol. 11, no. 2, p. 026001, Feb. 2016.
- [241] CyberGlove Systems LLC., San Jose, CA, USA. [Online]. Available: <http://www.cyberglovesystems.com/> (accessed on: Sept. 28, 2017).
- [242] Fifth Dimension Technologies (5DT), *Data Gloves*, Orlando, FL, USA. [Online]. Available: <http://www.5dt.com/data-gloves/> (accessed on: Sept. 28, 2017).
- [243] Humanware S.r.l., *HumanGlove*, Pisa, Italy. [Online]. Available: <http://www.hmw.it/en/humanglove.html> (accessed on: Feb. 03, 2017).
- [244] G. D. Kessler, L. F. Hodges, and N. Walker, "Evaluation of the CyberGlove as a whole-hand input device," *ACM Trans. Comput. Hum. Interact.*, vol. 2, no. 4, pp. 263–283, Dec. 1995.
- [245] P. Weber, E. Rueckert, R. Calandra, J. Peters, and P. Beckerle, "A low-cost sensor glove with vibrotactile feedback and multiple finger joint and hand motion sensing for human-robot interaction," in *2016 25th IEEE Int. Symp. Robot and Human Interactive Communication (RO-MAN)*, New York, NY, USA, pp. 99–104.
- [246] D. H. Kim, S. W. Lee, and H. S. Park, "Improving kinematic accuracy of soft wearable data gloves by optimizing sensor locations," *Sensors*, vol. 16, no. 6, p. 766, May 2016.
- [247] Dassault Systèmes SolidWorks Corp., *SolidWorks2015*, Waltham, MA, USA. [Online]. Available: <https://www.solidworks.com/> (accessed on Sept. 30, 2017).
- [248] EnvisionTEC, Inc., *Perfactory P3 Mini Multi Lens 3D Printer*, Dearborn, MI, USA. [Online]. Available: <https://envisiontec.com/3d-printers/perfactory-family/3-mini-multi-lens/> (accessed on Aug. 29, 2017).
- [249] EnvisionTEC, Inc., *RCP30*, Dearborn, MI, USA. [Online]. Available: <https://envisiontec.com/3d-printing-materials/perfactory-materials/rcp30/> (accessed on Aug. 29, 2017).
- [250] Farnell element14, *LED - KPG-1608ZGC*, Leeds, UK. [Online]. Available: <http://uk.farnell.com/kingbright/kpg-1608zgc/led-smd-0603-grn/dp/1686061> (accessed on Sept. 30, 2017).
- [251] E. O. Ltd., *High Contrast Linear Polarizing Film*, York, UK. [Online]. Available: <https://www.edmundoptics.co.uk/optics/polarizers/linear-polarizers/High-Contrast-Linear-Polarizing-Film/> (accessed on Sept. 30, 2017).

- [252] Farnell element14, *Photodiode - TEMD6200FX01*, Leeds, UK. [Online]. Available: <http://uk.farnell.com/vishay/temd6200fx01/ambient-light-sensor-0805/dp/2504146> (accessed on Sept. 30, 2017).
- [253] Thorlabs, Inc., *Black Masking Tape*, Ely, UK. [Online]. Available: <https://www.thorlabs.com/thorproduct.cfm?partnumber=T205-1.0> (accessed on Sept. 30, 2017).
- [254] Thorlabs, Inc., *NanoRotator Stage*, Ely, UK. [Online]. Available: <https://www.thorlabs.com/thorproduct.cfm?partnumber=NR360S/M> (accessed on Sept. 30, 2017).
- [255] Thorlabs, Inc., Ely, UK. [Online]. Available: <https://www.thorlabs.com/> (accessed on Sept. 30, 2017).
- [256] Thorlabs, Inc., *APT Stepper Motor Controllers*, Ely, UK. [Online]. Available: <https://www.thorlabs.com/thorproduct.cfm?partnumber=BSC201> (accessed on Sept. 30, 2017).
- [257] National Instruments, Corp., *LabVIEW*, Austin, TX, USA. [Online]. Available: <http://www.ni.com/en-gb/shop/labview.html> (accessed on Sept. 30, 2017).
- [258] The MathWorks, Inc., *MATLAB*, Cambridge, UK. [Online]. Available: <https://uk.mathworks.com/products/matlab.html> (accessed on Sept. 30, 2017).
- [259] Microsoft Corp., *Microsoft Visual C++*, Washington, DC, USA. [Online]. Available: <https://www.visualstudio.com/> (accessed on Sept. 30, 2017).
- [260] National Instruments, Corp., *USB-6211 Multifunction I/O Device*, Austin, TX, USA. [Online]. Available: <http://www.ni.com/en-gb/support/model.usb-6211.html> (accessed on Sept. 30, 2017).
- [261] G. Saggio, "Mechanical model of flex sensors used to sense finger movements," *Sens. Actuator A: Phys.*, vol. 185, pp. 53–58, 2012.
- [262] F. Tavernier and M. Steyaert, "From light to electric current-the photodiode," in *High-speed optical receivers with integrated photodiode in nanoscale CMOS*, 1st ed. NY, USA: Springer-Verlag New York, 2011, ch. 3, pp. 41–76.
- [263] Farnell element14, *Operational Amplifier-LTC6244HVIMS8#PBF*, Leeds, UK. [Online]. Available: [http://uk.farnell.com/linear-technology/ltc6244hvims8-pbf/cmos-op-amp-dual-50mhz-ln-8msop/dp/1715054?ost=1715054&isrcfnonsku=false&ddkey=http%3Aen-GB%2FElement14\\_United\\_Kingdom%2Fsearch](http://uk.farnell.com/linear-technology/ltc6244hvims8-pbf/cmos-op-amp-dual-50mhz-ln-8msop/dp/1715054?ost=1715054&isrcfnonsku=false&ddkey=http%3Aen-GB%2FElement14_United_Kingdom%2Fsearch) (accessed on Sept. 30, 2017).
- [264] Farnell element14, *Operational Amplifier-TLC2274CNE4*, Leeds, UK. [Online]. Available: [http://uk.farnell.com/texas-instruments/tlc2274cne4/op-amp-quad-cmos-rro-p-2274-pdip/dp/1234680?ost=TLC2274CNE4&isrcfnonsku=false&ddkey=http%3Aen-GB%2FElement14\\_United\\_Kingdom%2Fsearch](http://uk.farnell.com/texas-instruments/tlc2274cne4/op-amp-quad-cmos-rro-p-2274-pdip/dp/1234680?ost=TLC2274CNE4&isrcfnonsku=false&ddkey=http%3Aen-GB%2FElement14_United_Kingdom%2Fsearch) (accessed on Sept. 30, 2017).
- [265] J. G. da Silva, A. A. de Carvalho, and D. D. da Silva, "A strain gauge tactile sensor for finger-mounted applications," *IEEE Trans. Instrum. Meas.*, vol. 51, no. 1, pp. 18–22, Feb. 2002.
- [266] S. Wise, W. Gardner, E. Sabelman, E. Valainis, Y. Wong, K. Glass, J. Drace, and J. M. Rosen, "Evaluation of a fiber optic glove for semi-automated goniometric measurements," *J. Rehabil. Res. Dev.*, vol. 27, no. 4, p. 411, Fall 1990.

- [267] G. Saggio, A. Lagati, and G. Orenco, "Shaping resistive bend sensors to enhance readout linearity," *ISRN Electron.*, vol. 2012, 2012.
- [268] L. Wang, T. Meydan, P. Williams, and T. Kutrowski, "A proposed optical-based sensor for assessment of hand movement," in *Proc. IEEE Sensors 2015*, Busan, South Korea, pp. 1–4.
- [269] N. P. Oess, J. Wanek, and H. J. A. van Hedel, "Enhancement of bend sensor properties as applied in a glove for use in neurorehabilitation settings," in *2010 Annu. Int. Conf. IEEE Engineering in Medicine and Biology Society*, Buenos Aires, Argentina, pp. 5903–5906.
- [270] G. Orenco, A. Lagati, and G. Saggio, "Modeling and comparing the linear performance of non-uniform geometry bend sensors," in *3rd Int. Conf. Sensor Device Technologies and Applications*, Rome, Italy, 2012, pp. 52–55.
- [271] The ComPADRE Digital Resources for Physics & Astronomy Education, *Tracker Video Analysis and Modeling Tool*, ver. 4.9.8. [Online]. Available: <http://physlets.org/tracker/> (accessed on Sept. 30, 2017).
- [272] Farnell element14, *Digital Angle Ruler*, Leeds, UK. [Online]. Available: <http://uk.farnell.com/duratool/d01909/angle-ruler-digital/dp/2444479> (accessed on Dec. 12, 2017).

# **Appendix A**

## **Technical Drawings of the Electro-optical Goniometric Sensors**

**Technical drawing of sensor#1**

**Technical drawing of sensor#2**

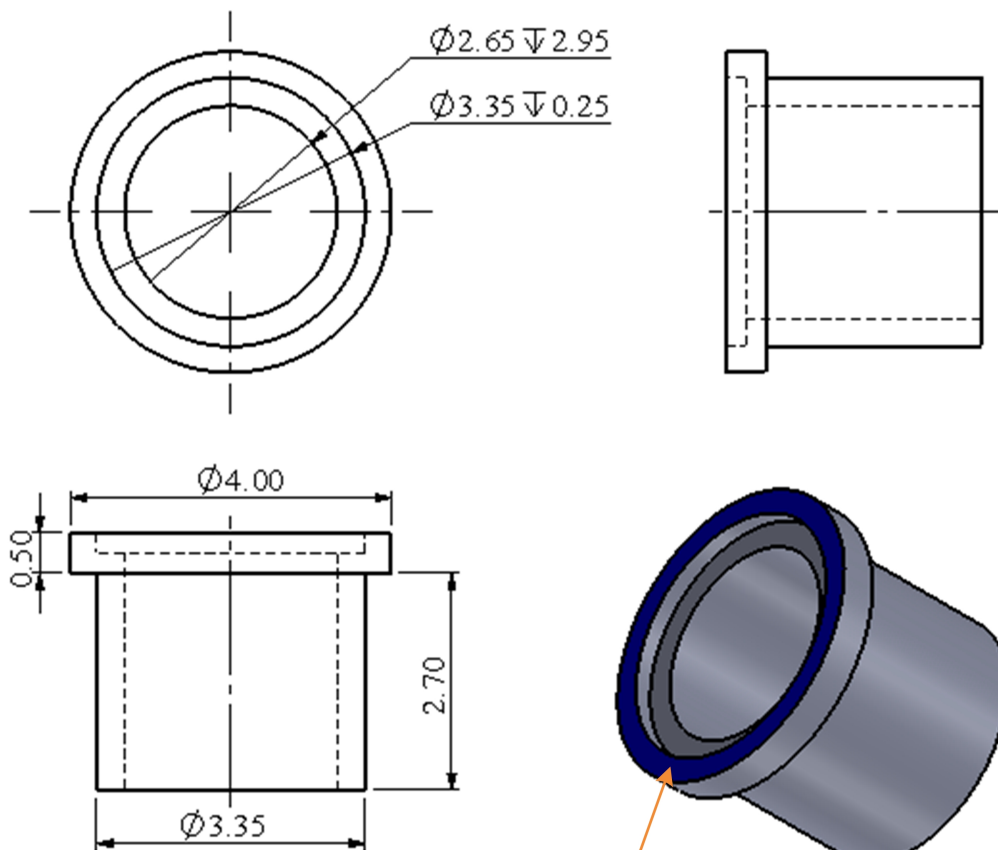
**Technical drawing of sensor#3**

## Technical drawing of sensor#1

The 3D components designed for the integration of sensor#1 comprise Photodiode holder, Holder for LED and polariser, Analyser holder, Wing 1, and Wing 2. Their technical drawings are presented as follows.

### Photodiode holder of sensor#1

Unit: millimetre

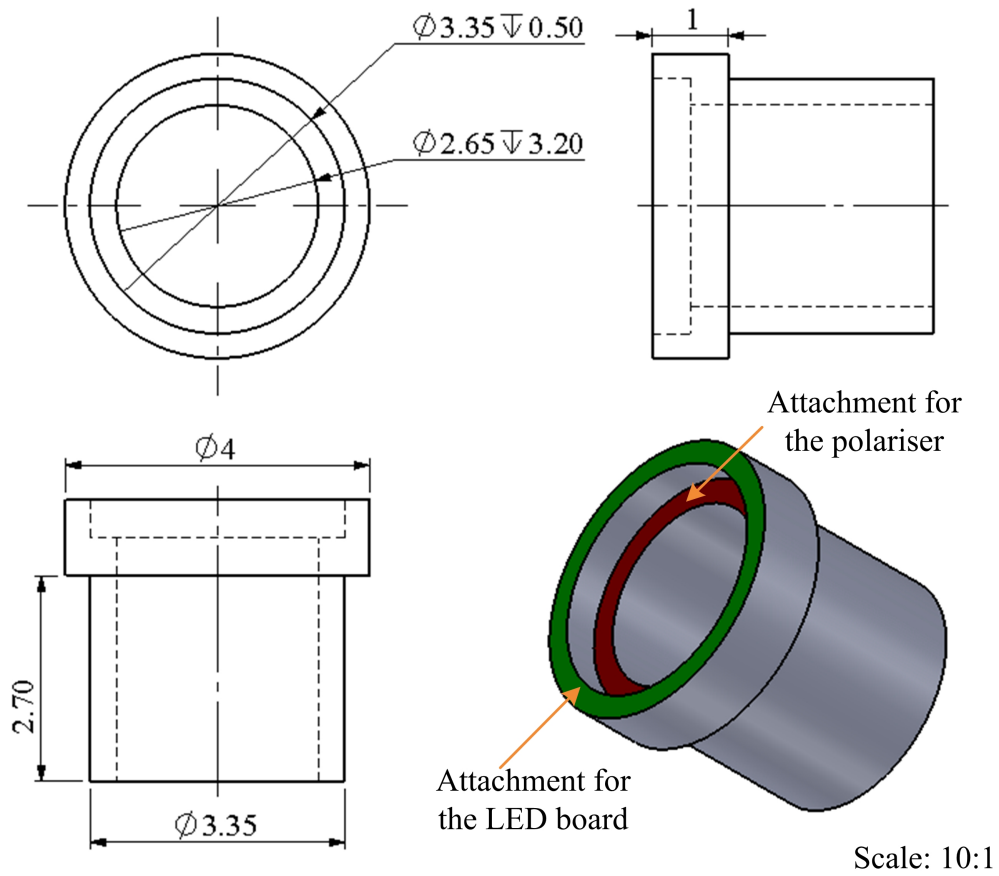


Scale: 10:1

Attachment for the photodiode board

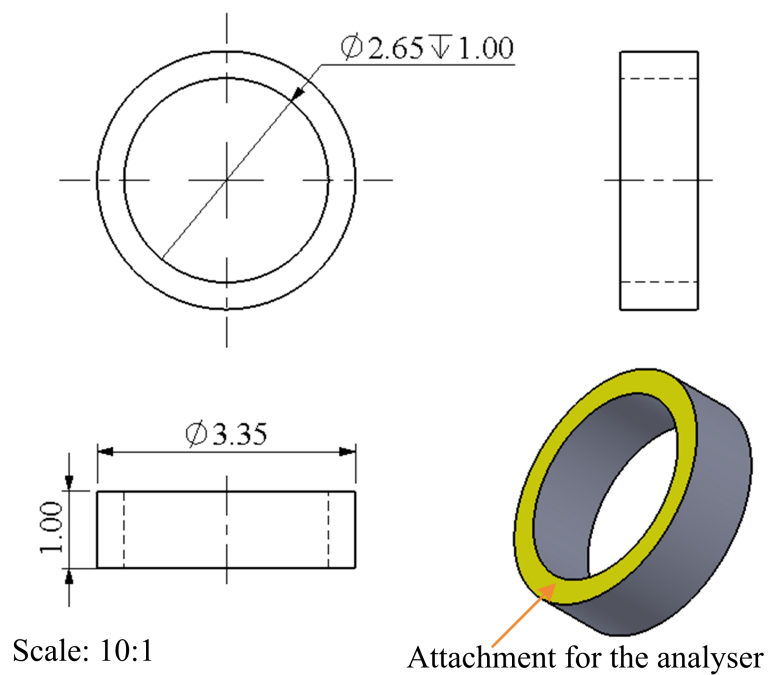
### Holder for LED and polariser of sensor#1

Unit: millimetre



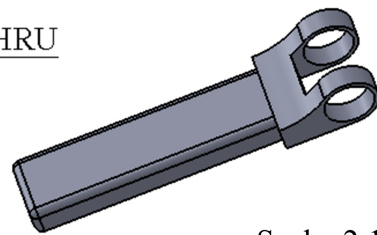
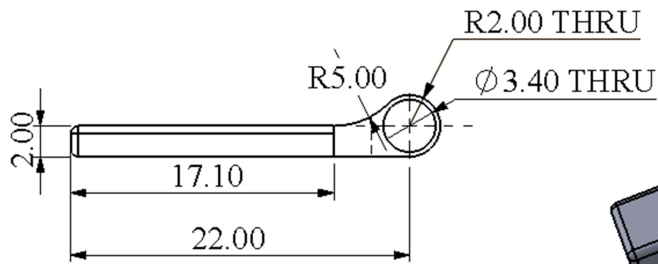
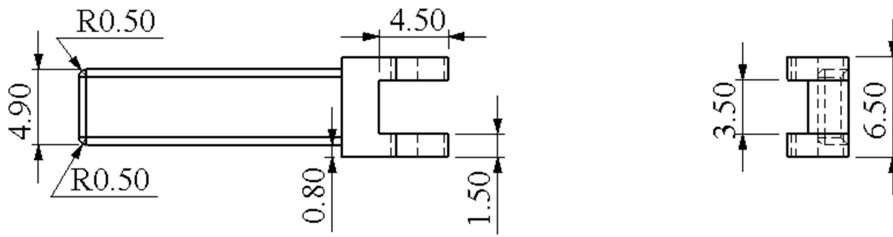
### Analyser holder of sensor#1

Unit: millimetre



**Wing 1 of sensor#1**

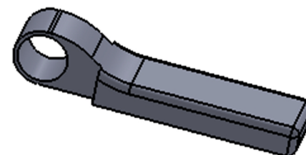
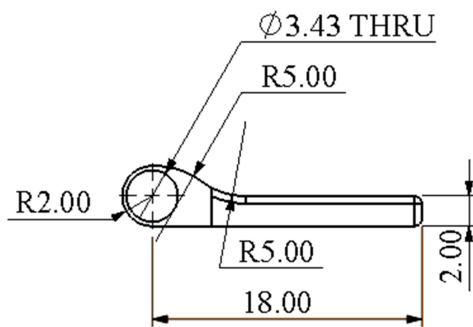
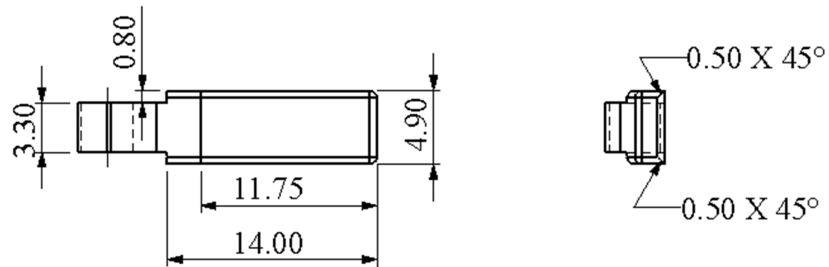
Unit: millimetre



Scale: 2:1

**Wing 2 of sensor#1**

Unit: millimetre



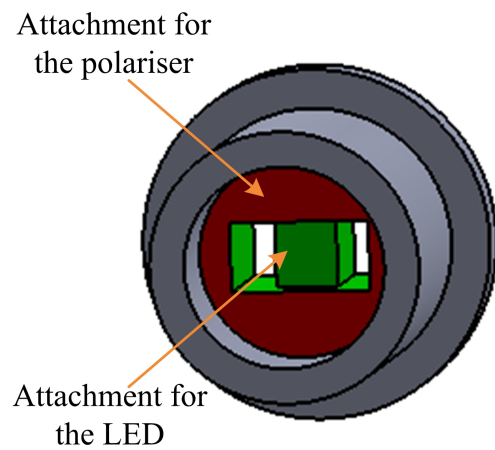
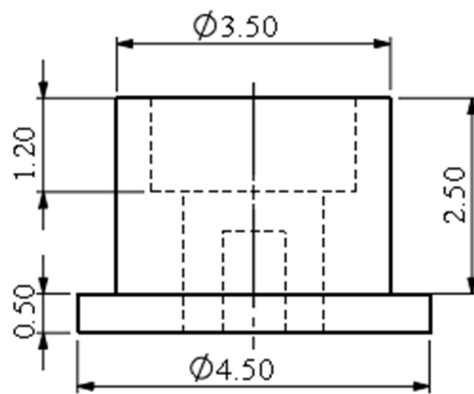
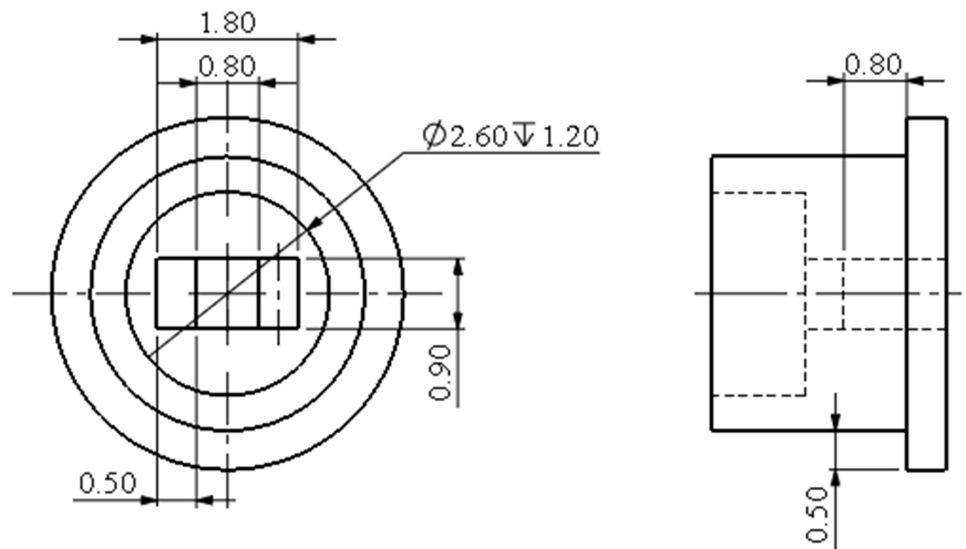
Scale: 2:1

## Technical drawing of sensor#2

The 3D components for sensor#2 consist of Holder for LED and polariser, Wing 1, Wing 2, and Holder for wires. Their technical drawings are shown below.

### Holder for LED and polariser of sensor#2

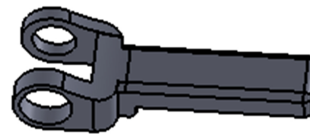
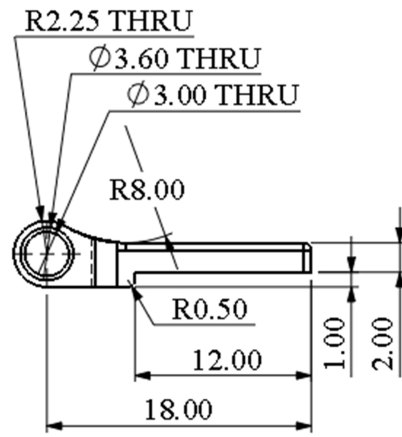
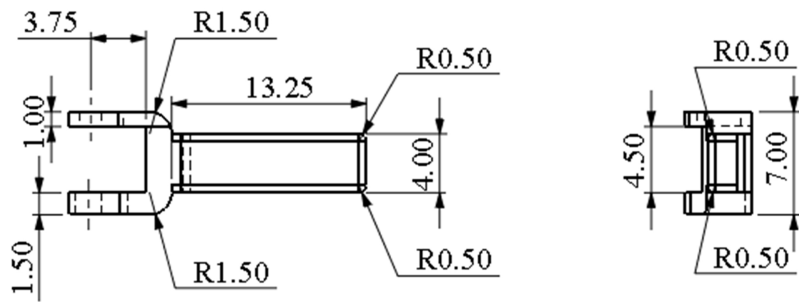
Unit: millimetre



Scale: 10:1

Wing 1 of sensor#2

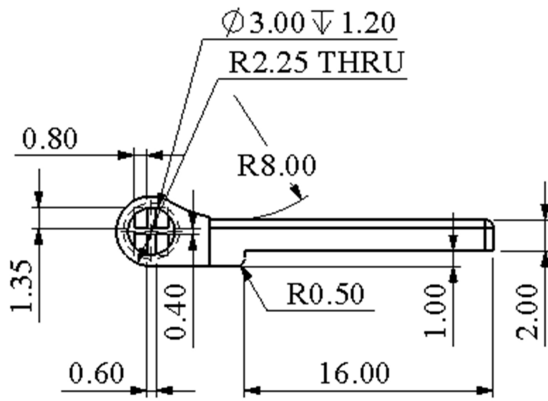
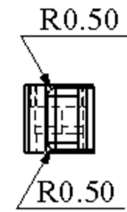
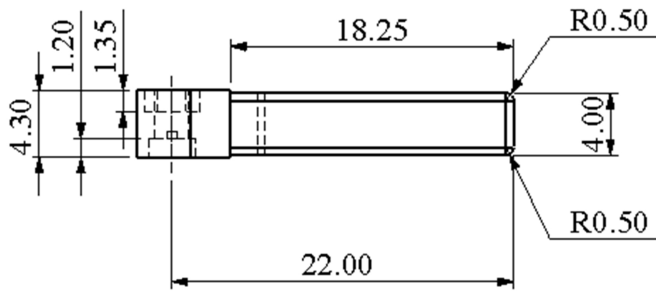
Unit: millimetre



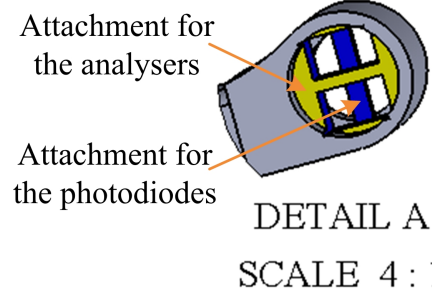
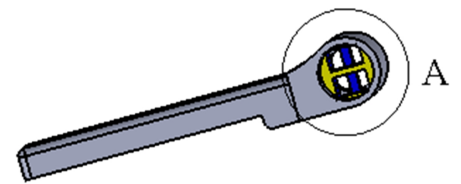
Scale: 2:1

**Wing 2 of sensor#2**

Unit: millimetre

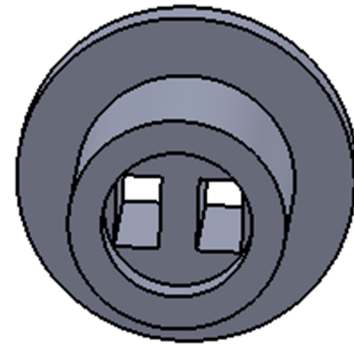
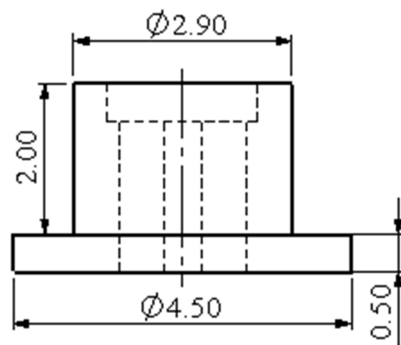
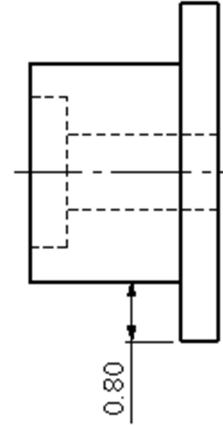
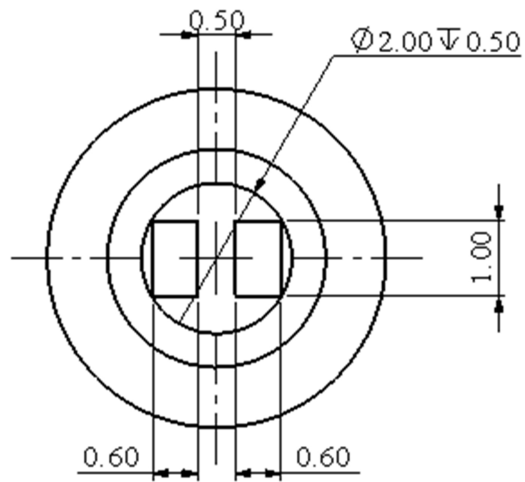


Scale: 2:1



**Holder for wires of sensor#2**

Unit: millimetre



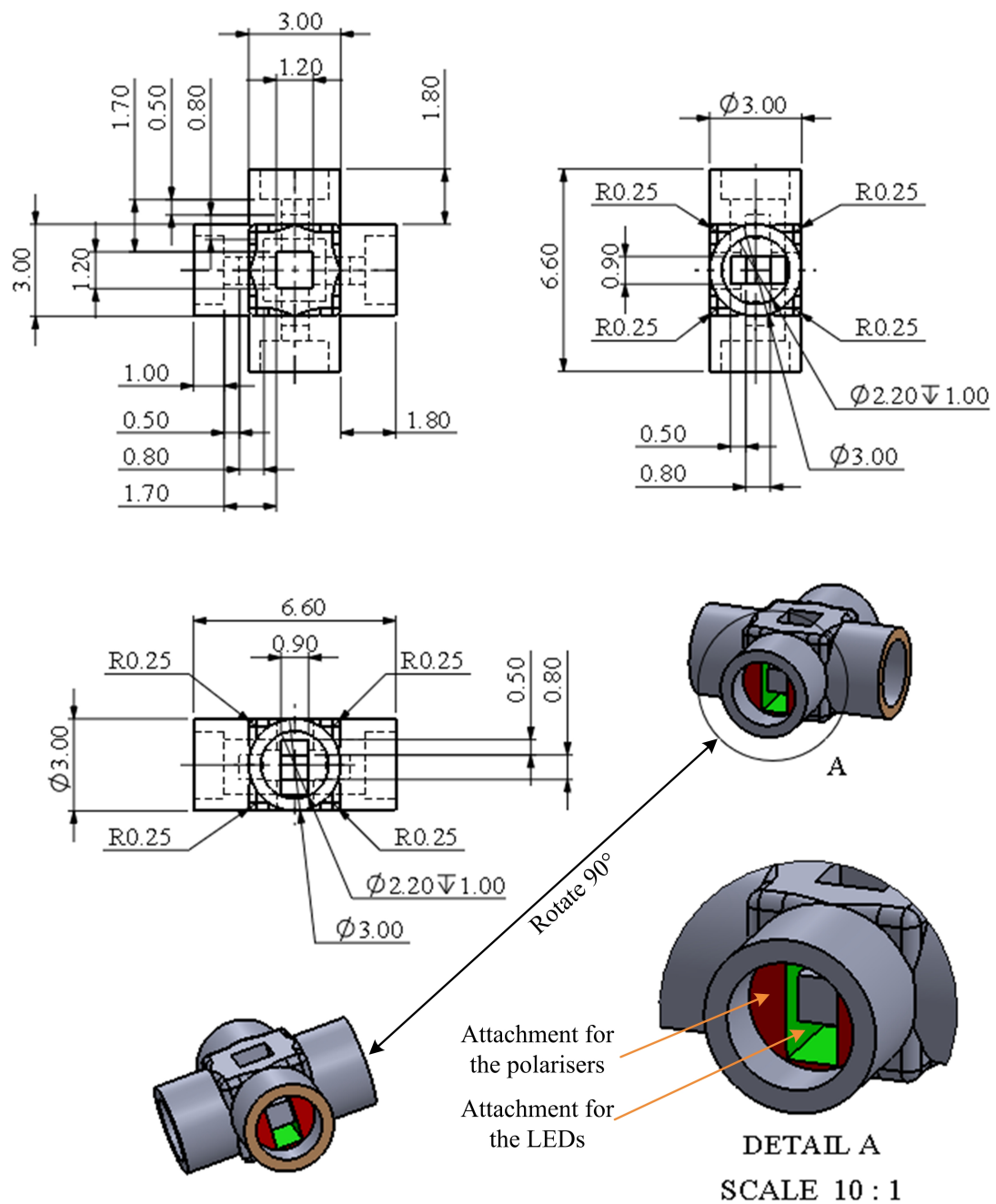
Scale: 10:1

## Technical drawing of sensor#3

The technical drawings of the 3D models of sensor#3 containing Holder for LEDs and polarisers, Wing 1, and Wing 2, are presented. The design of a rectangular part which is used to assist the sensor attachment is also introduced in the following.

### Holder for LEDs and polarisers of sensor#3

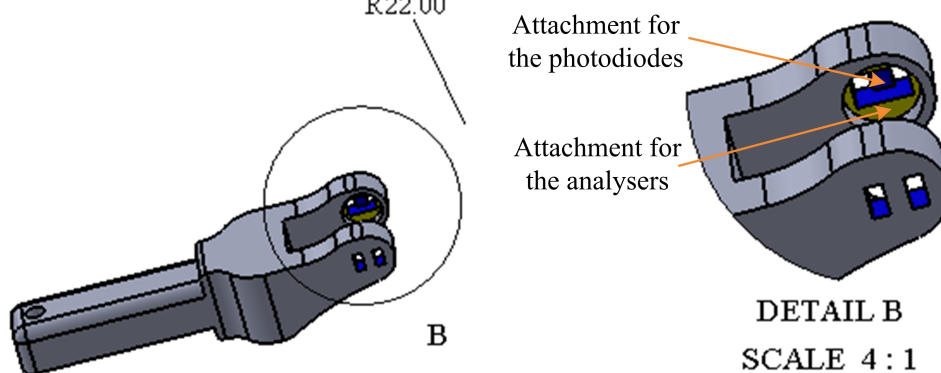
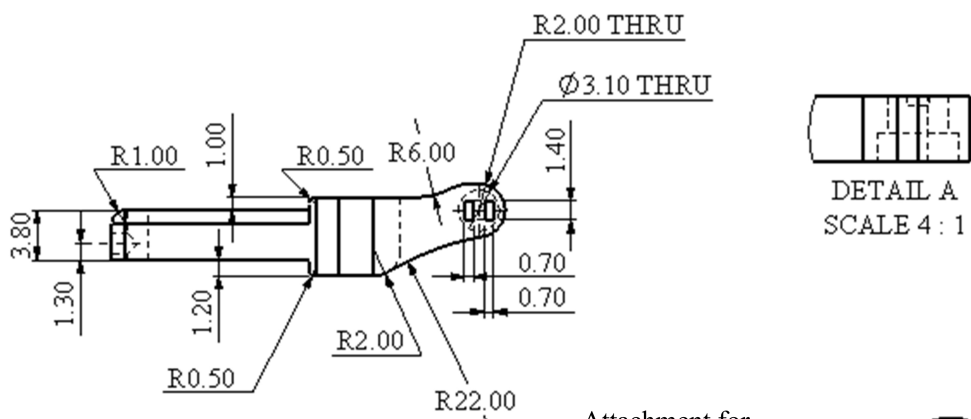
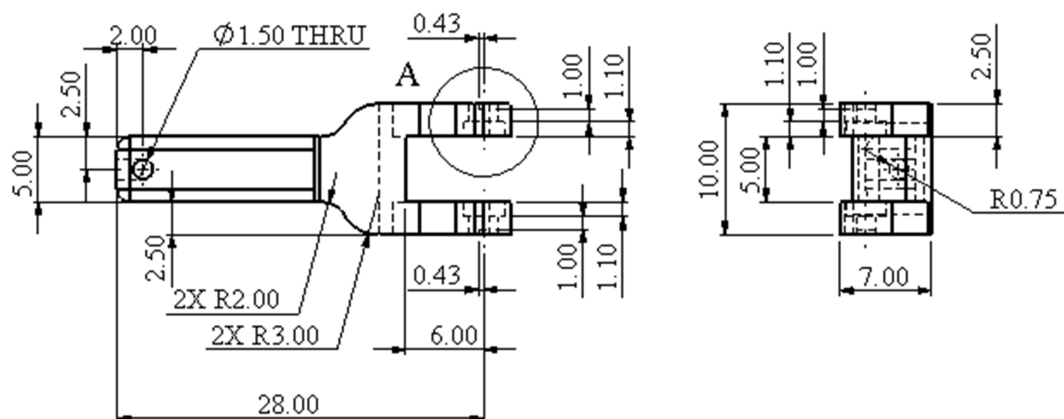
Unit: millimetre



Scale: 5:1

### Wing 1 of sensor#3

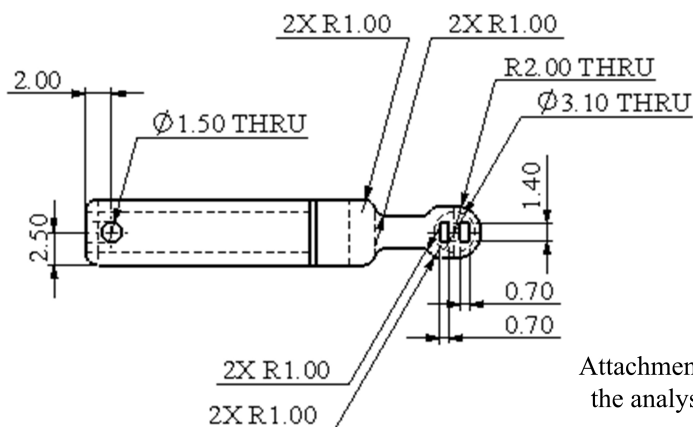
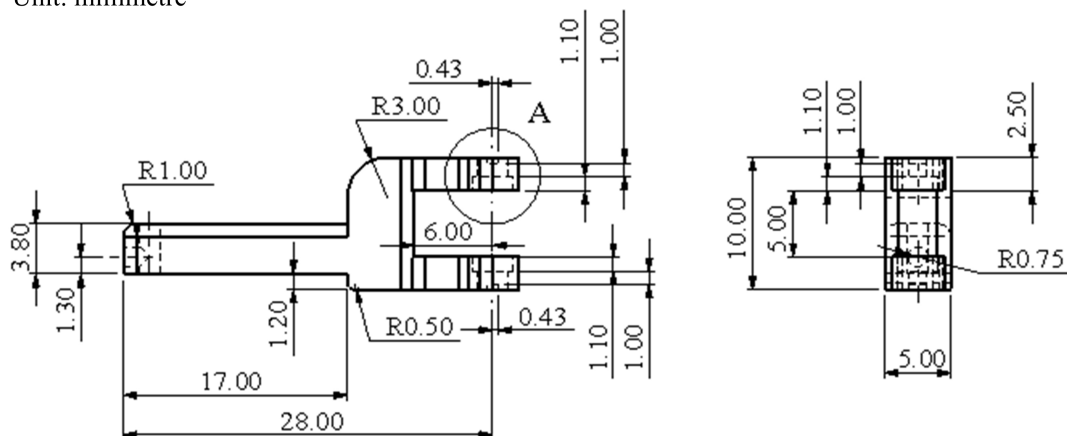
Unit: millimetre



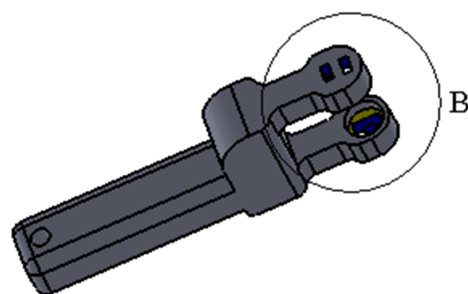
Scale: 2:1

### Wing 2 of sensor#3

Unit: millimetre

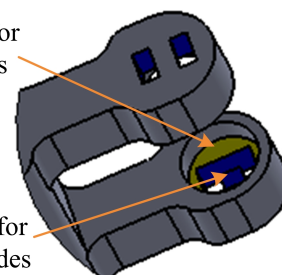


DETAIL A  
SCALE 4 : 1



Attachment for  
the analysers

Attachment for  
the photodiodes

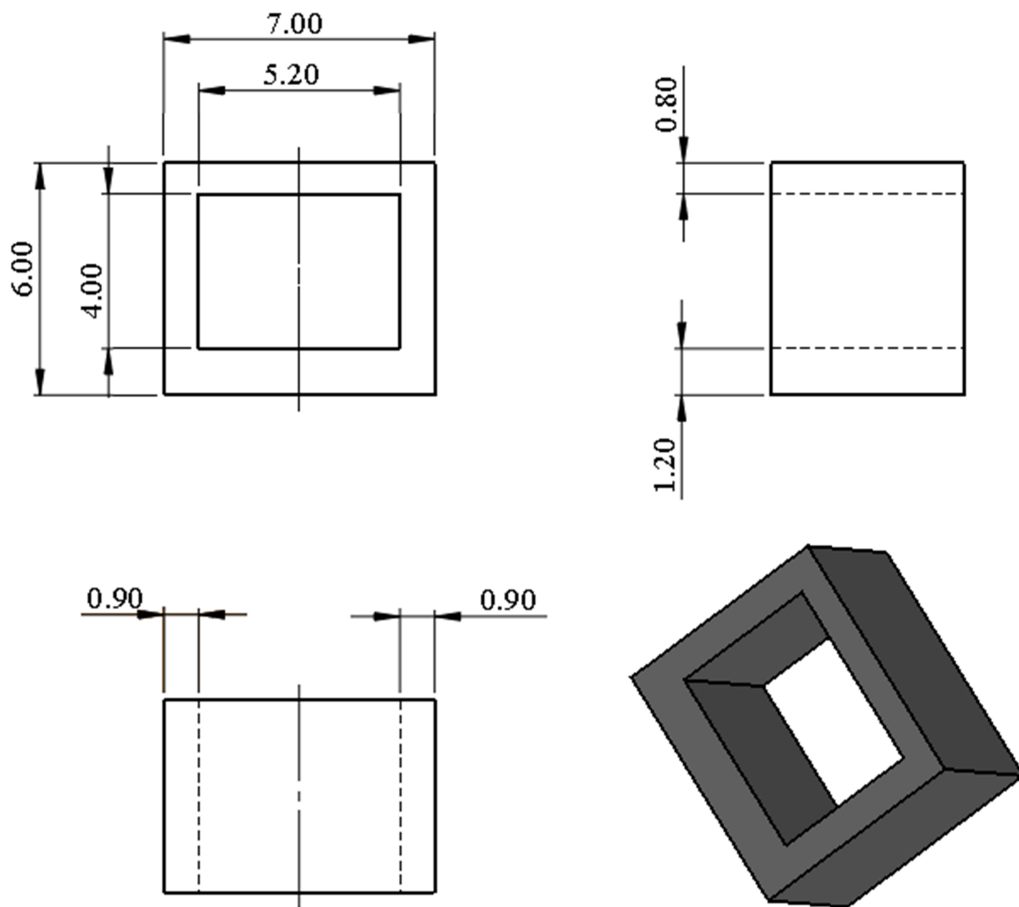


DETAIL B  
SCALE 4 : 1

Scale: 2:1

**Rectangular hollow part of sensor#3**

Unit: millimetre



Scale: 5:1

# **Appendix B**

## **Software Design**

**LabVIEW block diagram for sensor characteristics investigation**

**LabVIEW block diagram for assessing the data fusion method**

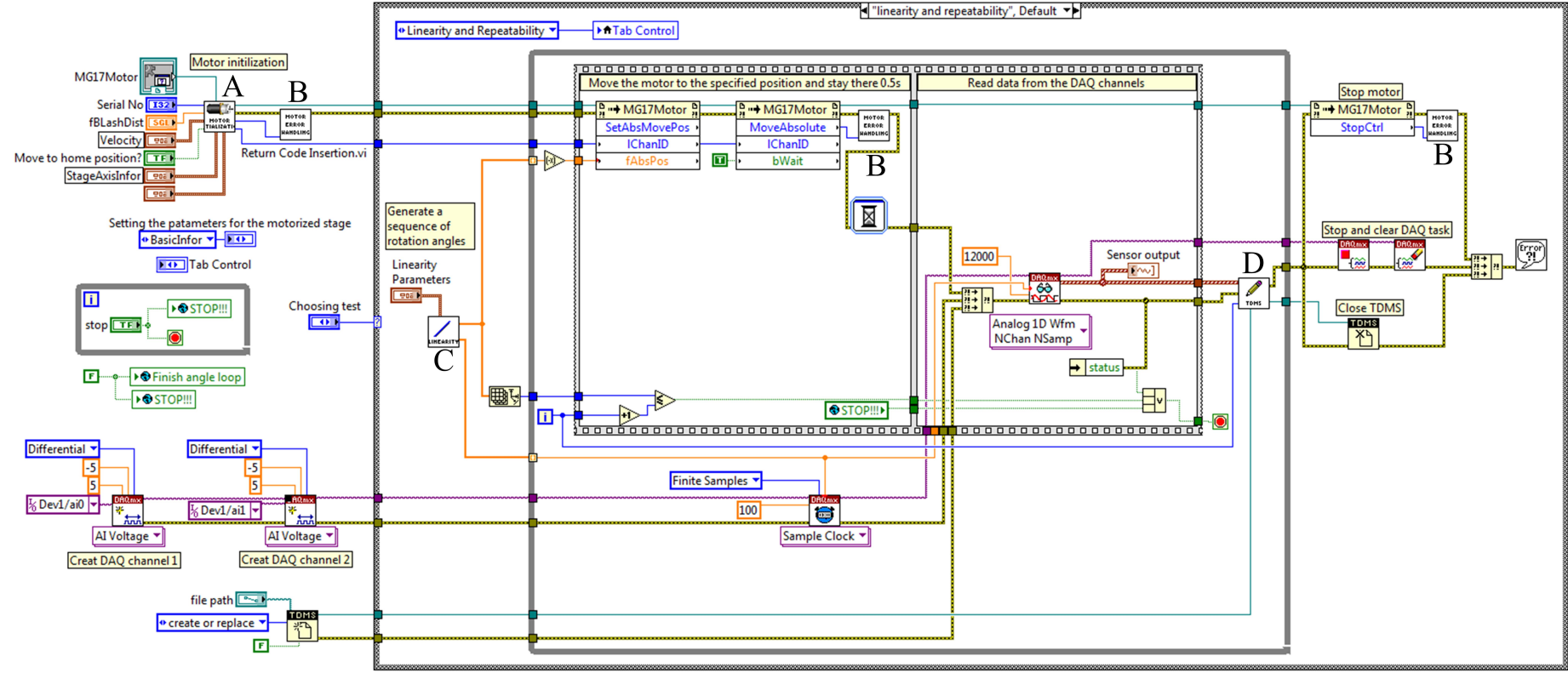
**LabVIEW block diagram for monitoring finger motion**

**Block diagram of the LabVIEW subVIs**

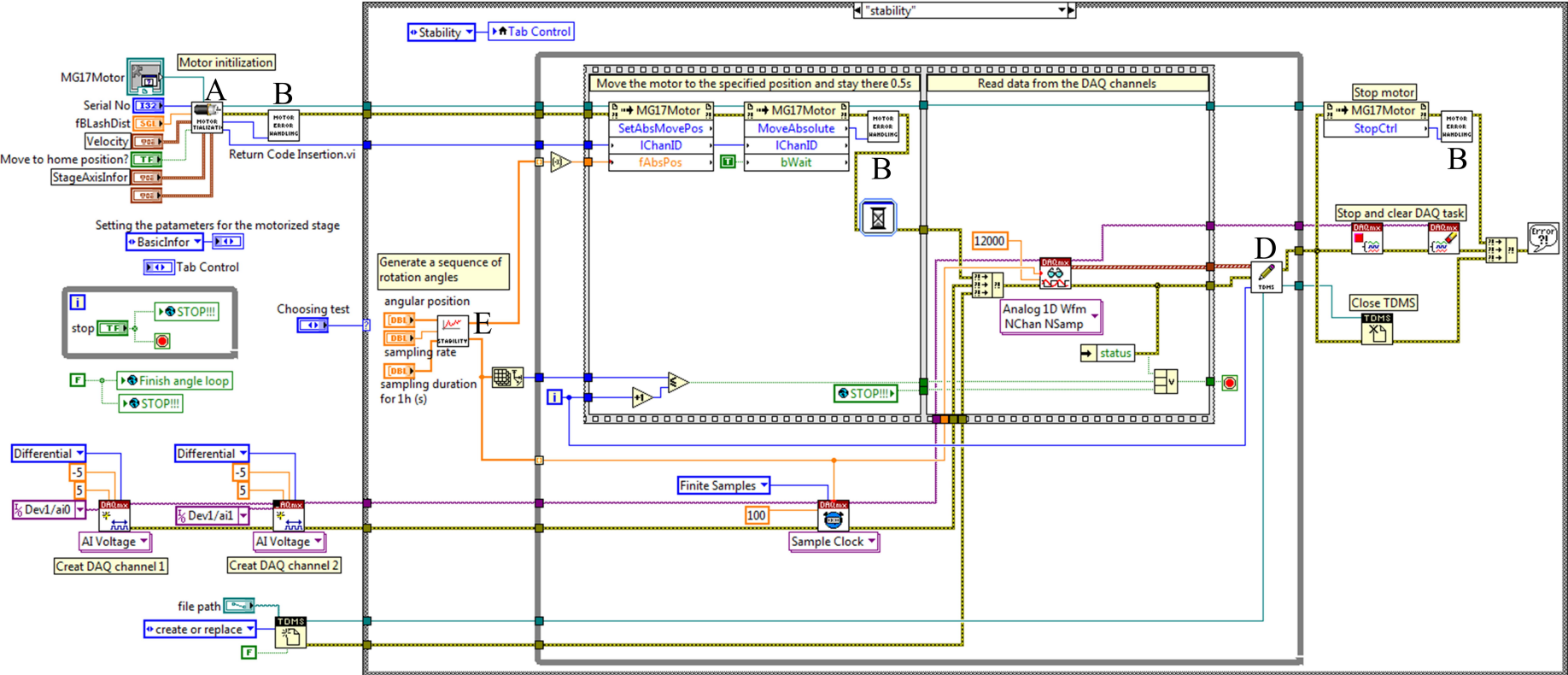
# LabVIEW block diagram for sensor characteristics investigation

To evaluate the sensor characteristics, LabVIEW programs are developed for controlling the measurements including the linearity and repeatability test, stability test, and also the dynamic response test. Each LabVIEW block diagram is presented as follows.

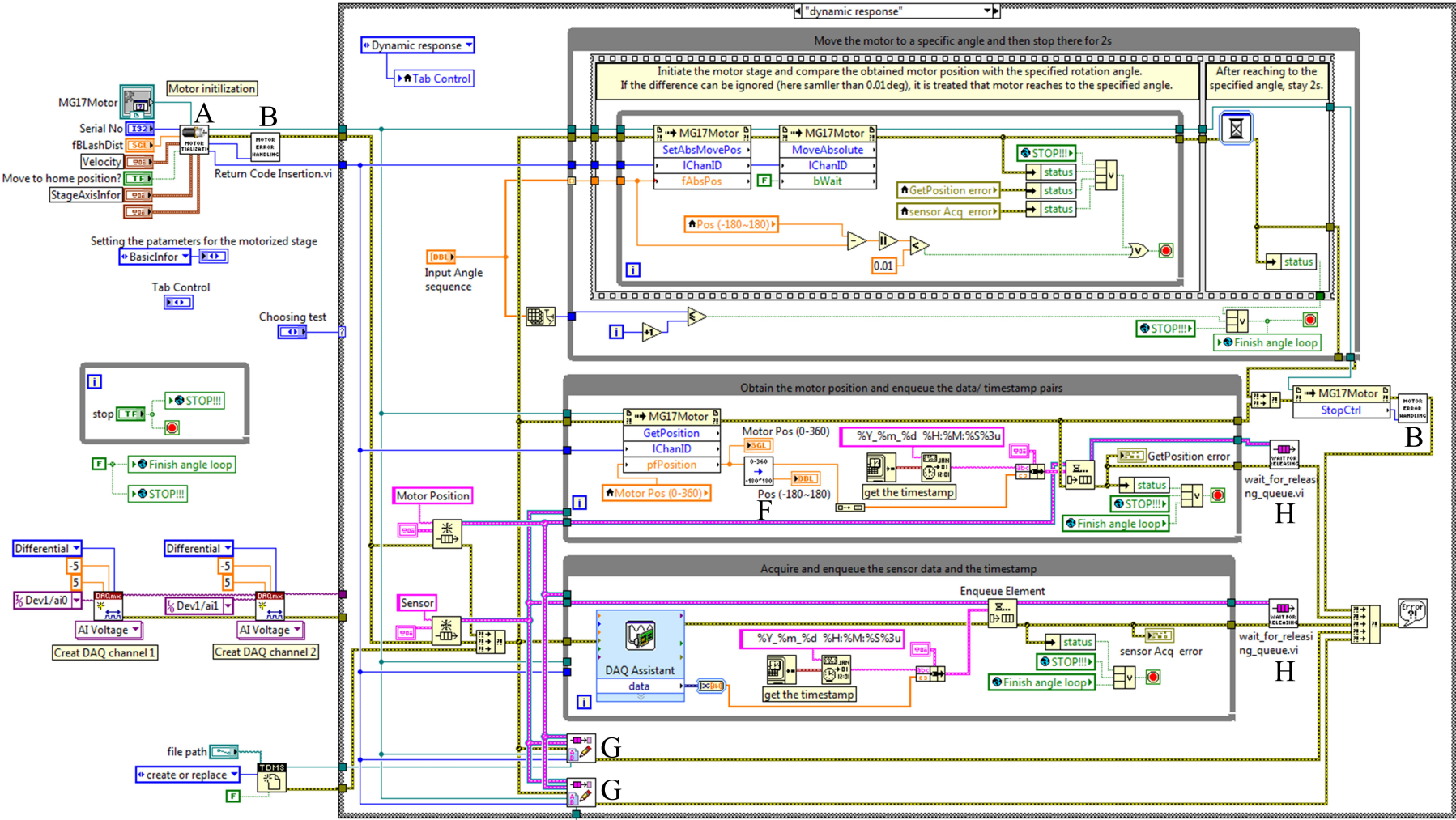
## Block diagram of the LabVIEW program for sensor linearity and repeatability testing



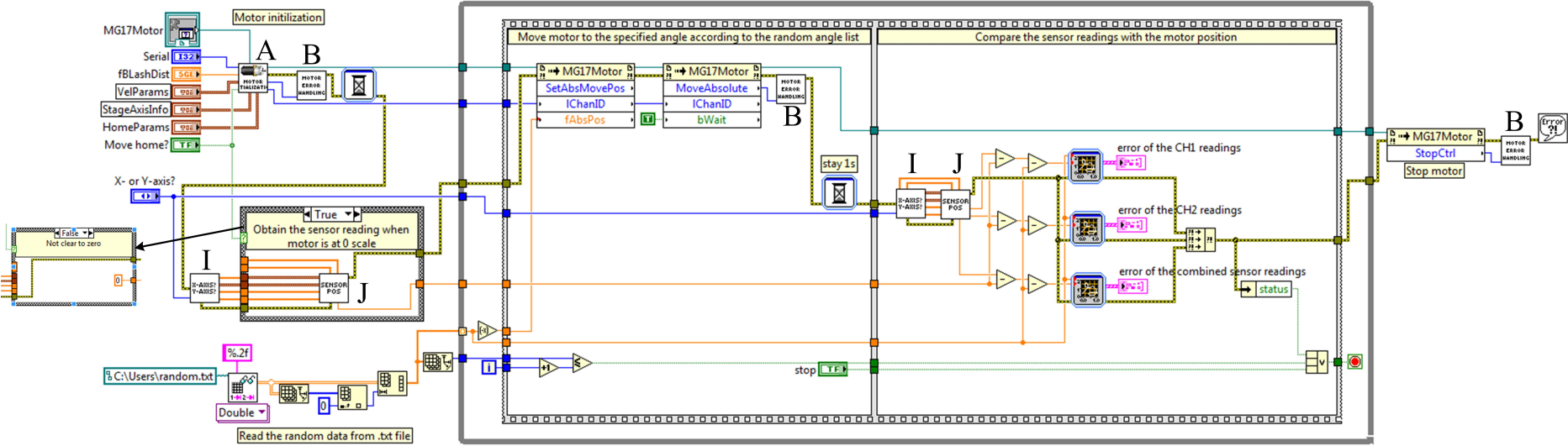
# Block diagram of the LabVIEW program for sensor stability testing



# Block diagram of the LabVIEW program for evaluating the sensor dynamic performance



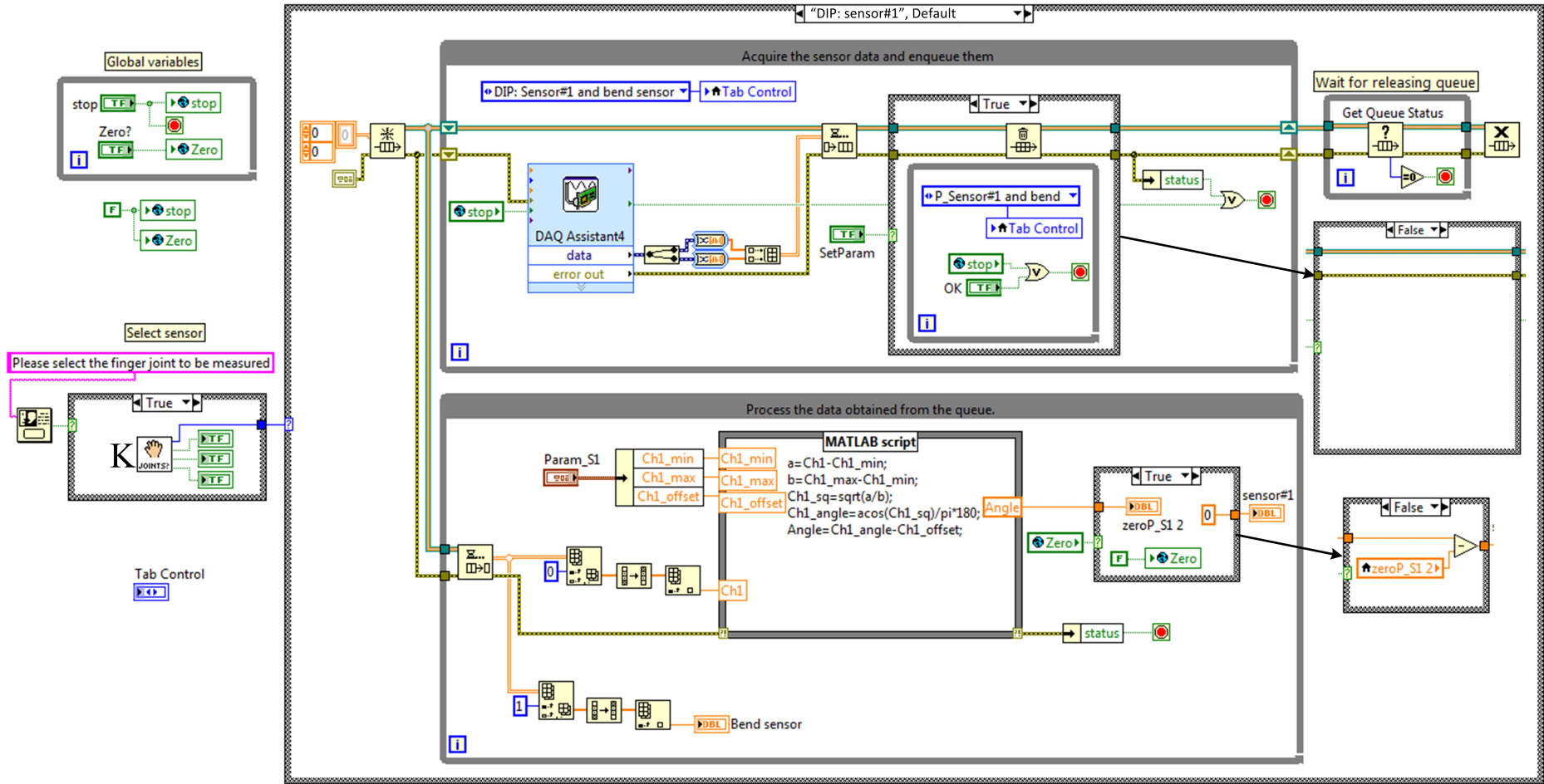
**LabVIEW block diagram for assessing the data fusion method**



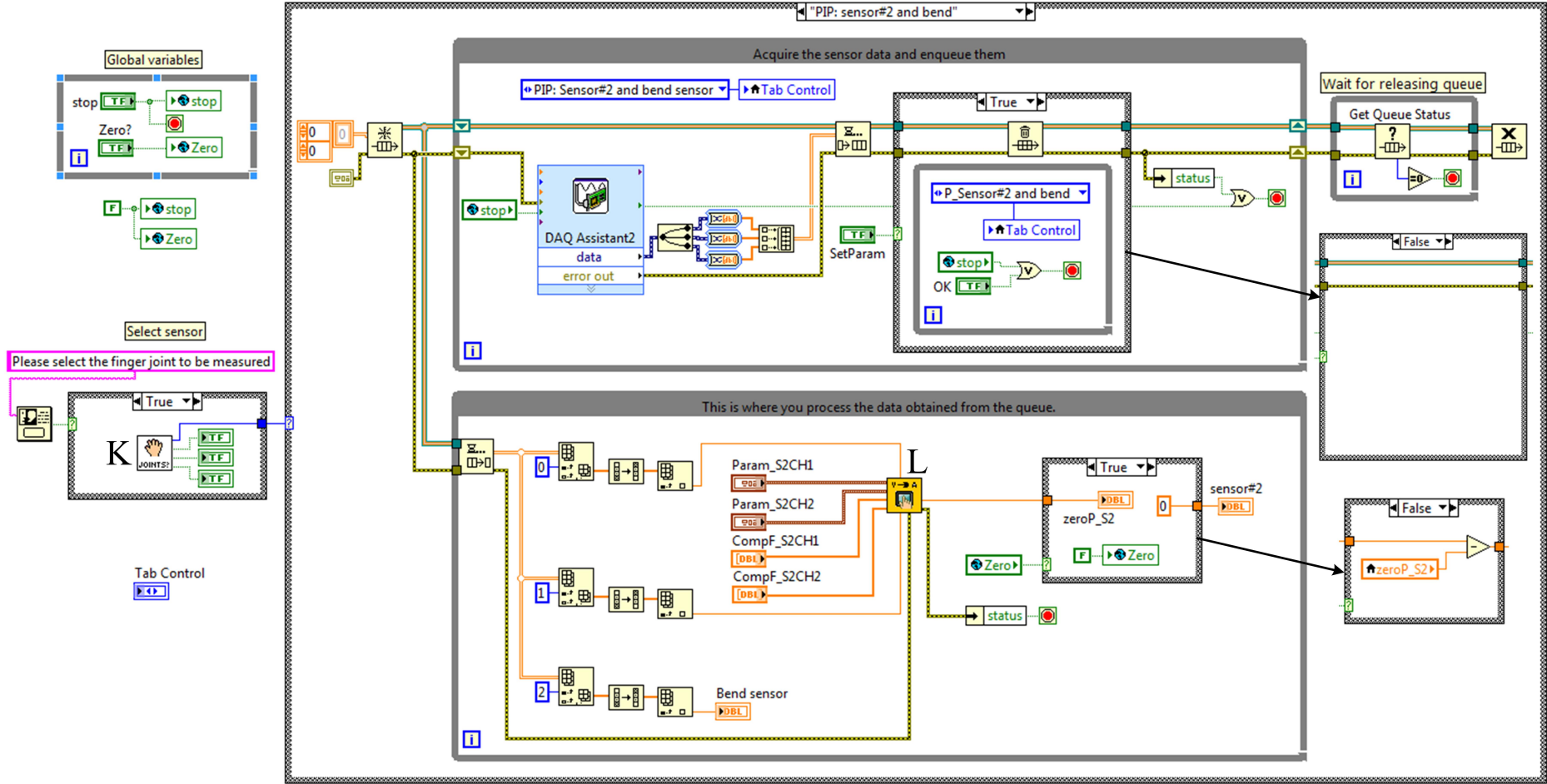
**LabVIEW block diagram for monitoring finger motion**

The following presented the LabVIEW block diagrams for controlling the finger motion measurements using sensor#1, sensor#2, sensor#3, and the commercial bend sensor.

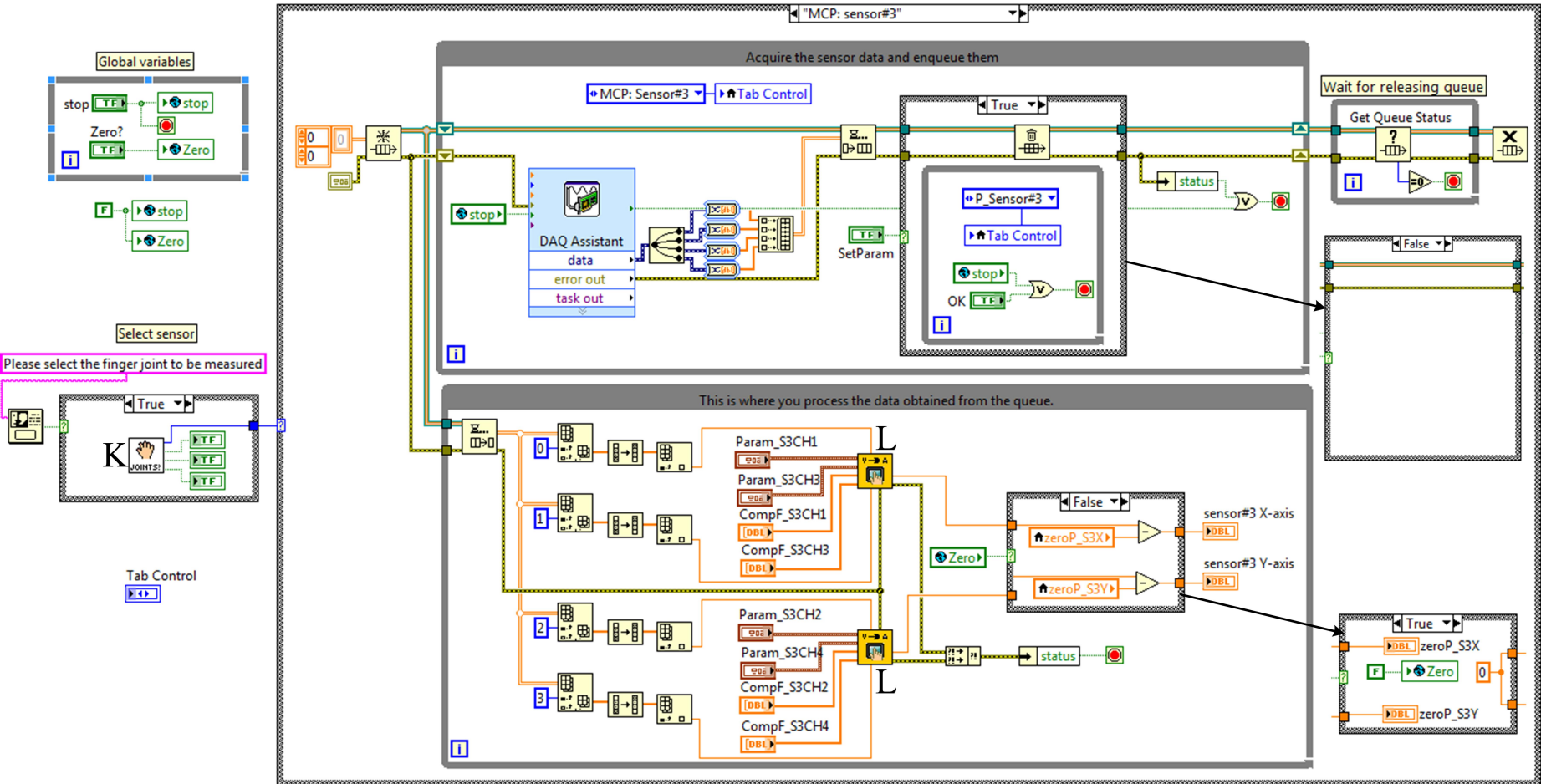
Block diagram of the LabVIEW program for monitoring the DIP joint using sensor#1



Block diagram of the LabVIEW program for monitoring the PIP joint using sensor#2 and the commercial bend sensor



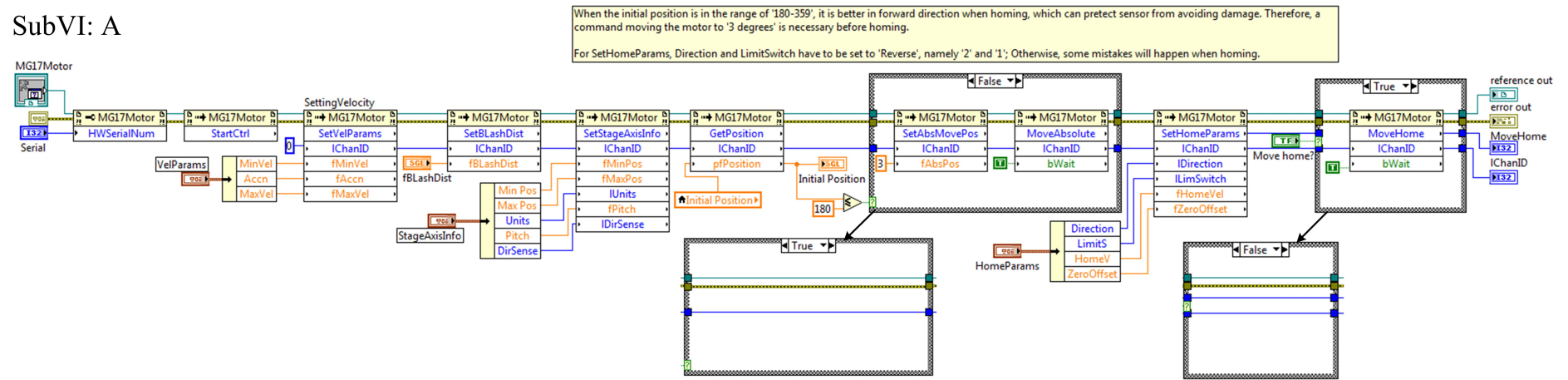
Block diagram of the LabVIEW programming for monitoring the MCP joint using sensor#3



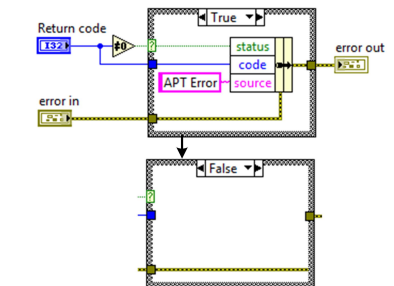
## Block diagram of the LabVIEW subVIs

All the subVIs used in the above LabVIEW programs are presented here.

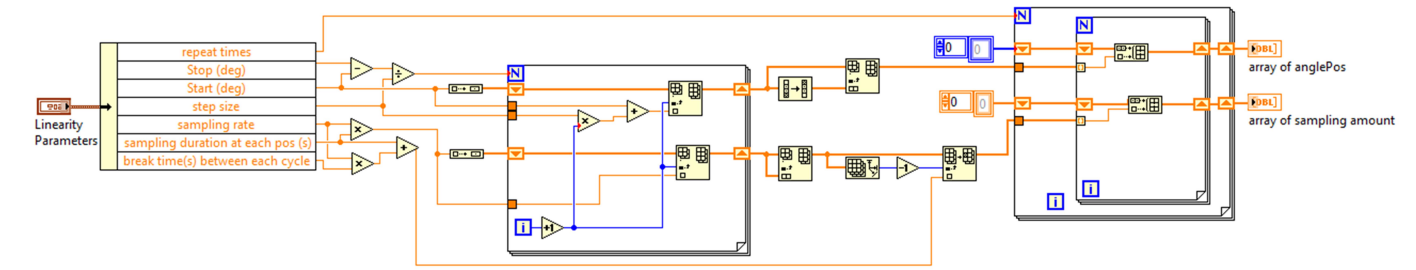
SubVI: A



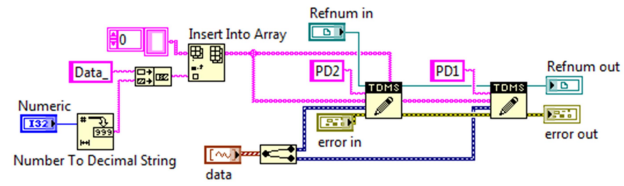
SubVI: B



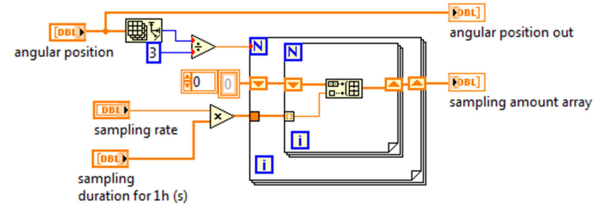
SubVI: C



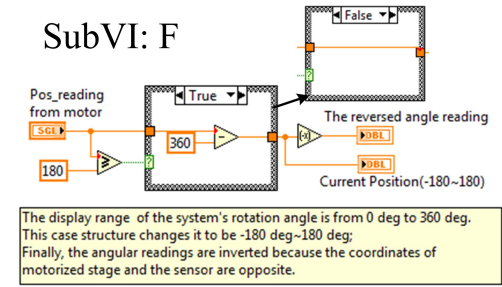
SubVI: D



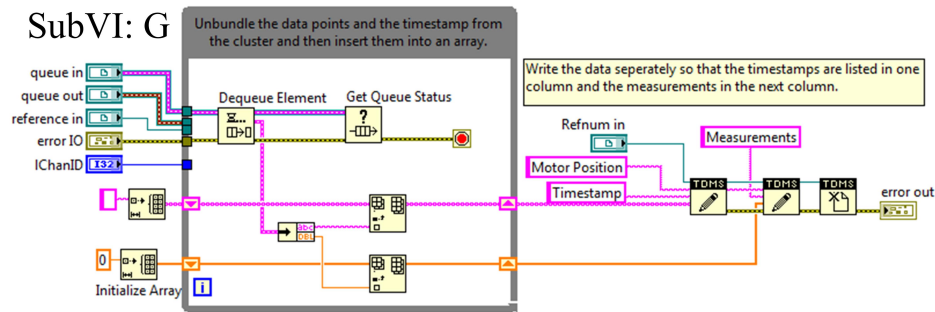
SubVI: E



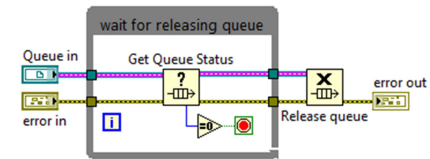
SubVI: F



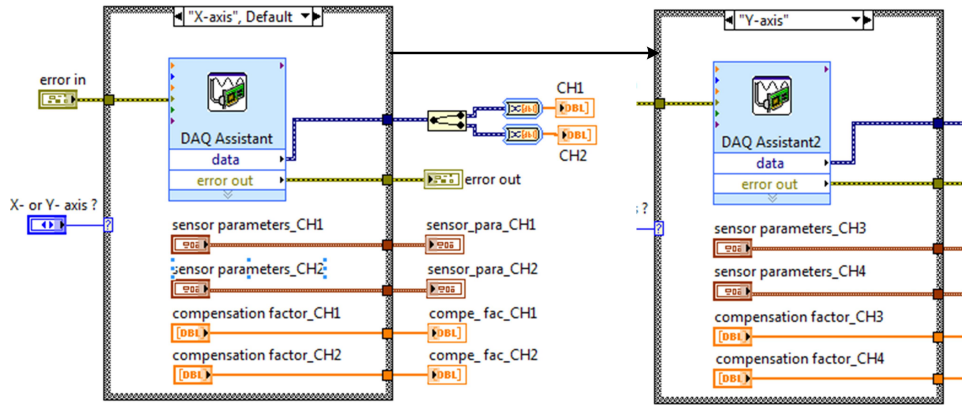
SubVI: G



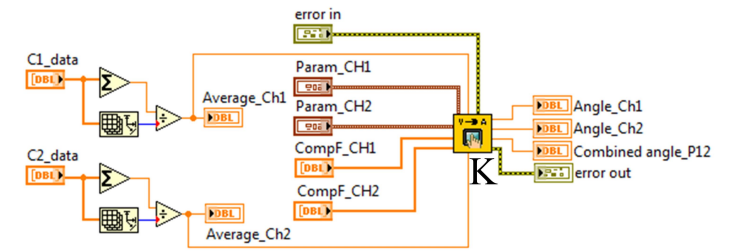
SubVI: H



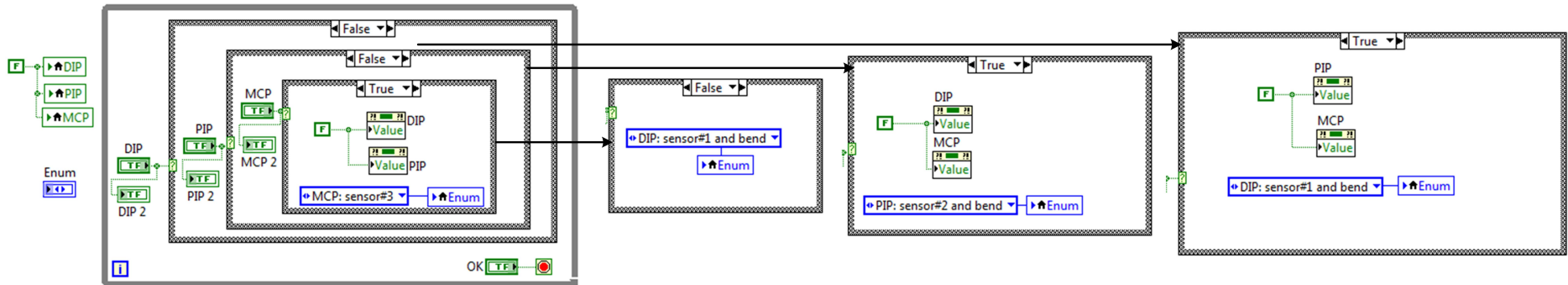
SubVI: I



SubVI: J



SubVI: K



## SubVI: L

